The Characterisation of Complex Fluids using Electrical Tomography

By

Thomas David Machin

A thesis submitted to

The University of Birmingham

For the degree of

DOCTOR OF ENGINEERING

School of Chemical Engineering
College of Engineering and Physical Sciences
University of Birmingham

February 2020

Abstract

Considered to be driving the fourth industrial revolution, digital manufacturing adopts an integrated approach to production systems that are interconnected, communicate and analyse process data for the optimisation of processes. A number of studies have highlighted that this approach can yield significant competitive advantages, through process optimisation, including, reduced operational and maintenance costs and increased sustainability. Despite such promise, a significant challenge exists to develop suitable in-line sensors and diagnostic methods that are capable of extracting real-time information to characterise formulated products.

Aligned with this challenge, a novel in-line tomographic sensing technique, termed Electrical Resistance Rheometry (ERR), has been developed which is capable of obtaining real-time rheological information of process fluids within pipe flows. By cross-correlating the fluctuations of computed conductivity pixels across and along a pipe, using non-invasive microelectrical tomography sensors, rheometric data is obtained through the direct measurement of the velocity profile. A range of model, Newtonian and non-Newtonian fluids, have been monitored using ERR with the obtained velocity profiles in excellent agreement with independent Particle Image Velocimetry (PIV) measurements. Comparison of the rheological parameters obtained from ERR with off-line rheometry demonstrated agreement in excess of 98 %. In-pipe spatial and temporal analyses additionally afford the simultaneous interrogation of localised and global mixing behaviour to offer new insights into in process characterisation of formulated products. Due to the success of this development, the commercialisation and product development of this technique by the sponsoring company has been discussed within this thesis. From this, a case study applying this technique at the pilot plant of a global manufacturer of personal and homecare products has demonstrated its

potential to monitor industrial fluids. The principles of ERR have additionally been extended to capture in-line formulation properties in agitated vessels.

A secondary innovative characterisation technique is additionally demonstrated, which is capable of elucidating key in-line structural and quality attributes of formulated products, termed Electrical Impedance Fingerprinting (EIF). Phase information from tomographic sensors is combined with multi-layered feedforward neural networks to directly obtain process information without the requirement of tomographic reconstruction. EIF has been exploited to capture the composition of a number of surfactant-electrolyte solutions, from which key quality attributes may subsequently be inferred. Using supervised machine learning algorithms, forty-four sodium lauryl ether sulphate formulations were able to be identified with an accuracy of 99.7 %. This is extended to an agitated vessel, with the electrolyte content able to be continuously predicted with a root mean squared error of 0.026 wt% for both trained and non-trained values. The understanding obtained from this technique is coupled with tomographic reconstruction to provide a comprehensive mixing analysis of surfactant-electrolyte systems.

The application of Electrical Impedance Tomography (EIT) has also been analysed in the context of multi-component slurries. EIT offers a non-nuclear alternative to the density measurement required in hydraulic conveying. However, the complex surface phenomena of colloidal clay dispersions are seen to impact upon this in-line measurement. Accordingly, the electrical properties of kaolin/sand slurries are investigated using Electrical Impedance Spectroscopy (EIS), with this obtained information then directly applied to optimise EIT measurements. From such studies, novel phase and susceptibility tomograms have been developed which are capable of enhancing the sensitivity of the densitometry measurement, whilst providing an ability to distinguish between the multiple components of the slurry.

Acknowledgements

I would like to express my gratitude to my academic supervisors, Prof. Mark Simmons and Dr. Richard Greenwood for providing me with this opportunity, providing crucial insights for my work and helping me to maximise the potential of this project. I would also like to thank everybody at Industrial Tomography Systems Ltd. for all of their never ending support, vital knowledge and ensuring that my project was a joy to conduct throughout. I reserve special thanks to Dr. Kent Wei, who has mentored me from the first day, tidied up my messy computer code and always there when I needed help. I cannot thank you enough for your input and I'm sure we'll enjoy many bubble teas together, my friend.

Alongside Industrial Tomography Systems Ltd, I would like to thank the EPSRC for sponsoring this project and allowing me the freedom to develop novel techniques within this research. This has also permitted me to present this work at major conferences and develop my communication skills greatly. I would also like to thank the remaining members of the EMFormR grant for your input into the project: Johnson Matthey, Unilever, University of Manchester and Innovate UK.

Το αγάπη μου, Elle, since the time I 'kind've, maybe asked you out for lunch', you have been such a positive influence on my life. When I'd had a bad day you never failed to make me smile, always encouraging about my work and have made every moment together incredible. Σε αγαπω παρα πολυ.

To my brother, Ben, and mother, Angela, I would like to thank you for your unwavering support, love and care throughout the project. You have worked so hard to ensure I was able to do everything I needed to and I could not have done this without you. This thesis is dedicated to my father, my hero, David Machin. I hope this work makes you proud.

Table of Contents

List of Figures

List of Tables

Chapter 1

Introduction

1.1 Background

The digital revolution has already breached a number of sectors including: media, finance, consumer products and healthcare; however, there is currently an emerging trend to apply these principles to the processing industries (Hartmann et al., 2019). Considered to be driving the fourth industrial revolution, digital manufacturing is an integrated approach to develop production systems which are not only interconnected, but communicate, analyse process data and use this information to optimise process decisions (Paritala et al., 2017). A number of studies have highlighted that digital manufacturing presents an opportunity to introduce competitive advantage, increased sustainability and reduced operational and maintenance costs through process optimisation (Holmstrom et al., 2016; Paritala et al., 2017; Choi et al., 2015).

Within digital manufacturing, a substantial challenge exists in the development of appropriate in-line sensors and diagnostic methods which can elucidate real-time information to characterise formulated products i.e. rheological properties and phase distributions (Forte et al., 2018). Tomographic methods, however, have considerable potential to address this challenge. With etymology derived from Ancient Greek, with tomos, meaning 'slice or section,' and grapho, meaning image, tomography is an imaging technique which generates image slices using a penetrating wave. A wide range of tomographic modalities have been successfully employed to monitor processes including X-ray computed tomography (Ford et al., 2008) and magnetic resonance imaging (Blythe et al., 2017). Despite such success, the

requirement for either high energy radiation or high intensity magnetic fields poses both safety and economic concerns, ensuring that in-plant applicability is drastically reduced.

Due to their non-invasive, safe and robust nature and suitability to interrogate process fluids without the limitation of optical opacity, electrical techniques provide a useful basis upon which to develop industrial characterisation techniques (Wang, 2015). Electrical Tomography (ET) exploits the propagation of an electrical field with signals acquired from the periphery of a process domain, to uncover process information about the nature and distribution of components within the sensing domain. Similarly to numerous other tomographic modalities, electrical techniques evolved from clinical applications. Swanson (1976) proposed an 'impedance camera' with electrode arrays placed upon the patient's chest and back in an attempt to image body tissues. This technique was adapted to process monitoring with the first industrial system, known as the 'Manchester system', developed in 1997 (Boone et al, 1997). Since its inception, the most prevalent applications of ET involve process mixing studies and multiphase flow monitoring and has been utilised in mixers (Carletti, 2014; Pakzad et al., 2008); industrial pipelines (Machin et al., 2018; Henningson et al., 2006; White et al., 2001); chemical reactors (Bolton et al., 2004; Vilar et al., 2008) and separators. As the technology is being applied by early adopters, there is a requirement for the fundamental understanding of how tomographic measurements relate to in-line quality attributes of key processing operations. In addition to 'traditional' tomographic analyses, greater information can be gained from tomographic measurements which are capable of affording new insights into the characterisation of fluids relevant to formulated products. Accordingly, within this thesis the products of interest are complex fluids which are either formulated products or the intermediate materials utilised to manufacture them.

1.2 Thesis Objectives

Developing an understanding of how key in-line quality attributes of processes may be obtained from information provided by electrical tomography is the overall aim of this thesis. However, this can be segregated into a number of individual objectives:

1. *Characterisation of product microstructure via a novel technique to extract rheological properties in-line, within both pipes and vessels*

The performance of formulated fluids is dependent upon achieving a target microstructure which may be evaluated by the rheological properties of the fluid. Typically, rheological properties are monitored via off-line rotational rheometry, with the product required to be removed from the process stream via careful sampling. Often, the information obtained from off-line rheometry is considered, without assumptions, as applicable to flows in real processes. However, this approach is in the majority unsatisfactory as the sample properties may not be representative of the product microstructure (as a function of the time-shear history received) during processing. In-situ measurements remove this deficiency as they are inherently conducted within the real flow environments and eliminate sampling issues. Accordingly, there is an ever-increasing demand for in-line rheometry techniques. Within this thesis a key objective is thus to develop novel techniques to extract rheological properties in-line, within both pipes and vessels, with the ultimate aim to elevate rheometry from a quality control tool to one which is capable of optimising and controlling processes.

2. *In-line characterisation of surfactant-electrolyte formulations using electrical impedance measurements*

Personal and home care products typically contain liquid surfactants such as sodium lauryl ether sulphate (SLES). These surfactants help to facilitate the core cleaning application and can also boost stability and improve texture and appearance of the products (Yu et al., 2008). Surfactants self-assemble into different mesophase structures depending upon their interaction with electrolytes, temperature and concentration in order to minimise the free energy of the system (Evans and Wennerström, 1999). Such assemblies give rise to drastic changes in many physical properties including: self-diffusion, surface tension, solubilisation and both shear and viscoelastic rheological properties. These evolving properties impact greatly upon both in-process efficiency and final product quality. Consequently, the in-line characterisation of such formulations affords the potential for process optimisation and control within both stirred vessels and industrial pipelines.

3. *In-line characterisation of the composition and density of non-Newtonian solid/liquid mixtures*

Electrical Tomography affords a non-nucleonic alternative to the measurement of density within hydraulic conveying systems. The removal of radioactive sources mitigates a vast number of safety and economic concerns during processing. However, within such installations the conveyed materials are often multi-component mixtures which observe complex interactions at the colloidal scale. The surface interactions of clay dispersions ensure that their electrical behaviour is greatly dependent upon the properties of the continuous phase, namely pH and ionic concentration. This thesis aims to understand how

such interactions impact upon tomographic, and ultimately density, measurements with a view to optimising the alternative to nucleonic density measurements within pipe flow.

1.3 Business Case – Industrial Tomography Systems Ltd.

Industrial Tomography Systems Ltd. (ITS), the industrial sponsor of this project, is a small to medium enterprise which specialises in the manufacture and application of innovative electrically-based process tomography systems into process industries. ITS operates globally, across in excess of twenty countries, within key process sectors including: fast-moving consumer goods, minerals, nuclear, pharmaceuticals and speciality chemicals. This project seeks to develop innovative data interpretation and sensing techniques to enhance and potentially expand the existing product range of ITS. These developments ensure that vital process parameters are able to be monitored by the end user with the obtained information utilised to reduce operational costs via process optimisation.

According to a study by Fior Markets (2019), the global market size for rheometry will grow to US$ 130 million in 2024, from US$ 120 million in 2019. Hitherto, within this growing market, no commercially viable technique has been developed capable of performing in-line rheometry efficiently across a wide range of fluids (Rees, 2014). If a minor share of this market was able to be occupied, this would still represent a significant revenue stream for the sponsoring company. Such a share is potentially attainable due to the substantial advantages obtained from in-line rheometry over conventional techniques. Aligned with the growth of digital manufacturing, the demand for effective in-situ characterisation techniques is expected to increase and hence provide an additional revenue stream.

The characterisation of density parameters is vital for the operation and optimisation of hydraulic conveying systems in dredging applications. These parameters are typically monitored using the attenuation of radiative sources with the majority of dredging operations possessing a nucleonic density meter. Industrial Tomography Systems Ltd. offers an

alternative to densitometry, which removes the safety and economic concerns of the radiative sources. Whilst this has been proven to be effective in marine dredging applications, measurement errors arise in the low conductivity applications, such as river and reservoir dredging. The optimisation of this measurement in low conductivity applications will enable the sponsoring company to increase its market share within this sector. Applications which observe large variations in continuous phase conductivity may also then be targeted, i.e. mining.

1.4 Thesis Layout

This thesis is composed of eight chapters including: an introduction; a technical review of electrical tomography techniques, four stand-alone results chapters and an industrial case study, followed by the overall conclusions. Whilst each results chapter utilises electrical tomography modalities, these chapters focus upon differing aspects of formulation characterisation with different methodologies applied accordingly. As a result, the results chapters are self-contained with appropriate literature reviews and methodologies outlined.

- Chapter 1 is an introduction to the thesis subject and defines the objectives and business case for the work undertaken.
- Chapter 2 contains a technical review of the Electrical Tomography techniques explored throughout this thesis with a particular focus upon aspects which impact upon the results.
- Chapter 3 describes the development of a novel in-pipe rheometry technique which is capable of extracting the in-situ rheological properties of a formulated product; this chapter contains information from published works. Due to the success of this development, the commercialisation of the technique is also discussed.

- Chapter 4 adapts the findings and techniques from the previous chapter to agitated vessels, with a technique described which is capable of determining the shear rate at a vessel wall and ultimately infer the viscosity within this region.
- Chapter 5 demonstrates an innovative formulation characterisation technique, based upon phase information from Electrical Impedance Tomography measurements. This was then utilised to characterise the structural properties of aqueous sodium lauryl ether sulphate solutions within both pipe flow and stirred tanks.
- Chapter 6 highlights the optimisation of an existing alternative to nucleonic density measurements within hydraulic transport. Multi-component slurries are initially characterised using Electrical Impedance Spectroscopy with the knowledge gained employed to optimise tomographic measurements.
- Chapter 7 is a case study which utilises the industrial in-line rotational rheometer, outlined in Chapter 3, to monitor in-line rheological properties of personal and homecare products. This was conducted at the pilot plant of a global manufacturer.
- Chapter 8 is the conclusion chapter to summarise the overall impacts of the work conducted and outline future work recommendations.
- A number of appendices additionally exist, which act as supplementary material for the results chapters.

1.5 Publications

Results presented within this thesis have been published in the following journals and conference proceedings:

Machin, T. D; Wei, H-S; Greenwood, R. W; Simmons, M. J. H. Simmons. (2018). In-pipe Rheology and Mixing Characterisation using Electrical Resistance Sensing. *Chemical Engineering Science:* 187, 327-341.

Machin. T. D; Wei, K; Greenwood, R. W; Simmons, M. J. H. (2018). Electrical Resistance Rheometry - The application of multi-scale tomography sensors to provide in-pipe rheology in complex processes. *Conference Proceedings: 9th World Congress of Industrial Process Tomography, 2nd - 6th September 2018: Bath, UK.* **Excellent Paper Award**

Machin, T. D; Wei, K; Greenwood, R. W; Simmons, M. J. H. (2017). The application of process tomography for the in-line measurement of rheology. *Conference Proceedings: The Annual European Rheology Conference 2017, 3rd - 6th April 2017: Copenhagen, Denmark.*

1.6 Conferences

Results presented in this thesis have been presented in the following conferences, with the speaker underlined:

Oral Presentation: Machin, T. D; Wei, K; Greenwood, R. W; Simmons, M. J. H. (2018). Electrical Resistance Rheometry: The application of multi-scale tomography sensors to provide in-pipe rheology in complex processes. *9th World Congress of Industrial Process Tomography, 2nd - 6th September 2018: Bath, UK.* **Excellent Presentation Award**

Poster Presentation: Machin, T. D; Wei, K; Greenwood, R. W; Simmons, M. J. H. (2017). Real-time rheology and mixing using process tomography. *10th World Congress of Chemical Engineering, 1st - 5th October 2017: Barcelona, Spain.*

Oral Presentation: Machin, T. D; Wei, K; Greenwood, R. W; Simmons, M. J. H. (2017). The in-line rheology of colloids. *UK Colloids 2017, 10th - 12th July 2017: Manchester, UK.*

Poster Presentation: Machin, T. D; Wei, K; Greenwood, R. W; Simmons, M. J. H. (2017). The application of process tomography for the in-line measurement of rheology. *Conference Proceedings: The Annual European Rheology Conference 2017, 3rd - 6th April 2017: Copenhagen, Denmark.*

Oral Presentation: Machin, T. D; Wei, K; Greenwood, R. W; Simmons, M. J. H. (2016). Rheology of complex multiphase fluids using process tomography. *Advanced Process Analytics and Control Tools: Chester, UK.*

1.7 References

Bolton, G; Hooper, C; Mann, R; Stitt, E.H. (2004). Flow distribution and velocity measurement in a radial flow fixed bed reactor using electrical resistance tomography. *Chemical Engineering Science.* 59, 1989-1997.

Boone, R; Barber, D; Brown, B. R. (1997). Review: Imaging with electricity: report of the European concerted action on impedance tomography. *Journal of Medical Engineering and Technology:* 21 (6), 201 – 232.

Blythe, T.W; Sederman, A; Stitt, E.H; York, A; Gladden, L. (2017). PFG NMR and Bayesian analysis to characterise non-Newtonian fluids. *Journal of Magnetic Resonance: 274, 103-114.*

Carletti, C; Montante, G; Westerlund, T; Paglianti, A. (2014). *Analysis of solid concentration distribution in dense solid-liquid stirred tanks by electrical resistance tomography. Chemical Engineering Science.* 119, 53-64.

Choi, S; Jun, C; Zhao, W. B; Noh, S. D. (2015). Digital Manufacturing in Smart Manufacturing Systems: Contribution, Barriers, and Future Directions. *Advances in Production Management Systems: 460, 21-29.*

Evans, D. F; Wennerström, H. (1999). *The Colloidal Domain - Where Physics, Chemistry, Biology and technology meet.* Wiley-VCH: New York.

Fior Markets. (2019). *Global Rheometer Market Growth.* Available: https://www.globalbankingandfinance.com/category/news/global-rheometer-market-2019-revenue-ta-instruments-anton-paar-thermo-fisher-scientific/. Last accessed 23rd Oct 2019.

Ford, J.J; Heindel, T.J; Jensen, T.C; Drake, J.B. (2008). X-ray computed tomography of a gas-sparged stirred tank reactor. *Chemical Engineering Science: 63(8), 6371-6380.*

Forte, G; Alberini, F; Simmons, M.J.H; Stitt, E.H. (2019). Measuring gas hold-up in gas-liquid/gas-solid-liquid stirred tanks with an electrical resistance tomography linear probe. *AIChE Journal.*

Hartmann, B; King, W. P; Narayana, S. (2019). *Digital manufacturing: The revolution will be virtualized.* McKinsey & Company: New York.

Holmström, J; Holweg, M; Khajavi, S. H; Partanen, J. (2016). The direct digital manufacturing (r) evolution: definition of a research agenda. *Operations Management Research, 1-10.*

Machin, T. D; Wei, H-S; Greenwood, R. W; Simmons, M. J. H. Simmons. (2018). In-pipe Rheology and Mixing Characterisation using Electrical Resistance Sensing. *Chemical Engineering Science:* 187, 327-341.

Pakzad, L; Ein-Mozaffari, F; Chan, P. (2008). Using electrical resistance tomography and computational fluid dynamics modelling to study the formation of caverns in the moxing of pseudoplastic fluids possessing a yield stress. *Chemical Engineering Science.* 63, 2508-2522.

Paritala, P. K; Manchikatla, S; Yarlagada, P. K. D. V. (2017). Digital manufacturing - applications past, current and future. *Procedia Engineering: 174, 982-991.*

Rees, J. (2014). Towards online, continuous monitoring of rheometry of complex fluids. *Advanced Colloid Interface Science:* 206, 294 - 302.

Swanson, D. K. (1976). *Measurement errors and the origin of electrical impedance changes in the limb (Ph.D. Thesis).* Dept. Electrical and Computer Engineering: University of Wisconsin, Madison.

Wang, M. (2015). *Industrial Tomography.* Elsevier: London

White, R. B; Simic, K; Strode, P. (2001). The Combined Use of Flow Visualisation, Electrical Resistance Tomography and Computational Fluid Dynamics Modelling to Study Mixing in a Pipe. *2nd World Congress on Industrial Process Tomography.*

Yu, Y; Zhao, J; Bayly, A. E. (2008). Development of Surfactants and Builders in Detergent Formulations. *Chinese Journal of Chemical Engineering: 16(4), 517-527.*

Chapter 2

Electrical Tomography: Technical Review

An industrial tomographic measurement requires the acquisition of signals from sensors located around the periphery of the subject domain, i.e. a pipeline or a vessel (Williams and Beck, 1995). Such signals are then able to uncover information about the nature and distribution of components that are located within the sensing domain. Thus, tomographic techniques are proven to be a powerful method for cross-sectional mapping of velocity and concentration distributions (Wang, 2015). The acquired data may then be employed, both quantitatively and qualitatively, to multi-component systems to aid process understanding, optimisation and control.

To attain such information, a vast number of tomographic modalities exist which exploit differing sensing media, including: acoustic tomography (Kohn, 1995); X-ray computed tomography (Kalender, 2006); magnetic resonance imaging (Cherry, 2004) and optical tomography (Zimnyakov and Tuchin, 2002). Across all tomographic techniques, there exists a trade-off between temporal and spatial resolution with process media also suited to specific tomographic modalities. Electrical Tomography (ET) techniques afford an imaging solution which is non-invasive, safe, dynamic and low cost by obtaining the impedance distribution within the sensing domain of interest (Wang, 2015). Accordingly, ET has been extensively employed within industrial applications to analyse production, with Electrical Impedance

Tomography (EIT) and Electrical Resistance Tomography (ERT) being the focuses of this thesis.

Aligned with numerous other tomographic techniques, EIT has evolved from clinical applications. In 1976, Swanson proposed an 'impedance camera' which utilised a large electrode on the patient's chest. This electrode was utilised to inject currents, of varying frequencies, which were monitored by an array of 100 electrodes located upon the patient's back in an attempt to image body tissues (Henderson et al., 1976). These principles were adapted to those utilised presently within process monitoring, with the first industrial EIT system introduced in 1997 and known as the 'Manchester system' (Boone et al., 1997). Since its inception, the most prevalent applications of EIT are the studies of process mixing and multiphase flow monitoring with EIT predominantly exploited within: chemical reactors (Vilar et al., 2008; Bolton et al., 2004); mixers (Pakzad et al., 2008; Carletti, 2014); separators and industrial pipelines (White et al., 2001; Giguere et al., 2008; Henningson et al., 2006). Further industrial applications of EIT can be found in an extensive list compiled by York (2001).

Similarly to the clinical measurement protocols, EIT obtains the impedance distribution within the sensing domain by applying alternating currents or voltages to the domain via a pair of electrodes; the response signals are subsequently captured at the remaining electrodes. In its simplest form, EIT can be interpreted as Ohm's law, Eq. 2.1. When applying a known voltage or current and measuring the responses, the impedance or resistance properties can be determined. These electrical properties are associated with the material properties within the domain, which may subsequently be inferred.

$$Z = \frac{V}{I} \tag{2.1}$$

where V is voltage in V; I is current in A and Z is impedance, in Ohms

The extraction of an impedance distribution requires the application of a number of components including: an EIT sensor; a data acquisition system and a data processor, all of which will be discussed throughout this chapter.

2.1 EIT Sensors

Archetypal EIT sensors consist of a set of electrodes, equally spaced around the periphery of the subject domain that are in contact with the process media and can be arranged and shaped in any orientation. Some examples of this are a U-shaped sensor which was utilised to monitor suspended sediments in open channel flow (Schlaberg et al., 2006) and a parallel bar sensor for the visualisation of liquid distribution in a heap leaching process (Hurry et al., 2004). Despite such adaptability, this thesis will focus upon the most established circular and linear arrays, whose configuration are depicted in Figures 2.1a and 2.1b, respectively. Within such figures, example conductivity distributions are also depicted, with a circular tomogram obtained from a circular array and the linear configuration yielding a rectangular tomogram. Circular arrays have been exploited extensively to obtain cross sectional impedance distributions within industrial pipelines and vessels and subsequently provide in-situ process monitoring (Carletti et al., 2016). Developed by Qiu et al. (1994) for the imaging of sub-sea bed porosity, linear arrays are hitherto mainly applied to monitor axial mixing within rotationally symmetrical stirred vessels (Richardson and Holdich, 2001; Bolton et al., 2004). Such linear arrays offer higher resolution in the axial direction and are also able to be retrofitted into existing reactor installations greatly improving in-plant applicability (Forte et al., 2018).

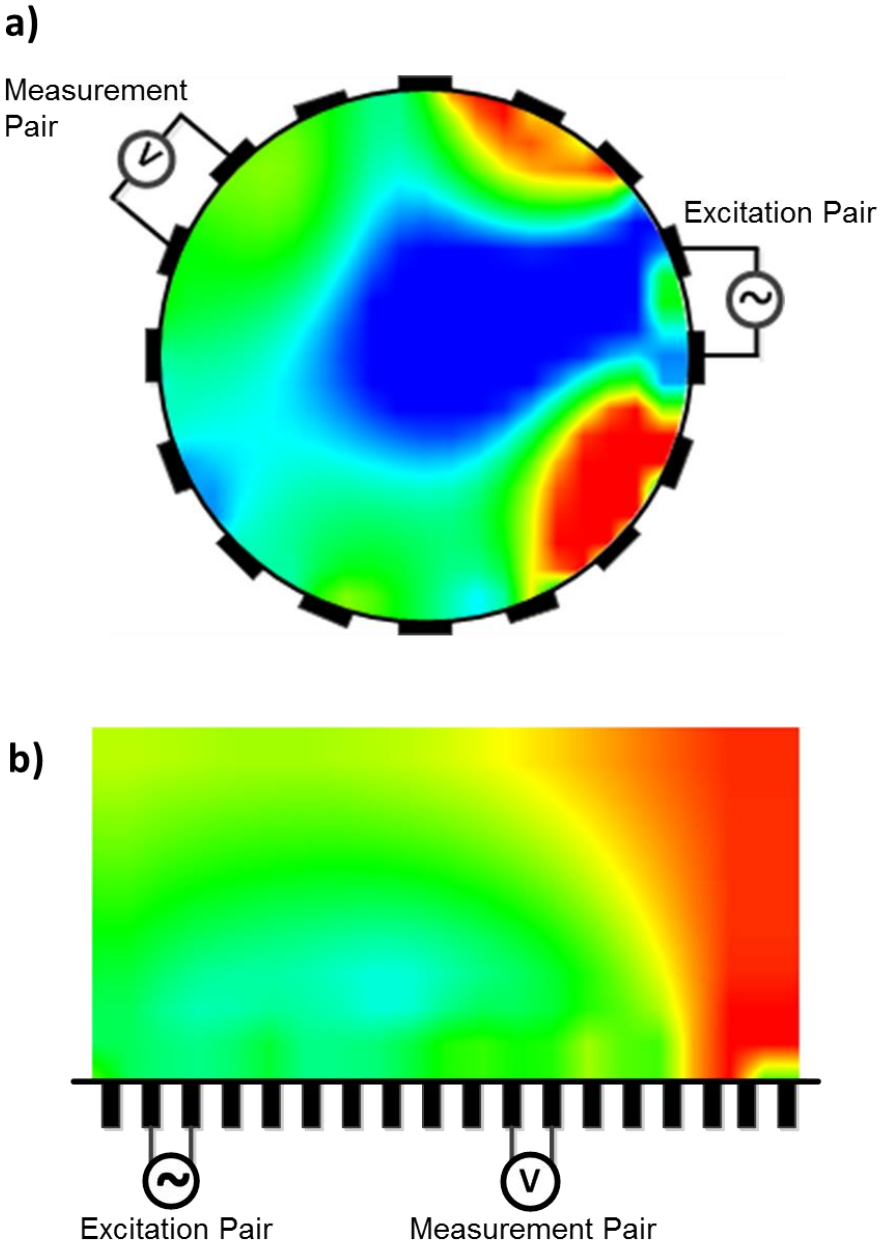

Figure 2.1 Sensor configurations and associated tomograms: a) circular array; b) linear array

In both sensing configurations, the adjacent electrode pair strategy is employed, as it possesses a high signal-to-common voltage ratio, a large number of independent measurements and simplicity of implementation (Brown et al., 1983). Using this strategy, the mutual impedance of the measurement electrode pairs is obtained from a sinusoidal injection current into a pair of electrodes (Jia et al., 2013). This is highlighted within Figures 2.1a and 2.1b, with a 16-electrode sensor yielding 104 independent electrode measurements; these

measurements are subsequently reconstructed into a distribution of electrical properties, or tomogram, using reconstruction algorithms, which will be discussed later within this chapter.

2.2 Electrical Tomography Instrumentation

2.2.1 Current Injection Excitation Signals

As stated previously, to perform EIT measurements either an applied voltage or injected current can be exploited as the excitation signal. Within this thesis, instruments which utilise both excitation signals have been studied. The majority of EIT systems exploit an alternating current (AC) injection due to its simplicity in implementation and robustness across the relatively low, desired, conductivity range, of 0.1 – 50 mS cm^{-1} (Jia et al., 2010). Example injection and response signals at differing electrode pairs are depicted within Figure 2.2a, with the change in the real component of impedance, resistance, determined by the alteration in amplitude of the two signals. This measurement protocol is performed using the Industrial Tomography Systems Ltd (ITS) p2+ EIT instrument for the characterisation of surfactant solutions and multi-component slurries, in Chapters 5 and 6, respectively.

Exploiting the excitation signal in an alternating waveform affords great improvements in the reduction of electrode polarisation and noise. Moreover, it enables access to the full electrical impedance demodulation to access complex electrical properties such as phase and susceptibility (Wang, 2015) and ultimately elucidate greater spatial information. In colloidal dispersions, the propagation of the AC field results in the layers of counter-ions and particles moving in opposing directions. Such movement gives rise to a fluctuating electrical current around the particle which manifests itself as an alternating dipole (O'Brien, 1986). The movement of counter-ions and particles gives rise to ionic gradients which provoke diffusion fluxes across the double layer. This polarisation effect is seen to fluctuate with the direction of the waveform, resulting in a phase lag between the movement of particles and ionic layer

(O'Konski, 1960). At reduced frequencies, <10 kHz, there is sufficient time for the system to relax within the direction of the electrical field (Zhao et al., 2012; Arroyo et al., 2000).

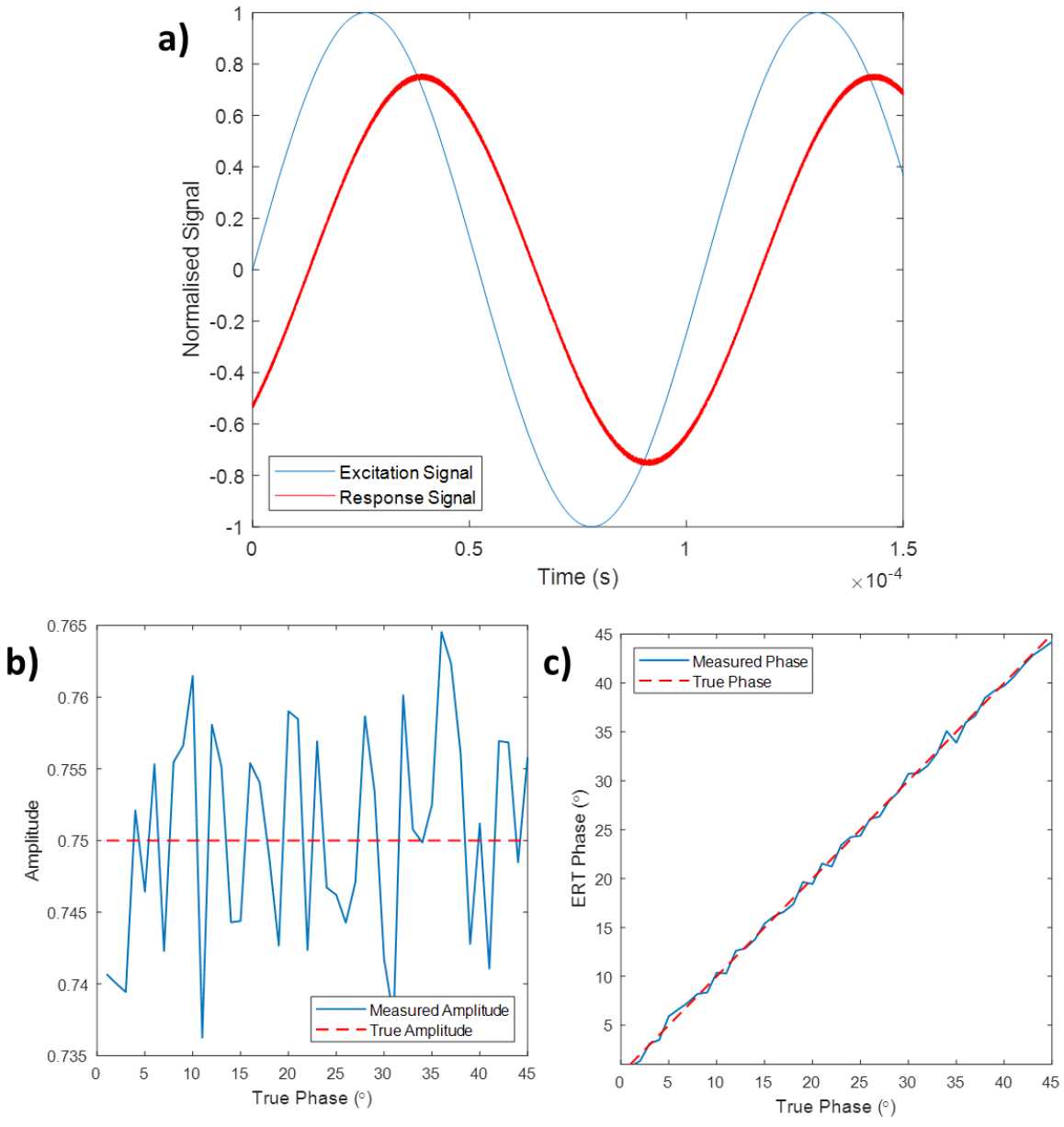

Figure 2.2 Two-point phase sensitive demodulation in ERT: a) excitation and response signal with ± 2.5 % noise; b) amplitude measurements; c) phase measurements

This frequency dependence is reflected in Eq. 2.2 which demonstrates the relationship between phase, frequency and other electrical properties for an equivalent circuit of a resistor and capacitor in parallel.

$$\theta = \tan^{-1}(j\omega RC) \tag{2.2}$$

where θ is the phase angle in °; j is the unit imaginary number; ω is the signal frequency in Hz; R is the resistance in Ohms and C is capacitance in Farads.

To monitor the position shift of the waveform cycle, phase sensitive demodulation (PSD) is performed with the extraction monitored via a two point method. Initially, the excitation signal is calibrated to ensure that stray, or parasitic, capacitance is removed reducing potential noise sources (Wang et al., 1993). This calibration also ensures that the excitation signal, A, acts as a sinusoid, with the response signal, R, measured relative to this. The magnitude of two phase measurements are acquired from the response signal at 90° intervals, preferably at 90° and 180°, with the phase measurement subsequently calculated using Eq. 2.3. Such measurements are simultaneously employed to capture the relative change in amplitude of the signals, via Eq. 2.4, for use in resistance measurements (Smith et al., 1992).

$$\theta = \tan^{-1}\left(\frac{R_{180}}{R_{90}}\right) \tag{2.3}$$

where R_{90} and R_{180} are the magnitudes of the response signal at 90° and 180°, respectively.

$$\frac{R}{A} = \sqrt{{R_{90}}^2 + {R_{180}}^2} \tag{2.4}$$

As both the phase and amplitude measurements rely upon just two points, distortion of the sinusoid and noise may result in an inaccuracy in the outputted data. To simulate the impact of this, a response signal, attenuated to 0.75 with ± 2.5 % of random noise added, was interrogated; this analysis was performed within MATLAB. This level of random noise is greater than that of the ITS p2+ instrument which possesses a precision of ± 0.5 %, see Table 2.1 (ITS, 2018). Such simulations were performed across a range of response signals

which possessed phase shifts at each integer between 1° - 45° to assess the impact of the phase measurement methodology. Despite this random noise, the two-point measurement is seen to perform adequately with a minor standard deviation of 0.0075 when capturing changes in the measured amplitude. In addition to repeatability, this technique possesses high accuracy of 99.93 % across the entire phase range.

A linear regression analysis was performed to compare the true and measured phases with a correlation coefficient and root mean squared error (RMSE) of 0.9985 and 0.511°, respectively. Such linearity and minor error demonstrate the suitability of the two-point phase sensitive demodulation method to extract impedance properties. Nonetheless, it must be acknowledged that the signal to noise ratio of the phase measurement can be decreased further by employing complete signal or digital demodulation i.e. quadrature demodulation of the response signals (Muller et al., 1996). The ITS z8000 EIT instrument, employs a four-point measurement to minimise errors and enhance the sensitivity of both amplitude and phase information to noise.

2.2.2 Applied Voltage Excitation Signal

A secondary electrical tomography sensing modality was utilised within this thesis, known as the ITS v5r ERT instrument. This employs a signal generator which applies a precisely controlled voltage source and resultant current in order to obtain bulk resistance measurements (Jia et al., 2010). Whilst PSD is once again exploited to extract phase measurements, the v5r instrument utilises this information to reduce capacitive effects and ensure the resistive component is outputted alone, reducing noise. This instrument demonstrates the ability to operate in highly electrically conductive media, up to 200 mS cm^{-1}, and also possesses an extremely high temporal resolution, up to 1270 Hz, to provide real-time measurements. Accordingly, it possesses a high selectivity to capturing velocity fields and is consequently employed in Chapters 3 and 4 to monitor velocity profiles within different process equipment and ultimately extract in-situ, rheological parameters.

The precise control of both the excitation source and applied current and the output impedance remaining relatively low enables greater control of the generated electrical field (Jia et al., 2010). This enables the development of novel tailored sensors, which are capable of targeting tomographic information to specific regions of interest with this novel concept discussed frequently throughout this thesis. A summary of all of the electrical tomography data acquisition systems utilised within this study are described in Table 2.1.

Table 2.1 Electrical tomography modalities system parameters

Instrument	**z8000**	**p2+**	**v5r**
Parameter	Impedance	Impedance	Resistivity
Excitation Source	Current	Current	Voltage
Response Signal	Voltage	Voltage	Resistance
Excitation Frequency (kHz)	10, 20, 40, 80	0.0075 – 153.6	10
Temporal Resolution (fps)*	100	3	625
Measurement Accuracy	± 0.5 %	± 0.5 %	± 0.7 %
Sensitivity (μV)	4.88	4.88	3.2
Spatial Resolution	5 %	3 - 5 %	5
Fluid Conductivity (mS cm^{-1})	0.1 - 70	0.1 – 70	0.1 – 200
Phase Measurement Protocol	PSD	PSD	PSD**
Demodulation Technique	4 - point	2 - point	4 – point
Phase Sampling	8, each electrode	1, adjacent pairs	N/A

* Temporal resolution was captured for measurements performed on a 16-electrode sensor with a single plane at a frequency of 9.6 kHz

** The phase measurement is utilised to reduce capacitive effects and not to capture impedance properties

2.3 The Forward Problem

When electrical signals are imposed, the response is dependent upon the internal distribution of the materials within the domain and the excitation sources employed. To solve the inverse admittivity boundary values, a forward solution is required to image the distribution of electrical properties; this is able to be derived from Maxwell's equation of matter (Wang, 2015). Composed of four equations, Maxwell's equations govern electromagnetic fields and describe the relationship between the generated electrical field and induced magnetic field. These equations represent Gauss's law; Gauss's law of magnetism; Faraday's law of induction and Ampere's circuital law, outlined in equations 2.5 to 2.8, respectively. Such equations govern all Electrical Tomography (ET) modalities and accordingly Maxwell's equations in matter form the basis of all computational models performed within this thesis. This mathematical formulation of ET is appropriate as Maxwell's equations are generally applied to macroscopic averages of fields, which vary on a microscopic scale, akin to the variations monitored by ET (Rodgers, 2011).

$$\nabla \cdot D = \rho \tag{2.5}$$

$$\nabla \cdot \mathrm{B} = 0 \tag{2.6}$$

$$\nabla \times E = -\frac{\partial B}{\partial t} \tag{2.7}$$

$$\nabla \times H = J + \frac{\partial D}{\partial t} \tag{2.8}$$

where D is the electrical field displacement in C m^{-2}; B the magnetic induction in T; E the electrical field in V m^{-1}; H the magnetic field in A m^{-1} and ρ and J are the charge and current density without induced polarisation in C m^{-3} and A m^{-2}, respectively.

For a linear isotropic medium, the charge density, magnetic induction and electrical field displacement can be described by the respective materials properties of permittivity, ε,

permeability, μ, and electrical conductivity, σ; this is reflected in the below relationships, Eqs. 2.9a to 2.9c (Wang, 2015).

$$D = \varepsilon E \quad (2.9a); \quad B = \mu H \quad (2.9b); \quad J = \sigma E \quad (2.9c)$$

Substituting these relationships into Maxwell's equations of matter, alongside the previously highlighted alternating excitation waveforms, Eq. 2.10, Faraday's law of induction and Ampere's circuital law become Eqs. 2.11 and 2.12, respectively (Sommersalo et al., 1992).

$$E = E_0 e^{j\omega t} \tag{2.10}$$

$$\nabla \times E_0 = -j\omega\mu H_0 \tag{2.11}$$

$$\nabla \times H_0 = (\sigma + j\omega\varepsilon)E_0 \tag{2.12}$$

where t is time in s

Using Gauss's law for magnetism, there exists a magnetic vector potential, A, which can be utilised to simplify the EIT formulation, Eq. 2.13 (Wang, 2015). This equation can be expanded to generalise the electrical field to Eq. 2.14, by substitution into Eq. 2.7. Subsequently, a time harmonic field is once again applied to reflect EIT measurements giving Eq. 2.15.

$$B = \nabla \times A \tag{2.13}$$

$$E = -\nabla u - \frac{\partial A}{\partial t} \tag{2.14}$$

$$E_0 = -\nabla u_0 - j\omega A_0 \tag{2.15}$$

where u is the electrical potential

The estimated magnetic vector potential, Eq. 2.16b, can be subsequently re-arranged to 2.16c and inputted into Ampere's circuital law (Wang, 2015). Concurrently, this is then substituted into Eq. 2.12, to derive the relationship in Eq. 2.17.

$$|B_0| = |\mu H_o| = |\nabla \times A_0| \quad (2.16a); \qquad |A_0| \approx \mu L_c |H_0| \quad (2.16b); \qquad |\nabla \times H_0| = \frac{|H_0|}{L_c} \quad (2.16c)$$

where L_c is the characteristic length of the magnetic field.

$$|E_0| = |\nabla u_0 + j\omega A_0| \approx \frac{\left(\frac{|H_0|}{L_c}\right)}{|\sigma + j\omega\varepsilon|} \tag{2.17}$$

It is then assumed that the electrical field induced by magnetic induction can be neglected; this has been assumption has been verified by Wang (2015). Applying this assumption to Eq. 2.17 with subsequent rearrangement, the governing formulation can be determined, Eq. 2.18. From this, the distribution of the admittivity, $\sigma+j\omega\varepsilon$, within the sensing domain may be imaged.

$$\nabla \cdot (\sigma + j\omega\varepsilon)\nabla u = 0 \quad (2.18a); \qquad \nabla \cdot \gamma \nabla u = 0 \quad (2.18b)$$

where γ is admittivity, or complex conductivity, in mS cm^{-1}

If resistive or capacitive properties of the interrogated media dominate, the electrical techniques can be segregated into Electrical Resistance Tomography (ERT) or Electrical Capacitance Tomography (ECT) to extract the conductivity and permittivity distributions, respectively.

$$\nabla \cdot \sigma \nabla u = 0 \quad (2.19a); \qquad \nabla \cdot \varepsilon \nabla u = 0 \quad (2.19b)$$

This thesis focusses upon ERT, Eq. 2.19a, and EIT techniques; however, Electrical Capacitance Tomography (ECT) has been extensively employed within industrial applications. As it focusses upon relative changes in permittivity, ECT, described by Eq. 2.19b, has been utilised to monitor dielectric material systems within fluidised beds (Wang et al., 2000); packed beds (Wang et al., 2014; White, 2002) and industrial pipelines (Pradeep et al., 2014; Li et al., 2013; Thorn et al., 2013). Whilst ECT has not been utilised in experimental measurements within this thesis, it has been discussed with future work with the potential to translate the techniques developed to dielectric materials such as gas-oil-water multiphase systems. A number of studies have also considered dual-modality systems which employ

spatial and temporal fusion methods to both ECT and ERT data to provide tomographic images which possess greater spatial resolution and material selectivity (Yang et al., 2011; Zhang et al., 2014; Wang et al., 2017).

2.4 Tomographic Reconstruction – The Inverse Problem

As the governing equation of EIT is elliptic in nature, the electrical potentials vary depending upon the alteration in electrical properties at any location within the domain (Wang, 2015). When the electric field lines encounter an interface of different conductivities, they are deflected (Bodenstein, 2009). Consequently, the reconstruction of the 104 measured amplitude changes to determine the admittivity distribution can be considered as 'ill posed'. This ensures that transmission tomography principles are unable to be directly adapted to the reconstruction of electrical tomography modalities and inevitably introduces noise (Soleimani, 2005). To overcome this, there is a requirement to estimate the path of an electrical current for a given sensing setup and conditions. In this case, a referenced electrical field path is determined for a known electrical property distribution; this is typically a homogenous media (Wang, 2015). The inclusion of additional process media, then distorts this electrical field with these distortions then able to be monitored by modified transmission tomography principles. This ensures that the integrity of the data depends greatly upon the selection of an appropriate reference, with relative changes in electrical properties monitored (Rodgers et al., 2011). Whilst this is vital across all ET applications, it is especially important when calculating dispersed phase concentrations, as discussed in Chapter 6. Rodgers (2011) performed a study to determine the impact of different references upon the same dataset for the injection of air into water. In this instance, references were taken at low and high water heights with the calculated gas hold-up 1.2 % and 5.9 % for the respective scenarios.

To demonstrate the application of transmission tomography principles to tomography, an analysis is performed for Electrical Resistance Tomography. To do so, there is a requirement

to linearise the relationship between the relative boundary change, b, normalised sensitivity matrix, s, and the vector of relative conductivity change, v, see Eq. 2.20. The sensitivity matrix, Eq. 2.21, is a projection that represents the mapping of the boundary change vector into an admittivity vector (Wang, 2015). These sensitivity maps have previously been computed for both linear and circular arrays and demonstrated here for ERT.

$$b = sv \tag{2.20}$$

$$s_{j,k} = \frac{s_{j,k}(\sigma_{meas})}{\sum_{k=1}^{w} s_{j,k}(\sigma_{ref})} \tag{2.21}$$

where σ_{ref} and σ_{meas} are the estimated conductivity values during the reference voltage and at the measurement voltage

An example of a normalised regional sensitivity map for the current path generated for an excitation signal between electrodes 1 – 16 and measurement pair electrodes 7 – 8, is depicted in Figure 2.3. This sensitivity was simulated using the Finite Element Method (FEM) for a single plane, 16-electrode circular array within EIDORS toolbox developed for MATLAB, applying a triangular mesh.

Solving the inverse problem, Eq. 2.20, has been studied extensively with a number of algorithms examined, including: linear back projection (LBP); scaled conjugated gradient (SCG); non-linear Gauss-Newton; Generalised Singular Value Decomposition (GSVD) and Tikhonov regularisation (Wei et al., 2015; Stephenson, 2008; Stephenson et al., 2007). Despite observing large image errors, up to 27.9 % (Stephenson, 2008), LBP is the most extensively employed within literature and in industrial applications due to its robust nature and high temporal resolution (Pagliante and Montante, 2018; Kazemzadeh et al., 2016; Forte et al., 2019).

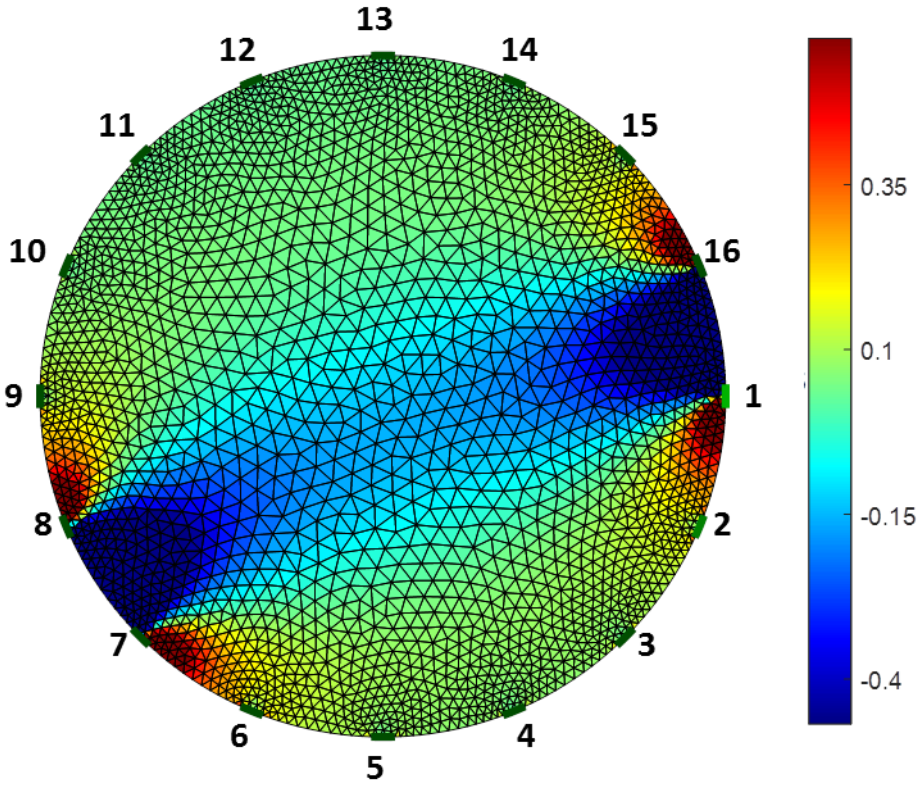

Figure 2.3 A simulated sensitivity matrix for a 16-electrode circular sensor

Based upon the LBP principles, the sensitivity coefficient back-projection algorithm (SBP) was first defined by Breckon and Pidcock (1987) and optimised for use in EIT by Kotre (1994). SBP, described by Eq. 2.22, takes the relative change in the differential at the boundary, which is linearly back projected to determine the distribution of electrical properties within the process domain as a function of the back projection ratio (Wang, 2002).

$$\frac{\Delta\bar{\sigma}_k}{\sigma_0} \approx -\frac{\sum_{j=1}^{P} \frac{\Delta V_j}{V_j} \cdot s_{j,k}(\sigma_0)}{\sum_{j=1}^{P} s_{j,k}(\sigma_0)} \tag{2.22}$$

$$\bar{\sigma}_k \approx \frac{\sigma_0 \cdot \sum_{j=1}^{P} s_{j,k}(\sigma_0)}{\sum_{j=1}^{P} \frac{V_j'}{V_j} s_{j,k}(\sigma_0)} \tag{2.23a}$$

where

$$V_j' = V_j + \Delta V \tag{2.23b}$$

This was then extended by Wang et al. (1996) to the modified SBP reconstruction algorithm (MSBP), due to the inverse relationship between voltage and conductivity. Based upon a non-linear relationship, MSBP is capable of reducing image error and increasing the applicable range of the algorithm (Wang, 2002). Consequently, the MSBP algorithm has been applied throughout this study to reconstruct the tomograms and may be described in the above equations, Eqs. 2.23a and 2.23b.

2.5 The Tomogram and Data Interpretation

Upon completing reconstruction, the tomogram can then be utilised to extract process information. This analysis is often dependent upon the unit operation and the desired output with the data from the image able to be interpreted in different manners. The tomogram may be utilised for visualisation of the process; within heterogeneous multiphase flows, this approach may identify interfaces of multiple phases. In mixing studies, the tomogram is often utilised to identify process end points. When the distribution of electrical properties is uniform across the sensing cross section, the interrogated fluid may be considered as homogeneous, with an uneven distribution indicating further processing is required. This is highlighted in Figures 2.4a and 2.4b which demonstrates the outputted tomograms homogenous and non-homogeneous aqueous xanthan gum solutions within a stirred vessel. The relative change of the outputted tomograms may also be monitored with a coefficient of variance approach to monitor mixing applied (Kazemzadeh et al., 2016). This approach to monitoring mixing is advantageous over conventional probe-based techniques, as the entire cross-section is considered, reducing sampling errors (Nienow et al., 1997).

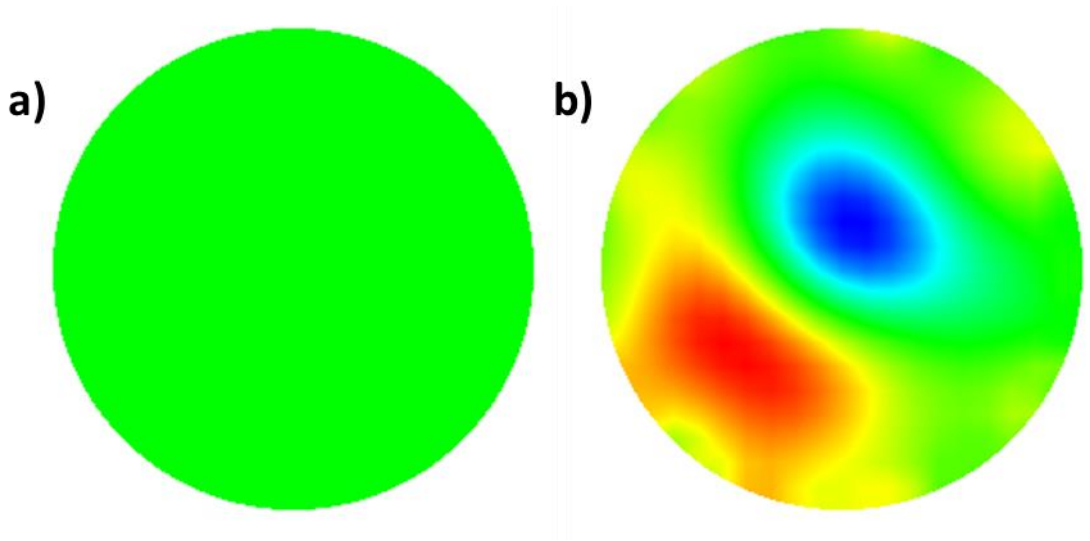

Figure 2.4 a) homogeneous circular tomogram; b) inhomogeneous circular

The tomogram is also extensively employed in hydraulic conveying systems to afford a non-nucleonic alternative to the measurement of data. Exploiting effective media approximations, such as the Maxwell-Garnett equations (Markel, 2016), enables the distribution of electrical properties to be converted into the concentration distribution within the pipe. Alongside a knowledge of the conveyed materials, this concentration distribution can be utilised to capture the slurry density, an important process optimisation parameter within dredging and mining sectors.

Whilst this section outlines the most established data interpretation methods in electrical tomography, more complex methods have been explored. This thesis will develop novel data interpretation techniques to expand the existing capabilities of ET to characterise complex fluids.

2.6 Summary

This chapter highlights the underpinning principles of the measurements conducted throughout this thesis. Information obtained from phase sensitive demodulation, Section 2.2, has been employed in the characterisation of both surfactant-electrolyte systems and

colloidal clay dispersions, Chapters 5 and 6 respectively. The reconstructed tomograms, as depicted in Figure 2.1, are also utilised to characterise colloidal dispersions and are exploited for the development of in-line rheometers, within both pipes and vessels. In the following chapter, fluctuations in the computed conductivity pixels of the tomograms are cross-correlated to directly obtain the radial velocity profile within laminar pipe flow. When this information is coupled with the measurement of differential pressure, rheological parameters can be captured in-line, affording novel insights into the processing of formulated products.

2.7 References

Arroyo, F.J; Carrique, F; Jimenez-Olivares, M.L. (2000). Rheological and Electrokinetic Properties of Sodium Montmorillonite Suspensions II: Low-Frequency Dielectric Dispersion. *Journal of Colloid and Interface Science*: 229 (1), 118-122.

Bodenstein, M. (2009). Principles of electrical impedance tomography and its clinical application. *Critical care medicine: 37(2), p13-24.*

Bolton, G. T; Qiu, C. H; Wang, M. (2002). A novel electrical tomography sensor for monitoring the phase distribution in industrial reactors. *Conference Proceedings: Conference on Mixing.*

Bolton, G; Hooper, C; Mann, R; Stitt, E.H. (2004). Flow distribution and velocity measurement in a radial flow fixed bed reactor using electrical resistance tomography. *Chemical Engineering Science.* 59, 1989-1997.

Boone, R; Barber, D; Brown, B. R. (1997). Review: Imaging with electricity: report of the European concerted action on impedance tomography. *Journal of Medical Engineering and Technology:* 21 (6), 201 – 232.

Breckon, W. R; Pidcock, M. K. (1987). Mathematical aspects of impedance imaging. *Clinical Physics and Physiological Measurement.*

Brown, B. H; Barber, D. C; Freeston, I. L. (1983). *Tomography.* UK Patent No. GB2119520A.

Carletti, C; Montante, G; Westerlund, T; Paglianti, A. (2014). *Analysis of solid concentration distribution in dense solid-liquid stirred tanks by electrical resistance tomography. Chemical Engineering Science.* 119, 53-64.

Carletti, C; Montante, G; De Blasio, C; Pagliante, A. (2016). Liquid mixing dynamics in slurry stirred tanks based on electrical resistance tomography. *Chem Eng Sci:* 152, 478-487.

Cherry, S. R. (2004). In Vivo Molecular and Genomic Imaging: New Challenges for Imaging Physics. *Physics in Medicine and Biology:* 49, 13 – 84.

Forte, G; Alberini, F; Simmons, M. J. H; Stitt, E. H. (2019). Measuring gas hold-up in gas-liquid/gas-solid-liquid stirred tanks with an electrical resistance tomography linear probe. *American Institute of Chemical Engineers.*

Giguere, R; Fradette, L; Mignon, D; Tanguy, P.A. (2008). Charcterization of slurry flow regime transitions by ERT. *Chemical Engineering Research and Design.* 86, 989-996.

Henderson, P. R; Webster, J. G; Swanson, D. K. (1976). A thoracic electrical impedance camera. *Conference Proceedings 29th Annual Conference on Engineering in Medicine and Biology: Boston.*

Hurry, R; Wang, M; Williams, R. A; Cross, C; Esdaile, L. (2004). Development and application of industrial process tomography to monitoring liquid distribution in heap and column leaching. *International Student Conference, Brisbane.*

Jia, J; Wang, M; Schalberg, I; Li, H. (2010). A novel tomographic sensing system for high electrically conductive multiphase flow measurement. *Flow Measurement and Instrumentation:* 21, 184 – 190.

Kalender. W. A. (2006). X-ray Computed Tomography. *Physics in Medicine and Biology:* 51, 29 – 43.

Kazemzadeh, A; Ein-Mozaffari, F; Lohi, A; Pakzad, L. (2016). Effect of the Rheological Properties on the Mixing of Herschel-Bulkley fluids with coaxial mixers: applications of tomography, CFD and response surface methodology. *Canadian Journal of Chemical Engineering: 94*

Kohn, D. H. (1995). Acoustic Emission and Nondestructive Evaluation of Biomaterials and Tissues. *Critical Reviews in Biomedical Engineering: 23: 221 – 306.*

Kotre, C. J. (1994). EIT image reconstruction using sensitivity weighted filtered back-projection. *Physiol Meas: 15.*

Li, Y; Yang, W; Xie, C; Huang, S; Wu, Z; Tsamakis, D; Lenn, C. (2013). Gas/oil/water flow measurement by electrical capacitance tomography. *Measurement Science and Technology: 24.*

Markel, V. (2016). Introduction to the Maxwell-Garnett Approximation. *Journal of Optical Society of America A:* 1, 1-12.

O'Brien, R.W. (1986). The high-frequency dielectric dispersion of a colloid. *Journal of Colloid and Interface Science*: 113 (1), 81-93.

O'Konski, C.T. (1960) Electric Properties of Macromolecules: V - Theory of Ionic Polarization of Polyelectrolytes. *The Journal of Physical Chemistry*: 64 (5), 605-619

Paglianti, A; Montante, G. (2018). Liquid Mixing Time and Solid Dissolution in Slurry Stirred Tanks. 9th *World Congress of Industrial Process Tomography Conference Proceedings.*

Pakzad, L; Ein-Mozaffari, F; Chan, P. (2008). Using electrical resistance tomography and computational fluid dynamics modelling to study the formation of caverns in the moxing of pseudoplastic fluids possessing a yield stress. *Chemical Engineering Science.* 63, 2508-2522.

Pidcock, M. K; Kuzuoglu, M; Leblebiciouglu, K; (1995). Analytic and semi-analytic solution in electrical impedance tomography: I. Two-dimensional problems. *Physiological Measurement: 1, 77-90.*

Pradeep, C; Yan, R; Vestol, S; Melaaen, M. C; Mylvaganam, S. (2014). Electrical capacitance tomography (ECT) and gamma radiation meter for comparison with and validation and tuning of computational fluid dynamics (CFD) modelling of multiphase flow. *Measurement Science and Technology: 25*.

Qiu, C. H; Dickin, F. J; James, A. E; Wang, M. (1994). Electrical resistance tomography for imaging sub-seabed sediment porosity: initial findings from laboratory-scale experiments using spherical glass beads. *Process Tomography – A Strategy for Industrial Exploitation:* 33 – 41.

Richardson, D. J; Holdich, R. G. (2001). A novel low cost probe for monitoring dispersed solids concentrations in liquids. *Chemical Engineering Research and Design:* 83, 569 - 574.

Rodgers, T. L. (2011). *Multiple-Scale Approach to Understanding Formulated Product Production (Ph.D. Thesis).* University of Manchester: Manchester.

Schlaberg, H. I; Jia, J. H; Wang, M; Best, J. L; Williams, R. A; Peakall, J. (2006). Electrical resistance tomography for suspended sediment measurement in open channel flows using a novel sensor design. *Particles and Particle Systems Characterization:* 23(3), 78.

Soleimani, M; Lionheart, W. (2005). Nonlinear Image Reconstruction for Electrical Capacitance Tomography using Experimental Data. *Measurement Science and Technology:* 16(10), p1987-1996.

Somersalo, E; Cheney, M; Isaacson, D. (1992). Existence and uniqueness for electrode models for electric current computed tomography. *SIAM Journal on Applied Mathematics:* 52, 1023 – 1040.

Stephenson, D. R; York, T. A; Mann, R. (2007). Choices and Implications in Practical EIT. 5th *World Congress of Industrial Process Tomography Conference Proceedings.*

Stephenson, D. R. (2008). *Choices and Implications in Three-Dimensional Electrical Impedance Tomography.* EngD Thesis, University of Manchester.

Swanson, D. K. (1976). *Measurement errors and the origin of electrical impedance changes in the limb (Ph.D. Thesis).* Dept. Electrical and Computer Engineering: University of Wisconsin, Madison.

Thorn, R; Johansen, G. A; Hjertaker, B. T. (2013). Three-phase flow measurement in the petroleum industry. *Measurement Science and Technology: 24, 17*.

Williams, R. A; Beck, M. S. (1995). *Process Tomography: Principles, Techniques and Applications.* Elsevier Science and Technology.

Wang, M. (2015). Industrial Tomography: Elsevier Science, Amsterdam.

Wang, A; Marashdeh, Q; Motil, B. J; Fan, L. (2014). Electrical capacitance volume tomography for imaging of pulsating flows in trickle beds. *Chemical Engineering Science: 119, 77 – 87.*

Wang, Q; Wang, M; Wei, K; Qiu, C. (2017). Visualization of Gas-Oil-Water flow in horizontal pipelines using Dual-Modality Electrical Tomographic Systems. *IEEE Sensors Journal: 17(24), 8146 – 8155.*

Wang, M; Mann, R; Dickin, F. J. (1996). A Large scale tomographic sensing system for mixing processes. *IWISP 1996 Conference Proceedings.*

Wang, M. (2002). Inverse solutions for electrical impedance tomography based on conjugate gradients methods. *Measurement Science and Technology:* 13, 101-117.

Wang, M. (2015). *Industrial Tomography.* Elsevier: London

Wang, S. J; Geldart, D; Beck, M. S; Dyakowski, T. (2000). A behaviour of a catalyst powder flowing down in a dipleg. *Chemical Engineering Journal: 77, 51 – 56.*

Wei, K; Qiu, C; Soleimani, M; Primrose, K. (2015). ITS Reconstruction Tool-Suite: An inverse algorithm package for industrial process tomography. *Flow Measurement and Instruementation: 46b, 292-302.*

White, R. B; Simic, K; Strode, P. (2001). The Combined Use of Flow Visualisation, Electrical Resistance Tomography and Computational Fluid Dynamics Modelling to Study Mixing in a Pipe. *2nd World Congress on Industrial Process Tomography.*

White, R. B. (2002). Using electrical capacitance tomography to monitor gas voids in a packed bed of solids. *Measurement Science and Technology: 13, 1842 – 1847.*

Yang, W; Li, Y; Wu, Z; Tsamakis, D; Learmonth, D; Xie, C; Huang, S; Lenn, C; Cutler, A. (2011). *Multiphase flow measurement by electrical capacitance tomography.* 2011 IEEE International Conference on Imaging Systems and Techniques.

York, T. A. (2001). Status of Electrical Tomography in Industrial Applications. *Journal of Electronic Imaging:* 10 (3), 608 – 619.

Zhao, Y; Wang, M; Hammond, R.B. (2012). Characterisation of nano-particles in colloids: Relationship between particle size and electrical impedance spectra. *Journal of Nanoscience and Nanotechnology*: 12, 1-5.

Zhang, R; Wang, Q; Wang; H; Zhang, M; Li, H. (2014). Data fusion in dual-mode tomography for imaging oil-gas two-phase flow. *Flow Measurement and Instrumentation: 37, p1-11.*

Zimnyakov, D. A; Tuchin, W. (2002). Optical Tomography of Tissues. *Quantum Electronics:* 32, 849 - 867

Chapter 3

In-pipe Rheology and Mixing Characterisation using Electrical Resistance Sensing[1]

3.1 Introduction

The rheological properties of a fluid system are critical in chemical and physical processing, since they govern both in-process efficiency and final product quality. Conventionally, the measurement of such properties is conducted off-line with careful sampling and removal from the product stream. The fluid rheology obtained from off-line rheometry is often considered, with assumptions, as applicable to flows in real processes. However, this approach is in the majority unsatisfactory since off-line measurements afford a retrospective characterisation of the sample structure which may not be representative of structure as a function of the time-shear history received during processing. In-situ measurements overcome this deficiency as they are inherently conducted within the flow environment and remove the possibility of degradation of the sample. Since in-line rheometer measurements are conducted within the process flow environment, they possess the capability to elevate rheometry from a quality control tool at process end-point to one which is able to control and optimise processes.

[1] The work presented in this chapter is published in part in Machin, T. D; Wei, K; Greenwood, R. W; Simmons, M. J. H. (2018). In-pipe rheology and mixing characterisation using electrical resistance sensing. Chem. Eng. Sci., 187, 327-341, https://doi.org/10.1016/j.ces.2018.05.017

Rides et al. (2011) suggested in-line techniques may also afford opportunities for new product development.

There is thus an ever-increasing demand for the development of in-line rheometers as the majority of industrial complex fluids exhibit non-Newtonian behaviour. Complex fluids may observe wall slip, thixotropy, shear-induced phase migration and shear banding during processing; interpretation via conventional rheology measurements is often demanding and complex (Olmsted, 2008). Such phenomena may be captured with localised rheological measurements, with velocity profiling being a preferred technique (Ovarlez et al., 2011). The low shear rate range of in-line rheometers, 0.05 - 100 s^{-1}, is typically relevant for the rheological phenomena observed in complex systems. Despite this, no such commercially viable technique has been outlined which is capable of performing this task efficiently across a wide range of fluids (Rees, 2014).

Aligned with this demand, numerous studies have been conducted which aim to uncover in-line rheological properties with a particular focus upon ultrasound Doppler-based velocity profiling (UVP) techniques (Wiklund et al., 2007), (Rahman et al., 2015). Despite some positive results, UVP is only applicable to systems which contain particles which act as tracers or to the velocity measurement of a dispersed phase in a two-phase system (Dong et al., 2016). As a result, the applications of this technique are limited with several setups additionally prone to several sources of correlated and uncorrelated noise (Wiklund et al., 2007). Moreover, UVP cannot be applied successfully in aerated systems, greatly limiting its in-plant applicability.

Blythe et al. (2017) recently implemented a Bayesian approach to pulsed field gradient Nuclear Magnetic Resonance (NMR), in one dimension, to derive in-line rheological parameters. The rheological characteristics of Carbopol 940 were successfully extracted, demonstrating a high repeatability. However, the practicality, costs and safety implications of implementing a NMR system (coil tuned to a frequency of 85.2 MHz and a 2 T superconducting magnet) onto a process plant are such that it is highly unlikely to be adopted

within industry. Low-field NMR techniques overcome these concerns; however, the effective application of this technique to rheometry is as yet unreported. Further attempts have been made to extract the velocity profile within a pipe employing laser Doppler anemometry (Meissner, 1983) and Doppler optical coherence tomography; however, these optical technique are unable to interrogate opaque fluids with the latter only currently applicable at the micro-scale (Haavisto et al., 2015).

Ren et al. (2017) utilised the conductivity response of shampoo to an alteration in shear rate to extract the velocity profile without the requirement of a tracer. Electrical Resistance Tomography (ERT) was employed to measure the conductivity of each tomogram pixel; these pixels were subsequently assigned to a value of shear rate and accordingly a velocity profile was determined. Despite the removal of a tracer, the aforementioned conductivity and shear rate relationship was not defined comprehensively, requiring extensive fitting assumptions to the extent that the ERT conductivity is no longer reflective of the outputted velocity profile and demonstrates poor repeatability. Shampoo additionally exhibits a comparatively large conductivity response from a minor alteration in temperature in relation to that brought about by a change in shear rate; this provides additional uncertainty (Ren et al., 2017). The aforementioned shear rate response is also unknown for a number of fluids and therefore this limits the general applicability of this technique.

The technique of electrical resistance sensing, however, still remains an extremely robust, non-invasive technique which is used to interrogate processes fluids without the limitation of optical opacity. This is derived from Electrical Impedance Tomography (EIT) which non-invasively exploits the distribution of electrical impedance to uncover information about the nature and distribution of materials located within the selected process domain (Dyakowski and Jaworkoski, 2003). The wide-ranging applicability and simple implementation of microelectrical tomography sensors to industrial processing affords an ideal basis for the development of an in-line rheometer. The application of such sensors to in-pipe rheometry is termed Electrical Resistance Rheometry (ERR).

Rheologically complex fluids can also be considered to contain numerous heterogeneously mixed components with the meso- and macroscopic mixing scales playing a key role in determining the sophisticated properties of the fluid (Abadi, 2016). Extensive literature exists concerning the application of ERT to monitoring of non-Newtonian fluid mixing with imaging performed within chemical reactors (Vilar et al., 2008; Bolton et al., 2004), mixers (Pakzad et al., 2008; Carletti et al., 2014), separators and industrial pipelines (White et al., 2001; Giguère et al., 2008; Hennigson et al., 2006), the latter being the focus of this study. With the interrogation of the cross-sectional impedance map, ERR possesses the capability to simultaneously elucidate such mixing behaviour alongside outputting parameters which monitor localised and global mixing performance.

An Electrical Resistance Rheometer (ERR) has been developed which is capable of extracting the velocity profile in symmetric, laminar pipe flow, and ultimately rheological parameters. This chapter outlines the methodology of this technique together with experimental measurements demonstrating the suitability of electrical resistance sensing for such a measurement. The chosen setup does not require the physical incorporation of tracer particles into the flow which may provide disturbances to both the product stream or contaminate the product and hence is highly advantageous over the majority of the techniques previously outlined in the literature. The capability for ERR to simultaneously extract both in-pipe rheology and local and global mixing parameters has additionally been demonstrated. Thus, ERR is able to combine two significant engineering quality and process control concepts of rheology and mixing to understand inhomogeneity and non-uniformity within a process to form a powerful process characterisation tool. The majority of the information presented within this chapter is taken from the published works by Machin et al. (2018). Due to the success of this development, the commercialisation of ERR, by the sponsoring company, has also been discussed within this chapter.

3.2 Development of Electrical Resistance Rheometry (ERR)

3.2.1 Electrical Resistance Velocimetry

Electrical Resistance Rheometry (ERR) enables the in-line characterisation of a fluid's rheological behaviour via the direct measurement of the radial velocity profile and thus to elucidate the shear rate profile within a pipe. To attain this profile, a cross-correlation algorithm has been implemented to monitor the fluctuations in computed conductivity pixels of a reconstructed tomogram, see Eq. 3.1; this permits the tagging of fluid motion across and within multiple measurement planes, or arrays (Papoulis, 1962). As the distance between the measurement arrays is fixed and known, the extracted time delay may simply be converted to velocity.

$$R_{fg}(\tau) = \int_{-\infty}^{\infty} f(t) \cdot g(t+\lambda)dt \tag{3.1}$$

where R_{12} is the cross correlation function; λ is the displacement between the two continuous functions, in seconds and f(t) and g(t) are continuous conductivity functions as a function of time.

3.2.2 Development of Tailored Linear Arrays

Sharifi and Young (2013) attempted to utilise a step change in concentration of a saline solution to tag the motion across two planes, also known as arrays, of circular ERT sensors using AIMFLOW software, developed by Industrial Tomography Systems, ITS (ITS, 2016). However, the acquired velocity measurements do not capture the velocity profile effectively due to a lack of sensitivity in the pipe-wall boundary region.

To ensure a complete velocity profile is acquired, a novel, in-line ERR sensor configuration was developed which consists of a combination of both linear and circular arrays. The addition of linear arrays enables the specific targeting of electrical sensitivity to a desired region of interest, in this instance near to the wall. The manipulation of the linear array length,

and consequently electrical field penetration, has been utilised for the first time in this study. This provides an opportunity for the development of a number of further electrical resistance sensing techniques.

To validate this targeted multi-scale approach, a number of three-dimensional, pipe-based, COMSOL Multiphysics models have been developed. These models aim to determine the distribution of electrical current density when the rheology sensor interrogates a fluid of conductivity of 1 mS cm^{-1} and relative permittivity of 78. Alongside two planes of circular arrays, a range of multi-scale sensor arrays, of lengths 6 – 24 mm, were examined using the 8-electrode linear ERT setup (Qiu et al., 1994). This configuration consists of eight coplanar measurement electrodes and two ground electrodes, all of which were fabricated from copper and separated by an acrylic insulation gap. The ratio of the electrode width to insulation gap width remained as 1:1 across all interrogated array lengths. The electrode arrays were positioned axially along the pipe with each electrode encompassing half of the pipe circumference, and located in the lower half of the pipe, to prevent the detection of large volumes of air within the flow. This electrode configuration can be observed in Figures 3.2a and Figure 3.3. Moreover, due to the axisymmetric nature of laminar pipe flow, it is initially stipulated than an increase in interrogation area of linear arrays (Qiu et al., 1994), will improve the robustness of the rheology measurement due to increased velocity information. This concept is additionally verified using the COMSOL model.

An alternating electrical current excitation signal was applied across two measurement electrodes using the linear adjacent measurement protocol; the excitation signal possessed an amplitude of 15 mA and frequency of 19.2 kHz. A single stimulation cycle was selected using the first electrode as a terminal for the current injection with the eighth electrode subsequently acting as a ground. This represented the case which is likely to cause the deepest penetration of the electrical field into the interrogated fluid. The remaining measurement electrodes were selected to act as floating potentials with the electrode configuration depicted in Figure 3.1a.

The selected model exploited Maxwell's equations in matter, described in Chapter 2, which govern the mathematical formulation of all electrical tomography modalities and hence are considered appropriate to model the tailored linear arrays (Wang, 2015). The models neglect induction and assume that the electrical field is curl free. Due to the diminutive nature of the smallest tailored electrodes arrays, an extremely fine mesh was selected. This is represented in Figure 3.2a, which depicts this mesh for a rheology sensor with a 24 mm tailored array.

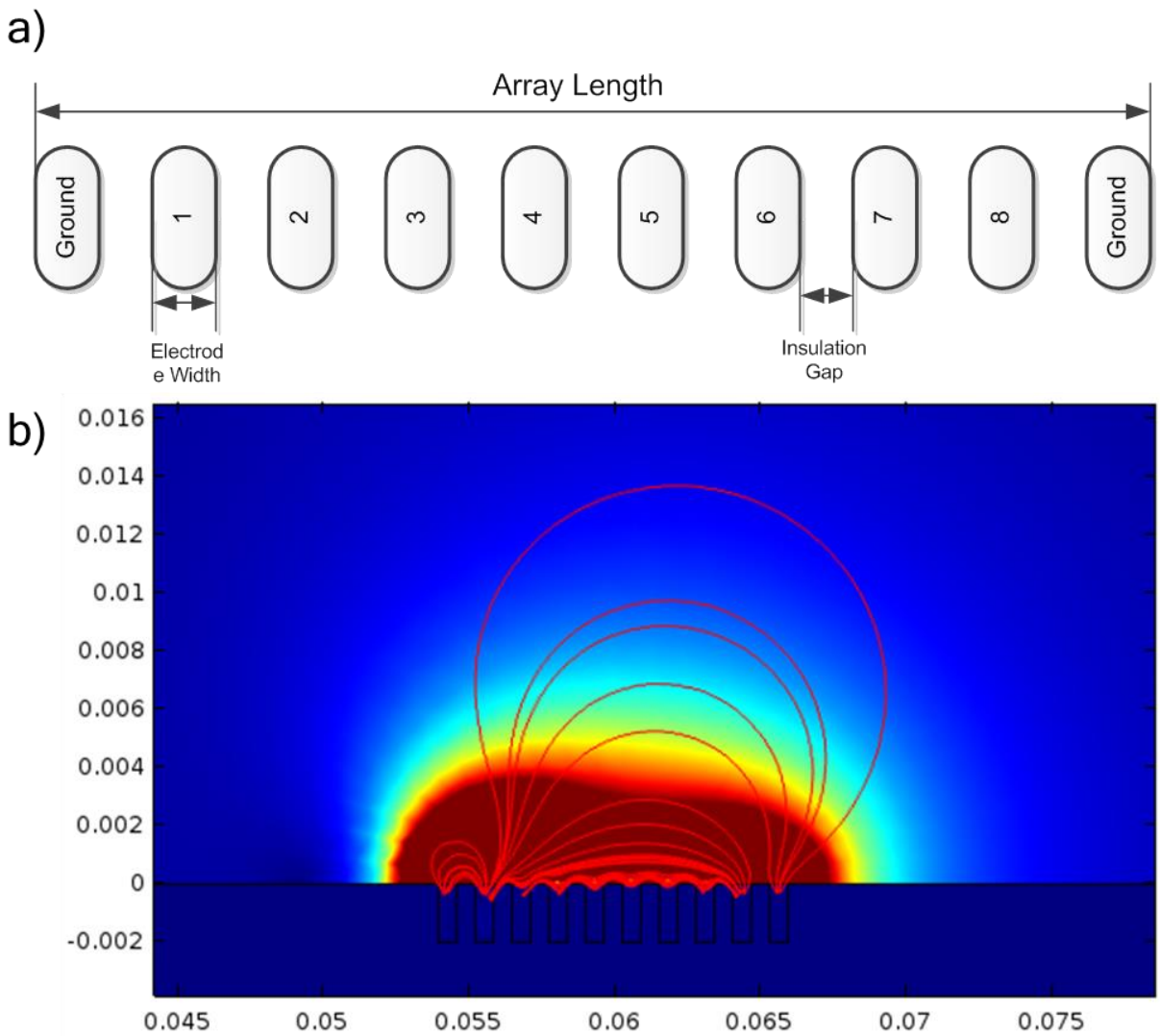

Figure 3.1 a) 8-electrode linear array electrode configuration; b) electrical current density of a 24 mm array

When an alternating current is applied to two similar parallel conducting strips, the electrical field is elliptical in nature (Smythe, 1989). As the distance between these strips is increased, the penetration of the electrical field into the interrogated sensing media is increased accordingly. From an initial observation, the computed electrical field from the linear array models is also approximately elliptical in nature, as described by Smythe (1989). This is highlighted in Figure 3.1b which depicts a two-dimensional slice across a 24 mm array length. Moreover, this is in agreement with a study conducted by Bolton et al. (2002) who modelled the electrical field generated within a linear probe using the Maxwell 3D field simulator. The demonstration of the elliptical nature of the field provides confidence in the validity of the developed model.

Due to the elliptical nature of the electric field, the electrical current density is seen to decrease in penetration depth at the outer measurement electrodes, which may result in an increase in noise in associated regions of the tomogram. The cross-sectional current density distribution within the pipe was also studied at the centre of the multi-scalar array, equidistant between the two ground electrodes. These cross sectional images for the 6, 12 and 24 mm rheology arrays are depicted in Figures 3.2c, 3.2d and 3.2e, respectively. From such computations, as the length of the array is increased, so does the penetration of the electrical field into the fluid. The regions with the greatest electrical current density can likened to the area interrogated by tomographic measurements. Hence, the observed trend of increasing electrical field penetration and tomographic interrogating region with increased array length this validates the multi-scale sensing concept enabling the targeting of this tomographic information to regions of interest via manipulation of the electrode geometry. Such behaviour has additionally been validated experimentally using tomographic measurements, with the optimised array length found to be 12 mm, for a 25.4 mm diameter pipe; this study is outlined in Appendix A1.

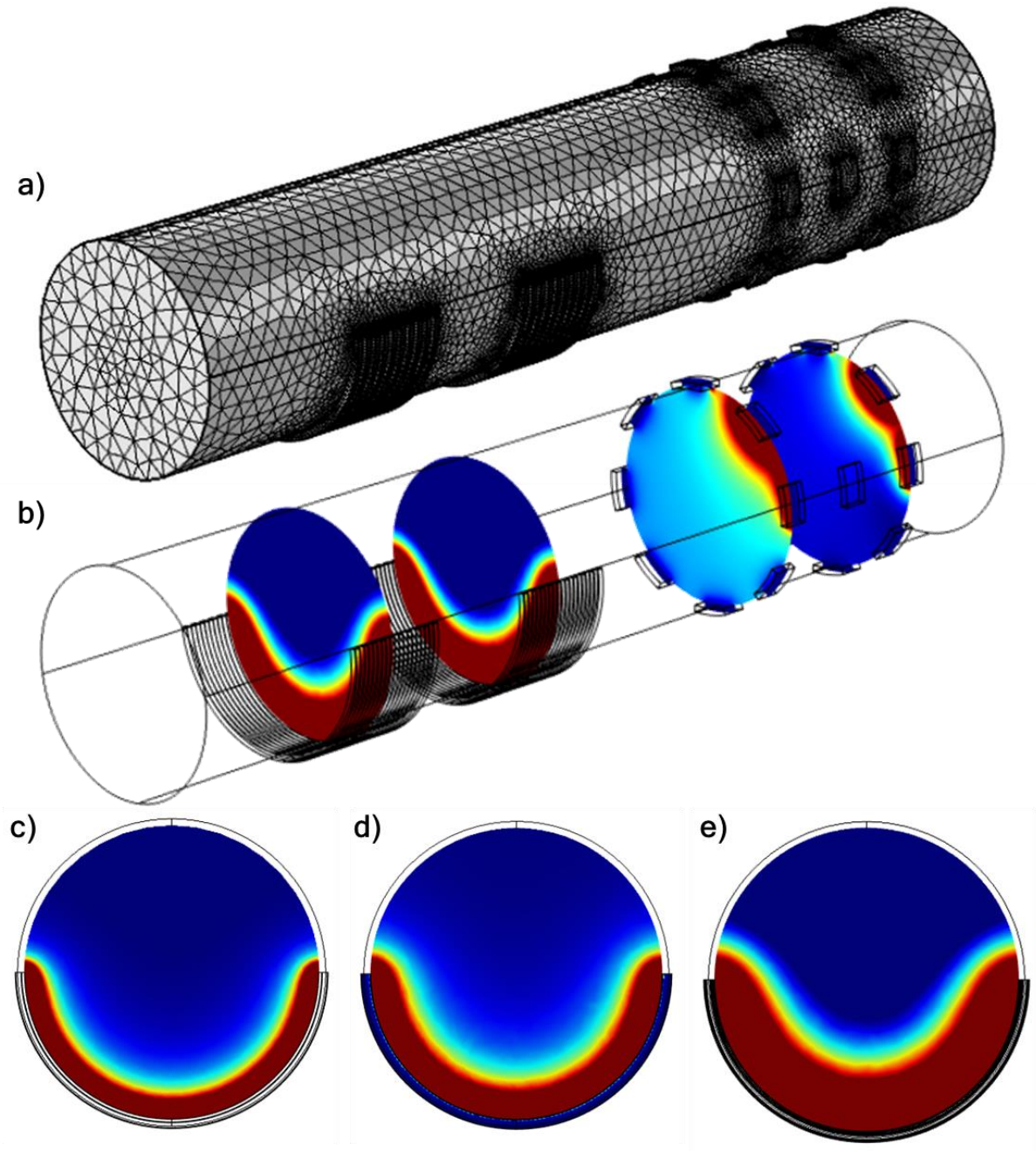

Figure 3.2 Rheology sensor computational model: a) mesh; b) electrical current density distribution (ECDD) of entire model; c) 6 mm – ECDD; d) 12 mm – ECDD; e) 24 mm - ECDD

Whilst it is difficult to quantitatively relate these computational models to tomographic measurements, it has been qualitatively demonstrated that an increase in electrode array length results in an increase in the electrical field penetration. This phenomenon has been

exploited in the rheological measurement to specifically target the near-wall region of the pipe, from which little information is obtained from the circular array outside of the central pipe region. It must also be acknowledged, that tailored linear sensors may be applied to a number of additional processing applications, in which the tomographic information is able to be specifically targeted to regions of interest. An example of this would be in cleaning-in-place (CIP) applications, in which the near-wall region may be targeted directly to determine whether a process is clean.

Such computational studies have additionally qualitatively validated the electrode design of this novel arrangement. Despite an increase in electrode length and large curvatures of the linear electrodes, uniform and predictable electrical current distributions have been observed at a fixed pipe radius. With such uniform fields and the axisymmetric nature of laminar flow velocity profiles, the optimal design of each electrode encompasses half of the pipe diameter. This is a secondary example that the manipulation of the electrode geometry is able to target and enhance information to process regions of interest.

3.2.3 Velocity profile extraction

The completed ERR sensor design utilises four arrays of eight electrodes, consisting of two linear arrays and two other arrays in a circular configuration resulting in the output of four tomograms. This novel arrangement is operated using the ITS v5r system which is capable of operating a sensor consisting of a maximum of 32 electrodes; the arrays are made up of 8 electrodes as to provide the greatest temporal resolution of the v5r system and ultimately sensitivity to velocity. Linear array measurements are reconstructed to rectangular tomograms which comprise of 10 × 20 pixels and a circular tomogram consisting of 316 pixels; example tomograms produced from these sensor types are displayed adjacent to the ERR sensor in Figure 3.3. The inclusion of such circular sensors additionally permits the visualisation of the cross-sectional impedance map to interrogate simultaneously localised and global mixing behaviour in-line. This enables the capture of parameters such as

heterogeneity index, plane-to-plane mixing index and mixing times including 95 % and 99 % mixing times.

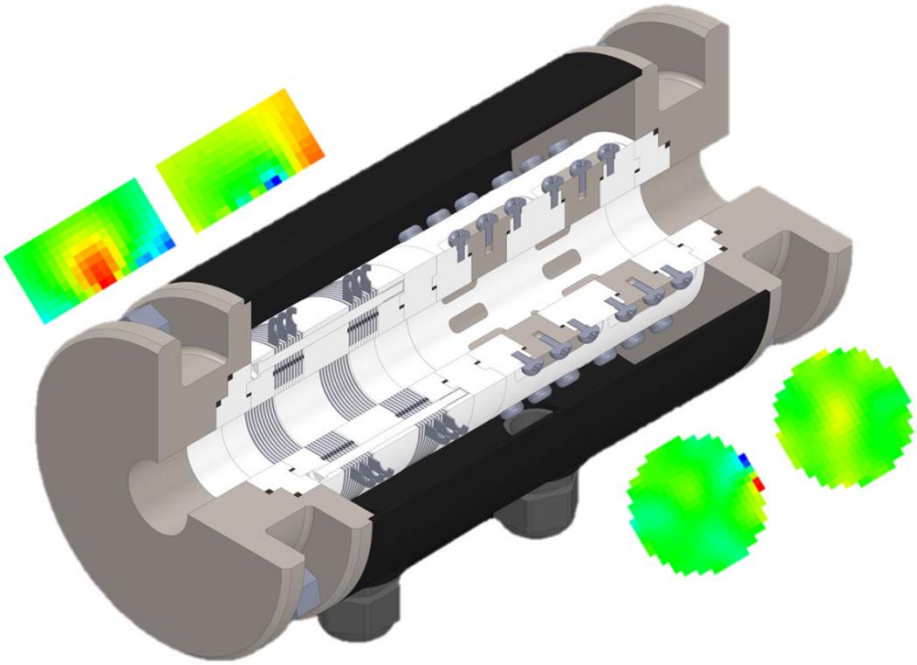

Figure 3.3 The Electrical Resistance Rheometry sensor design with accompanying computed tomograms

The linear and circular tomograms may be segmented into zones of interest to develop a number of radial velocity measurement positions in the pipe cross-section; the zone schemes for the aforementioned tomogram types are depicted in Figure 3.4. To remove noise, the bottom layer of the linear, or multi-scale, tomogram has been removed alongside the first and last three pixels, in the direction of flow, to yield nine radial velocity measurements. These nine measurements may then be further reduced to four, with pixel layer 1 of Figure 3.4a removed and two pixel layers averaged to just one. This alteration was implemented to introduce an ‘effective’ weighting to the fitting with a greater number of measurement points located in the central region of the velocity profile which pertain to the low shear rate region, whilst ensuring a complete velocity profile is obtained. When experimenting upon complex fluids, which observe wall phenomena, the entire zone scheme displayed in Figure 3.4a can

be utilised to provide enhanced detail of the velocity profile near to the wall. In a similar manner, the circular tomogram has been segregated with eight zones selected based upon radial position. For each of these zones, the obtained conductivity is averaged and normalised and afterwards the cross-correlation algorithm is performed across and within measurement arrays. ERR possesses a greater temporal resolution than rotational rheometry, when considering a complete shear rate range, with an acquisition time of 30 seconds which enables the monitoring of dynamic processes. This temporal resolution is a reduction of almost 100 % when compared to NMR techniques (Blythe et al., 2017) and is also able to be further improved with the cross-correlation algorithm implemented continuously to meet the real time criterion (Kapinchev, 2015).

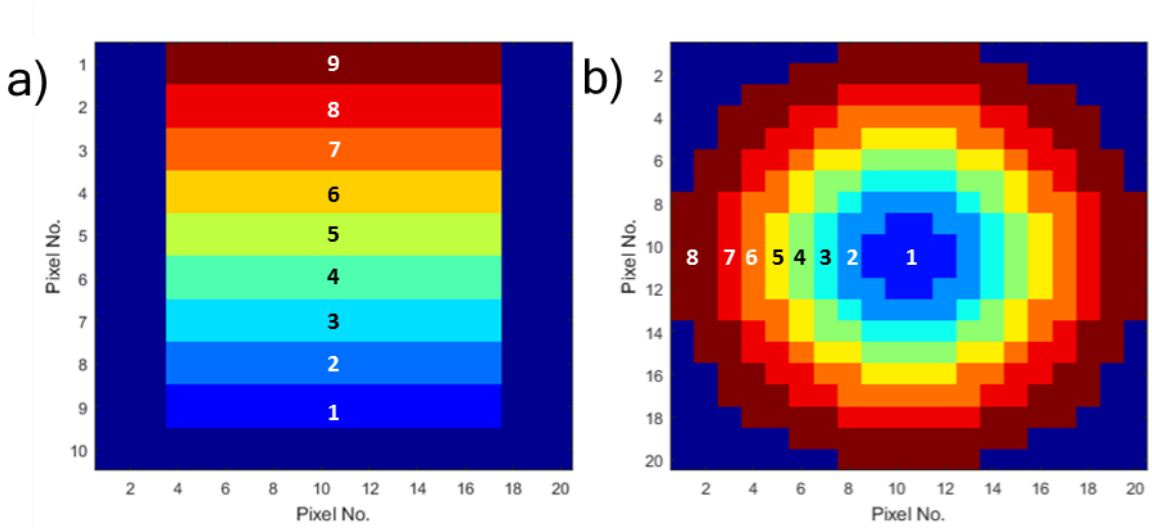

Figure 3.4 Tomogram Zone Scheme: a) Linear (Multi-Scale) Tomogram: b) Circular Tomogram

For this application, a pulsed ohmic heater (C-Tech Innovation, UK) was developed to provide the required conductivity perturbation by delivering a small increase in temperature over a short time period. This operates by imparting an alternating current, of frequency 50 Hz - 100 kHz, and hence electrical energy, to the fluid which is rapidly converted to thermal energy (Knirsch et al., 2010). An example of the produced signal, for a pixel in zone 1 in each circular array is exhibited in Figure 3.5a. Due to the requirement of a relatively conductive

media, the range of conductivities of the test media is identical to those suitable for electrical resistance sensing, in excess of 1 mS cm^{-1}. Moreover, ohmic heating is advantageous as it provides uniform heating of the pipe cross-section; converts electrical energy to thermal energy with 95 % efficiency; has the capability for automation; does not require the physical inclusion of a tracer and minimal degradation of thermosensitive products. This extent of degradation is further limited with a required temperature rise for the ERR sensor to perform its function of only 0.7°C for 0.5 s. It is also assumed that a negligible impact upon flow properties is brought about by the affecting conductive heat dissipation; this may be quantified by the thermal Péclet number (Pe), defined as the ratio of the advective and diffusive heat transport rates and is described by Eq. 3.2 (Paul et al., 2004).

$$Pe = \frac{\bar{u} \cdot D_p}{\alpha} \tag{3.2}$$

where Pe represents the Péclet Number, $\bar{u}$ is the average flow velocity, in m s^{-1}, D_p is the pipe diameter, in m, and α is the thermal diffusivity in m^2 s^{-1}.

The thermodynamic and physical properties used within the above equation were extracted, from Yaws (2003), for both glycerol and water to calculate the thermal Péclet numbers. However, such properties are unavailable for the aqueous xanthan gum and Carbopol solutions. As the majority of these solutions consist of water, their thermal diffusivity was estimated assuming the Stokes-Einstein relationship, where thermal diffusivity is inversely proportional to viscosity. All values of Pe calculated in these experiments exceeded 18,000 throughout, thus the assumption of negligible thermal diffusivity (Pe > 200) is easily justified.

Ohmic heating has extensively been applied within the food industry and as a result this robust conductivity perturbation technique is able to be operated under hygienic conditions, with rheology a critical quality control parameter in the optimisation, processing methodology and the development of many products within this industry (Maloney and Harrison, 2016). The employment of this ohmic heater develops a repeatable conductivity perturbation as depicted in Figure 3.5a. The subsequent implementation of the cross-correlation algorithm

can yield both two and three-dimensional velocity profiles. However, the velocity profile within the laminar regime is known to be axisymmetric and hence there is only a requirement for the use of the two-dimensional velocity profile in the determination of rheology (Incropera et al., 2007). The extraction of two-dimensional velocity profile also reduces the computational requirements to achieve the desired high temporal resolution.

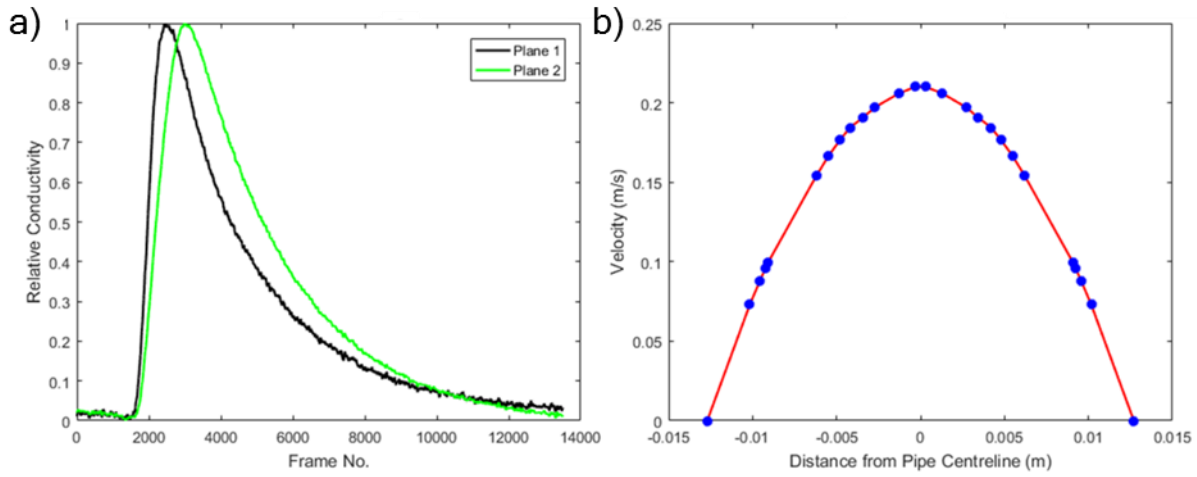

Figure 3.5 Electrical Resistance Rheometry sensor measurement: a) normalised ohmic heater conductivity perturbation; b) 75 wt% glycerol two-dimensional velocity profile

3.2.4 Rheological Parameter Extraction

The rheological properties of a fluid strongly influence the shape of the velocity profiles in laminar pipe flow due to a shear rate response of the fluid. Consequently, the raw velocity measurements may alone act as a fingerprinting tool; this can be utilised to infer rheological behaviour exhibited by complex fluids systems i.e. shear-banding, wall depletion and shear-induced phase migration. However, if the rheological behaviour is known to adhere to conventional rheological models, the velocity profile shape can be related to the constitutive equation of the fluid, with the desired parameters being directly outputted. The specific constitutive equation for a power law fluid is given as:

$$\tau = k\dot{\gamma} = k\left(-\frac{du}{dr}\right)^n \tag{3.3}$$

where τ is shear stress, in Pa; k is consistency index, in Pa s^n; $\dot{\gamma}$ is shear rate, in s^{-1}, n is consistency index; u is velocity within the pipe, in m s^{-1}, and r is radius, in m.

Once extracted, the velocity profile may then be coupled with the measurement of differential pressure, ΔP, per unit length, L, to obtain the linear shear stress profile in steady state, incompressible, laminar flow as derived from a force balance on an annular element in cylindrical pipe geometry (Wilkinson, 1960).

$$\tau = \frac{\Delta P \cdot r}{2L} \tag{3.4}$$

where ΔP is the differential pressure drop, in Pa, along a pipe length, L, in m, with r representing a pipe radius, in m.

With the substitution of Eq. 3.4 into Eq. 3.3, subsequent re-arrangement and integration and implementing the boundary conditions of u = 0 at r = R and u = u at r = r, the laminar velocity profile, u(r), for a power law fluid is obtained.

$$u(r) = \left(\frac{\Delta P}{2kL}\right)^n \left(\frac{n}{n+1}\right)\left(R^{\frac{n+1}{n}} - r^{\frac{n+1}{n}}\right) \tag{3.5}$$

From the first boundary condition, it can be seen that the no-slip condition has been implemented as the velocity is zero at the pipe wall radius, R; however, a correction may be made to this model for the inclusion of fluids which observe a slip layer. Rahman (2013) suggested that the combination of the imaging of the cross-sectional conductivity distribution alongside the simultaneous measurement of velocity profile or rheology may be able to provide a detailed understanding of wall-slip behaviour in rheologically complex fluids.

A parametric fitting of the raw ERR data to the theoretical velocity profile of a fluid may then be applied in the extraction of the desired rheological parameters. To derive such

parameters, the Levenberg-Marquadt algorithm, a robust variant of the Gauss-Newton algorithm which solves non-linear least squares problems iteratively, was employed (Marquadt, 1968). As this selected algorithm does not possess second derivatives the overall computational time is reduced affording the aforementioned high temporal resolution. This algorithm has been utilised previously within ERT experiments; however, acting as a reconstruction algorithm (Tan et al., 2011).

The analysis may additionally be performed without the assumption of a rheological model and no prior knowledge of the material. A point-wise rheological characterisation is performed by the fitting of a fourth order polynomial to the velocity profile to obtain the velocity profile as a function of radius. A fourth order polynomial was selected as it is the greatest fitting order without the equation becoming badly conditioned. The first derivative of this polynomial equation directly yields the shear rate profile with the shear stress profile calculated using the aforementioned differential pressure measurement. A shear stress against shear rate plot is able to be ascertained; this output is analogous to that of a rotational rheometer with the desired rheological parameters able to be extracted in the same manner as traditional rheometry. Such an approach offers a limited shear rate range, with high shear rates unreliable as a result of averaging effects near the pipe-wall (Norton et al., 2010).

3.2.5 Residence Time Distribution

An additional application of this sensor is the in-line measurement of the residence time distribution (RTD) within the pipe. The pulse generated from the ohmic heater may be likened to the input delta function of an RTD measurement, as a result of uniform cross-sectional heating. The continuous conductivity ERR pulse is representative of the RTD response, or E-curve, which can subsequently be fitted to an appropriate mixing model such as a stirred tanks in series or axial dispersion model. From the acquisition of the velocity profile, it has been observed that the thermal diffusivity and heat loss is insignificant, due to the relatively short distance travelled and hence this technique may be considered applicable for RTD measurements.

3.3 Methodology

3.3.1 Materials

Three model aqueous-based fluids were selected to exhibit behaviour of three common rheological constitutive models, namely solutions of: glycerol (Darrant Chemicals, UK); xanthan gum, *from Xanthomonas Campestris* (Sigma-Aldrich, UK) and Carbopol 940 (Lubrizol, UK).

The formulated test fluids consisted of the mixing of 75 wt%, 85 wt% and 92.5 wt% glycerol in water and dissolving 0.1 wt%, 0.5 wt% and 1.0 wt% xanthan gum powder in water to form 15 L of aqueous solutions which exhibit Newtonian and shear thinning power law behaviour, respectively. Two Carbopol formulations were selected for this study, 0.1 wt% Carbopol, pH 7 and 1.0 wt% Carbopol, pH 7 as these are known to act as a rheological mimetic for industrial fluids (Simmons et al., 2009). The pH of the aqueous Carbopol solutions was adjusted via the incorporation of 0.1 M sodium hydroxide, supplied by Sigma-Aldrich, to induce a gel matrix whose rheological behaviour may be described using the Herschel-Bulkley constitutive law (Alberini et al., 2014). The mixing of all fluids was carried out slowly to prevent the incorporation of air bubbles. A portable conductivity meter, supplied by Hanna Instruments was utilised to determine the electrical conductivity of the fluids. All of the experimental fluids observe an electrical conductivity within the range of 1 - 9 mS cm^{-1} and hence are suitable for ERR.

The rheological properties of the fluids were analysed using an AG R2 rotational rheometer (TA Instruments) equipped with a smooth-walled, 4.006° stainless steel cone and plate geometry, of diameter 40 mm. The sample was held at 23 ± 0.1°C using an Peltier plate, before a logarithmic shear rate ramp was applied across the shear rate range of 0.01 - 1500 s^{-1}, over a duration of 600 seconds with 20 points per decade. The selected temperature was chosen as it is reflective of the temperature of the fluid in the subsequent flow experiments. To analyse the obtained data, a non-linear least squares regression was applied in the

TRIOS software, developed by TA instruments, to extract fitted rheological parameters; this analysis is similar to that utilised in the ERR analysis to elucidate rheological parameters. Such a fitting was performed at the low shear rate range, 0.01 - 100 s^{-1}, which is analogous to shear rates observed in pipe flow and removes errors which may occur due to weighting of the velocity profile. This low shear rate region is often the area of greatest interest when extracting more complex rheological behaviour. The resultant rheological properties acquired are presented in Table 3.1, Section 3.4.3.

3.3.2 Electrical Resistance Tomography

A simple recirculating pipeline was setup, Figure 3.6, which consisted of an agitated 60 L vessel and a controlled positive displacement pump (Fristam Ltd., UK) operated by a personal computer to circulate the fluid at a desired flow rate. The electrical resistance rheometer sensor, of diameter 25.4 mm, was placed in-line, with the ohmic heater located prior to the ERR sensor in series. The measurement of differential pressure was captured across the length of both the ohmic heater and ERR sensor and logged alongside the parameters of flow rate and temperature. The flow rate was monitored using a micro motion Coriolis flow meter (Emerson Ltd., UK).

Each of the fluids were interrogated across the flow rate range of 40 – 350 L hr^{-1}, with the ERR sensor connected to and operated by a v5r ERT instrument (Industrial Tomography Systems (ITS) Ltd., UK). A configuration of 4 planes, or arrays, of 8 electrodes was utilised alongside the adjacent electrode measurement protocol. The sensor was operated with two linear arrays, of length 12 mm, and two circular arrays employed. To enable a frame rate of 318 frames per second, the v5r was operated in block mode and one sample delay cycle. For a single measurement 12,000 (37 seconds) frames were taken to monitor the desired conductivity perturbation generated by the ohmic heater, whose voltage injection was set in the range of 1 – 1.5 kV for 0.5 – 1 s. The entire experimental procedure was repeated 20 times at each flow rate for each fluid to assess repeatability.

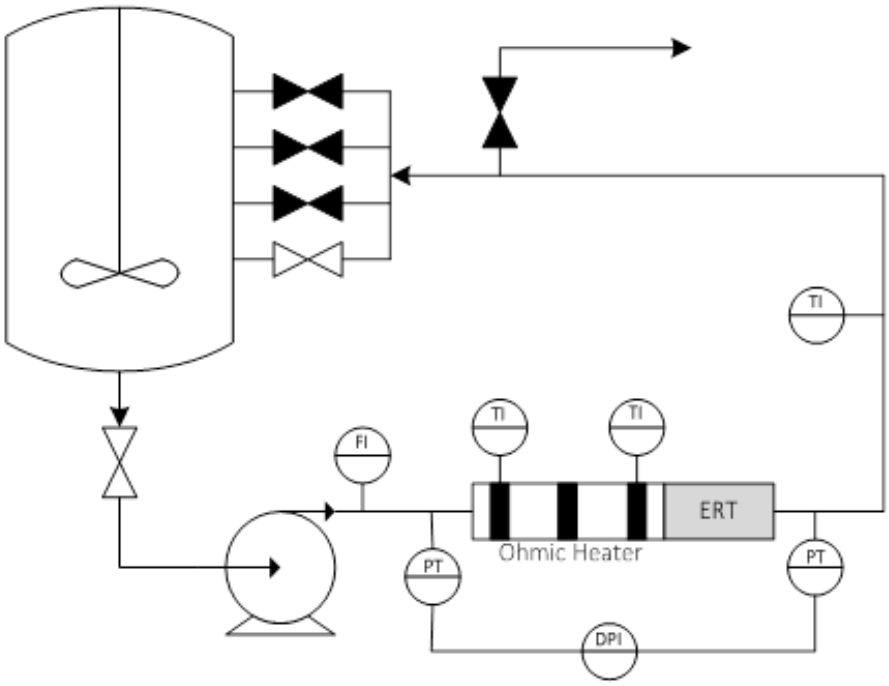

Figure 3.6 Experimental flow loop setup schematic

The obtained raw data was fed into a MATLAB code which contained the Modified Standard Back projection algorithm (Wang, 2002), described in Section 2.2, to reconstruct the tomogram image, and the subsequent rheological analysis. Supplementary experiments were undertaken to determine the capability of simultaneous capture of both rheological and mixing behaviour. This was conducted using 15 L of aqueous 0.1 wt% xanthan gum solution with a step change in xanthan gum concentration brought about with the addition of a 3.5 wt% solution; the resultant batch volume and concentration was 17 L and 0.5 wt%, respectively. The xanthan gum powder in the concentrated solution was mostly, but not entirely, dissolved as to interrogate more variable mixing phenomena with some polysaccharide agglomerates present. Across 25 minutes, the rheological properties and mixing times of the recirculating fluid were examined using a code developed in MATLAB; the ITS p2+ V8 software was employed to investigate mixing behaviour in a more thorough manner.

3.3.3 Particle Image Velocimetry

Validation of the cross-sectional velocity profile has been provided by 2-D PIV measurements made using a TSI PIV system. A 532 nm (green) laser (Litron Nano PIV), pulsing at 100 Hz, is synchronised to a single TSI Power view 4MP (2048 x 2048 pixels) 12 bit CCD camera using a synchroniser (TSI 610035) assigned to a personal computer. The TSI Insight 4G software was utilised to control the software, process data and generate velocity fields with subsequent radial velocity profile measurement averaging performed in MATLAB. The Nyquist PIV algorithm, developed by TSI, was used to obtain such velocity fields; this setup is analogous to the one used by Alberini et al. (2017) but has been adapted to monitor pipe flow.

PIV measurements were conducted within a circulation loop without the inclusion of the ohmic heater to determine the extent of its effect upon the measured velocity profile. For each of the assigned flow rates, 500 images were captured, erroneous data removed, and the remaining data combined with average flow field determined. The erroneous data occurred as a result of vibration of the rig perpendicular to the flow direction between pulses; this was observed on an average of 10 frames per 500 captures, however, is not problematic due to the laminar nature of the flow. The spatial resolution of such a setup, supplied by TSI Inc, was 12 μm $pixel^{-1}$ with an interrogation area set to 64 x 64 pixels and the Gaussian peak method applied to identify single particles (Westerweel, 1997). All of test fluids were experimented upon with the exception of 1.0 wt% xanthan gum due to its opaque nature.

3.4 Results and Discussion

3.4.1 Electrical Resistance Velocimetry

3.4.1.1 In-pipe Velocity Profiling

Critical to the in-situ determination of rheology, the measurement of the velocity profile must first be interrogated with the obtained results for each fluid outlined in Figure 3.7.

The velocity profiles within this figure are acquired from the cross-correlation of a single conductivity perturbation passing through the sensor; these perturbations typically have a duration of 20 seconds. From the obtained velocity profiles, it is evident that the Newtonian glycerol solutions observe the conventional parabolic velocity profile of laminar pipe flow, Figures 3.7a and 3.7b, which is observed when applying both fitting algorithms, Levenberg-Marquadt and gradient-based techniques and within the raw data. Such a parabolic shape implies that hydrodynamic entrance effects have apparently been overcome in this measurement allowing the application of laminar flow theory to rheological extraction to be successful. Not only is the parabolic shape in agreement with the theoretical laminar velocity profile, but the maximum velocity mirrors that expected from the measured flow rates.

When changing the fluid to the shear-thinning, xanthan gum solutions, the difference in shear rate response yields the expected increased blunting of the originally parabolic velocity profile with increased xanthan gum content. This flattening of the velocity profile is indicative of the expected shear-thinning behaviour and is illustrated in Figure 3.7c. During experimentation, unfortunately, an identical flow rate was unable to be attained when measuring 0.5 wt% and 1.0 wt% xanthan gum and hence a perfect comparison is not able to be conducted. However, in Figure 3.7d, it can still be seen that for a 1.0 wt% xanthan gum solution the obtained velocity profile observes increased flattening, and hence degree of shear-thinning, in comparison to the aqueous, 0.5 wt% xanthan gum solution, despite the former conducted at a greater flow rate.

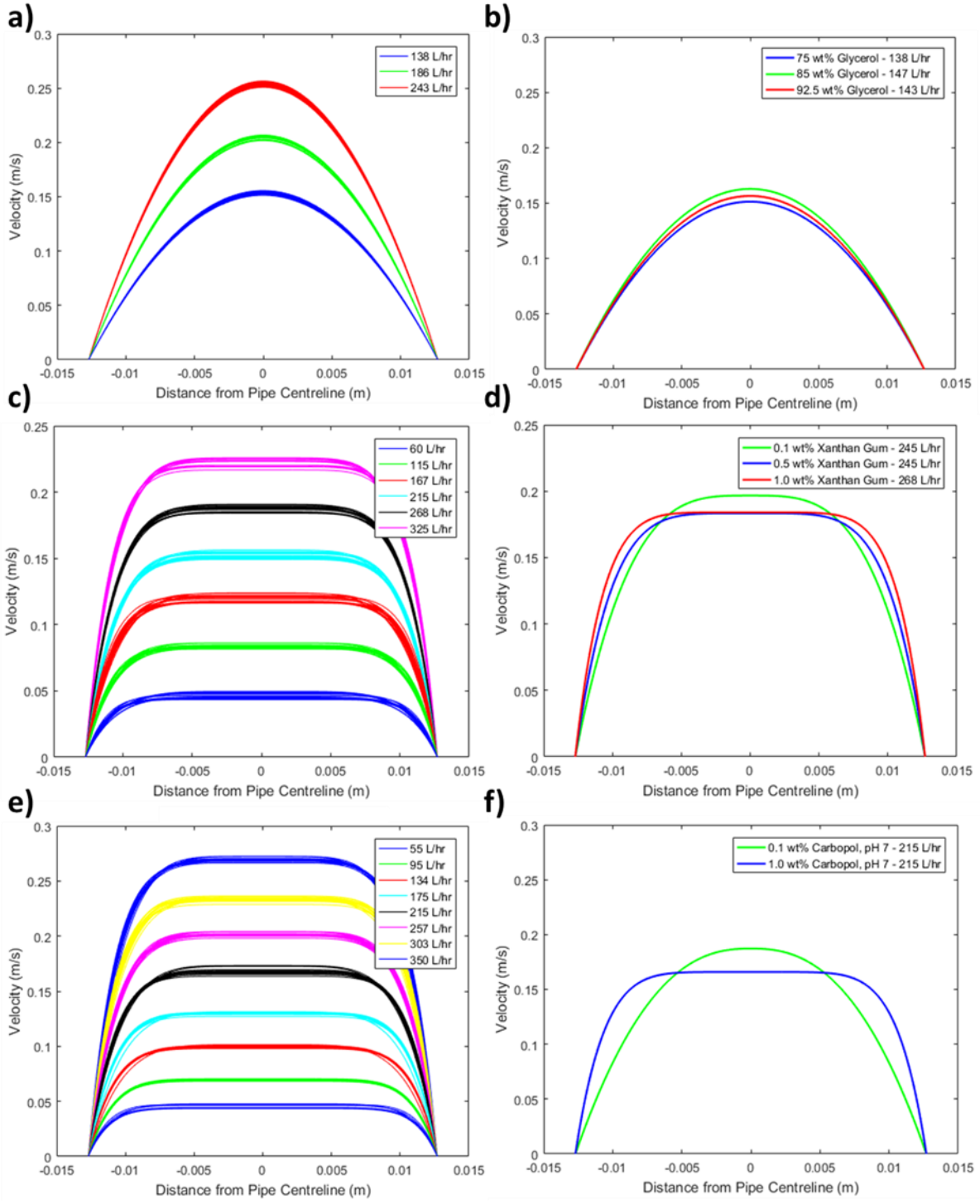

Figure 3.7 Electrical Resistance Rheometry Velocity Profiles: a) 75 wt% glycerol – multiple flow rates; b) averaged velocity profiles - 75, 85, 92.5 wt% glycerol; (c) 1.0 wt% xanthan gum – multiple flow rates; (d) averaged velocity profiles - 0.1, 0.5 and 1.0 wt% xanthan gum; (e) 1.0 wt% Carbopol, pH 7 – multiple flow rates; (f) averaged velocity profiles - 0.1 wt%, pH7 and 1.0 wt%, pH 7 Carbopol 940

A similar shape is observed during the extraction of the Herschel-Bulkley modelled Carbopol 940 solutions, Figure 3.7e, with the flattened region instead indicative of a plug flow and thus the presence of a yield stress. As the flow rate increases, the radius of such a plug is reduced signifying that the yield stress is being tracked; this is due to the increased magnitude of the opposing shear stress profile at an increased flow rate. Initially, it can be seen that the features of the outputted velocity profiles are in accordance with expected theoretical velocity profiles. Moreover, a comparison of the two Carbopol concentrations observes a large difference in the length of the plug region of the velocity profiles which is indicative of the higher yield stress of the more concentrated 1.0 wt%, pH Carbopol solution. It could therefore be stipulated that the velocity profiles mimic the theoretical velocity profiles of the fluids which have been tested upon and demonstrate repeatability throughout with minor variations of the velocity profile observed at a constant flow rate.

To quantify such promising results, a statistical analysis has been performed across 20 independent ERR velocity profiles for each discrete radial velocity position; this yields an average 95 % confidence interval of ± 2.93 % when compared to the mean. This variation manifests as a mean standard error in velocity of just 0.0043 m s^{-1} which is seen to be consistent across all radial positions. Resultantly, measurement points located near the wall observe a greater uncertainty; however, this is dampened in the overall fitting due to an 'effective' weighting with more discrete radial velocity measurement at the centre of the pipe. This is also an important factor when determining rheological parameters, with the region of interest typically the low shear rate region which coincides with the velocity at the centre of the pipe. The radial velocity profile obtained by ERR may be considered to be in close agreement with the theoretical laminar velocity profile with a typical correlation coefficient, R^2, of 0.99 between raw and accepted velocity values which additionally lie within one standard error of one another.

3.4.1.2 Coriolis Flow Meter Validation

The use of a positive displacement pump for this test gives rise to potential pulsation within the flow with a variation in flow rate, Q, logged using the Coriolis flow meter, of ± 2 %. This is analogous to the outputted data by Electrical Resistance Rheometry and hence the measured velocity profiles can be said to lie within experimental error. The presence of this flow meter within the flow loop provides a further basis for comparison against an independent and established measurement technique. Using the general relationship, Eq. 3.6, derived from flow through an annular element of radius r and width dr, the acquired velocity profile can subsequently be utilised to determine the flow rate within the pipe.

$$Q = \frac{\pi R^3}{{\tau_w}^3} \int_0^{\tau_w} \tau^2 f(\tau) d\tau \tag{3.6}$$

where τ_w is the shear stress at the wall in Pa.

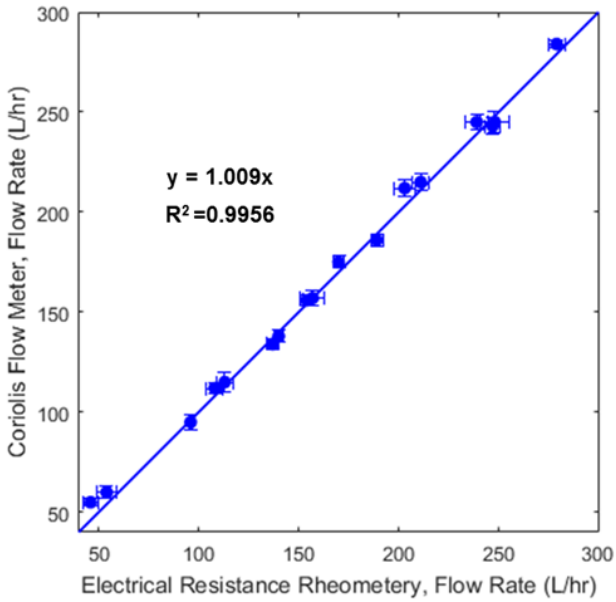

Figure 3.8 A parity plot comparing the measured flow rate from a Coriolis Flow Meter and Electrical Resistance Rheometry

A parity plot, Figure 3.8, may be used to compare the obtained flow rates from a Coriolis Flow meter and Electrical Resistance Rheometry with excellent agreement, yielding a correlation coefficient of 0.9956. Despite observing a greater variability, ERR produces a mean standard error of ± 6 L hr^{-1} and consequently may be considered repeatable. This affords validation of the ERR technique with an independent measurement technique which is well-established.

3.4.1.3 Velocity Profile analysis (no prior knowledge)

As outlined in Section 3.2.2, an alternative velocity profiling methodology, gradient-based, may be applied to the fitting, which does not require prior knowledge of the fluids rheological behaviour. Subsequently, this may be compared with the Levenberg-Marquadt fitted velocity profile with a resultant correlation coefficient of 0.997 for aqueous glycerol solutions. Such a high correlation indicates that the extent of the parametric fitting is minimal and hence the raw data is an accurate representation of the velocity profile. With an increased blunting of the velocity profile, the degree of correlation is reduced to 99.0 %, 98.0 %, 97.3 % and 96.1 % for aqueous solutions of 0.5 wt% xanthan gum, 1.0 wt% xanthan gum, 0.1 wt% Carbopol 940 and 1.0 wt% Carbopol 940, respectively. This occurs due to the existence of localised maximum and minima in the polynomial fitting in the flat region of the velocity profile. Consequently, it is recommended that the gradient-based methods are not applied to fluids which exhibit high levels of 'apparent' shear-thinning behaviour; this is in agreement with Wiklund et al. (2010).

However, in such cases the raw velocity profile data points alone may be utilised as a rheological fingerprinting tool, especially when considering more complex rheological phenomena that do not adhere to conventional models. If the rheological properties of the interrogated fluid are unknown, the theoretical velocity profiles of each constitutive equation may be fitted simultaneously, using the Levenberg-Marquadt algorithm, to ensure a more robust analysis. The Akaike Information Criterion may subsequently be employed to select the optimal rheological model and associated parameters.

3.4.2 Particle Image Velocimetry

Despite providing a valuable comparison, the Coriolis flow meter does not provide a direct validation of the measured velocity profile shape and magnitude. However, the application of Particle Image Velocimetry (PIV) allows Electrical Resistance Rheometry to be quantifiably validated against a widely accepted and extensively studied velocimetry technique of superior spatial resolution. The obtained results from 75 wt% aqueous glycerol solution at a flow rate of 240 L hr^{-1} are displayed in Figure 3.9b and 3.9c alongside an example capture, Figure 3.9a, with the anticipated parabolic velocity profile observed.

A comparison of the theoretical Newtonian velocity profile and the PIV measurement yields a residual sum of squares of 4.43×10^{-4} m^2 s^{-2} and a correlation coefficient of 0.9992 and accordingly, the glycerol velocity profile can truly be considered parabolic. This provides a vital result as the irrotational flow regime has been achieved due to the removal of hydrodynamic entrance effects, which permits the application of traditional laminar flow theory. This regime ensures that the laminar hydrodynamic boundary layer has encompassed the entire pipe diameter and prevents the flattening of the traditional velocity profile (Incropera et al., 2007). To achieve irrotational flow, an entrance length, described by Eq. 3.7, is required to permit the development of the boundary layer.

$$L_{lam} = 0.05 \cdot Re \cdot D_p \tag{3.7}$$

where L_{lam} is the laminar entrance length, in m; Re is Reynolds number and D_p is the pipe diameter, in m.

The Reynolds number of a 75 wt% glycerol solution is the largest of the experimental flow conditions with a resultant hydrodynamic entrance length, of 20 cm, due to its relatively low viscosity and high density. This is in agreement with the experimental design since the circular sensor arrays, which monitor the central pipe region, are located 41 cm from the closest potential flow disturbance, the live ohmic heater electrode. Therefore, the assumptions of fully developed laminar flow is no longer an assumption affording laminar flow

theory and specific constitutive rheological models to be applied, during the rheology extraction, across all of the interrogated fluids. Moreover, the flow field can be seen to be axisymmetric; this is an additional assumption which has been made during the rheological determination which may now be verified.

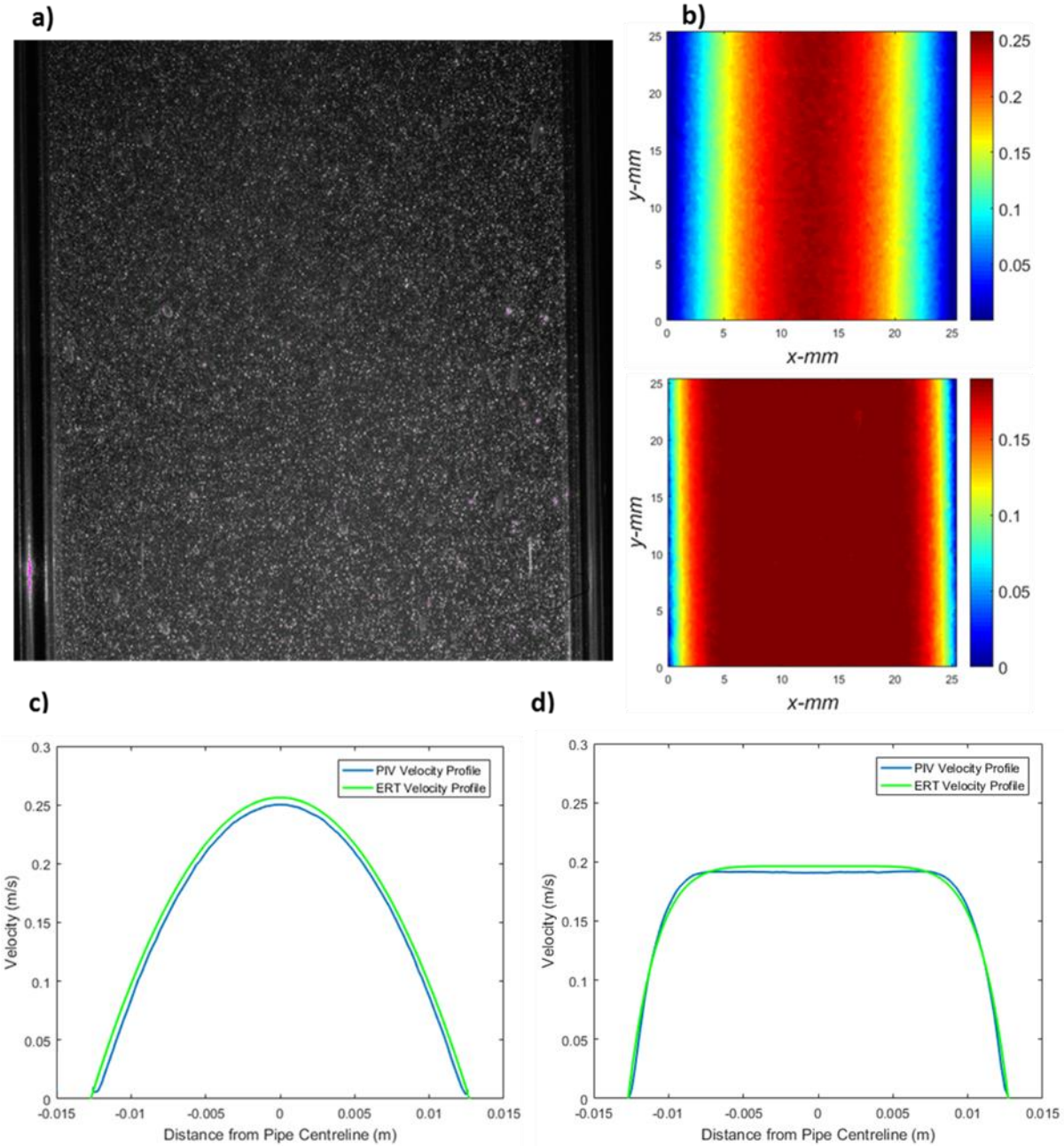

Figure 3.9 PIV Cross-Sectional Velocity Profile: (a) example PIV capture; (b) PIV velocity magnitude for glycerol at 240 L hr^{-1} (top) and 1.0 wt% Carbopol 940, pH 7 at 260 L hr^{-1} (bottom); (c) comparison of the ERR and radially averaged PIV glycerol velocity profiles; (d) comparison of the ERR and radially averaged PIV Carbopol velocity profiles.

Not only does the parabolic nature remove assumptions, both the shape and magnitude of the radially averaged velocity mimic the velocity profiles obtained by electrical resistance sensing. The velocity vectors are all present in the axial direction of flow with a negligible radial velocity component; this is also indicative of traditional laminar theory. When the observed velocity outside the diameter is excluded, a correlation coefficient, R^2, of 0.99 exists between the ERR and PIV glycerol velocity profiles with a root mean squared error (RMSE) of just 0.0064 m s^{-1}; this is representative of 3.7 % of the average velocity. Therefore, the independent velocity profile measurements displaying excellent agreement for the Newtonian glycerol solution.

This is also true when the rheology of the process media is changed. The aforementioned blunted velocity profile characteristic of the yield stress fluid, 1.0 wt% Carbopol, pH 7, is obtained in both the PIV and ERR measurements. A similar comparison as conducted for glycerol may be performed with an outputted RMSE of 0.0048 m s^{-1}, 2.8 % of the average velocity, and correlation coefficient of 0.99. Despite this experiment being conducted without the presence of the ohmic heater, the acquired velocity profiles obtained from both PIV and ERR are analogous. Thus, it may be stipulated that the thermal energy dissipation has a negligible impact upon the flow. The similarity between the comprehensive PIV measurement, theoretical laminar velocity profiles and Electrical Resistance Tomography is a significant validation of this novel in-line velocity profile measurement technique.

The obtained velocity profile may therefore be utilised unaccompanied as a fingerprinting in-line rheometer, especially in the case of more rheologically complex fluids which do not adhere to specific constitutive models and equations. This study has also verified the electrical field penetration of the linear arrays velocity vectors, within the conductivity range of 1 - 9 mS cm^{-1}. It must be noted that the radial velocity positions remained constant throughout all experiments and is expected that this electrical field penetration is also applicable to fluids of conductivity in excess of 10 mS cm^{-1}.

3.4.3 Rheological Parameter Extraction

The rheological parameters determined by ERR are compared to off-line rotational rheometry in Table 3.1. In the measurement of accuracy, the rheological parameters outputted by the rotational rheometer may be considered as the 'true' value; however, it is known that a direct comparison of the two rheometry techniques is imperfect as ERR affords a characterisation within the flow environment. It must be noted the experimental data acquired by the AR G2 rotational rheometer was performed once, with only one sample taken and hence may not be entirely reflective of the product stream.

Using ERR, the mean obtained viscosities for 75 wt%, 85 wt% and 92.5 wt% glycerol solutions were 0.0223 Pa s, 0.0982 Pa s and 0.250 Pa s, respectively. With the requirement of just a single parameter to be extracted, the viscosity of a Newtonian fluid is able to be achieved with excellent reliability with the 95 % confidence interval approximately 2.5 % of the mean value. This may be observed in Figures 3.10b and 3.10c which observe minimal difference between the rotational rheometer and ERR. Despite being small, this variation in viscosity is seen to portray a relationship between the experimental temperatures of the interrogated fluid with the inverse proportionality temperature and viscosity observed. The rheological behaviour of glycerol is known to be highly thermosensitive (Chen and Pearlstein, 1987).

In addition to such repeatability, the measured viscosity displays good agreement with the accepted technique within industrial processing, a rotational rheometer with an average accuracy of 99.1 %. Therefore, the rheological parameters obtained by off-line rheometers are analogous to that of ERR in the same case of simple fluids; this may differ depending on the complexity of the fluid and off-line experimental protocol. However, it can be said that this technique is able to act as an in-line viscometer.

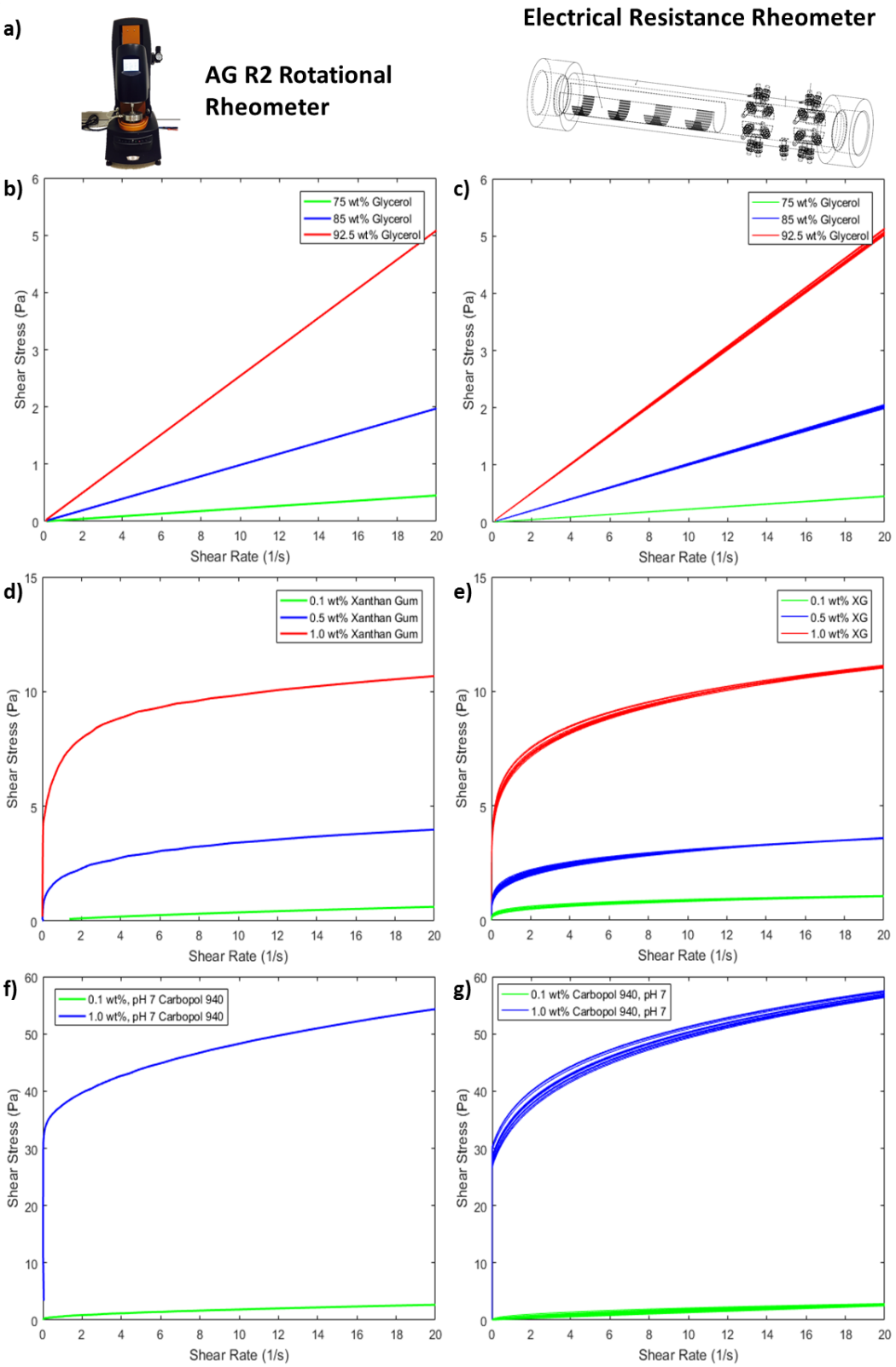

Figure 3.10 Comparison of ERR and rotational rheometry: a) Images of the rotation and ERR rheometer; b), d) and f) shear stress vs. shear rate plot generated from a rotational rheometer for glycerol, xanthan gum and Carbopol, respectively; c), e) and g) shear stress vs. shear rate plot generated for glycerol, xanthan gum and Carbopol using ERR, respectively

As the complexity of the selected constitutive model increases, a simple univariate model validation is not adequate. The parameter estimation becomes an ill-conditioned mathematical problem; the constitutive models may be described by two or more parameters with the analysis performed from a single velocity profile. Owing to the ill-conditioned nature of this mathematical problem, the parametric fitting of this model against a single objective function does not validate entire model and does not support model outputs (Stitt et al., 2015). A measure of the residual squares alone, R^2, can be said to be an inadequate criterion in the analysis of a parametric fitting with the mathematical form of equations able to contribute to an apparent 'good' fit. However, the adjustable parameters of the fitting can be poorly predicted with the least squares alone an unreliable indicator of quality of model fit or model discrimination. Stitt et al. (2015) reported that in nineteen reaction kinetics models fitted to the same datasets with R^2 values in excess of 95 % were observed with many in exceeding 99 %.

Although the inadequacies of the residuals squares analysis alone are evident, this technique has been traditionally utilised across all rheometry. In the analysis of ERR, the evaluation of the quality of fit has been extended to the statistical quality of the parameter estimates, with the common approach of 95 % confidence interval of the adjustable parameters interrogated across the 20 independent measurements. Moreover, this confidence interval possesses an inherent link between observations, noise within the data and the degrees of freedom to yield a more complete analysis of the obtained data (Sjöblom, 2009). The extracted rheological parameters are displayed in Table 3.1, alongside both the least squares residuals and 95 % confidence intervals.

Table 3.1 A comparison of an off-line rotational rheometer with the ERR. Note: the uncertainty presented within this table is the 95 % confidence interval for the fitted parameters

	TA R2 Rotational Rheometer			Electrical Resistance Rheometer		
Material	**μ, Pa s**			**μ, Pa s**		
75 wt% Glycerol	0.0226 (R^2=0.9997)			0.0223 ± 0.0004 (R^2 = 0.994)		
85 wt% Glycerol	0.0986 (R^2=0.9993)			0.0982 ± 0.003 (R^2 = 0.995)		
92.5 wt% Glycerol	0.254 (R^2=0.9993)			0.250 ± 0.004 (R^2 = 0.992)		
	τ_y, Pa	**k, Pa s^n**	**n**	**τ_y, Pa**	**k, Pa s^n**	**n**
0.1 wt% XG		0.0712	0.723 (R^2 = 0.990)		0.0740 ± 0.003	0.704 ± 0.04 (R^2 = 0.990)
0.5 wt% XG		1.27	0.350 (R^2 = 0.991)		1.21 ± 0.04	0.348 ± 0.02 (R^2 = 0.990)
1.0 wt% XG		6.13	0.195 (R^2 = 0.995)		6.18 ± 0.2	0.197 ± 0.01 (R^2 = 0.993)
0.1 wt% Carbopol, pH 7	0.350	0.342	0.604 (R^2 = 0.999)	0.32 ± 0.02	0.372 ± 0.02	0.601 ± 0.04 (R^2 = 0.99)
1.0 wt% Carbopol, pH 7	29.7	5.93	0.460 (R^2 = 0.991)	29.1 ± 1.7	5.80 ± 0.3	0.486 ± 0.04 (R^2 = 0.994)

The power law behaviour of xanthan gum is described by both the consistency index, k, and power index, n, and hence poses an ill-conditioned problem; however, the incorporation of the Levenberg-Marquadt algorithm has been seen to be vital to dampen the instability and increase confidence in the measurement. Contrary to this, the acquired ERR rheological parameters are seen to mimic those obtained from a conventional rotational rheometer possessing an accuracy of 97.4 % and 98.5 % for k and n, respectively. It can be seen that the fitting of the 0.1 wt% and 0.5 wt% xanthan gum shear rate ramp represents the lowest

correlation coefficient of 0.99; this is analogous to the fitting of the raw ERR velocity data to the theoretical profile.

As expected, the introduction of a third parameter through the utilisation of the Herschel-Bulkley model produces the greatest variability of the measurement at around ± 6 %. Despite the outputted rheological parameters observing increased uncertainty, when compared to a rotational rheometer, the values obtained from ERR can be seen to be in good agreement. This arises as a consequence of the parametric fitting with the off-line rheometer parameters yielding a theoretical velocity profile which has a correlation coefficient of 0.97 with the ERR velocity profile. This may be reflected as the outputted values from the off-line rheometer lie within the 95 % confidence interval of the ERR rheometry. Although Carbopol solutions are typically considered not to exhibit thixotropic properties, shear-dependent history at > 0.2 wt% concentration has been witnessed (Lubrizol, 2002) which may give rise to a difference in the obtained rheological properties. It must additionally be acknowledged that the 0.1 wt% Carbopol 940 solution may be modelled with a power law rheological model as a result of the presence of a small yield stress. When fitting to off-line rheometry data, 0.1 wt% Carbopol yielded a correlation coefficient of 0.999 for both power law and Herschel-Bulkley constitutive equations.

Overall, the non-linear least square fitting from the ERR accurately and repeatedly outputs the desirable rheological parameters which mimic conventional rotational rheometry. ERR can therefore be utilised as an effective, robust, in-line rheometer when the Levenberg-Marquadt algorithm is employed. However, when employing the gradient based method, instabilities may arise with numerous oscillations between local minima and maxima due to the polynomial fitting. This is in agreement with Wiklund et al. (2007) who recommend that this analysis methodology should be employed for profiles which are relatively parabolic. If the fluids are not known to adhere to conventional rheological models this velocimetry technique may additionally act as a standalone fingerprinting tool for rheology without the requirement of the measurement of differential pressure.

3.4.4 Mixing Analysis

3.4.4.1 Mixing Time and Rheometry

As it provides the mapping of electrical impedance across the cross-section of the sensing domain, ERT has extensively been utilised to monitor the mixing performance across numerous unit operations. With the inclusion of a circular array within the ERR sensor design such an analysis is permitted during the simultaneous capture of rheometry. A step increase in the concentration of aqueous xanthan gum solution, as described in Section 3.2, has been successfully interrogated with the tomogram capable of providing an averaged cross-sectional conductivity within the pipe. Due to xanthan gum possessing a dissimilar conductivity to water, the averaged tomogram conductivity affords a detailed examination of mixing time. A 95 % mixing time, θ_{95}, of 13 minutes 22 seconds and 99 % mixing time, θ_{99}, of 20 minutes 4 seconds was ascertained using a coefficient of variance approach for the mixing of these aqueous xanthan gum solutions; 80 %, 85 % and 90 % mixing times were also calculated. When blending in stirred tanks, the concentration differences are seen to decrease exponentially; this is demonstrated in Eq. 3.8 (Paul et al., 2004).

$$\frac{d(1-C)}{d\theta} = -k(1-C) \tag{3.8}$$

Integrating the above equation, between the boundary conditions C = 0, θ = 0 and C = C, θ = θ, yields a linear relationship between the natural log of the concentration difference and mixing time; this may be utilised to predict mixing times of different extents. Figure 3.11c, displays such a plot with the aforementioned linear relationship observed with a gradient of -0.191 min^{-1} and residual squares of 0.9854. The reliability of the mixing time measurement is enhanced when compared with traditional mixing time calculations which utilise a single point conductivity or temperature probes; the ERR measurement is performed across two pipe regions and interrogates the entire cross-section. Figure 3.11a, demonstrates the average tomogram pixel conductivity utilised for this mixing time computation and within this

measurement exists four pulses from the ohmic heater which are utilised to simultaneously elucidate rheology.

The ERR methodology was utilised alongside the parametric Levenberg-Marquadt algorithm fitting, to output the rheology from the four aforementioned pulses. A pulse may be observed just after 30 seconds prior to the step increase in xanthan gum concentration with the computed ERR flow curve and rheological parameters mirroring those of a 0.1 wt% aqueous solution outlined in section 3.4.3. However, upon the addition of xanthan gum an evolution in the rheological behaviour may be observed with an apparent increase in both the consistency index and shear-thinning nature of the fluid; this is to be expected. The final rheological parameters acquired during this test, at 18 minutes and 30 seconds, are a consistency index and power index of 1.17 Pa s^n and 0.40, respectively; this is similar to the parameters obtained from 0.5 wt% xanthan gum rheological measurements. Such results may be observed in Figure 3.11b. This time may be considered the point at which the rheology is almost completely evolved which is in alignment with the measured 95 % mixing time measurement as these rheological parameters were extracted upon the completion of mixing.

Although, in this instance, rheometry data was collected at six minute intervals, the ERR system possesses a much greater temporal resolution with the interval time able to be reduced to 30 seconds. This evolving rheological measurement in other processes may be linked with the monitoring displacement of fluids within a pipe which can be utilised during product changeover, start-up and shutdown. Henningsson et al. (2007) was able to monitor the rinsing step, in which yoghurt is displaced by water with the use of a hygienic ERT sensor system and displayed good agreement with Computational Fluid Dynamics (CFD).

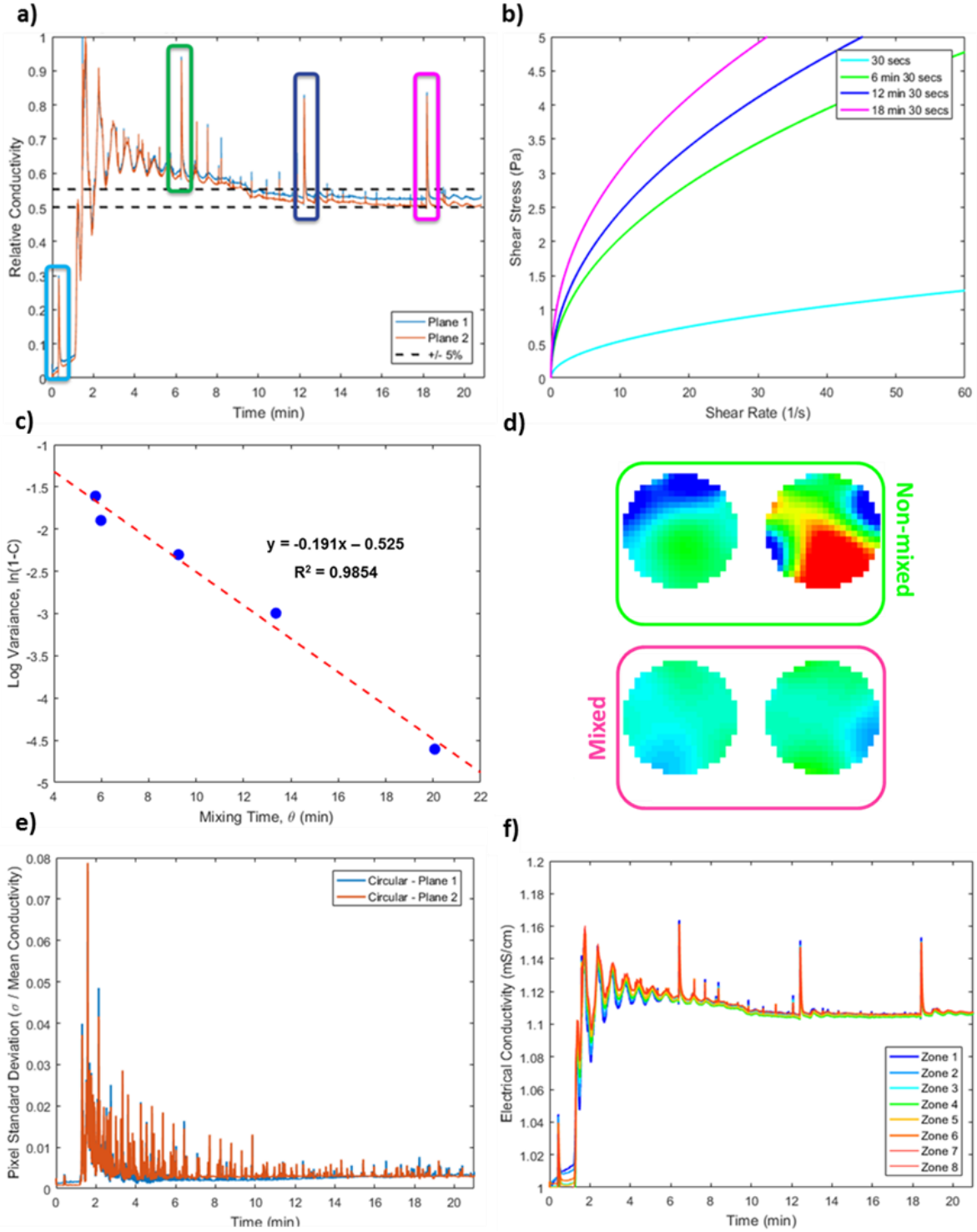

Figure 3.11 Step change in xanthan gum concentration with the addition of a 3.5 wt% aqueous solution to a 0.1 wt% solution: (a) relative conductivity with ohmic heater pulses highlighted; (b) evolving xanthan gum rheology with time; (c) log variance against mixing time; (d) circular tomograms at 5 minutes (top) and 20 minutes (bottom); (e) tomogram pixel standard deviation with time; (f) zone average conductivity.

3.4.4.2 Localised Mixing

The mixing phenomena may be interrogated further with the use of the tomogram produced by the two circular arrays. Such arrays afford the visualisation of the pipe cross-section and consequently interrogate radial mixing phenomena, as demonstrated in Figure 3.11d. This highlights a timewise reduction in the more conductive polysaccharide agglomerate size until only a single phase was observed. The location of these agglomerates was additionally able to be traced across two arrays to ensure that no build-up occurred.

The tomograms depicted in Figure 3.11d can then be scrutinised further on a pixel basis to determine localised mixing behaviour, with an analysis of pixel standard deviation and zoned averages able to be performed. Figure 3.11e, displays the standard deviation of measured conductivity across each of the 316 pixels of a circular tomogram to provide an understanding radial homogeneity within the pipe and is comparable to the global mixing parameter, coefficient of variance. A sharp rise in standard deviation is initially observed which then appears to decay exponentially until a plateau is reached; this plateau is in agreement with the mixing time relationship established previously within this section.

Moreover, numerous perturbations, of decreasing magnitude, exist within this measurement which also elucidates the presence of polysaccharide agglomerate. From this figure it may additionally be concluded, that the impact of the temperature rise, and therefore conductivity change, brought about by the ohmic heater is minimal relative to those brought about by the mixing phenomena and hence is not likely to impede on the analysis of mixing.

The tomogram may be segmented further to determine whether any localised mixing phenomena have occurred, with the selected zones the same as those utilised for the rheological analysis, Section 3.2. Figure 3.11f presents the conductivity for each of these zones; however, as each of the zones observes a similar trend, minimal information is able to be extracted. It can be seen that closer to the wall, Zone 8, the presence of high concentration xanthan gum is witnessed around 20 seconds later than in Zone 1.

Furthermore, it is in agreement with the pixel standard deviation described previously with the conductivity value of all zones converging to 1.113 mS cm^{-1} and hence is considered radially homogenous.

3.4.4.3 Residence Time Distribution

The electrical response attained from the ohmic heater pulse itself can additionally be utilised in the measurement of residence time distribution (RTD); however, this refers to the pipe alone and not the entire re-circulation setup. The ERR continuous conductivity function, Figure 3.5a, is representative of the conventional output RTD response, E-curve, with the typical exponential decay of the laminar profile observed. This signal, Figure 3.12a, may be fitted to a Newtonian laminar flow in pipes model which may be described by Eq. 3.9 (Levenspiel, 1999). This resulting E-curve may then be summed cumulatively to produce the cumulative RTD, or F-curve.

$$E(t) = \frac{\tau^2}{4t^3} \tag{3.9}$$

where E(t) is the mean residence time distribution, t is time, in seconds, τ is the average residence time, in seconds.

As the ohmic heater pulse provides uniform heating across a length of 20 cm and over a time period 0.5 seconds, the conventional delta input is not applied. Accordingly, the input pulse has been calculated and subsequently applied to the laminar flow in pipes model; this outputted E-curve is pictured in Figure 3.12a.

The outputted ERR signal and theoretical laminar E-curve can be seen to be in good agreement, with a correlation coefficient of 0.94. As a consequence of this similarity in the measurement domain, the conductivity, or heat, perturbation delivered by the ohmic heater may be considered as both uniform and at steady state over the applied time period. This demonstrates an additional potential of this ERR setup to be utilised in the in-line extraction of RTD when more complex flows patterns are present i.e. in the presence of a static mixer.

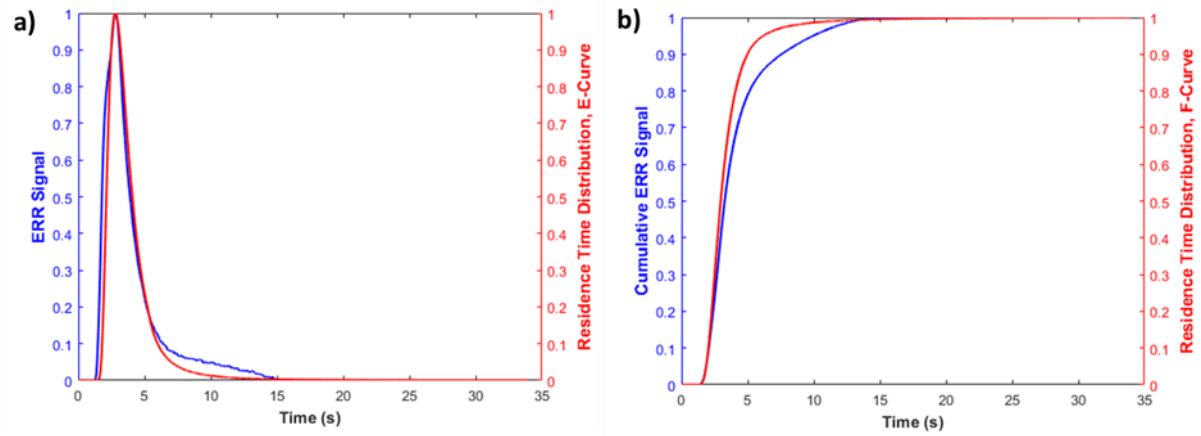

Figure 3.12 Comparison of the ERR and theoretical laminar flow in pipes RTD for 75 wt% glycerol at 156 L min^{-1}: a) E-curve; b) F-curve.

3.5 Electrical Resistance Rheometer - Commercialisation

Due to the success of this project, Electrical Resistance Rheometry is being developed further with a view to the commercialisation of the product by the sponsoring company. To do so, the mechanical design of the sensor has been enhanced to comply with industrial operating requirements. This entailed the migration of the electrode design, described in Section 3.2, to develop a robust sensor capable of operating at elevated temperatures and pressures; the commercialised ERR sensor is depicted in Figure 3.13a and 3.13b.

Figure 3.13 Industrial in-line rheometer: a) ERR sensor; b) ERR sensor with tri-clamp flange fittings

To facilitate the industrial ERR measurement, a guided user interface and operating software have also been developed for use within industry. This involved the migration of algorithms highlighted throughout this chapter from MATLAB to LabVIEW software, developed by National Instruments; this is the existing operation platform for the ITS v5r instrument. This software executes the entire ERR measurement protocol, from the acquisition of raw data, through tomographic construction to the output of the in-line rheological parameters. An example screenshot of the develop software and rheology outputs for a shear-thinning power law fluid, is depicted in Figure 3.14. This setup has been utilised at the site of a global

manufacturer of personal and homecare products with a focus upon characterising the in-line rheological properties of shampoo and fabric wash formulations. This pilot scale study is outlined later in this thesis, in Chapter 7.

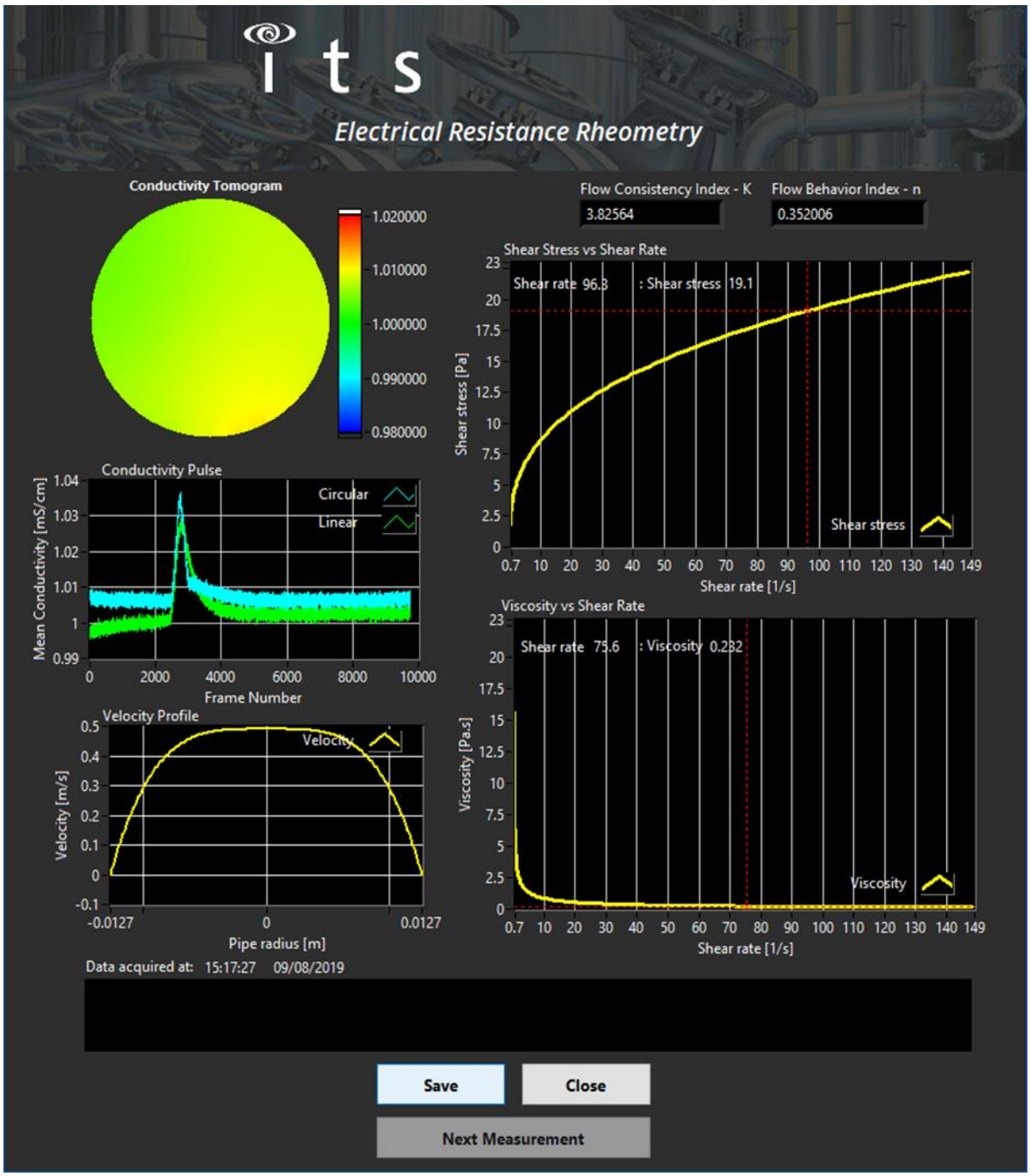

Figure 3.14 ERR industrial analysis software for a shear thinning power law fluid

3.6 Conclusions

An Electrical Resistance Rheometry (ERR) technique has been presented which utilises a novel arrangement of non-invasive, microelectrical tomography arrays to elucidate the in-situ rheological behaviour of process fluids. This technique is advantageous over conventional off-line techniques as it is able to be directly applied to the process environment and removes the requirement for physical sampling. This in-line measurement has been achieved utilising the cross-correlation of computed conductivity pixels to tag the motion of a fluid in the pipe and extract a radial velocity profile. A novel electrical resistance sensor has been developed which consists of two electrode arrangements, linear and circular. The manipulation of the linear array length, and ultimately electrical field penetration, to target sensitivity to the near-wall region and ensure a complete velocity profile was achieved. To validate this concept, a three-dimensional computation model was developed to monitor the electrical current density distribution (ECDD) of a range of multi-scalar array lengths, 6 – 24 mm. From this a uniform, elliptical ECDD was observed, which is supported within literature. As the lengths of the arrays were increased, the penetration of the electrical field was seen to increase accordingly. This is a qualitative validation of tailor linear arrays; however, the ability to specifically target tomographic information to process regions of interest may be highly beneficial in unit operations such as stirred tanks.

The model aqueous-based fluids were selected which exhibit three common rheological constitutive models, namely: Newtonian, shear-thinning power law and Herschel-Bulkley models. The acquired velocity profiles were then validated using the well-established technique of Particle Image Velocimetry, which not only was in excellent agreement, but also validated the assumptions made in the rheological extraction. As the correlation coefficient between these two techniques was found to be 0.99, the electrical resistance rheometer can be said to act as a velocimetry fingerprinting tool for rheology for both Newtonian and non-Newtonian fluids. This agreement for a Newtonian fluid ensures that hydrodynamic entrance effects may be negated and the laminar flow assumptions which the rheological extraction

rely upon are valid. The acquired velocity profile was additionally validated against a Coriolis flow meter with the flow rate able to also be determined with a correlation coefficient of 0.9956.

Coupling the velocity profile with the measurement of differential pressure and a subsequent parametric fitting to rheological constitutive equations enabled the extraction of rheological parameters. The fitting of a fourth order polynomial to the velocity profile may also be utilised to extract rheological behaviour without the assumption of a fluid model; however, instabilities were found when fitting to highly shear-thinning fluids. Employing the former technique was seen to be in excellent agreement with rotational rheometry across a range of fluids described by differing constitutive behaviour. This comparison yielded an agreement of 98 % for rheological parameters of both Newtonian and non-Newtonian fluids. Such agreement demonstrates the capabilities of a novel, in-line rheometer.

Spatial and temporal analysis of the pipe cross-section additionally affords the simultaneous interrogation of mixing behaviour with extensive mixing information captured. Traditional ERT mixing analyses and parameters have been performed with mixing times, visualisation of mixing phenomena and residence time distributions extracted. These mixing analyses were seen to agree with traditional theory with a linear regression of the natural log of the concentration difference and mixing time yielding a correlation coefficient of 0.9854. Hence, two significant formulation quality concepts were then able to be combined with the simultaneous analysis of mixing behaviour. This sensor therefore offers new capabilities of the in-situ analysis of fluids relevant to formulated products with respect to process optimisation, understanding and control.

Due to the success of this development, ERR is being developed further with a view to the commercialisation of a product by the sponsoring company. To attain this, the mechanical design of the sensor has been enhanced to adhere to elevated industrial operating temperatures and pressures. To facilitate the operation of the measurement, a software and

guided user interface have also been developed to execute the entire measurement protocol and analysis algorithms of ERR within LabVIEW software.

3.6.1 Future Work

As this technique has been demonstrated to be highly successful upon a research scale, it is likely that ERR may in the future be migrated to industrial plants, with a case study at a global manufacturer presented in Chapter 7. In addition to the in-line characterisation of product microstructure for either quality or process control purposes, the rheological properties during liquid-liquid displacement may be exploited to signify complete product changeover, or when pipes are clean.

The principles explored within this chapter may be extended to Electrical Capacitance Tomography (ECT) to extract rheological properties of dielectric materials. In 2019, 62.02 % of the global rheometer market value lay within polymer and petrochemicals industries (Fior Markets, 2019) and hence this presents an opportunity to increase the market share. Across a wide range of industrial applications, the control of the viscosity of fuel oils is vital to achieved optimised combustion. When a fuel is injected, it is mixed with steam to enable its atomisation. The correct atomisation is dependent upon the droplet size and spray pattern produced by the injectors and if a fuel of excess viscosity is received by the boiler, it results in the formation of large droplets. With such large oil droplets, incomplete combustion arises with some of the fuel expelled as atmospheric contamination. Smaller droplets may also form unwanted side reactions; this additionally reduces the efficiency of a fuel. This presents an opportunity to apply the rheology principles to ECT to optimise this efficiency of fuel combustion.

Within this chapter, it has been highlighted that novel, tailored linear arrays may be exploited to extract tomographic information from process regions of interest. An application of this is the extraction of the near-wall velocity measurement within a stirred tank for use in inferential in-vessel viscometry; this will be discussed within the next chapter.

3.7 References

Abadi, S. (2016). *The Role of Rheology in the Flow and Mixing of Complex Fluids.* PhD Thesis University of Birmingham: Birmingham.

Alberini, F; Simmons, M.J.H; Ingram, A; Stitt, E.H. (2014). Use of an areal distribution of mixing intensity to describe blending of non-Newtonian fluids in a Kenics KM static mixer using PLIF. *AIChE Journal*. 60, 332-242.

Alberini, F; Liu, L; E.H. Stitt, M.J.H. Simmons. (2017). Comparison between 3-D-PTV and 2-D-PIV for determination of complex fluids in a stirred vessel. *Chemical Engineering Science.* 171, 189-203.

Blythe, T.W; Sederman, A; Stitt, E.H; York, A; Gladden, L. (2017). PFG NMR and Bayesian Analysis to Characterise non-Newtonian Fluids. *Journal of Magnetic Resonance.* 274, 103-114.

Bolton, G; Hooper, C; Mann, R; Stitt, E.H. (2004). Flow distribution and velocity measurement in a radial flow fixed bed reactor using electrical resistance tomography. *Chemical Engineering Science.* 59, 1989-1997.

Carletti, C; Montante, G; Westerlund, T; Paglianti, A. (2014). *Analysis of solid concentration distribution in dense solid-liquid stirred tanks by electrical resistance tomography. Chemical Engineering Science.* 119, 53-64.

Chen, Y; Pearlstein, A. (1987). Viscosity-Temperature Correlation for Glycerol-Water solutions. University of Illinois: Chicago.

Dong, X; Tan, C; Dong, F. (2016). Oil-water two-phase flow measurement with combined ultrasonic transducer and electrical sensors. *Measurement Science and Technology.* 27(12).

Dyakowski, T; Jaworski, A. (2003). Non-Invasive Process Imaging – Principles and Applications of Industrial Process Tomography. *Chemical Engineering Technology*. 26(6), 697-706.

Fior Markets. (2019). *Global Rheometer Market Growth.* Available: https://www.globalbankingandfinance.com/category/news/global-rheometer-market-2019-revenue-ta-instruments-anton-paar-thermo-fisher-scientific/. Last accessed 23rd Oct 2019.

Giguere, R; Fradette, L; Mignon, D; Tanguy, P.A. (2008). Charcterization of slurry flow regime transitions by ERT. *Chemical Engineering Research and Design.* 86, 989-996.

Haavisto, S; Koponen, A; Salemela, J. (2015). New insight into rheology and flow properties of complex fluids with Doppler optical coherence tomography. *Frontiers in Chemistry: Fibres and Biobased Materials.*

Incropera, F; De Witt, D; Bergman, T.L; Lavine, A. (2007). *Fundamentals of Heat and Mass Transfer. 6th Ed.* John Wiley and Sons: New York.

Industrial Tomography Systems PLC (ITS). (2016). *AIMFLOW.* Available: https://www.itoms.com/products/aimflow/. Last accessed 8th Jan 201827.

Kapinchev, K; Bradu, A; Barnes, F; Podoleanu, A. (2015). GPU implementation of cross-correlation for image generation in real time. *IEEE Xplore.*

Knirsch, M; dos Santos, C; de Oliveira Soares Vicente, A; Vessoni Penna, C. (2010). Ohmic Heating, A Review. *Trends Food Sci.* 21(9), 436-441.

Levenspiel, O. (1999). *Chemical Reaction Engineering.* John Wiley and Sons: New York.

Lubrizol Advanced Materials Inc, Flow and Suspension Properties of Carbopol© Polymers, Technical Data Sheet (TDS-180). (2002). The Lubrizol Corporation: Ohio, 369-276.

Maloney, N; Harrison, M. (2016). *Innovation and Future Trends in Food Manufacturing and Supply Chain Technologies.* Elsevier: Amsterdam.

Marquadt, D. (1963). An algorithm for least squares estimation on non-linear parameters. *SIAM J App Maths.* 11, 431-444.

Meissner, J. (1983). Polymer Melt Flow Measurements by Laser Doppler Velocimetry. *Polymer. Test.* 3 (4), 291-301.

Norton, I; Spyropoulos, F; Cox, P. (2010). *Practical Food Rheology.* Wiley-Blackwell: London, 33-41.

Olmsted, P. (2008). Perspectives on shear banding in complex fluids. *Rheologica Acta.* 47, 283-300.

Ovarlez, G; Mahaut, F; Bertrand, F; Chateau, X. (2011). Flows and Heterogeneities with a vane tool: Magnetic resonance imaging measurements. *J. Rheol.* 55, 197-223.

Pakzad, L; Ein-Mozaffari, F; Chan, P. (2008). Using electrical resistance tomography and computational fluid dynamics modelling to study the formation of caverns in the moxing of pseudoplastic fluids possessing a yield stress. *Chemical Engineering Science.* 63, 2508-2522.

Papoulis, A. (1962). *The Fourier Integral and Its Applications.* McGraw-Hill: New York. 244-253.

Paul, E.L; Atiemo-Obeng, V; Kresta, S. (2004). *Handbook of Industrial Mixing: Science and Practice*. Wiley-Interscience: New York.

Rahman, M; Hakansson, U; Wiklund, J. (2015). In-line Rheological Measurements of Cement Grouts: Effects of water/cement ratio and hydration. *Tunneling and Underground Space Technology.* 45, 34-42.

Rahman, N. (2013). *Wall Slip in Pipe Rheometry of Multiphase Fluids.* PhD Thesis, University of Manchester: Manchester.

Rees, J. (2014). Towards online, continuous monitoring for rheometry of complex fluids. *Advances in Colloid and Interface Science.* 206, 294-302.

Ren, Z; Kowalski, A; Rodgers, T.L. (2016). *Estimating Inline Velocity Profile of Shampoo using Electrical Resistance Tomography (ERT).* 8th World Congress of Industrial Process Tomography.

Ren, Z; Kowalski, A; Rodgers, T. (2017). Measuring Inline Velocity Profile of Shampoo by Electrical Resistance Tomography (ERT). *Flow Measurement and Instrumentation.* 58, 31-37.

Rides, M; Jezek, J; Derham, B; Moore, J; Cerasloi, E; Simler, R; Perez-Ramirez. (2011). Viscosity of concentrated therapeutic protein compositions. *Advanced Drug Delivery Reviews:* 63(13), 1107-1117

Sharifi, M; Young, B. (2013). Electrical Resistance Tomography (ERT) for flow and velocity profile measurement of a single phase fluid in a horizontal pipe. *Chemical Engineering Research and Design:* 91 (7), 1235-1244.

Simmons, M.J.H; Edwards, I; Hall, J.F; Fan, X; Parker, D.J; Stitt, E.H. (2009). Techniques for Visualisation of Cavern Boundaries in Opaque Industrial Systems. *AIChE Journal.* 55(11), 2765-2772.

Sjöblom, J. *Parameter Estimation in Heterogeneous Catalysis.* PhD Thesis, Chalmers University of Technology: Sweden.

Stitt, H; Marigo, M; Wilkinson, S; Dixon, T. (2015). How Good is Your Model? *Johnson Matthey Technol. Rev.* 68(2), 74-89.

Tan, C; Xu, Y; Dong, F. (2011). Determining the boundary conditions of inclusions of known conductivities using a Levenberg-Marquadt algorithm by electrical resistance tomography. Meas. Sci. Technology. 22.

Vilar, G; Williams, R; Wang, M; Tweedie, R. (2008). On line analysis of structure of dispersions in an oscillatory baffled reactor using electrical impedance *tomography*. *Chemical Engineering Journal:* 141, p58-66.

Wang, M. (2002). Inverse Solutions for Electrical Impedance Tomography Based on Conjugate Gradients Methods. *Measurement Science and Technology*. 13, 101-117.

Wang, M. (2015). *Industrial Tomography.* Elsevier Science: Amsterdam

Westerweel, J. (1997). Fundamentals of digital particle image velocimetry. *Meas. Sci. Technol.* 8, 290, 294-301.

White, R; Simic, K; Strode, P. (2001). The Combined Use of Flow Visualisation, Electrical Resistance Tomography and Computational Fluid Dynamics Modelling to Study Mixing in a Pipe. *2nd World Congress on Industrial Process Tomography.*

Williams, RA; Nisbet, A; Dickin, F.J; Taylor, S. (1995). Microelectrical Tomography of Flowing Colloidal Dispersions and Dynamic Interfaces. *Biochem. Eng. J.* 56(3), 143-148.

Wilkinson, W.L. (1960). *Non-Newtonian Fluids – Fluid Mechanics, Mixing and Heat Transfer*. Pergamon Press Ltd: London, 1-38.

Wiklund, J; Shahram, I; Stading, M. (2007). Methodology for In-line Rheology by Ultrasound Doppler Velocity Profiling and Pressure Difference Techniques. *Chemical Engineering Science*. 62(1), 4277-4293.

Wiklund, J; Stading, M; Trägårdh, C. (2010). Monitoring liquid displacement of model and industrial fluids in pipes by in-line ultrasonic rheometry. *Journal of Food Engineering*. 99(1*), 330-337.*

Yaws, C. (2003). *Yaws Handbook of Thermodynamic and Physical Properties of Chemical Compounds.* Knovel. Online version available at:

https://app.knovel.com/hotlink/toc/id:kpYHTPPCC4/yaws-handbook-thermodynamic/yaws-handbook-thermodynamic. Last accessed: 20/01/2018.

Yenjaichon, W; Grace, J; Lim, C; Bennington, C. (2013). Characterisation of gas mixing in water and pulp-suspension flow based on electrical resistance tomography. *Chemical Engineering Journal.* 214, 285-297.

Chapter 4

The Application of Electrical Resistance Sensing to Monitor Viscosity in Stirred Vessels

4.1 Introduction

Alongside applications to pipe flow, electrical resistance sensing has been extensively employed to monitor stirred vessels, with a particular focus upon process mixing. Numerous studies afford a visualisation of mixing alongside identification of process end points such as mixing times and degree of mixing (Mann et al., 2001). Such unit operations are governed by rheological parameters with the development of in-line techniques necessary for rapid and continuous process monitoring (Chhabra and Richardson, 2008). In the previous chapter, electrical resistance sensing has been demonstrated to be highly effective when monitoring rheological properties within pipe flow applications. The understanding gained during the development of the in-pipe rheometer can be adapted to develop an enhanced understanding of the properties of fluids with evolving rheology inside stirred tanks.

A number of attempts have been made to develop an inferential, vessel viscometer. The most significant work was conducted by Wunderlich et al. (2017) and Schelden et al. (2016) who developed an inferential viscosity measurement within bioreactor systems. This technique exploited the relationship between the heat transfer mechanics at the wall and the

flow properties of the material. Whilst this technique has been demonstrated to be successful, there is a requirement for precise temperature control and measurement, which is not always present within industrial applications limiting the in-plant applicability of this technique.

Bird, Stewart and Lightfoot (1960) developed a relationship in which the flow properties at the wall were related to the shaft torque, fluid viscosity and the pressure impinging upon the baffle. Grenville (1992) exploited this model to derive a number of correlations to predict blending times in viscous Newtonian and pseudo plastic fluids. These relationships are based upon the knowledge of the shear rate in the near-wall region, which until now has been unable to be monitored via an industrial protocol. A knowledge of blend times is vital in fluids of increased viscosity due to the increased difficulty of processing. Grenville (1992) additionally highlighted that the reduction in pumping capacity near to the wall leads to zones which are poorly mixed with an understanding of rheological properties at the wall is vital for the blending of non-Newtonian fluids. A similar study was performed by Elson (1990) who correlated the wall shear rate to mixing data in yield stress fluids.

As demonstrated in the previous chapter, tomographic information obtained from linear arrays may be targeted to regions of interest, by simply manipulating their geometry. The use of small industrial microelectrical tomography sensors, located at the wall, enables the near-wall region to be targeted with greater information extracted. This is presented within this chapter, which demonstrates the capability of tailored linear arrays to extract flow and mixing information in the near-wall region of agitated vessels. When coupling this information with the measurement of torque upon an impeller, an ability to distinguish between materials of differing viscosity and structural properties is presented. Such a characterisation and understanding can further lead to the optimisation of a number of processes with associated reduction in blend times and operating costs. This also acts to demonstrate the wide-ranging applicability of tailored linear arrays to differing process requirements and unit operations.

4.2 Development of Electrical Resistance Velocimetry for use in agitated vessels

4.2.1 Near-wall velocity profiling

The inferential measurement of viscosity in a vessel affords the characterisation and optimisation of mixing processes via the direct measurement of the velocity profile in the near-wall region. The in-situ velocity measurements are attained using the cross-correlation algorithm which monitors fluctuating computed conductivity pixels obtained from microelectrical tomography sensors. This algorithm, also exploited to extract the in-pipe velocity profile, Eq. 3.1, enables the tracing of the fluid motion across and within multiple measurement planes to extract the displacement between the fluctuating signals (Papoulis, 1962). As the measurement geometry is fixed, and known, the cross-correlated time delay may be converted to velocity.

The sensor design utilised to extract the near-wall velocity, depicted in Figure 4.1a, consists of four linear arrays of eight electrodes which enables both the axial and tangential components of near-wall velocity to be extracted. The data from this setup can then be reconstructed to output four rectangular tomograms. These arrays, arranged in a cross-hair configuration, are operated using the ITS v5r system which has the capability to perform a measurement with 32 electrodes with a data acquisition rate of 318 frames per second. To enhance the temporal resolution of the measurement and ultimately sensitivity to velocity, eight electrodes were once again selected.

The Modified Standard Back Projection (MSBP) algorithm is used to extract the rectangular, tailored tomograms which consist of 200 pixels arranged in 20 x 10 pixel layers. Each of the tomograms are segmented into zones of interest to develop a number of velocity measurements at differing radial distances from the wall. Of the ten pixel layers, the layer closest to the wall is removed to reduce noise, yielding nine radial velocity measurements. Similarly, the first and last two pixels in the tangential direction of flow are removed to further

reduce noise. The resulting tomogram zones are depicted in Figure 4.1b with the orientation of these tomograms is perpendicular to the individual electrodes also as demonstrated in Figure 4.1b. The reconstructed tomograms additionally provide the cross-sectional impedance map at the wall to allow localised mixing studies to be performed simultaneously.

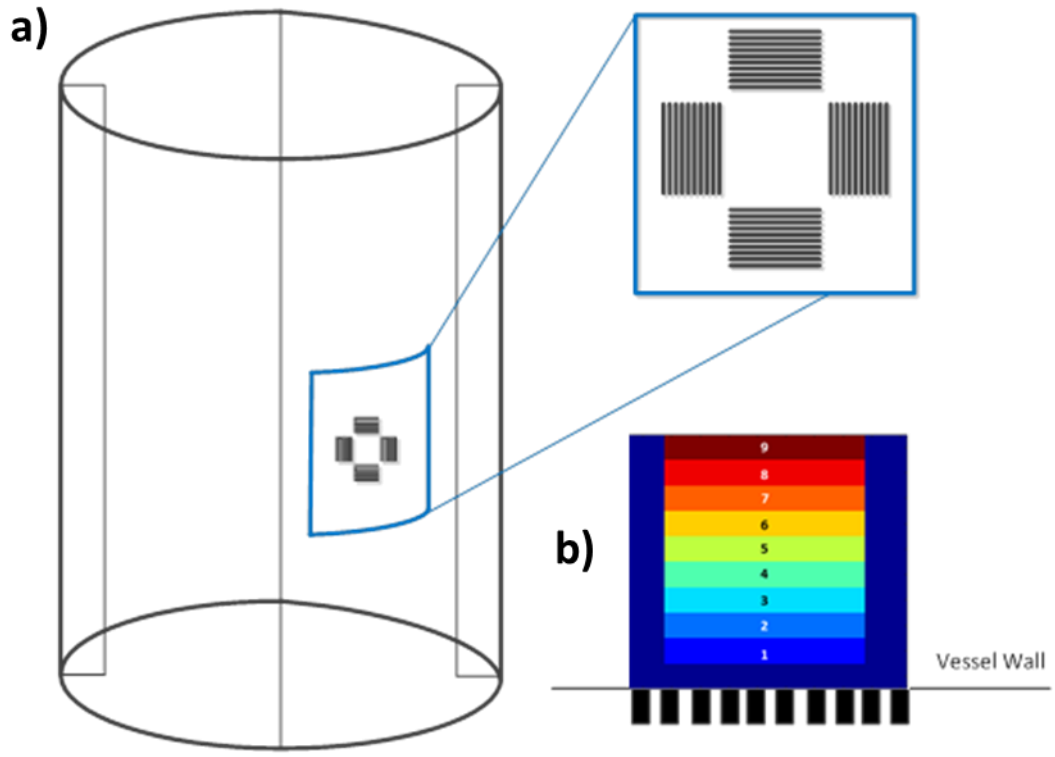

Figure 4.1 Electrical resistance sensing setup: a) stirred vessel with electrode arrays; b) zone scheme of the linear arrays

The velocity measurement approach is similar to that carried out by Machin et al. (2018). However, due to the increase of complexity of flows in vessels, compared to pipe flow, the analysis of the tomographic data is further refined. The values of fluctuating conductivity pixels are averaged across each of the tomogram layers to give rise to a single continuous conductivity function for each layer. For similar layers of the tomogram, the signal to noise ratio and Pearson cross-correlation coefficient, Eq. 4.1, are extracted and utilised as criteria to determine the most similar array signals. This is performed to determine an initial direction of flow for each layer and save further computational processing.

$$PCC(f,g) = \frac{1}{N-1}\sum_{i=1}^{N}\overline{\left(\frac{f_i - \bar{f}}{\sigma_f}\right)\left(\frac{g_i - \bar{g}}{\sigma_g}\right)} \tag{4.1}$$

where PCC is the Pearson correlation coefficient, N is the number of frames within the signal and σ is the standard deviation.

Once the appropriate tomograms are selected, the Pearson cross-correlation coefficient can once again be extracted for each of the remaining 16 pixels per layer to give rise to the most similar pixel signals at each radial velocity position. Upon selecting the pixel conductivity functions, the cross-correlation algorithm, Eq. 3.1, can be employed to determine the signal displacement. As the geometry of the sensor is fixed and known, the tangential and axial components of velocity are subsequently resolved.

4.2.2 Vessel-based Viscometry

With the velocity profile in the near-wall region of the vessel acquired, the material viscosity may be inferred. It must be noted that the associated theory is less well-defined compared to pipe flow and hence is only to be used as an inferential measurement. Derived from a force balance, Bird, Stewart and Lightfoot (1960) developed a relationship, Eq. 4.2, to relate the shaft torque to the fluid viscosity, velocity gradient at the wall and the pressure which impinges upon a baffle.

$$\Gamma = \mu \iint_S R\left(\frac{\partial V_\theta}{\partial r}\right) dS + \iint_A R \cdot P_{baff}\ dA \tag{4.2}$$

where Γ is torque, μ, is viscosity, R is the radial distance to a surface element from the impeller axis of rotation, v_θ is the tangential velocity in the baffle region, r is radial distance from the wall, S is surface area of the fluid in contact with the vessel, P_{baff} is baffle pressure and A is area of the baffle wall.

Grenville (1992) demonstrated that the effect of the pressure drop due to the fluid impinging on the baffles is seen to be much smaller than that of the shear stress at the wall and hence

Eq. 4.2 may be simplified to Eq. 4.3. This equation highlights the relationship between measured torque on the shaft, velocity at the wall and the viscosity of the fluid at the wall. As tangential component of velocity is measured by electrical resistance sensing, this relationship can be used to infer viscosity within a given vessel geometry. It must be acknowledged, that the measured velocity is additionally dependent upon impeller type as they impart different flow patterns.

$$\Gamma = \mu \cdot \left(\frac{dV_\theta}{dr}\right)_w \iint_0^S R \, dS \tag{4.3}$$

Grenville (1992) utilised Eq. 4.2, and developed it further for the estimation of blend time; however, a number of assumptions were made. The most significant is the assumption of constant shear stress at the wall which oversimplifies the true relationship between shear stress and shear rate. Despite this, the developed relationship showed high correlation of in-vessel blend times, for both Newtonian and non-Newtonian fluids. The inference of viscosity can be combined with conventional tomography measurements using temporal and spatial analyses to permit the simultaneous study of this localised mixing behaviour.

4.3 Methodology

4.3.1 Materials

The formulated Newtonian working fluids were 65 wt%, 75 wt% and 85 wt% aqueous solutions of glycerol (Darrant Chemicals, UK). A single phase, Newtonian fluid has been selected for the demonstration of this technique as the viscosity remains constant throughout the entire vessel. This enables a more effective comparison of the vessel viscosity measurements to off-line rotational rheometry. The effect of this comparison is heightened due to the lack of time-shear dependence of the glycerol during agitation. All of the

aforementioned fluids were mixed slowly to ensure that air bubbles were not incorporated into the formulation.

An AG R2 rotational rheometer (TA Instruments Inc, USA) was utilised to extract the rheological properties of the working fluids. The rheometer was equipped with a smooth-walled, 4.006° stainless steel, cone and plate geometry, of diameter 40 mm. Using a Peltier plate, the sample was allowed to reach 23 ± 0.1°C before performing the measurement; this temperature is reflective of the temperature of the fluid in the subsequent flow experiments. Upon reaching this temperature, a logarithmic shear rate ramp was applied across the shear rate range of 0.01 – 1500 s^{-1} with sampling of 20 points per decade. The acquired data was analysed using a non-linear least squares regression within TRIOS software, developed by TA instruments. This method of elucidating the rheological parameters was performed over the shear rate range of 0.01 – 100 s^{-1} to mirror the shear rates observed in the tailored array sensing conditions. These obtained viscosity measurements are depicted in Table 4.1.

Table 4.1 Viscosity of glycerol solutions

Glycerol concentration (wt%)	Viscosity (mPa s)
65	12.6 (R^2 = 0.9990)
75	22.6 (R^2 = 0.9997)
85	98.6 (R^2 = 0.9993)

4.3.2 Electrical Resistance Sensing

The fluids were placed within an acrylic flat bottomed vessel, of diameter, T = 190 mm, and agitated by an up-pumping six blade, pitched-blade turbine (PBT-u). The diameter of the impeller was 63 mm, $D = T/3$, with each blade angled at 45° to the horizontal. Accordingly, the vertical projected height of the blades was $W = 7$ mm, $0.036T$. A torque meter, supplied by TorqSense UK, was attached to the shaft of the impeller with the impeller speed varied in

the range of 200 – 500 rpm. Four acrylic longitudinal baffles were mounted within the vessel at 90° intervals and of width *0.1T*.

For the measurement of near-wall velocity, the electrical tomography sensing configuration, described in Section 4.2, was affixed to the vessel wall. The near-wall velocity was measured using four non-intrusive, 8-electrode sensing arrays, of 8 mm length. This size was selected, based upon prior knowledge obtained from pipe flow measurements, to ensure the interrogation area of the tomogram was within approximately 2.7 mm from the vessel wall. The centre of the orthogonal array arrangement was located at T/2 and connected to a v5r ERT instrument (Industrial Tomography Systems Ltd. (ITS), UK); the overall setup of this system is depicted in Figure 4.2.

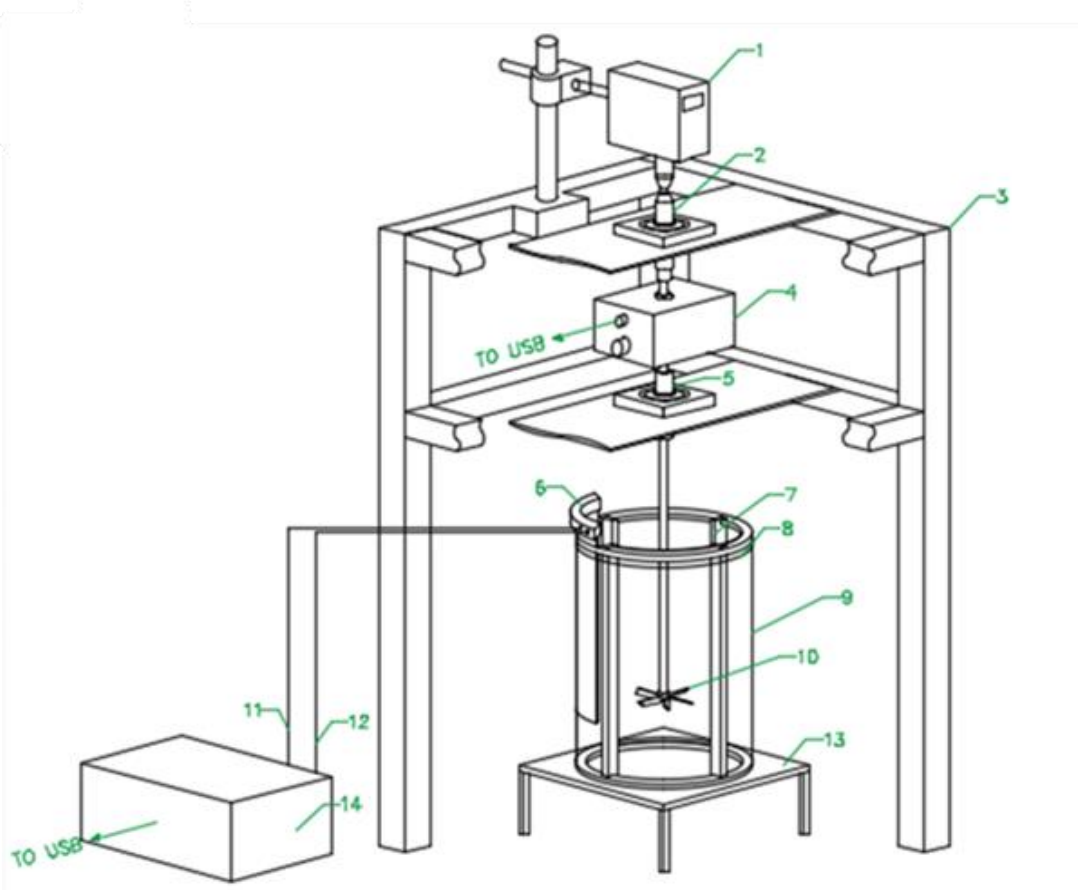

Figure 4.2 ERT vessel setup: (1) motor, (2, 5) torque meter adapter, (3) aluminium frame, (4) torque meter, (6) multi-scale sensor, (7) baffles (T/10), (8) glycerol level, (9) Perspex vessel, (10) impeller, (11, 12) multi-scale sensor cable, (13) vessel support, (14) v5r instrument

The v5r instrument was connected to a personal computer which is operated by ITS v5r software. The 4 planes, of 8 electrodes configuration was utilised alongside the adjacent electrode measurement protocol. The v5r instrument was operated in block mode with one sample delay cycle selected with a resultant capture rate of 318 frames per second; this is the highest attainable frame rate for a four array setup. A single near-wall velocity measurement required the capture of 10,000 frames (31 s) to monitor a conductivity perturbation completely. At the beginning of these captures, the desired conductivity perturbation was provided by a PHD 2000 syringe pump (Harvard Apparatus, USA) which delivers 4 mL of the solution present in the vessel at a constant rate of 1.6 mL s^{-1}. The injection contained an addition of 1 wt% sodium chloride (Sigma-Aldrich, UK) dissolved within the working fluid to increase the conductivity and act as a perturbation. Using the fluid present within the vessel as a tracer minimises the impact of gravitational and viscous effects upon the tracer motion. The capture time selected in this case was an overestimation to ensure the entire conductivity perturbation has passed through the sensor and ensures that macroinstabilities are minimised (Roussinova et al., 2000). This additionally removes the requirement for the measurement to be angle-resolved due to time for a single rotation of the impeller was at least two orders of magnitude less (200 - 500 rpm) than the 31 s of time over which the near-wall velocity is acquired.

The raw voltage measurements obtained from the v5r instrument were fed into a MATLAB code which contains the MSBP algorithm (Wang, 2002). This code was utilised to reconstruct the tailored linear tomograms, select the appropriate tomograms and perform the subsequent velocity and viscosity analyses. Supplementary experiments were performed in the same vessel to demonstrate the capability of the system to monitor the blend time of the fluid in turbulent conditions. To do so, the 98 % mixing time, θ_m, of a 25 wt% aqueous glycerol solution of viscosity 1.92 mPa s was captured. The interrogated impeller speeds range from 300 to 1000 rpm which have associated Reynolds numbers of 13,437 and 44,789, respectively, and hence are considered close to and fully turbulent respectively (for turbulent

flow Re > 2 x 10^4, see Paul et al., 2004). The average conductivity of the four tomogram planes were monitored for a single injection of glycerol solution with sodium chloride added.

4.3.3 Particle Image Velocimetry

The validation of the vessel-based near-wall measurements has been provided by 2-D PIV measurements attained from a TSI PIV system. A 532 nm (green) Litron Nano PIV laser, pulsed at 100 Hz, is synchronised to a single TSI Power view 4MP (2048 x 2048 pixels^2) 12 bit CCD camera. The synchronisation of the camera to the laser pulses was performed by a TSI 610035 synchroniser and operated by the TSI Insight 4G software installed on a personal computer. The aqueous glycerol solutions were seeded with 10 µm SGS silver coated hollow glass spheres, which possess a sufficiently small relaxation time to consider that the motion of the fluid is followed. For each experimental condition, 500 images were captured with the resultant data analysed in the TSI software. The Nyquist PIV algorithm was used and the resultant spatial resolution of the setup was 87 µm pixel^{-1} with an interrogation area of 16 x 16 pixels selected (Westerweel, 1997).

The vessel setup, described in Section 4.1, was immersed in a glass rectangular tank, filled with water to minimise errors which arise from the curvature of the inner vessel (Alberini et al., 2017); the schematic of this setup is presented in Figure 4.3. The vertical laser plane was positioned at an angle of 5° from the nearest baffle. Whilst a number of PIV studies have been performed which bisect the baffles, there is often a mismatch of refractive index between the fluid and the baffle, which acts to distort the image (Gabriele et al., 2009). Three additional horizontal laser planes were interrogated at T/6, T/3 and T/2, with the latter directly applicable to the ERT measurement. Angle resolved images were performed using a triggering device which was synchronised to the image capture. The velocity fields were obtained when the impeller blades are in-line with the baffle (0°) and when bisected by the baffle (30°). When performing the analysis, only half of the vessel was considered to reduce computational requirements based on the assumption of rotational symmetry.

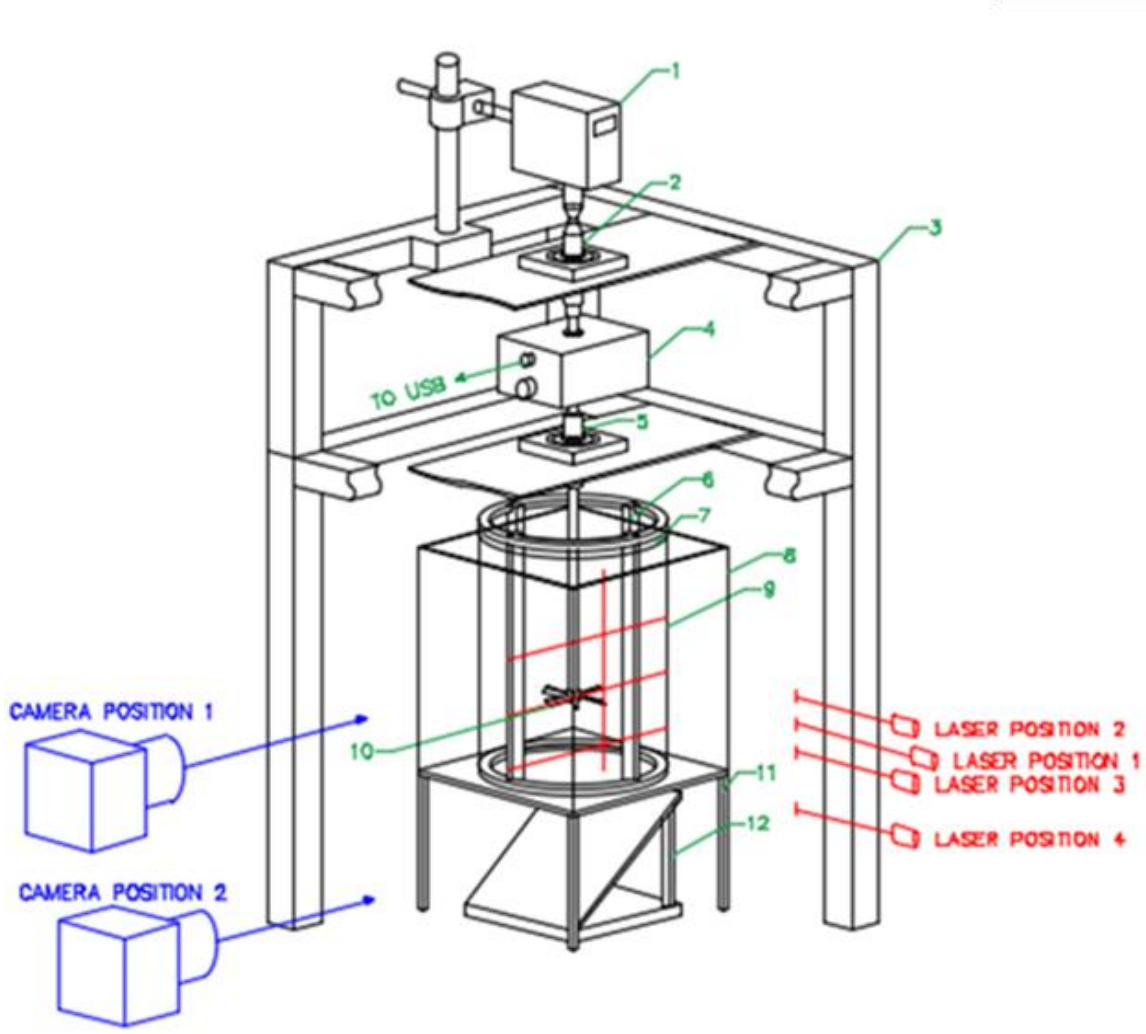

Figure 4.3 PIV vessel setup: (1-5, 9-10) as setup in Figure 4.2 (6) baffles (T/10), (7) glycerol level, (8) square perspex box filled with water, (11) stand and (12) mirror

4.4 Results and Discussion

4.4.1 Near-wall Velocity Profiling

Critical to the in-situ inference of viscosity within a vessel, the velocity profile in the near-wall region is initially interrogated with the obtained results depicted in Figure 4.4. Due to an 8 mm tailored array being employed within this study, these velocity profiles represent flow within 2.7 mm from the vessel wall. Flow within this region is most likely to lie within the laminar

sub-layer due to a reduction in the pumping capacity from the impeller (Kawase, 2002). As a result, such axial and tangential velocity measurements are dependent upon viscous forces in the laminar and transitional regimes (Rice et al., 2006).

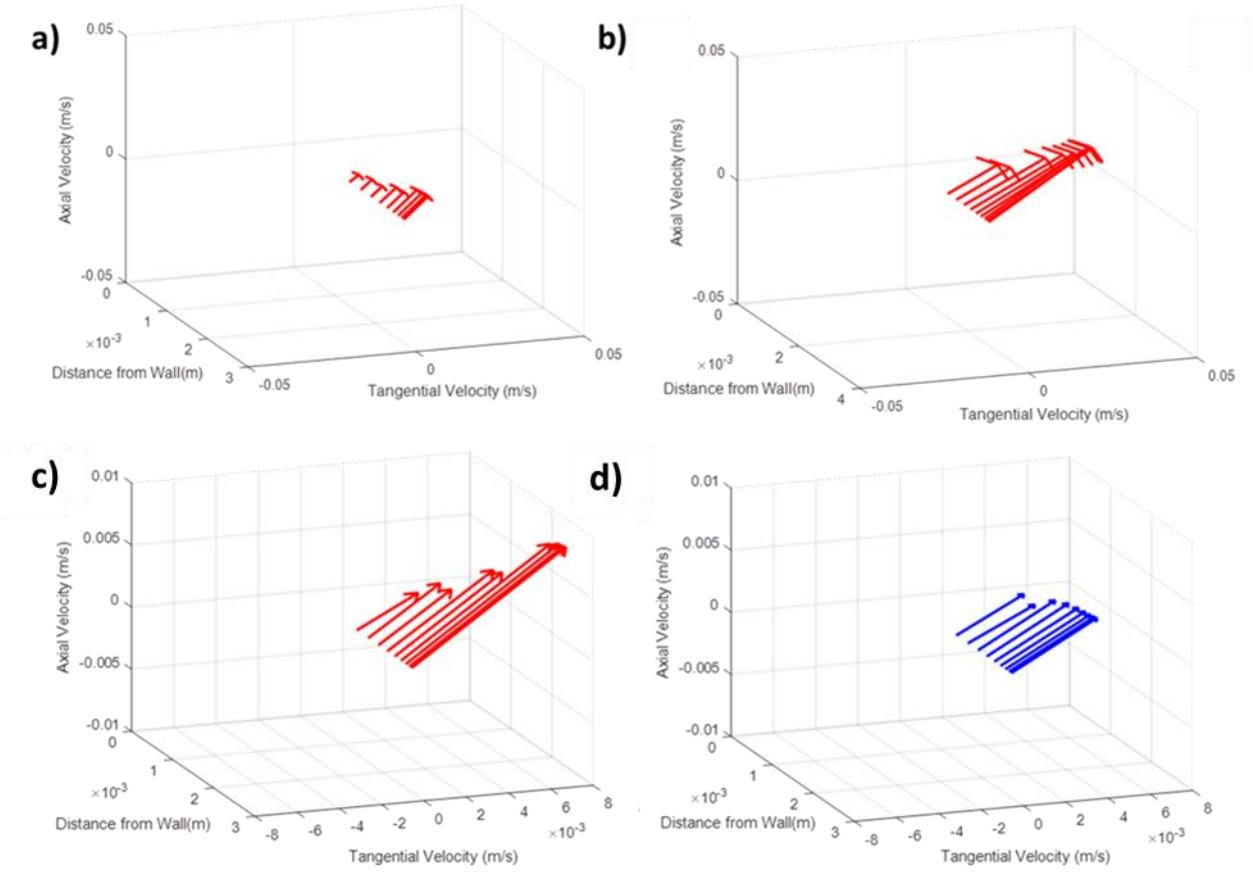

Figure 4.4 ERT Velocity fields for glycerol solutions. a) 65 wt%, 200 rpm; b) 65 wt%, 400 rpm; c) 65 wt%, 200 rpm, vertical laser plane; d) 75 wt%, 200 rpm

Accordingly, this is reflected in the outputted velocity profiles captured by the electrical resistance sensing technique. As expected, when the impeller speed is constant, an increase in the viscosity of the measured fluid yields a reduction in the magnitude of velocity; this is reflected in Figures 4.4c and 4.4d. Considering the outermost velocity vector from the electrical resistance sensing measurement, when the impeller speed is fixed to 200 rpm, the magnitude of velocity was found to be 0.018 ms^{-1}, 0.006 ms^{-1} and 0.004 ms^{-1}, for 65, 75 and 85 wt% glycerol solutions respectively. Such behaviour is additionally represented across all of the monitored impeller speeds, presented in Table 4.2, with such reductions observed due

to increased dissipation of energy as a function of the viscosity of the fluid (Paul et al., 2002). This provides initial confidence in the capability of the near wall velocity to infer viscometric data within vessels.

Table 4.2 Near wall velocity measurement experimental and hydrodynamic conditions

Glycerol Concentration (wt%)	Impeller Speed (rpm)	Reynolds Number	Tip Speed ($m\ s^{-1}$)	Outer ERT Wall Velocity ($m\ s^{-1}$)	Wall Velocity/Tip Speed (%)
65	200	869	0.66	0.018 ± 0.008	2.73
	300	1303	0.99	0.023 ± 0.007	2.32
	400	1737	1.32	0.041 ± 0.011	3.11
	500	2172	1.65	0.062 ± 0.014	3.76
75	200	372	0.66	0.006 ± 0.002	0.91
	300	558	0.99	0.011 ± 0.004	1.11
	400	744	1.32	0.025 ± 0.006	1.89
	500	930	1.65	0.048 ± 0.007	2.91
85	200	148	0.66	0.004 ± 0.002	0.61
	300	223	0.99	0.009 ± 0.003	0.91
	400	297	1.32	0.011 ±0.004	0.83
	500	371	1.65	0.023 ± 0.015	1.39

Similarly as expected, an increase in the impeller speed for a fixed glycerol concentration, demonstrates an increase in the velocity vector magnitude; this is depicted in Figures 4.4a and 4.4b. When considering a 65 wt% aqueous glycerol solution, the velocity vector magnitude is seen to increase from 0.018 ms^{-1} to 0.062 ms^{-1} for impeller speeds of 200 rpm and 500 rpm, respectively. It must be noted that this also represents an increase in ratio between the velocity magnitude and impeller tip speed, from 2.73 % – 3.76 %. This indicates an increase in the pumping capacity in the region near to the wall and hence improvements in overall mixing. A number of studies, concerning viscous blending, have stated the importance of wall phenomena and shear rates upon overall mixing time (Tulus et al., 2018; Gabelle et

al., 2013). The ratio is seen to be more impactful when the glycerol concentration is increased to 75 wt%, which possesses values of 0.91 %, 1.11 %, 1.89 %, 2.91 % for impeller speeds of 200 – 500 rpm, at 100 rpm intervals, respectively. Increasing the impeller speed from 200 – 300 rpm, yields only a minor increase in the pumping capacity near to the wall; however, large improvements can be observed when increasing the impeller speed to 500 rpm, drastically reducing overall mixing times. This is additionally reflected in the increase in the vector angle from 41.3° at 200 rpm, to 49.8° at 500 rpm, implying that axial flow patterns are becoming more dominant.

The aforementioned flow patterns captured from electrical resistance sensing are also reflective of those typically generated by a PBT-u impeller. The discharge from this impeller splits into a two loop structure with a strong downward flow below the impeller at the wall (Gabriele et al., 2009). An additional counter rotating flow loop is also observed which contains a smaller part of the flow and is present above the impeller. With the clearance of the tailored arrays lying at T/2 and the impeller clearance T/3 the latter loop structure is applicable. As less intense velocity fields are observed within this loop, there is an increased likelihood that the laminar sub-layer will be present, validating the selected location of the sensor (Rice, 2006). Moreover, this upward flowing counter flow loop typically observes angles between the axial and tangential velocity components in excess of 45° (Gabriele et al., 2009). The obtained velocity vector angles from electrical resistance sensing are similar to this, as demonstrated previously, providing further qualitative confidence in the velocity vectors obtained within this study.

4.4.2 Particle Image Velocimetry

To provide a quantitative validation of the obtained ERT velocity measurements, Particle Image Velocimetry (PIV) was performed. From Figure 4.5a, the previously assumed two-loop structure is observed for an 85 wt% glycerol solution agitated at 200 rpm. This system

represents the lowest inertial forces alongside the highest viscous forces to demonstrate that the two-loop structure, captured by ERT, is present across all hydrodynamic conditions experimented upon (Gabriele et al., 2009). This further supports the qualitative analysis highlighted within the previous section. Figure 4.5b highlights that the tangential and radial flow components are dominant for the aforementioned hydrodynamic conditions.

A detailed comparison of the velocity vectors is then performed to validate the electrical resistance velocimetry technique. As the outermost velocity vector obtained from PIV can be prone to noise, the second velocity vector was selected; based upon the assigned PIV setup, this represents a distance of 3.42 mm from the vessel wall. As the outermost velocity vector obtained from ERT measurements is located at 2.72 mm from the vessel wall; this vector magnitude was utilised for comparison to PIV measurements. It must be acknowledged, that differences may arise in the output of the two measurements techniques as a result; however, PIV may provide a useful insight into the validity of the ERT measurement.

The impeller speeds of the flow experiments range between 3.33 - 8.33 Hz; this is two orders of magnitude greater than the acquisition rate of the ERT measurements, 0.0326 Hz. Resultantly, ERT measurements are insensitive to the flow fields generated at different impeller positions. To provide a more effective comparison to the ERT data, the angle-resolved data from all PIV measurements was averaged regardless of whether the blade is parallel with the baffle or bisected by it.

The detailed comparison of the velocity vector magnitudes, obtained from PIV, are depicted for glycerol solutions of 65 wt% and 85 wt% in Figures 4.5c and 4.5d, respectively. It is evident that, the aforementioned trend of an increase in fluid viscosity gives rise to a decrease in velocity magnitude. This supports the capability of in-situ electrical resistance sensing to distinguish between materials of differing viscosity. Moreover, the expected increase in the near-wall velocity with impeller speed is captured. The similarity in the trend of the PIV measurements is observed when performing a linear regression between both ERT

and PIV measurements, for an 85 wt% glycerol solution with a correlation coefficient of 0.990.

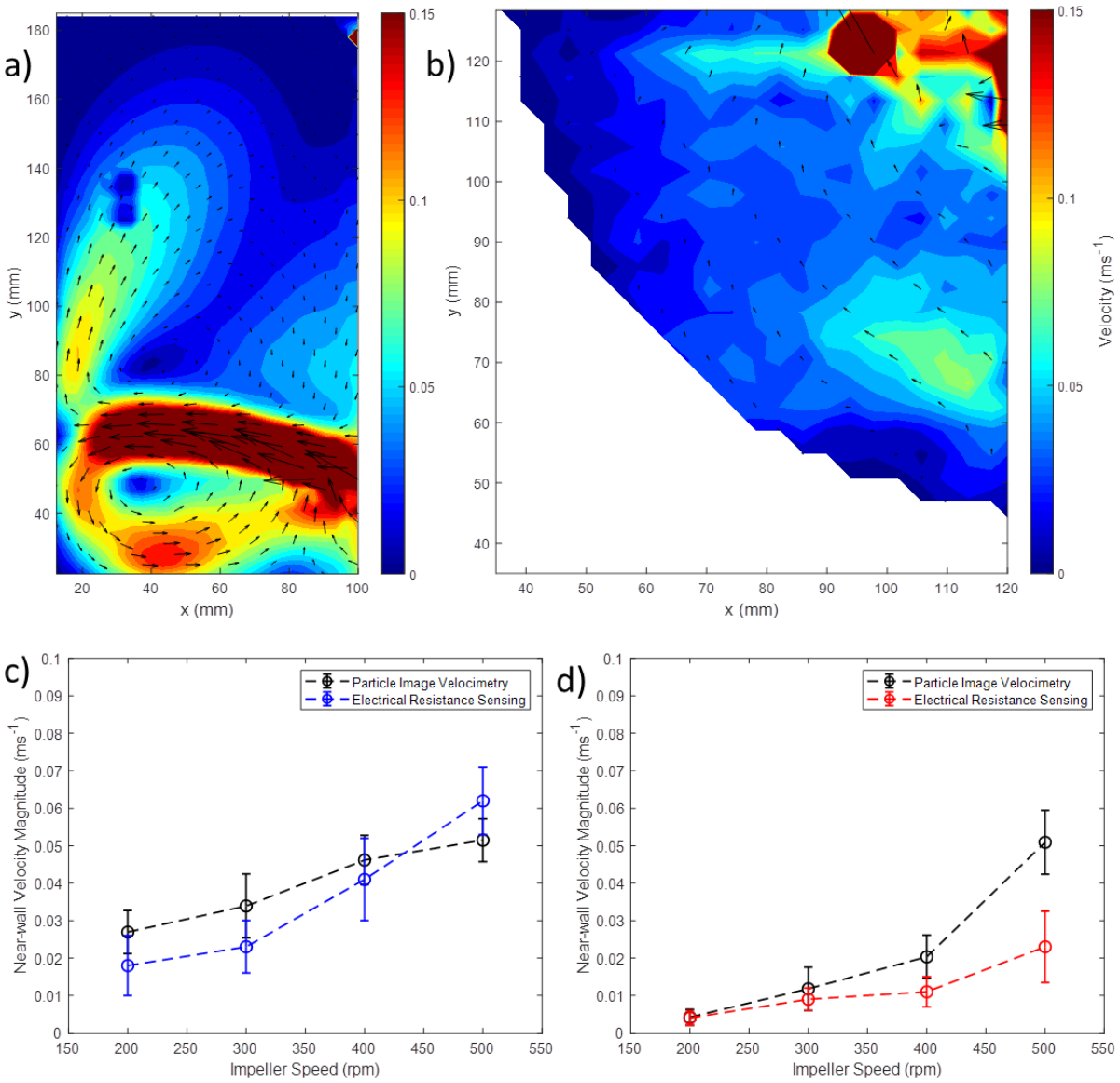

Figure 4.5 PIV near wall velocity measurement: a) vertical laser plane; b) horizontal laser plane 2; c) average near-wall velocity, 65 wt% glycerol; d) average near-wall velocity, 85 wt% glycerol

It is acknowledged, that the magnitude of these techniques are not identical, this is likely due to the time period which the measurements are performed over with ERT reducing macroinstabilities which are associated with the transitional flow region and the differing distances from the vessel wall which the PIV and ERT vectors were computed. When

considering a 65 wt% glycerol solution, the difference in the average PIV and ERT measurements was found to possess a RMSE of 0.0091 ms^{-1}. Such measurements possess 95 % confidence intervals of 0.0087 ms^{-1} and 0.0067 ms^{-1} for the electrical resistance and optical technique of PIV, respectively. Whilst PIV possesses a much greater spatial resolution than ERT techniques, only a little reduction in the uncertainty of the measurement is observed.

Whilst the values obtained by PIV and ERT techniques are not identical, the trends are seen to mimic each other, reinforcing the capability of electrical resistance measurements to distinguish between materials of differing viscosities, based upon the near-wall shear rate.

4.4.3 Inferential Viscosity Measurements

The velocity vectors may be employed to elucidate the shear rate in the near-wall region. This is extracted with the use of gradient-based methods via the fitting of a third order polynomial fitting and subsequent differentiation. The shear rate profile for a 65 wt% glycerol solution agitated at 200 rpm is depicted in Figure 4.6a with the shear rates segregated into the tangential and axial components.

This shear rate information may then be coupled with the measurement of torque to gain in insight into the energy imparted to the fluid by the impeller and ultimately provide the inferential measurement of viscosity. The torque data, presented in Figure 4.5b, demonstrates a linear increase in torque with an increase in impeller speed at each glycerol concentration. However, minor differences were observed when changing the viscosity of the two least viscous fluids, with just a 3 % difference in the average torque. Thus, distinguishing between differing fluids based upon torque measurements alone becomes impractical. When interrogating 75 wt% glycerol at 200 rpm, the torque is seen to be lower than when the glycerol content is 65 wt%. This is attributed to flows lying within the transitional regime and thus unsteady flow phenomena is observed and other inertial effects are contributing to the dissipation of energy in the bulk of the vessel. Hence to provide increased selectivity to

viscosity, there is a requirement to include the measurement of near-wall velocity to more effectively characterise microstructural changes within the vessel.

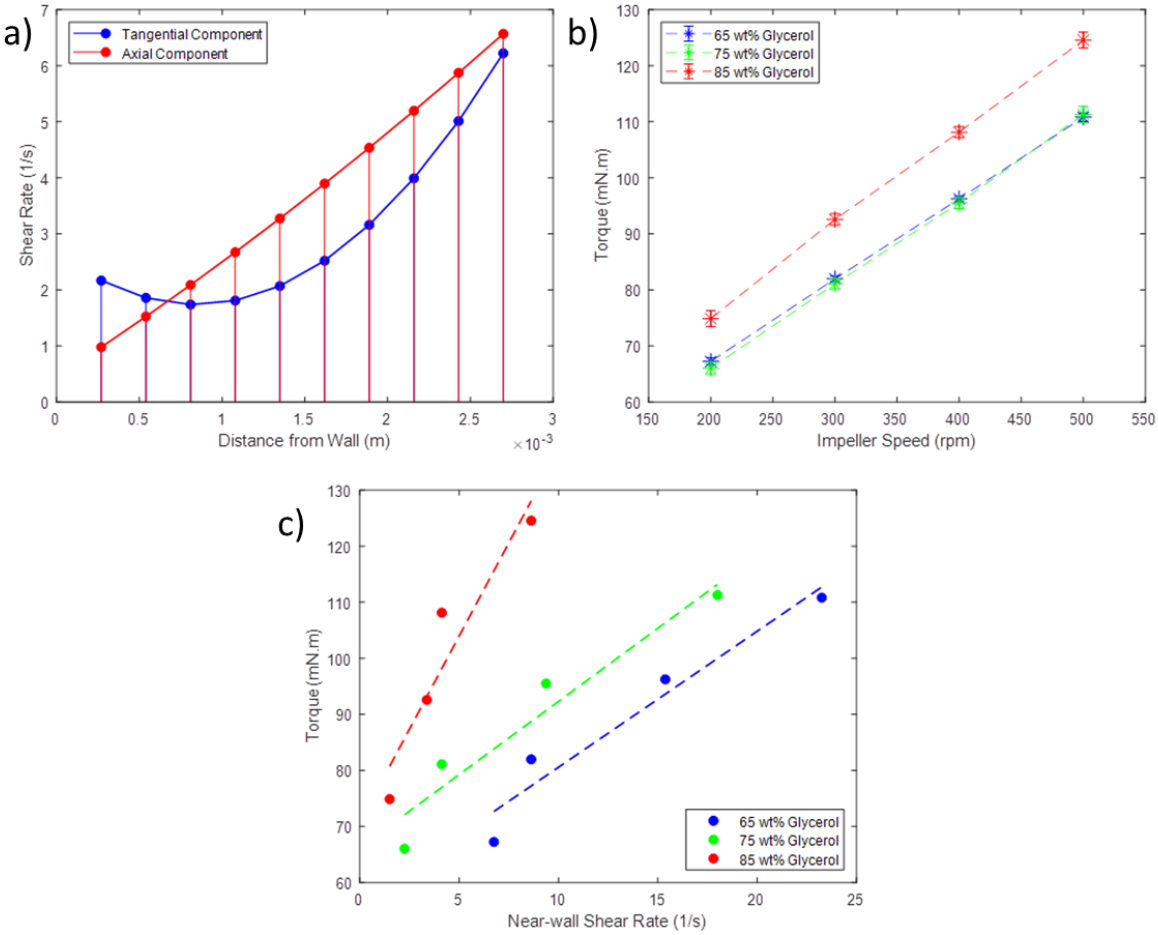

Figure 4.6 a) Near-wall shear rate; b) torque measurements; c) relationship between torque and near-wall shear rate

Thus, to enable a viscosity to be calculated the force balance is finalised with the geometry of the vessel incorporated based upon a small surface element of the vessel wall. Inputting the appropriate geometric values into Eq. 4.3 yields the relationship between viscosity and torque measurements, Eq. 4.4a, which may subsequently be re-arranged to form Eq. 4.4b.

$$\Gamma \approx \mu \left(\frac{dv_\theta}{dr}\right)_w \cdot 1.83T^3 \quad (4.4a); \qquad \mu \approx \frac{\Gamma}{\left(\frac{dv_\theta}{dr}\right)_w \cdot 1.83T^3} \quad (4.4b)$$

It is acknowledged that this equation is an oversimplification of the relationship, with a number of factors not being considered. The most prevalent of these is the velocity field distributions generated by the impeller and the assumption that the pressure impinging upon the baffle is negated. Nevertheless, this can act as a method to infer the viscosity within a vessel for a known setup. However, within typical applications where vessel geometries are fixed and known with only the fluids being changed; this setup is capable of being non-intrusively retrofitted into such vessels.

When interrogating the relationship between the measured torque and average shear rate at the wall, Figure 4.5c, each fluid displays a different behaviour. Performing a linear regression of the two variables reveals an increase in the gradient is observed with an increase in glycerol content. This ranged from 0.00243 – 0.0103 Nm s, with the largest correlation coefficient found to be 0.927. Despite this the Akaike Information Criterion (AIC; Akaike, 1981) revealed that the optimal fitting for all datasets was a second order polynomial fitting and is reflected in an increase in the average correlation coefficient to 0.975. This non-linearity arises due to the impact which the impingement of the fluid on the baffles has upon the torque measurement, as described by Bird et al. (1960). In this instance, once fitted the second order polynomial was differentiated to determine the relationship between the variables. The gradient of such differentials were found to be negative and relatively small within the range of -0.1524 and -0.0933, which is in agreement with Grenville et al. (1992).

The averaged values of this differential within the measured shear rate ranges were extracted with the 65 wt%, 75 wt% and 85 wt% glycerol solutions yielding 0.00124 Nm s, 0.00177 Nm s and 0.0712 Nm s, respectively. When substituting these values into Eq. 4.4b, the corresponding inferred viscosities were found to be 0.0987 Pa s, 0.141 Pa s and 0.567 Pa s. This represents the anticipated increase in the inferred viscosity with glycerol concentration as captured by the off-line rotational rheometer. This demonstrates the potential of this novel technique to characterise in-situ formulations within stirred vessels.

Despite a correlation coefficient between the off-line rotational rheometer and electrical resistance sensing measurements of 0.979, ERT is seen to provide an over estimation of viscosity by a factor of 6.4. This overestimation arises within the force balance derived by Bird, Stewart and Lightfoot Eq. 4.2, which does not account for non-uniform flow fields generated by different impellers and assumes that the wall shear stress is uniform across the entire vessel. However, this is known to be an oversimplification with extensive literature, including this study, demonstrating the majority of the pumping capacity generated from a PBT-u is within a strong downward loop (Fawcett, 1989; Gabriele et al., 2009). With the sensing region being located above this loop, the pumping capacity is reduced giving rise to smaller velocities captured by both the ERT and PIV measurements. Subsequently, these reduced velocities result in a large overestimation of the viscosity due to their inverse proportionality, Eq. 4.5b. This ensures each vessel setup will observe a different relationship between the measured torque and shear rate at the wall, due to the flow fields generated by the impeller and geometry. For a fixed setup, this relationship may be investigated and subsequently employed to elucidate in-situ changes in viscosity. The understanding gained from this inferential measurement could afford an enhancement in the control and optimisation of mixing processes. Moreover, this highlights the application of the novel tailored microelectrical tomography sensors to vessels and thus increasing the unit operations in which they are suitable for.

4.4.4 Blend Times

Alongside the inferential measurement of viscosity, the tailored linear arrays can be simultaneously exploited for the qualification and quantification of mixing phenomena (Wang, 2015; Bolton et al., 2004; Vilar et al., 2008; Forte et al., 2018). Employing both spatial and temporal analyses of the obtained data permits the simultaneous extraction of mixing behaviour. From each of the computed tomograms, examples may be observed in Figures 4.7a and 4.7b, the pixel averaged conductivity was monitored to determine the mixing time of a brine tracer in dilute glycerol solutions within the fully turbulent flow regime, Re > 20,000

(Paul et al., 2002). The turbulent regime was chosen to facilitate use of extensive existing correlations to predict mixing times, θ_m, such as the widely accepted correlation developed by Nienow (1997), Eq. 4.5. To achieve the turbulent regime, 20 wt % glycerol solutions were agitated in the impeller speed range of 500 – 1000 rpm, giving rise to Reynolds number in excess of 20,000.

$$\theta_m \approx 5.3 \cdot \frac{Po^{-\frac{1}{3}}}{N}\left(\frac{D}{T}\right)^{-2} \tag{4.5}$$

where N is impeller speed, in Hz and Po is the power number as represented by Eq. 4.6.

$$Po = \frac{P}{\rho N^3 D^5} \tag{4.6}$$

where P is the power consumption, in W and ρ is the density of the fluid, in kg m^{-3}.

The correlated mixing time may then be compared to the mixing time extracted from the experimental pixel-averaged conductivity information using a coefficient of variance, COV approach, Eq. 4.7. In this instance four pointwise measurements, n, were selected, each of which relate to a single tomogram of the near-wall array.

$$COV = \frac{1}{n-1}\sum_{1}^{n}\sqrt{(C_i - C_\infty)^2} \tag{4.7}$$

A linear regression between the predicted and experimental mixing time is depicted in the form of a parity plot in Figure 4.7c. When comparing to the identity line, *y = x,* an extremely positive correlation, of 0.97 is observed. This not only indicates excellent agreement between the predicted mixing times and those obtained from electrical resistance sensing, but also linearity between the two mixing times. Such agreement demonstrates the capability of this sensing arrangement to accurately determine a process end point within the turbulent regimes, in addition to inferring the viscosity within a vessel. It must be acknowledged, that this is expected as the sensing array effectively acts as a conductivity probe, with an

enhanced interrogation area, thus is ostensibly the same technique from which the correlation by Nienow (1997) was developed.

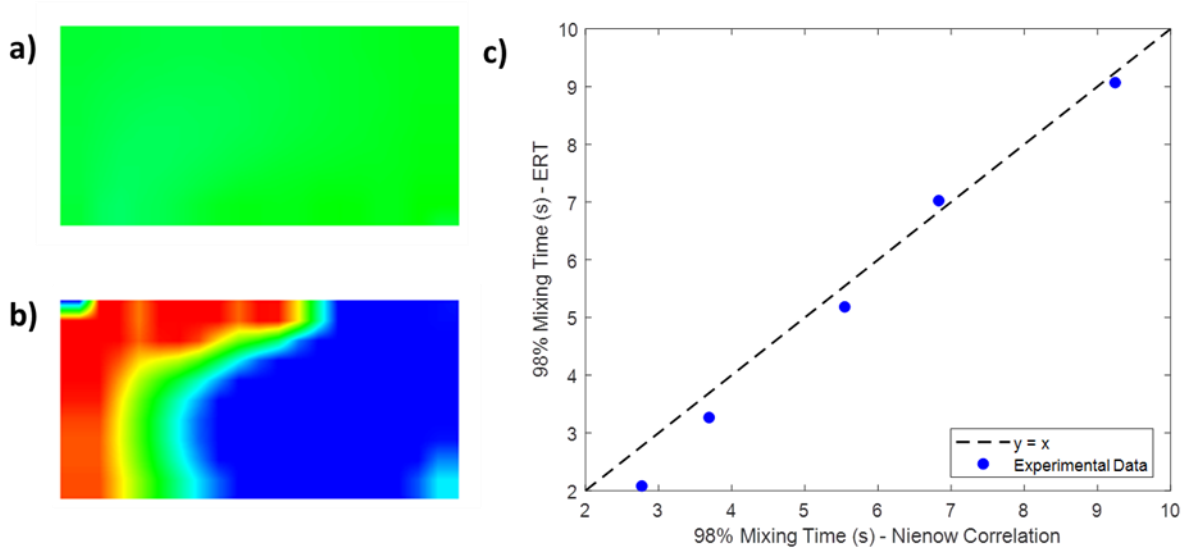

Figure 4.7 Vessel mixing analysis: a) homogeneous linear tomogram; b) tomogram capturing tracer movement; c) comparison of mixing time correlations and ERT mixing time

However, benefits may be observed when monitoring mixing times within the laminar flow regime. In laminar mixing, both conductivity and temperature probes hinder mixing due to the formation of a boundary layer surrounding them. This ensures that the regions which they interrogate possess poor mixing and are not representative of the remainder of the vessel. However, the non-invasive nature of the tailored linear arrays prevents the formation of additional boundary layers. A number of correlations have additionally been developed based upon the measurement of shear rate at the wall (Grenville, 1993; Elson, 1992), an in-situ knowledge of the shear may be utilised to predict mixing times and identify process end points. The aforementioned capabilities to monitor the shear rate in the near-wall region and mixing time may be coupled to enhance process understanding and optimisation, in-line during processing.

4.5 Conclusions

The application of novel tailored microelectrical tomography arrays to monitor rheometric data has been expanded to agitated vessels. Via manipulation of their geometry, such sensors have been utilised to target tomographic information < 2.7 mm from the vessel wall. Flow within this region often lies within the laminar sub-layer due to a reduction in the pumping capacity of the impeller and as a result fluid motion is dependent upon viscous forces. To capture this flow a novel sensing arrangement has been exploited alongside the cross-correlation of computed conductivity pixels, with the tangential and axial velocity components resolved. This chapter demonstrates the first industrial sensor capable of extracting velocity components in the near-wall region and ultimately shear rate at the wall.

Derived from a force balance, Bird, Stewart and Lightfoot (1960) developed a relationship to relate the torque upon an impeller shaft to the fluid viscosity, velocity gradient at the wall and the pressure which impinges upon a baffle. Accordingly, torque and electrical resistance measurements were performed upon a vessel agitated by an up-pumping pitched blade (PBT-u) to infer the in-situ viscosity of aqueous glycerol solutions. As expected, the measured near-wall velocity profiles were seen to decrease with an increase glycerol concentration due to the increase in viscous forces. This is highlighted when the impeller speed is fixed at 200 rpm, the largest velocity vector magnitudes were found to be 0.018 ms^{-1}, 0.006 ms^{-1} and 0.004 ms^{-1} for glycerol solutions of 65 wt%, 75 wt% and 85 wt% concentration respectively. Moreover, the captured flow fields were also as expected with the sensor capturing the secondary counter rotating loop of generated by a PBT-u.

These conventional flow fields have been confirmed using the independent technique of Particle Image Velocimetry (PIV). PIV has also been performed to quantitatively validate the obtained velocity profiles from electrical resistance sensing. Applying a linear regression to PIV and ERT measurements an 85 wt% glycerol across a number of impeller speeds yields a correlation coefficient of 0.99, providing confidence in the application of tailored linear arrays to capture appropriate velocity profiles.

The average shear rate may be extracted from the obtained velocity profiles and subsequently be coupled with the measurement of torque to act as an in-situ inferential measurement of formulation viscosity. Initially, the torque was interrogated alone; however, there was a difference of just 3 % in torque for 65 wt% and 75 wt% glycerol solutions due to transitional flow effects. When the shear rate is considered, the glycerol formulations can be easily characterised with the ratios of torque to wall shear rate found to be 0.0012 Nm s, 0.0018 Nm s and 0.0712 Nm s, for 65 wt%, 75 wt% and 85 wt% glycerol solutions, respectively. Considering the aforementioned force balance, the viscosity may be inferred in-situ with the glycerol solutions deemed to be 0.0987 Pa s, 0.141 Pa s, and 0.567 Pa s in order of ascending glycerol concentration. Such results mimic the trend observed from off-line rotation rheometry; however, it is seen that electrical resistance measurements provide an overestimation by a factor of 6.4. This arises due to the underlying assumptions of the Stewart, Bird and Lightfoot force balance which is based upon uniform shear stress across the entire vessel without consideration of the flow fields. Whilst this assumption ensures that the analysis technique is not a general solution across all geometries and impeller types, it still possesses the capability to act as an inferential viscosity measurement and help afford the in-vessel characterisation of materials during mixing.

Spatial and temporal analyses near to the vessel wall additionally afford the simultaneous interrogation of mixing behaviour with extensive mixing information being able to be captured. To validate this turbulent mixing times were correlated with experimental measurements and found to be in excellent agreement with a correlation coefficient of 0.97 to the identity line. This novel application demonstrates the wide applicability of tailored sensors arrays for the in-situ analysis of fluids to afford enhancement in process optimisation and understanding relevant to formulated products.

4.5.1 Future Work

Outside of the concept of rheology, the applications of such tailored arrays to target tomographic information regions of interest may be expanded i.e. the near-wall region within pipes or vessels for cleaning applications. Within this thesis, the concept has been extended to monitor the continuous phase conductivity measurement in horizontal slurry bed flows. This is discussed in Chapter 6, with the continuous phase conductivity vital in the optimisation of a non-nuclear alternative to slurry density measurement in hydraulic conveying systems.

4.6 References

Alberini, F; Liu, L; E.H. Stitt, M.J.H. Simmons. (2017). Comparison between 3-D-PTV and 2-D-PIV for determination of complex fluids in a stirred vessel. *Chemical Engineering Science.* 171, 189-203.

Bird R. B, Stewart W. E, Lightfoot E. N. (1960) *Transport Phenomena*. John Wiley and Sons: New Jersey, 905.

Blythe, T.W; Sederman, A; Stitt, E.H; York, A; Gladden, L. (2017). PFG NMR and Bayesian Analysis to Characterise non-Newtonian Fluids. *Journal of Magnetic Resonance.* 274, 103-114.

Bolton, G.T; Qui, C; Wang, M. (2002). A novel electrical tomography sensor for monitoring the phase distribution in industrial reactors. *Fluid Mixing VII Conference Proceedings.*

Bolton, G; Hooper, C; Mann, R; Stitt, E.H. (2004). Flow distribution and velocity measurement in a radial flow fixed bed reactor using electrical resistance tomography. *Chemical Engineering Science.* 59, 1989-1997.

Carletti, C; Montante, G; Westerlund, T; Paglianti, A. (2014). *Analysis of solid concentration distribution in dense solid-liquid stirred tanks by electrical resistance tomography. Chemical Engineering Science.* 119, 53-64.

Chhabra, R. P; Richardson, J. F. (2008). *Non-Newtonian Flow and Applied Rheology: Engineering Applications.* 2nd ed. Butterworth-Heinemann: Oxford.

Dong, X; Tan, C; Dong, F. (2016). Oil-water two-phase flow measurement with combined ultrasonic transducer and electrical sensors. *Measurement Science and Technology.* 27(12).

Dyakowski, T; Jaworski, A. (2003). Non-Invasive Process Imaging – Principles and Applications of Industrial Process Tomography. *Chemical Engineering Technology*. 26(6), 697-706.

Elson, T.P. (1990). The Growth of Caverns formed around rotating impellers during the mixing of a yield stress fluid. *Chemical Engineering Communications:* 96, 303-319.

Fawcett, N.J.S. (1989). The mean flow in the discharge of pitched blade turbines. *FMP Interim Report 1046.*

Forte, G; Clark, P.J; Wale, O; Hall, J.F; Zumaeta, N; Simmons, M.J.H; Stitt, E.H. (2016). Extending the application of electrical resistance tomography using linear probes in fluid mixing diagnosis. World Congress of Industrial Process Tomography, Iguassu Falls.

Gabriele, A; Nienow, A.W; Simmons, M.J.H. (2009). Use of angle resolved PIV to estimate local specific energy dissipation rates for up- and down-pumping pitched blade agitators in a stirred tank. *Chemical Engineering Science:* 64, 126-143.

Giguère, R; Fradette, L; Mignon, D; Tanguy, P. A. (2008). Characterization of slurry flow regime transitions by ERT. *Chemical Engineering Research.* 86, 989-996.

Grenville, R.K. (1992). *Blending of Viscous Newtonian and Pseudoplastic Fluids.* Cranfield Institute of Technology: Cranfield.

Haavisto, S; Koponen, A; Salemela, J. (2015). New insight into rheology and flow properties of complex fluids with Doppler optical coherence tomography. *Frontiers in Chemistry: Fibres and Biobased Materials.*

Houson, I. (2010). *Process Understanding: For Scale-Up and Manufacture of Active Ingredients.* Wiley-VCH: Darmstadt.

Industrial Tomography Systems. (2018). *Interface Detection.* Available: https://www.itoms.com/applications/interface-detection/. Last accessed: 17/10/2018

Jia, J; Wang, M; Schlaberg, I; Li, H. (2010). A novel tomographic sensing system for highly electrically conductive multiphase flow measurement. *Measurement Science and Technology:* 21, 184-190.

Machin, T.D; Wei, H; Greenwood, R.W; Simmons, M.J.H. (2018a). In-pipe Rheology and Mixing Characterisation using Electrical Resistance Sensing. *Chemical Engineering Science:* 187, 327-341.

Machin, T.D; Wei, H; Greenwood, R.W; Simmons, M.J.H. (2018b). Electrical Resistance Rheometry: The application of multi-scale sensors to provide in-pipe rheology of complex processes. *Conference Proceedings: 9th World Congress of Industrial Process Tomography (WCIPT9),* Bath: 3rd – 7th September 2018.

Meissner, J. (1983). Polymer Melt Flow Measurements by Laser Doppler Velocimetry. *Polymer. Test.* 3 (4), 291-301.

Nienow, A.W; Edwards, M.F; Harnby, N. (1997). *Mixing in Process Industries.* Butterworth-Heinemann: Oxford.

Pakzad, L; Ein-Mozaffarri, F; Chan, P. (2008). Using electrical resistance tomography and computational fluid dynamics modelling to study the formation of caverns in the mixing of pseudoplastic fluids possessing yield stress. *Chemical Engineering Science:* 101, 642-654

Papoulis, A. (1962). *The Fourier Integral and Its Applications.* McGraw-Hill: New York. 244-253.

Paul, E.L; Atiemo-Obeng, V.A; Kresta, S.M. (2004). *Handbook of Industrial Mixing – Science and Practice.* John Wiley and Sons: New Jersey.

Qui, C; Dickin, F.J; James, A. E; Wang, M. (1994). Electrical resistance tomography for imaging sub-seabed sediment porosity: initial findings from laboratory-scale experiments using spherical glass beads. *Proc. of 3rd European Concerted Action of Process Tomography.* Oporto, Portugal.

Rahman, N. (2013). *Wall Slip in Pipe Rheometry of Multiphase Fluids.* PhD Thesis, University of Manchester: Manchester.

Roussinova, V.T; Grgic, B; Kresta, S.M. (2000). Study of macro-instabilities in stirred tanks using a velocity decomposition technique. *Chemical Engineering Research and Design:* 78 (A7), 1040-1052.

Schleden, M; Lima W; Doerr, E.W; Wunderlich, M; Rehmann, L; Büchs J. (2017). Online measurement of viscosity for biological systems in stirred tank bioreactors. *Biotechnol Bioeng* 114(5): 990-997.

Simmons, M.J.H; Edwards, I; Hall, J.F; Fan, X; Parker, D.J; Stitt, E.H. (2009). Techniques for Visualisation of Cavern Boundaries in Opaque Industrial Systems. *AIChE Journal*. 55(11), 2765-2772.

Smythe, W.R. (1989). *Static and Dynamic Electricity.* 3rd Ed. Hemisphere Publishing Corporation: Philadelphia.

Vilar, G; Williams, R; Wang, M; Tweedie, R. (2008). On line analysis of structure of dispersions in an oscillatory baffled reactor using electrical impedance *tomography*. *Chemical Engineering Journal:* 141, p58-66.

Wang, M. (2002). Inverse Solutions for Electrical Impedance Tomography Based on Conjugate Gradients Methods. *Measurement Science and Technology*. 13, 101-117.

Wang, M. (2015). *Industrial Tomography.* Elsevier Science: Amsterdam

Westerweel, J. (1997). Fundamentals of digital particle image velocimetry. *Meas. Sci. Technol*. 8, 290, 294-301.

White, R; Simic, K; Strode, P. (2001). The Combined Use of Flow Visualisation, Electrical Resistance Tomography and Computational Fluid Dynamics Modelling to Study Mixing in a Pipe. *2nd World Congress on Industrial Process Tomography.*

Wiklund, J; Shahram, I; Stading, M. (2007). Methodology for In-line Rheology by Ultrasound Doppler Velocity Profiling and Pressure Difference Techniques. *Chemical Engineering Science*. 62(1), 4277-4293.

Wiklund, J; Stading, M; Trägårdh, C. (2010). Monitoring liquid displacement of model and industrial fluids in pipes by in-line ultrasonic rheometry. *Journal of Food Engineering*. 99(1*), 330-337.*

Wunderlich M, Trampnau PP, Lopes EF, Büchs J, Regestein L. (2016). Online in situ viscosity determination in stirred tank reactors by measurement of the heat transfer capacity. *Chem Eng Sci* 152, 116–126.

Chapter 5

Electrical Impedance Fingerprinting – A Novel Formulation Characterisation Technique

5.1 Introduction

Whilst applicable to complex fluids, the analyses which have been performed thus far have employed single phase model fluids. Within this chapter, EIT is utilised to explore complex fluids which contain a number of surfactant mesophases. In such systems, rheological and other structural properties have increased significance upon both in-process efficiency and final product quality. Complex fluids may also observe thixotropy, shear induced phase migration and shear banding during processing with off-line characterisation of these phenomena typically demanding and requires careful sampling (Olmsted, 2008). In-situ characterisation is inherently conducted within real process flows and hence affords enhancements in process understanding, optimisation and control, relative to formulated products. Rides et al. (2011) additionally stipulated that real-time, in-situ measurement techniques afford opportunities in new product development. Electrical Impedance Fingerprinting (EIF) is a novel technique which enables the real-time identification of formulations within processes based upon phase information obtained from non-invasive microelectrical tomography sensors. Once recognised, the fluid fingerprint can then be directly related to a number of the aforementioned key quality and structural attributes i.e.

rheology and product composition. This direct relation to product and process parameters is often of greater interest than their estimation from reconstructed tomographic images. Stephenson (2008) demonstrated that an image reconstructed by the robust linear back projection algorithm can give rise to an image error up to 27.9% with a direct relation consequently preferred.

Electrical techniques demonstrate great potential for formulation characterisation due to their low cost, temporal resolution and non-invasive nature. Within the literature, the majority of process characterisation studies using tomography focus solely upon Electrical Resistance Tomography, ERT, (Carletti et al., 2018; Pagliante and Montante, 2018; Kazemzadeh et al., 2016) or Electrical Capacitance Tomography, ECT, (Li et al., 2013; Wang et al., 2014). Using ECT, Mohamad-Saleh and Hoyle (2002) directly estimated the component fraction in multiphase flows based upon raw inter-electrode capacitance measurements and *a priori* knowledge of the composition. This was achieved using multi-layered feed forward neural networks (MLFFNN) with a volume fraction accuracy of 99 % for an oil-water-gas system. Johansen et al. (2018) employed a similar ECT approach utilising long short-term neural networks to predict the flow regime of a water-air system; however, ambiguous results were observed in the slug, plug and annular flow regimes. Neural networks have also been utilised alongside ECT measurements to detect interfaces within horizontal pipes for an oil-based system (Ru et al., 2011). It must be acknowledged, such studies are limited to dielectric materials and the outputted results are likely to be unsuitable for large diameter sensors such as those applied to industrial stirred vessels.

Electrical Impedance Spectroscopy is another technique which has been utilised to monitor product formulations by exploiting the frequency-dependent response of a material (Nahvi and Hoyle, 2008a). However, there is often a limited interrogation area associated with this technique and sampling bias may be observed. Hitherto, phase information obtained from tomographic sensors has not been employed individually. However, the use of complex electrical properties provides enhanced selectivity to differing product formulations as it

considers both resistive and capacitive electrical properties of the interrogated media. This is shown in the determination of the phase derived from a resistor and capacitor in parallel in Eq. 5.1 below.

$$\theta = \tan^{-1}(j\omega RC) \tag{5.1}$$

where θ is phase (°), j is the imaginary unit, ω is angular frequency (Hz), R is resistance (Ω) and C is capacitance (F). This equation also highlights the dependence of electrical properties upon excitation signal frequency.

To demonstrate EIF for the application of formulation identification, the preparation of an anionic surfactant solution has been studied. Sodium lauryl ether sulphate (SLES) is a tri-block surfactant which is extensively utilised in personal care applications due to its detergency properties. Surfactants self-assemble into different mesophase structures depending upon their concentration, interactions with electrolytes, temperature and surfactant structure (Evans and Wennerström, 1999). In dilute concentrations, SLES is solubilised as unimers; however, when this concentration is increased self-assembly occurs with micelles formed to minimise the free energy of the system. This process onsets at the critical micelle concentration (CMC) after which many physical properties undergo drastic changes, including: surface tension, solubilisation, self-diffusion and turbidity (Lindman and Wennerström, 1980). In addition, large variations in both the shear and viscoelastic rheological properties of SLES solutions are observed (Abdel-Rahim et al., 2014). At low SLES concentrations, a micellar solution is formed with a similar viscosity and surface tension to water; however these properties vary drastically at high concentrations forming a soft solid due to the presence of rod-like micelles (Abdel-Rahim et al., 2014). These evolving structures impact greatly upon both process efficiency and final product quality with a real-time, in-situ understanding of these formulations and structures from EIF affording new insights into formulated products.

As stated in previous sections, extensive literature exists concerning the application of Electrical Tomography modalities to monitor both Newtonian and non-Newtonian fluid mixing. The interrogation of the impedance map, produced from Electrical Impedance Tomography (EIT), permits the visualisation of mixing phenomena and has been performed in chemical reactors, mixers and industrial pipelines. Rodgers et al. (2009) utilised ERT to monitor mixing and dissolution times of 70 wt% SLES with water using a Cowles disk-style agitator in large-scale emulsion preparation. This process consists of dissolution of micellar agglomerates and miscible blending which was monitored using volume averaged conductivity. This study demonstrated that within the turbulent regime, mixing times may be predicted accurately using existing correlations (Grenville and Nienow, 2004). However, when materials with large viscosity differences are mixed, the blending and dissolution time is seen to be dependent upon operating conditions and mixer scale. These impacting factors, such as agglomerate size and number, greatly increase the dissolution rate and overall mixing time (Rodgers, et al., 2009).

With key quality and structural attributes obtained from EIF, spatial and temporal analyses of computed conductivity pixels can be performed simultaneously to provide a comprehensive understanding of such mixing processes. Combining 'traditional' tomography mixing analyses and visualisation offers new capabilities of in-situ analysis of fluids relevant to formulated products. EIF is additionally capable of supporting these tomography functionalities via appropriate reference and algorithm selection to enhance the integrity of the tomographic data collected.

This chapter outlines the principles of EIF and consequently applies them for recognition of SLES/water/electrolyte formulations. Initially, EIF is optimised in the context of pipe flow for both categorical and continuous formulation identification problems; to demonstrate EIF as a quality or feedforward process control tool. EIF is then expanded to characterise surfactant solutions within agitated vessels in real-time. 'Traditional' EIT mixing analyses and

rheological properties are then combined with EIF to permit new understanding for in-situ analysis of formulated products.

5.2 Development of Electrical Impedance Fingerprinting

5.2.1 Electrical Impedance Fingerprint

According to the circular adjacent EIT measurement protocol, a 16 electrode sensor provides 104 individual phase measurements which can act as an electrical fingerprint of a formulation. It has been observed, in low admittivity media this fingerprint remains uniform, with a parabolic shape witnessed for each measurement cycle. However, as the admittivity is increased this structure becomes progressively disordered until the measurement cycles become no longer discernible. This fingerprint alteration forms the basis of EIF and is highlighted in Figures 5.1a and 5.1b for water with conductivity adjusted to 0.1 mS cm^{-1} and 20 mS cm^{-1}, respectively, via the addition of sodium chloride. The fingerprint is optimised by normalising the phase data across each measurement cycle and captured at an interrogating current frequency of 19.2 kHz. As the phase measurement does not require reconstruction to be performed nor is it based upon a reference, this technique is advantageous over traditional tomography, as it is directly related to absolute electrical properties.

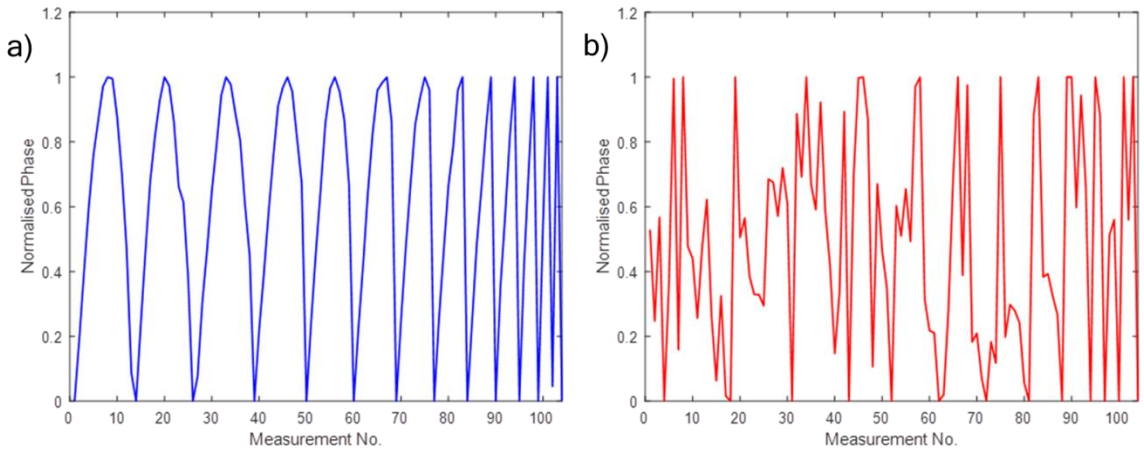

Figure 5.1 Electrical Impedance Fingerprint of water: a) 0.1 mS cm^{-1}; b) 20 mS cm^{-1}

The measurement of phase within the ITS p2+ EIT instrument is performed using phase sensitive demodulation, as described in Chapter 2 (Wang, 2015). This technique gives rise to a number of potential origins of the EIF phenomenon including: confinement of the electric field, stray capacitance, contact impedance of the electrodes and common-mode rejection ratio, CMRR, (Rosell and Riu, 1992). To define the cause, a series of experimental and computational experiments were performed.

5.2.1.1 Fingerprint Validation

Unlike the ITS v5r instrument utilised in previous sections, the ITS p2+ instrument utilises a sinusoidal current injection with the electrodes more likely to observe effects from contact impedance (Chitturi and Farrukh, 2017). To ensure that this electrode behaviour does not impact upon the phase fingerprint, initial tests were performed using resistor adapters. Resistor adapters consist of a series of constant accuracy resistors to form a network which create a 'dummy' path for the electrical field (Wang and Yin, 2001). Two ITS resistor adapters, 'standard' and high resistances, were connected directly to the instrument, without a sensor, to remove the presence of contact impedance. When the resistance is high, analogous to relatively low conductivity media, the uniform behaviour fingerprint behaviour is once again observed. Once replaced with a standard adapter, equivalent of higher conductivity media, this behaviour begins to once again break down with this depicted in Figures 5.2a and 5.2b. Whilst this analysis is qualitative, it highlights the alteration in phase shape with admittivity as a function of the bulk fluid and not the interactions within and between sensing electrodes. As it is confirmed that the bulk fluid and entire process domain is being interrogated, the applicability of EIF is greatly improved.

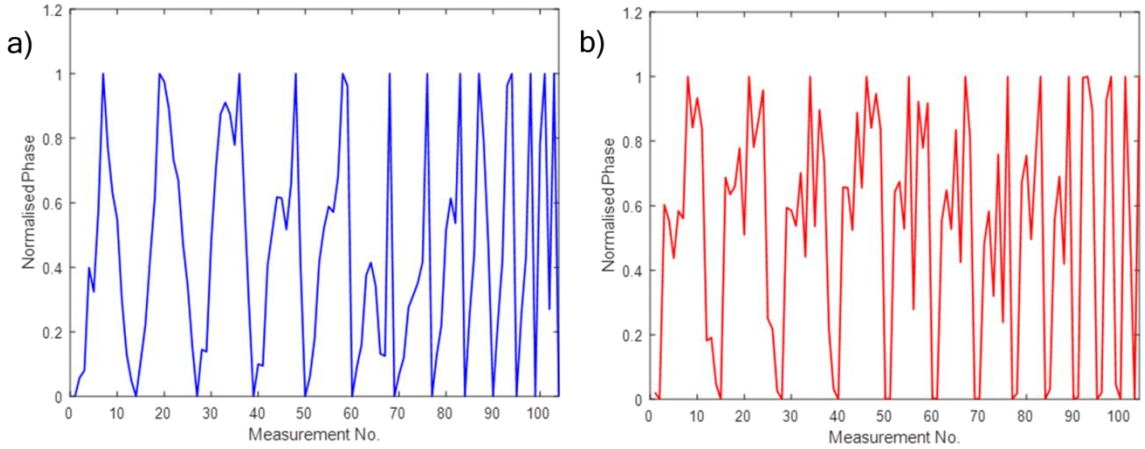

Figure 5.2 Electrical Impedance Fingerprint using resistor adapters: a) high resistance adapter; b) 'standard' adapter

Experimentally, EIF was validated using water with impedance properties adjusted via the addition of sodium chloride. These systems have also been explored in greater detail within the next chapter for the optimisation of an alternative to nucleonic density measurements in multi-component slurries. The impact of the alternating current signal generator upon the fingerprint was investigated by varying the following inputs: current source, current magnitude, sample cycles, gain map and frequency. Using initial p2+ settings of a 15 mA injection current from the current source rated 1.5 – 15 mA, 20 sample cycle delays and 19.2 kHz frequency, 10 impedance fingerprints were captured for water. The average fingerprint was computed and compared to the altered signal generator settings. Performing a linear regression of all 104 phase measurements yielded correlation coefficients of 0.997, 0.998, 0.999 and 0.993 when the current source, current magnitude, sample delay cycles and gain are changed, respectively. This indicates the parameters of the signal generator have little impact upon the shape of the phase measurement with this behaviour depicted in the parity plot, Figure 5.3a. The p-values for this fitting were also found to be below 0.001, indicating a high level of statistical significance exists between the two fingerprints. The applicability of this characterisation technique is hence enhanced as the integrity of tomographic data may be preserved with the optimal signal generator settings able to be selected whilst little variation in the fingerprint is observed. This is due to the calibration of the phase signal

settings being performed prior to the acquisition of the reference signal. The removal of the reference further enhances the potency of EIF as process information is directly obtained without the requirement of estimation from a reconstructed image. This was highlighted in a study by Stephenson (2008) who demonstrated that a tomogram reconstructed using the linear back projection algorithm can give rise to an image error for central and edge conclusions of 16.1 % and 27.9, respectively.

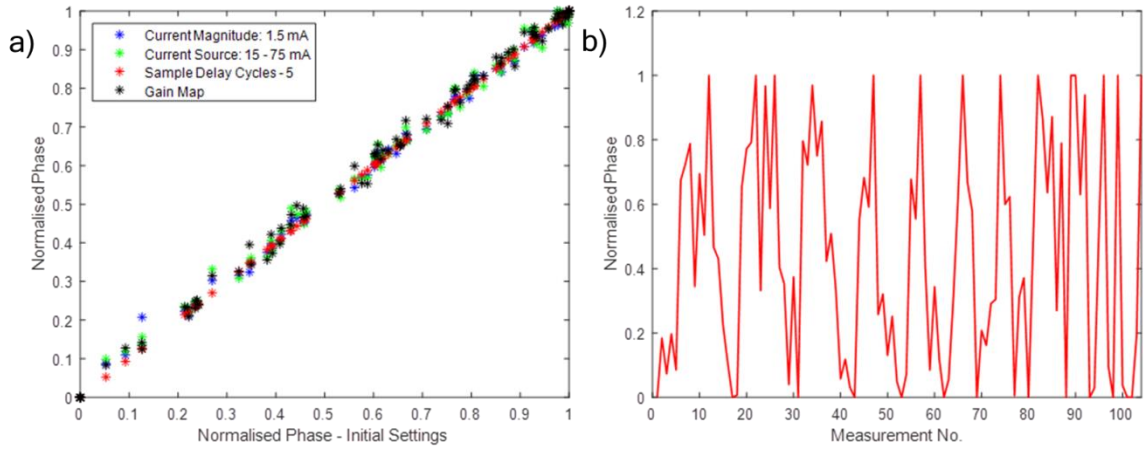

Figure 5.3 Impact of signal generator settings: a) parity plot; b) 0.1 mS cm^{-1} water, 4.8 kHz

A similar regression analysis is performed with correlation coefficients of 0.145 and 0.716 obtained at respective frequencies of 4.8 and 9.6 kHz. Despite this, when the frequency of the injection current is lowered to 4.8 kHz this progressive breakdown in the uniform fingerprint, with increasing admittivity, is observed for a fixed fluid, Figure 5.3b. This is expected as the response of electrical properties to the interrogating frequency is well-studied and forms the basis of Electrical Impedance Spectroscopy (O'Brien, 1986). Whilst this ensures a fixed frequency is required for direct comparison, the sensitivity of EIF may be increased further when applied to wideband multi-frequency EIT (Nahvi and Hoyle, 2008b). This has not been studied within this analysis with an optimal frequency of 19.2 kHz selected.

An independent EIT instrument was utilised to ensure that the pattern recognition was not a function of the ITS p2+ electronics, i.e. stray capacitance and common-mode rejection ratio (CMRR). The ITS z8000 EIT system possesses a different data acquisition protocol as the

phase is measured at each electrode. The 104 differential phase data points are then calculated across adjacent electrode pairs without averaging to remove potential smoothing effects (Wang, 2004). The sensitivity of z8000 phase measurement to noise is additionally dampened greatly as four-point phase sensitive demodulation (PSD) is employed, compared to the two-point PSD utilised in the p2+ measurement protocol outlined in Chapter 2. The electrical properties of water were adjusted using sodium chloride to produce four electrolyte solutions with conductivities in the range of 0.5 – 10 mS cm^{-1}. These fluids were interrogated using a current injection frequency of 20 kHz, to ensure a similar electrical impedance fingerprint was obtained. The selected injection current setting was '80' which equates to an amplitude of 25 mA. Despite exhibiting different phase measurement protocols, the z8000 impedance fingerprint behaviour mirrors that outputted in the p2+ instrument, as highlighted in Figure 5.4. In relatively low conductivity media, 0.5 mS cm^{-1}, a uniform fingerprint is observed with each measurement cycle easily discernible. However, as the admittivity is increased, the fingerprint repeatedly begins to break down.

As the independent EIT modalities exhibit similar behaviour, it can be said that this alteration in phase behaviour is universal across electrical impedance tomography modalities and cannot be solely attributed to the ITS p2+ instrument. This increases the reliability, wide-ranging applicability and robustness of EIF which is outlined within this thesis. A COMSOL model has additionally been developed which exploits the governing theory and mathematical formulation of all electrical tomography modalities, see Chapter 2. Using a 16-electrode circular arrangement a single excitation cycle was interrogated with the results supporting the independent EIT modality; this study is located in Appendix A2.

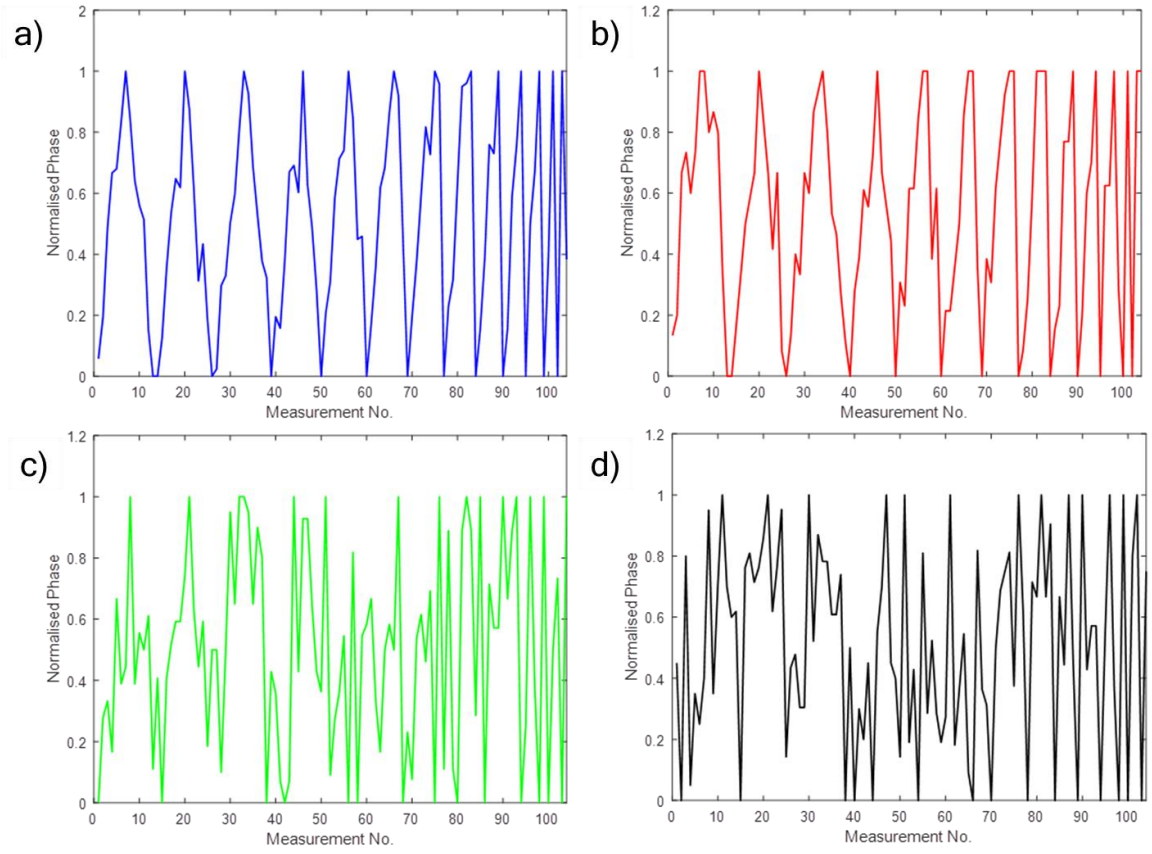

Figure 5.4 Electrical Impedance Fingerprint – z8000: a) 0.5 mS cm^{-1}; b) 1 mS cm^{-1}; c) 5 mS cm^{-1}; d) 10 mS cm^{-1}

As the fingerprint pattern is independent of the instrument circuity, it is likely that stray capacitance and CMRR do not give rise to the phenomenon (Rosell and Riu, 1992). As the admittivity of the interrogated fluid changes, so does the confinement of the electric field in three dimensions. With the positions of the electrodes fixed and the electrical field fluctuating according to the complex electrical properties, a unique electrical fingerprint is developed.

5.2.2 Artificial Intelligence

Upon obtaining the electrical fingerprint, supervised artificial intelligence (AI) techniques may be employed to extract valuable process information. Based upon *a priori* knowledge, AI algorithms are trained to recognise the features of the fingerprint and develop models from experience of independent experimental data. The developed fingerprint models are flexible

and are able to monitor a wide range of key quality attributes i.e. formulation and flow regimes. Such techniques are increasingly of interest to industry for process analytics and control enabling predictive models to be developed adaptively (Bernardes and Costelo-Branco, 2017). Furthermore, machine learning techniques are being adopted within Electrical Tomography; Johansen et al. (2018) applied long-short term memory neural networks to identify flow regimes using Electrical Capacitance Tomography measurements. For both classification and characterisation problems, 'traditional' machine learning algorithms and artificial neural networks have been explored for the optimisation of EIF.

5.2.2.1 'Traditional' Machine Learning

The application of traditional algorithms for the fingerprint recognition was investigated using initial SLES formulation data. A pre-processing feature extraction step was performed to determine twenty-four features of the fingerprint which vary from simple statistics such as the mean and median to more complex spectral parameters i.e. the spectral entropy of the signal. The features are then utilised to select the optimal training algorithm which was trained based upon the accuracy when compared to known results for classification and regression problems. Using an initial trial and error approach, a variety of training algorithms were investigated including: support vector machines, decision trees, nearest neighbour classifiers and discriminant analyses. It was evident that the optimal machine learning predictor for this application was bootstrapped aggregated (Bagged) decision trees based upon the criteria of accuracy, interpretability, adaptability and efficiency (Breiman, 1994). This ensemble method averages the output across a collection of bootstrap samples to reduce variance and instabilities observed in single decision trees. Yildiz et al. (2016) described this predictor as effective for shape quantisation and recognition which aligns with the requirement to distinguish between electrical impedance fingerprints. It is also capable of performing rapid re-classification as the decision trees may be refined without being reconstructed to develop an algorithm which is highly adaptive.

To develop the predictor, a number of fine decision trees, with a minimum of 8 leaves, were grown using the extracted features. The nodes of the decision trees were trained using the Gini impurity selected as the split criterion, Eq. 5.2 (Hastie et al., 2008), as it is more amenable to numerical optimisation. It is acknowledged that cross-entropy may also be utilised (Hastie et al., 2008). The Gini impurity, G_i, at any given node is the conditional probability of class c_i given that the node, t, is summed across all possible cases, with k number of classes; once trained, the trees were not pruned.

$$G_i = 1 - \sum_{i=1}^{k} p(c_i|t) \tag{5.2}$$

This technique is appropriate for both categorical and continuous problems, with 3 example decision trees depicted in Figure 5.5. When predicting a class, the bagged tree decision algorithm performs a plurality vote with the most common outcome selected; in the below example the outputted class would be 2. Averaging of the tree outputs is utilised when predicting a continuous variable with the below example generating a value of 1.67.

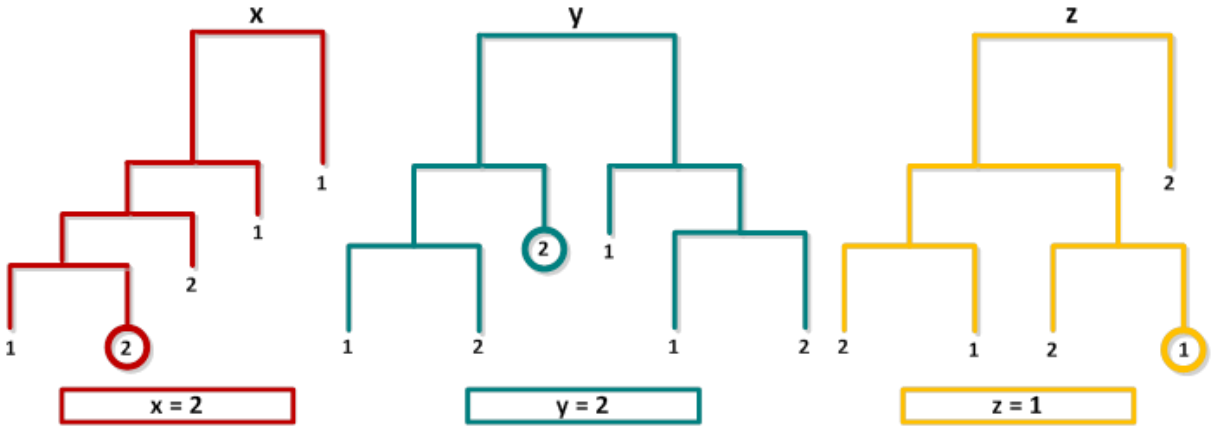

Figure 5.5 Example of bagged decision trees

This technique may be prone to overfitting of the training data and accordingly, 5-fold cross-validation was utilised to prevent this (Cawley and Talbot, 2010). A variable importance analysis was additionally performed in MATLAB to determine features with minor importance on the trained algorithm with these variables subsequently removed. To determine obsolete

features, changes in the mean squared error of the output are summed due to the splits at each feature. Once simplified, the training process was repeated with the reduced number of features to improve temporal resolution, adaptability and interpretability of the predicting algorithm.

5.2.2.2 Artificial Neural Networks

Artificial Neural Networks (ANN) are powerful predicting tools which consist of an interconnected assembly of elements, known as neurons, with functionality similar to an animal neuron (Gurney, 1997). Such systems extract linear combinations of measurement inputs and then model the target data as a non-linear function forming an extremely powerful forecasting tool (Hastie et al., 2008).

With differences in the fingerprint visible by eye, the required network architecture remained relatively simple without the requirement for deep learning approaches. Consequently, for both classification and continuous prediction scenarios, two-layer feedforward neural network architectures were investigated (Agarwal, 2018). Such networks contain measurement inputs, a hidden layer and an output layer (Agarwal, 2018); this architecture has been previously applied to ECT measurements by Mohamad-Saleh and Hoyle (2002) for use in multiphase flows.

In EIF, the 104 normalised measurements, p, of the fingerprint were directly inputted into the neural network without the requirement for feature extraction and accordingly reduce computational requirements. Each of these inputs is attributed a gain, w, due to their influence, which are optimised during the training. This is then passed to a hidden or output layer where each neuron is associated bias, b, with the total of these components determining the value of a single neuron, via Eq. 5.3 (Hagan et al., 1996).

$$y = w_1 p_1 + w_2 p_2 + w_3 p_3 \dots\dots\dots + w_{104} p_{104} + b \tag{5.3}$$

This equation may be written in matrix form, as below, Eq. 5.4.

$$y = Wp + b \tag{5.4}$$

The signal for this neuron, y, is then passed to a transfer function to determine the output, z. In both classification and continuous problems, a logistic sigmoidal transfer function was selected in the hidden layer, as it provides improved results when compared to the conventional step activation function (Gurney, 1997). This transfer function, described by Eq. 5.5, and highlighted in Figures 5.6 and 5.7, is also extremely common within multi-layer neural networks (Rashid, 2016).

$$z_h(y_h) = \frac{1}{1 + e^{\frac{\beta - y_h}{\varepsilon}}} \tag{5.5}$$

where y_h is a neuron signal of a hidden layer neuron, z_h is the output of the hidden layer neuron, β and ε are constants depending upon the selected network architecture

The output of any output neuron, z, is then dependent upon the selected threshold logic unit (TLU). If the output is less than the designated TLU, then the neuron will not fire with the output being 0; however, if it is greater, the value of z will be outputted. Within the hidden layer, n neurons are present with the same process repeated at each neuron. Whilst the hidden layers of the classification and continuous problems are identical, the output layers differ. This is highlighted in the network architecture of a classification problem depicted in Figure 5.6.

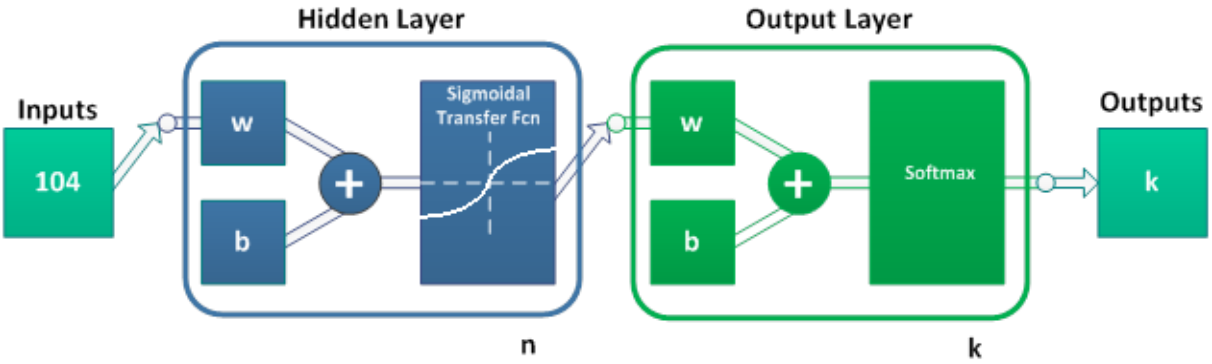

Figure 5.6 Optimised neural network architecture for classification outputs

The output layer for classification problems consists of k neurons equal to the desired number of classes to be outputted. The softmax transfer function has been selected as it has extensively been utilised in neural network studies for pattern recognition (Goodfellow et al., 2016). This normalises the output using an exponential function into a probability distribution of k classes with the highest probability selected, Eq. 5.6 (Goodfellow et al., 2016).

$$z_o(y_{o,i}) = \frac{e^{y_{o,i}}}{\sum_{j=1}^{k} e^{y_{o,j}}} \tag{5.6}$$

where y_o is the neuron signal of an output layer neuron, z_o is the output of a neuron in the output layer.

In continuous problems, the output layer consists of a single neuron and a linear transfer function as depicted in Figure 5.7.

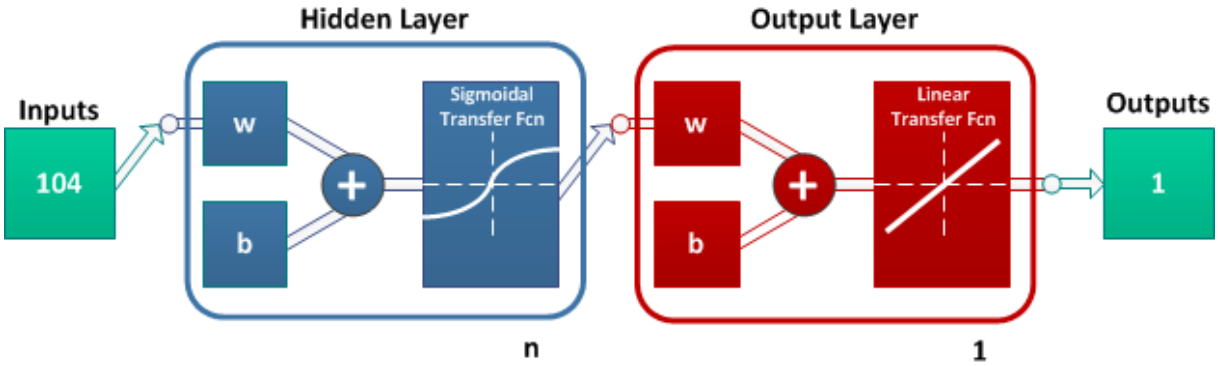

Figure 5.7 Optimised neural network architecture for continuous problems

With the network structure fixed, the weights and neuron biases are then trained. As the sigmoid transfer function has been selected within the hidden layer, backpropagation algorithms are preferred as the function is differentiable (Rashid, 2016). The most common backpropagation algorithms are the Levenberg-Marquadt algorithm, LM, (Marquadt, 1963) and the scaled conjugate gradients methods, SCG (Birgin and Martinez, 2001). Both of these algorithms have been extensively utilised in tomographic reconstruction with the former also employed for rheological parameter extraction in pipes, Chapter 3 (Na et al., 2015; Machin et al., 2018). LM is known to be inefficient for characterising classification problems and hence

the SCG algorithm is selected for training in this instance (Hastie et al., 2008). In continuous characterisation each algorithm will be evaluated using experimental data later within this chapter, alongside the popular Bayesian Regularisation (Neal, 1996).

5.3 Methodology

5.3.1 Materials

Four aqueous surfactant solutions were formulated by dissolving 27 wt% SLES, supplied by Mistral Chemicals UK, into water. The aqueous solutions of concentration 5, 10, 15 and 20 wt%, were mixed slowly to prevent the incorporation of air into the system and foaming of the detergent. The electrolyte content of the base solutions were altered via the addition of sodium chloride, supplied by Sigma-Aldrich UK. To each solution, salt was dissolved in aliquots of 0.75 wt% until a maximum of 7.5 wt% was dissolved. This gives rise to forty-four discrete formulations consisting of SLES, water and salt to be characterised. These formulation concentrations were selected to encompass a wide range of micellar properties and hence key physical and structural attributes (Voggt et al., 2017). The conductivity of each formulation was determined using a handheld conductivity probe, supplied by HANNA Instruments, UK.

The rheological properties of each formulation were analysed using a Discovery HR-1 rotational rheometer, supplied by TA Instruments, equipped with a smooth-walled, 4.006°, stainless steel cone and plate geometry of diameter 40 mm. The sample was held at 23 ± 0.1°C using a Peltier plate before a logarithmic shear rate ramp was applied across the shear rate range of 0.01 – 1500 s^{-1}, over a duration of 600 seconds with 20 points per decade. The measurement temperature was selected as it is reflective of the subsequent flow experiments. The obtained data was then analysed in TRIOS software, developed by TA Instruments, with a specific constitutive rheological model fitted using a non-linear least

squared regression to extract the rheological properties. A second sample was then loaded into the rheometer to perform a logarithmic oscillating amplitude sweep across an oscillation strain rate range of 0.01 – 100 s^{-1} at a fixed frequency of 1 Hz to examine for the presence of a linear viscoelastic region within the formulations.

5.3.2 Electrical Impedance Tomography

Two 16-electrode, circular EIT sensors of diameter 25.4 mm and 200 mm were employed to interrogate the selected fluids within pipe flow and a stirred vessel, respectively, as shown in Figure 5.8. The former was positioned within a simple recirculating loop, akin to that described in Chapter 3. This loop consisted of a flexible impeller pump (Liverani Pumps, UK), electromagnetic flow meter (Endress and Hauser, UK) and the 25.4 mm EIT sensor, as depicted in Figure 5.8a.

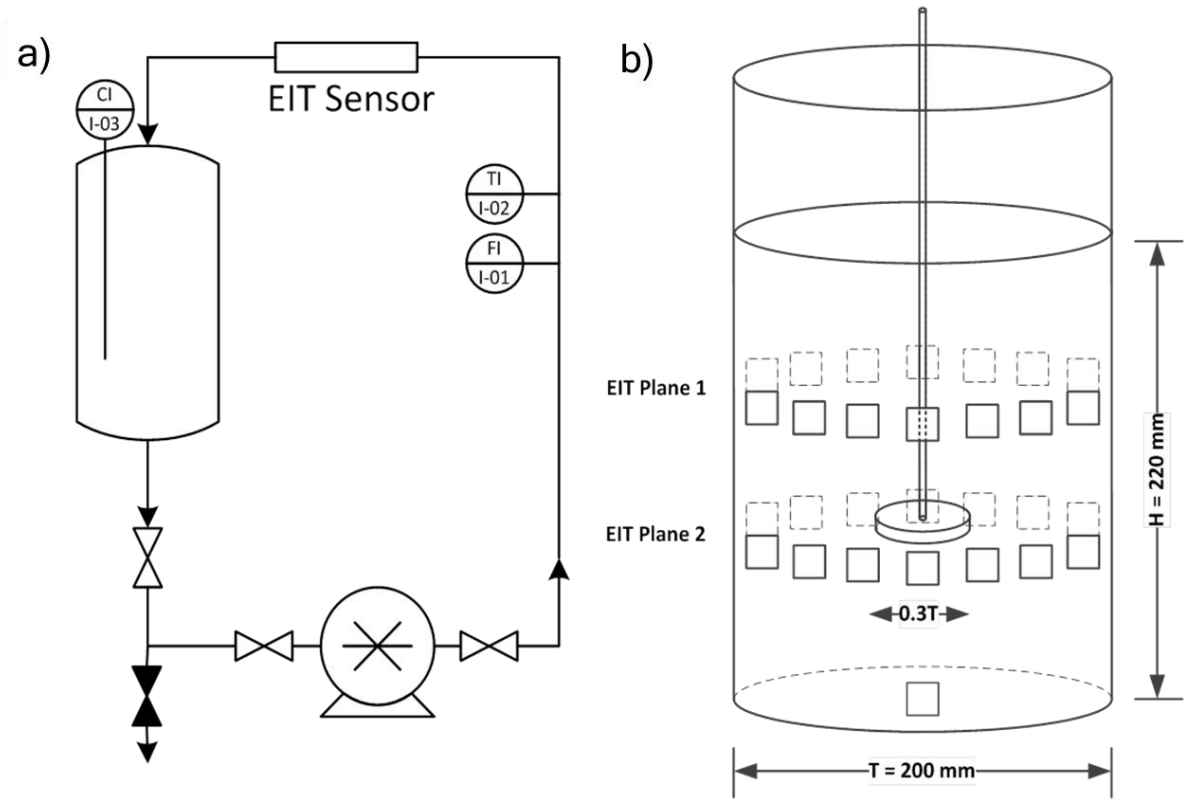

Figure 5.8 Experimental setup: a) pipe flow; b) stirred vessel

The EIT sensor was connected to the ITS p2+ EIT instrument with the circular complex adjacent measurement protocol selected with partial gain. The excitation signal in each case was fixed to 30 mA and the optimised frequency of 19.2 kHz, section 5.2.1.1. This ensured that the raw voltage measurements were large enough to be reconstructed based upon the admittivity of the selected fluids. The working fluids were loaded into the pipe rig and circulated at a constant flow rate of 300 L hr^{-1}. Once each system had reached steady state conditions, 250 frames were captured to ensure enough information was available for training of the algorithm whilst removing the potential for class imbalance. The prevention of class imbalance eliminates the requirement to use more complex predictors such as RUSBoost, AdaBoost and SMOTEBoost (Seiffert et al., 2010; Freund, 2006; Chawla et al., 2003).

Using the same EIT settings, the formulations were interrogated within an unbaffled, dual-plane EIT vessel sensor, *T = 200 mm*, depicted in Figure 5.8b. A three blade hydrofoil impeller, *60 mm, D = 0.3 T*, was utilised to agitate the system at a constant impeller speed of 600 rpm. Each blade of the impeller swept an angle of 120° with a vertical projection height of 8.7 mm and positioned at a clearance of *T/3.* The impeller was fabricated from non-conducting polypropylene to minimise interference with the EIF and EIT measurements. The base SLES formulations were added to this vessel to a fill height, *H,* of 220 mm; this level was selected to prevent the detection of the air interface during EIT measurements, known as level artefacting. Step additions of 0.75 wt% sodium chloride were added to the SLES solutions with the mixing continually monitored by EIT and EIF. Once the variation in volume averaged conductivity, across two planes, was seen to be ± 2 %, it was assumed that the system was fully mixed and a further 250 frames were captured under these steady state conditions to be utilised for training.

5.3.3 Electrical Impedance Fingerprinting

Upon collection, the raw voltage measurements were directly fed into a MATLAB code, which combined the real and imaginary voltages with the phase measurements determined from

the manipulation of Eq. 5.1. The phase measurements were extracted via phase sensitive demodulation then normalised across each EIT measurement cycle to obtain the final phase fingerprint.

This code additionally performed feature extraction for the training of the bagged trees predictor. Such pre-processing is not required for the training of the Artificial Neural Networks, with the normalised phase measurements directly fed into the training algorithm. The two-layer feedforward network structures described and illustrated in Section 5.2.2.2 were selected for training which was performed in the MATLAB machine learning toolbox. To develop the predictor, the complete datasets were randomly sub-divided into training, validation and test datasets which consist of 70 %, 15 % and 15 % of the phase information. Supervised machine learning techniques were utilised to determine predictive algorithms based upon known, desired outputs including, salt concentration, conductivity and pH alongside the training data. The performance of training algorithms was analysed using the cross-entropy error (CEE) and mean squared error (MSE) for classification and continuous predictors of the validation dataset, respectively. The CEE, or multinomial log-likelihood, determined by Eq. 5.7, was additionally monitored for classifications to ensure that overfitting did not occur (Hastie et al., 2008). In this instance, the classification output probability, z_o, is determined by the softmax function, Eq. 5.5.

$$CEE = -\frac{1}{N}\sum_{n=1}^{N}(z_n \log z_o + (1 - z_n)\log z_o) \tag{5.7}$$

where z_n is the known output, 1 or 0.

During training, gradient based methods were utilised to continually minimise the MSE and CEE of the training data with the validation set monitored. Once the error within the validation set began to increase, the training data set was further optimised for six validation checks to ensure that a universal minimum had been obtained. This technique is advantageous as it prevents overfitting of the training data and ensure good generality of the trained predictor.

Within the selected machine learning architectures these criteria were utilised to determine the optimal number of decision trees, number of neurons in the hidden layer and fitting algorithm.

An additional code was written which utilised the raw voltage measurements and sensitivity map, alongside the Modified Sensitivity Back Projection algorithm (Wang, 2015) to output the real, modulus and novel imaginary and phase tomograms. It must be noted that in this study only the real tomographic component (ERT) was utilised in the simultaneous analysis of mixing behaviour and formulation recognition. The use of the aforementioned phase and imaginary tomograms will be discussed in the next section for their use in the characterisation of complex multi-component slurries.

5.4 Results and Discussion

5.4.1 In-pipe Characterisation

The capability of EIF to determine formulation composition, and ultimately infer key quality attributes, was investigated within pipe flows. Each of the forty-four formulations were initially classified based upon their known salt concentration. This reflects a real-time measurement to distinguish if a material formulation achieves quality control standards or act as a feedforward process control tool for optimisation purposes. Using the bagged trees algorithm, the stepped salt concentration in SLES solution was monitored. For each surfactant concentration, the number of bagged trees was varied between 1 and 50 to determine the optimal predictive algorithm. The importance of bootstrap aggregation was highlighted across all studies with a single tree providing a misclassification rate in salt concentration of 7.2 % for a 5 wt% SLES solution. Single trees can also often lead to either large variances or biases depending upon their size. When increasing the number of aggregated trees to five, a large increase in the accuracy is observed with a misclassification rate of just 2.8 %. This trend

continues until thirty decision trees are aggregated at which point the algorithm is 99.3 % accurate, as depicted in Figure 5.9 and in the confusion matrix, Figure 5.10. Upon increasing the number of aggregated trees further, no discernible increase in accuracy was ascertained whilst the interpretability decreases. Consequently, the optimal bagged tree algorithm for classification of salt concentration within SLES formulations consists of thirty decision trees with a maximum of eight leaves. This aligns with Breiman et al. (1996) who recommended that 25 – 50 aggregated trees provide optimal predicting algorithms based upon the criteria of accuracy, computational efficiency, stability and interpretability. This developed predictor is capable of categorically recognising 18,000 formulations per second, which is vastly in excess of the data acquisition rate of EIF (0.5 Hz) when utilised in parallel with conventional tomographic measurement. If EIF is exploited alone, this temporal resolution can be enhanced with the removal of tomography reconstruction algorithms, to 2 Hz, to enable the capture of fast evolving processes.

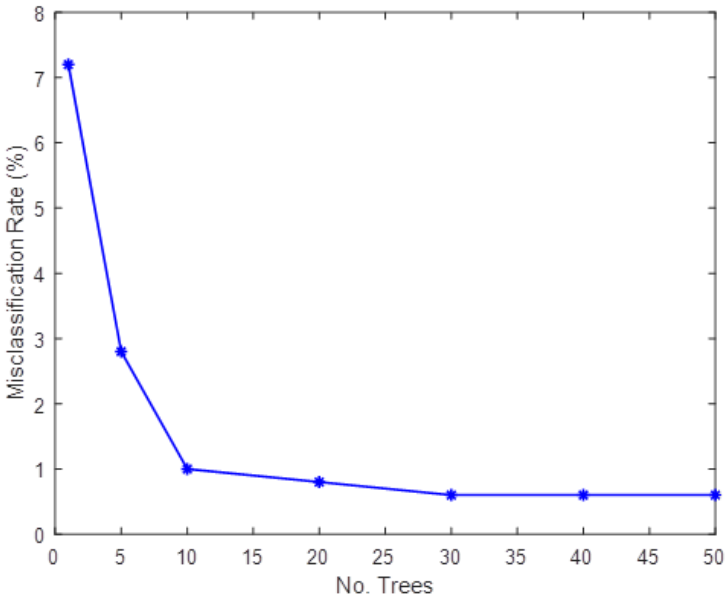

Figure 5.9 Optimisation of Bagged Decision Tree Algorithm

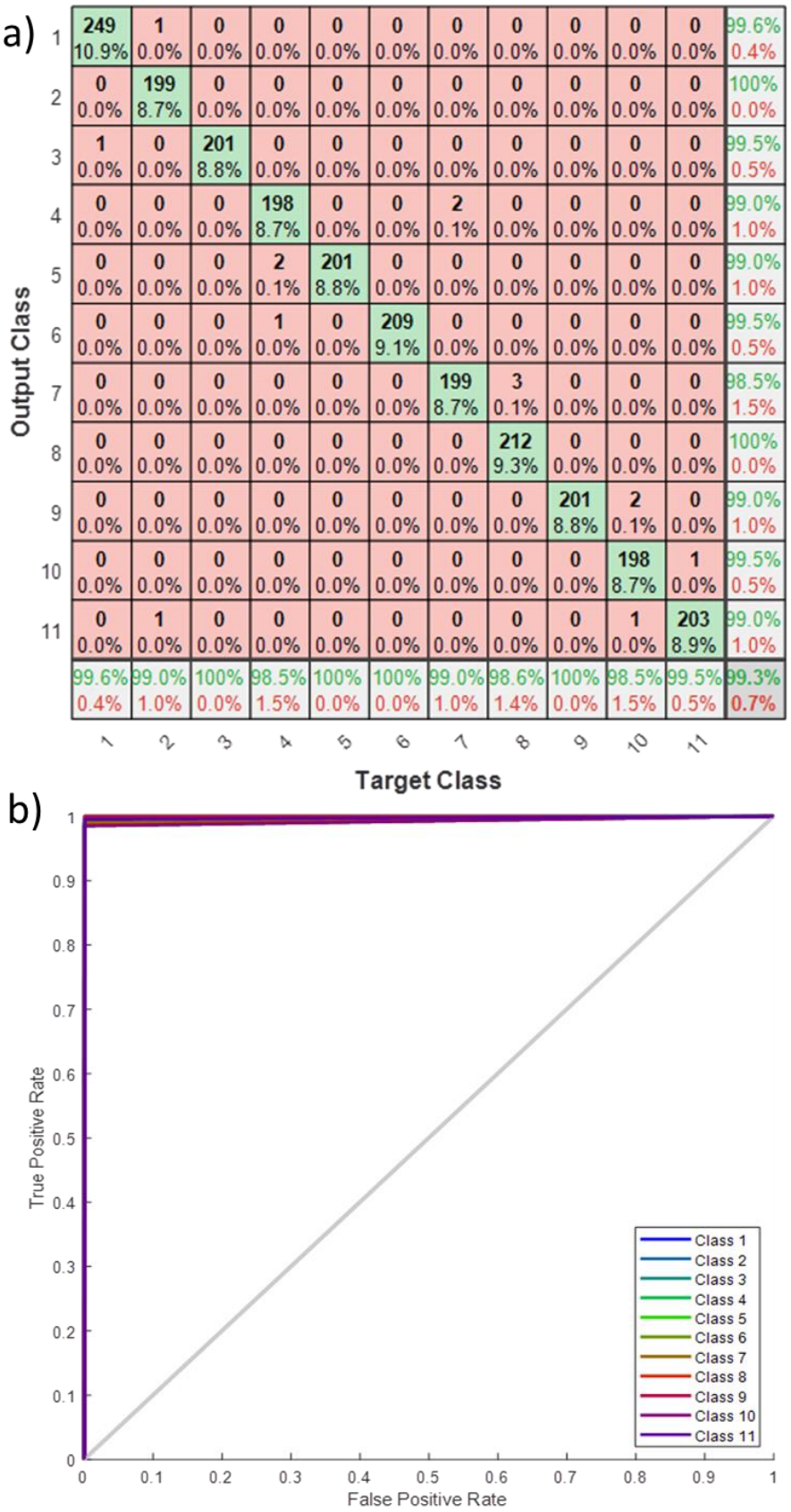

Figure 5.10 Bagged Trees Classification Performance: a) confusion matrix, b) ROC curve

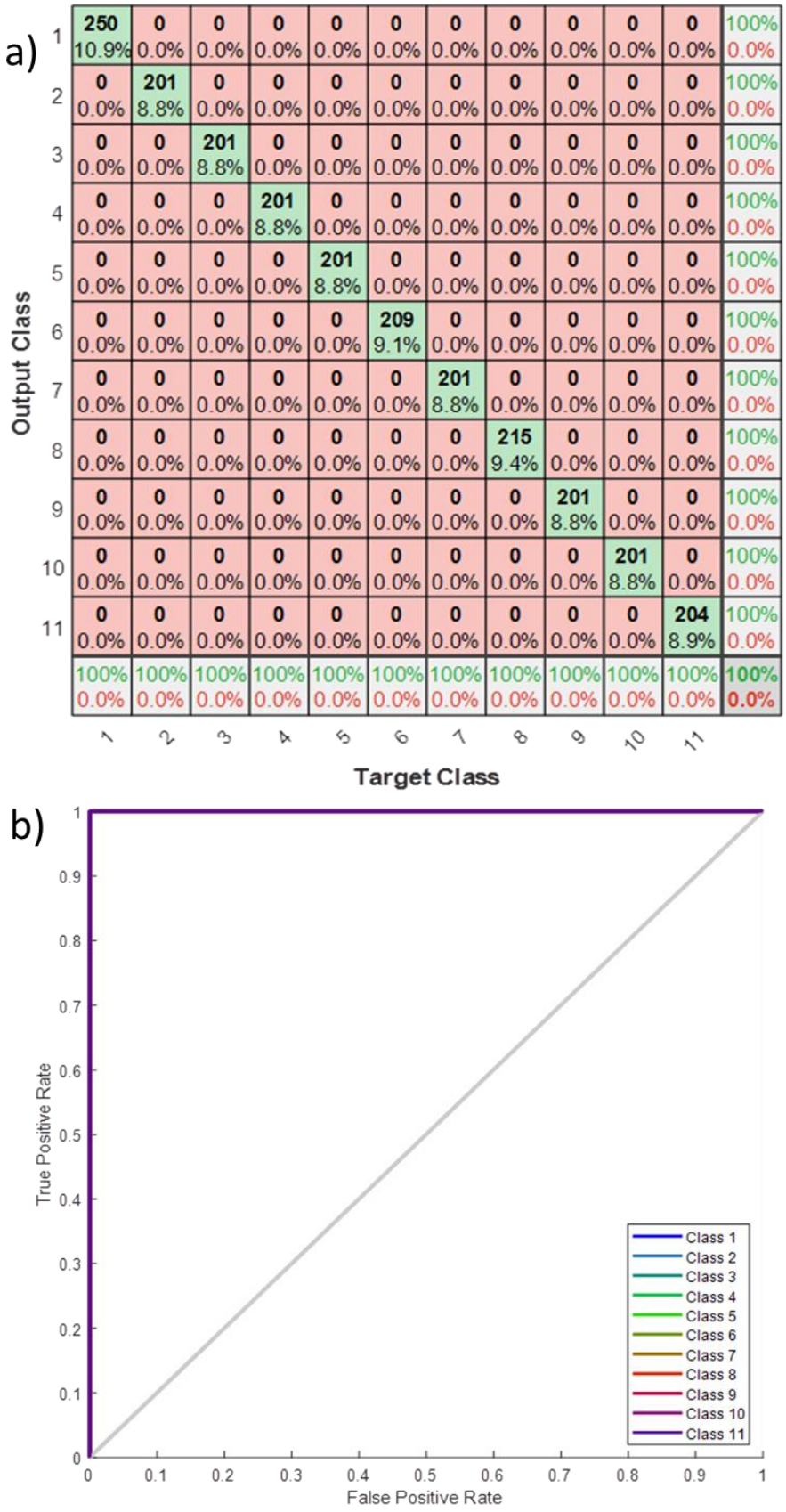

Figure 5.11 ANN classification performance: a) confusion matrix; b) ROC curve

The prediction rate may be increased further via the removal of features which do not contribute to the prediction; this is achieved by determining the increase in MSE when the feature is removed. The feature is removed if its contribution is less than 2 % of the feature with the greatest contribution. Five features were removed including the number of peaks and a number of power and spectral entropy features to require nineteen features for prediction. The accuracy of this predicting algorithm with the reduced number of features is preserved with the new confusion matrix depicted in Figure 5.10a. The receiving operating characteristic (ROC) curve is additionally presented with the fall-out rate monitored, Figure 5.10b. This algorithm has an enhanced training rate of 10.9 ms per frame with 183 EIF data frames trained during the time a single EIT frame is captured and reconstructed, giving rise to a highly adaptable algorithm for EIF.

A similar analysis can be performed using the Artificial Neural Network (ANN) structure highlighted in Figure 5.11. For classification problems, the output layer is fixed to the number of classification labels; however, the number of neurons within the hidden layer requires optimisation. By varying this number of neurons trained by the scaled conjugated gradients method (SCG), the optimal hidden layer was defined. Using forty hidden neurons, EIF is capable of predicting the formulation without a single frame mis-classified. Figures 5.11a and 5.11b demonstrate the confusion matrix and ROC curve, respectively, to monitor salt concentration for a 10 wt% solution. The CEE was monitored for all data groups to estimate the extent of overfitting with the training performance depicted in Figure 5.12. Within the test dataset, the CEE was 3.37×10^{-7} with 2.93×10^{-7} the calculated CEE for the training dataset. In addition to being a small error, the similarity of the training and test CEE indicates that overfitting has not occurred and the algorithm is capable of accurately predicting outputs of unseen data, Figure 5.12.

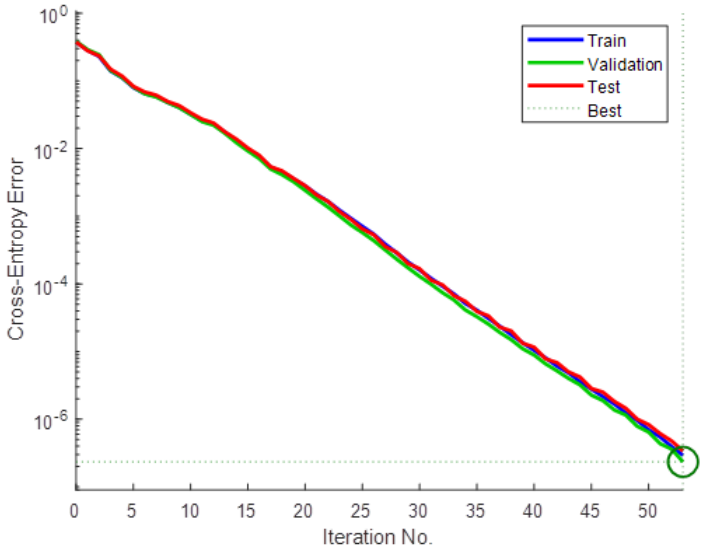

Figure 5.12 Training performance of an algorithm to predict salt concentration in a 20 wt% SLES solution

This analysis can be extended to all of the forty-four SLES and salt formulations with a misclassification rate of 0.31 % across the 11,000 data frames acquired, as reflected in the in Figure 5.13. This rate was 2 % when employing the optimised bagged tree learner which further demonstrates the selection of ANNs for the fingerprint recognition. Across the aforementioned formulations, the rheological properties are seen to vary drastically with the consistency index and power index ranging from 4.64 x 10^{-3} - 72.1 Pa s^n and 0.14 - 1, respectively, when utilising the power law constitutive equation. The rheological parameters for all experimental SLES formulations are presented in Appendix A4. As stated in Section 5.1, a number of other parameters are impacted when new micellar structures are formed including: surface tension and solubilisation. Such changes impact greatly upon the in-process efficiency and final product performance, so there is considerable potential if this information can be accurately captured by EIF for quality control or in process optimisation.

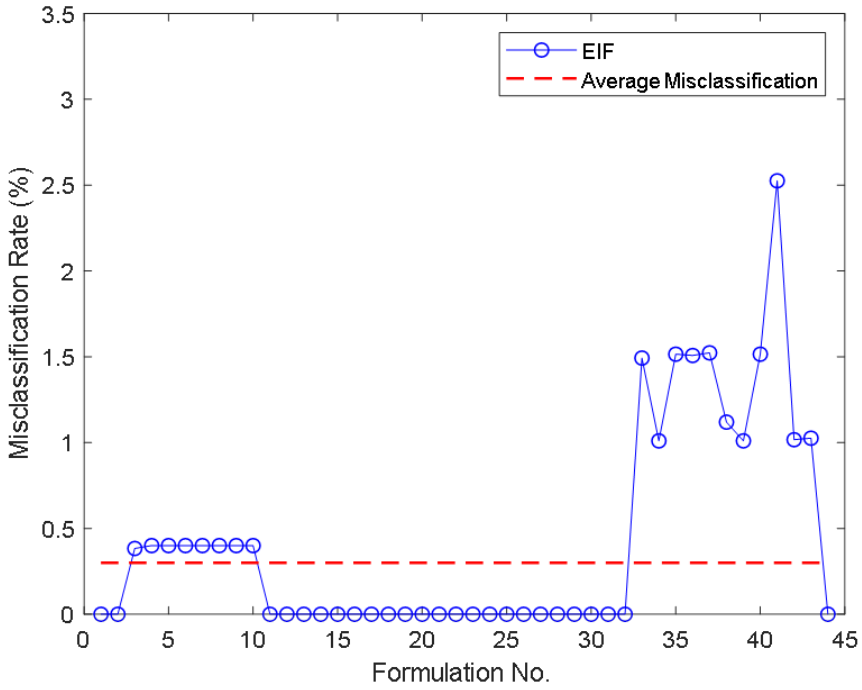

Figure 5.13 Misclassification rates of all SLES formulations

It must be noted that the conductivity range of the working fluids was 11.3 – 43.9 mS cm^{-1} with a number of formulations possessing similar conductivity values. The capability of this technique to distinguish between materials of similar conductivity with high accuracy, 99.7 %, demonstrates that the fingerprint behaviour arises as a function of admittivity with capacitive behaviour also considered. In addition to interrogating the entire process domain, the increased selectivity of EIF to capacitive properties reinforces its improved performance over simple probe setups.

Despite the bagged tree algorithm possessing high accuracy and interpretability, the optimal training algorithm for the recognition of the phase fingerprint is a two-layer feedforward neural network (TLFFNN) with a hidden layer of forty neurons. The ANN additionally possessed greater temporal resolution and hence adaptiveness, with the algorithm trained in three seconds based upon 2,750 frames of data. This also highlights the vast potential of EIF for the application to recognise dynamic and evolving formulations and key quality parameters

within pipes. An additional training analysis was performed which was capable of predicting the SLES concentration, irrespective of salt concentration, with zero frames misclassified.

This technique is extended to continuous predictions of measured salt concentration based upon the trained data. This can be achieved using both the bagged tree and ANN structures. To optimise the performance, the selected training algorithm is analysed. Whilst unsuitable for classification problems, the Levenberg-Marquadt (LM) algorithm, which also has been exploited for in-pipe rheological property extraction (Machin et al., 2018), offers advantages when analysing continuous problems. A Bayesian probabilistic approach to the training has also been explored (Neal, 1996).

Using the continuous TLFFNN structure highlighted in Figure 5.6, each of the aforementioned algorithms have been utilised to train continuous models. Whilst Bayesian Regularisation (BR) affords the smallest root mean squared error (RMSE) of the validation dataset of just 0.019 wt%, the training time required for this algorithm was in excess of 4.5 hours. This ensures that a model capable of being rapidly retrained using new experimental data is unable to be created using a Bayesian approach, which is not preferable. However, the LM model also remains highly accurate, RMSE of 0.026 wt%, with a much reduced training time of less than a minute. Figure 5.14a and 5.14b demonstrate this behaviour alongside the SCG and bagged trees algorithm. BR is suited to noisy training data which is difficult to generalise; however, there is little improvement observed in accuracy compared to the LM gradient based method. This highlights the amenability of the phase fingerprint to machine learning techniques with the change in the fingerprint visible by eye. The potential of EIF is likely to be extended to recognise more complex relationships and interactions than explored within this chapter with BR then potentially required. Although the chosen algorithm is dependent upon the process requirements i.e. accuracy and training time, the LM algorithm has been selected to act as the optimal training algorithm for the continuous identification of surfactant formulations.

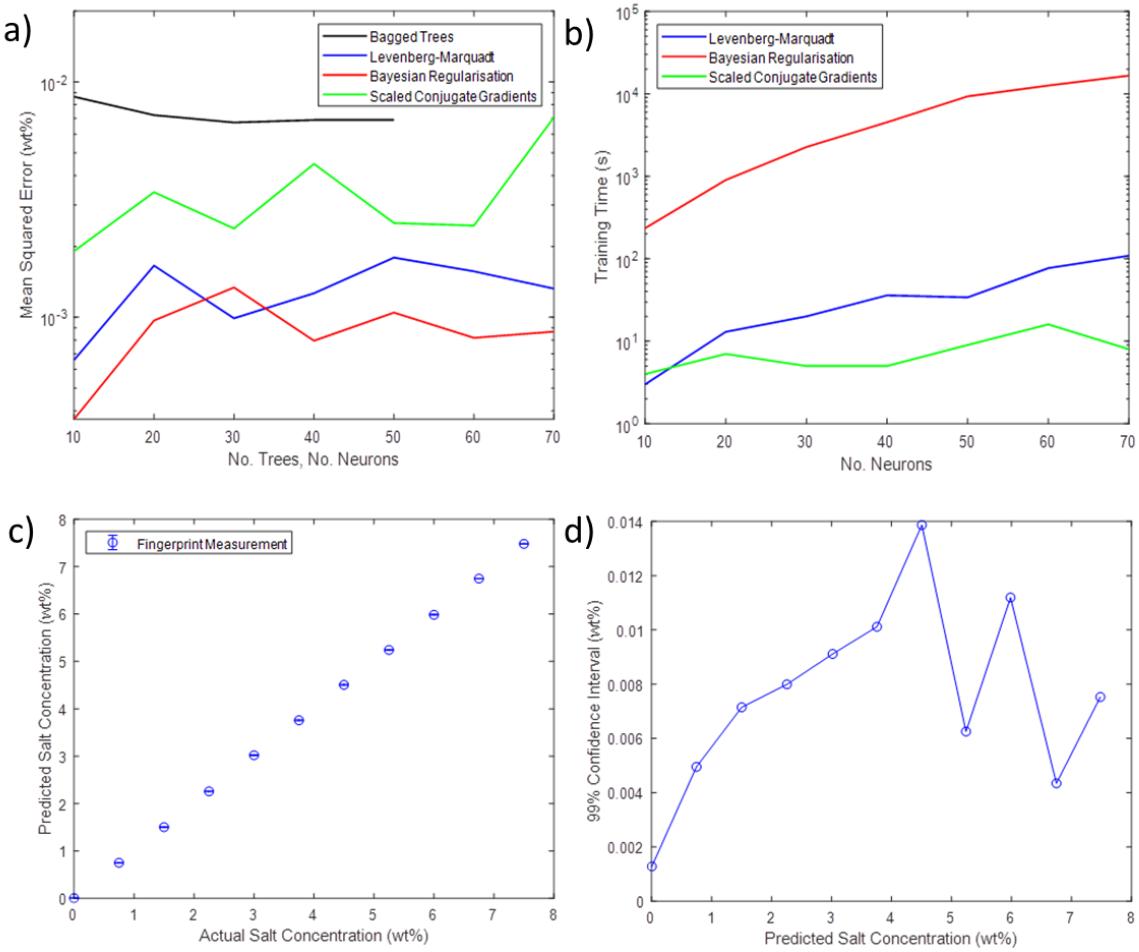

Figure 5.14 Continuous characterisation of salt concentration in a 20 wt% SLES solution within pipes: a) algorithm optimisation – error; b) algorithm optimisation – training time; c) parity plot; d) 99% confidence intervals

The linearity provided by this algorithm has been demonstrated using a linear regression of all predicted and measured salt concentrations. This yielded an average correlation coefficient of 0.9992, with a gradient of 1.00 and an intercept of 0.0026. The 99 % confidence intervals, CI_{99}, have also been computed to assess uncertainty in the measurement using a normal distribution, Eq. 5.8, and depicted in Figure 5.14d.

$$CI_{99} = 2.576 \cdot \frac{\sigma}{\sqrt{n}} \tag{5.8}$$

where σ is the standard deviation and n is the number of measurements.

The largest confidence interval was 0.014 wt%, at 4.5 wt % salt for a 20 wt % SLES solution; this depicted in Figure 5.14d with repeatable behaviour reflected across all formulations. Such a minor uncertainty in the measurement demonstrates the capability of EIF to repeatedly, continuously and accurately identify a number of surfactant formulations within pipe flow. From this recognition the quality and structural properties can then be inferred i.e. rheology and solubilisation to develop a real-time, in-situ process characterisation tool for both process and quality control applications.

A number of additional characterisation experiments were also performed, within the pipeline setup, using two additional model aqueous-based fluids, namely: xanthan gum, *from Xanthomonas Campestris* (Sigma-Aldrich, UK) and Carbopol 940 (Lubrizol, UK). The concentration of xanthan gum and change in pH of Carbopol 940 due to the addition of sodium hydroxide (Sigma-Aldrich, UK) were predicted with results displayed in Appendix A3. The concentration of xanthan gum was predicted with 99.9 % accuracy with the pH, and associated evolving rheology, presenting an RMSE of 0.082 to demonstrate the capability of EIF to predict a range of fluid parameters within both simple and complex formulated fluids.

5.4.2 Vessel Characterisation

To assess the applicability of EIF to formulation characterisation in mixing operations and at larger scales, the fingerprint technique has been applied to an agitated, un-baffled vessel in Figure 5.8b. Formulation recognition within vessels presents an opportunity to optimise mixing performance and identify process end points based upon the associated in-situ characterisation of rheological and mass transfer properties. Whilst observing minor differences to the pipe geometry, the progressive breakdown of the fingerprint with increased admittivity once again is present and analogous to Figure 5.1.

The mixing behaviour, arising from a 3-blade hydrofoil impeller at a constant impeller speed of 600 rpm, was continually monitored using EIF. A training dataset was developed when the system was fully mixed using the criteria outlined in Section 5.3.2. A similar analysis to

Section 5.4.1 was performed with the optimised artificial neural network architectures employed.

Despite increasing the sensor diameter by a factor of eight, and the presence of an impeller, similar, if not improved, accuracy is ascertained for classification problems when compared to pipe flow. Once again, the salt concentration for each electrolyte solution was predicted with an accuracy of 100 %. Accordingly, an identical confusion matrix and receiving operator characteristic as depicted in Figure 5.11a and 5.11b were outputted. When considering all forty-four surfactant formulations, a reduction in misclassification is observed with just three frames out of 10,417 mis-classified, yielding an accuracy of 99.96 %. This high accuracy demonstrates scalability of the EIF technique across a range of sensor diameters and unit operations. Furthermore, a continuous approach revealed a reduction in MSE by factors between 1.34 and 1.58 for each SLES concentration, compared to the high accuracy characterisation already demonstrated within pipe flow, Section 5.4.1. The linearity and uncertainty of this model was examined with a linear regression yielding correlation coefficients of 1.00, 0.99, 1.01, and 1.00 and for 5, 10, 15 and 20 wt% SLES solutions, respectively. A parity plot and confidence intervals for a 20 wt% solution are depicted in Figures 5.15a and 5.15b with the largest CI_{99} values 0.022, 0.028, 0.013 and 0.012 wt%.

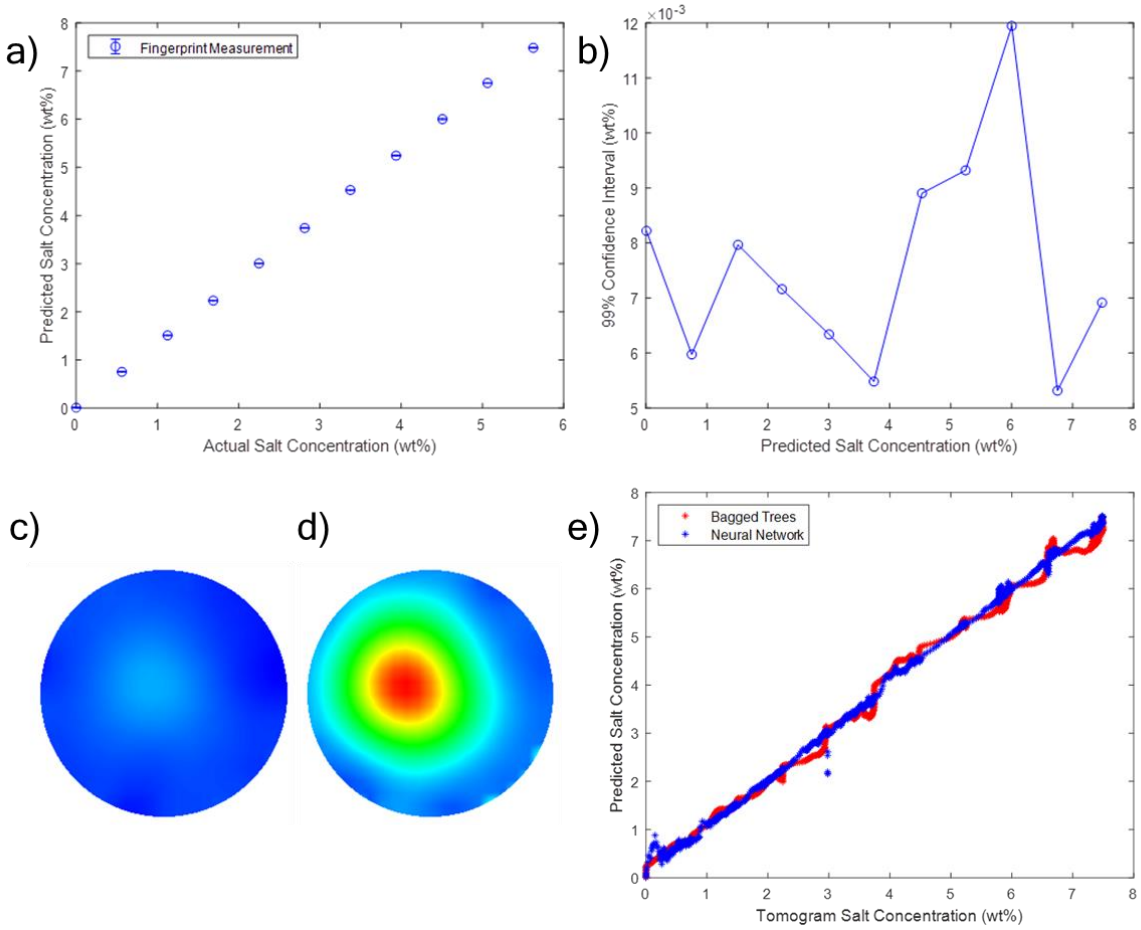

Figure 5.15 Continuous characterisation of 20 wt% SLES formulations within an agitated vessel: a) parity plot – complete mixing; b) confidence intervals; c) homogeneous tomogram; d) un-mixed tomogram; e) parity plot during mixing

This derived neural network can then be applied to the entire data set for the continuous identification of salt concentration without the requirement of a reference. To assess the ability of this system to predict the presence of non-trained formulations, tomographic data was analysed with example tomograms displayed in Figures 5.15c and 5.15d. Using the average of computed conductivity pixels, Maxwell's effective media approximation can be utilised to determine the volumetric salt concentration, Eq. 5.9 (Choy, 2016). This equation is also utilised in a non-nuclear slurry density measurement which is discussed in the next chapter.

$$\alpha = \frac{2\sigma_1 + \sigma_2 - 2\sigma_m - \left(\frac{\sigma_m \sigma_2}{\sigma_1}\right)}{\sigma_m - \left(\frac{\sigma_m \sigma_2}{\sigma_1}\right) + 2(\sigma_1 - \sigma_2)} \tag{5.9}$$

where α is the volume fraction of the secondary phase

As tomography is based upon relative changes in properties, the initial volume averaged conductivity, σ_1, was selected as 1 with the mixed conductivity, σ_m, equal to the relative change of each frame. To determine the secondary phase conductivity, σ_2, the known, trained salt concentration values were matched to the tomographic data, by making the secondary phase the subject of Eq. 5.9. From this, the relative discrete phase conductivities were 41.0, 16.9, 9.6 and 7.4 for 5, 10, 15 and 20 wt% SLES solutions, respectively. These values were then utilised to determine the evolving salt concentrations of the untrained data within the sensing plane. The volumetric salt concentration may then be converted to the mass concentration, X, with Eq. 5.10 derived from a mass balance.

$$X = \frac{\alpha \rho_{NaCl}}{\alpha \rho_{NaCl} + (1 - \alpha)\rho_{SLES}} \tag{5.10}$$

where ρ is density

A parity plot, Figure 5.15e, may be used to compare the predicted and tomogram salt concentrations with excellent agreement observed throughout when using both the bagged trees and neural network architectures. For a 20 wt% surfactant solution, correlation coefficients, obtained from a linear regression, of 0.992 and 0.999 were extracted with gradients of 1.003 and 1.001 ascertained when the bagged trees and ANN predictors are employed, respectively. Such correlation between these independent electrical techniques highlights the capability of EIF, when using ANNs, to predict non-trained values i.e. evolving rheological properties on a continuous basis. This further reinforces the selection of two-layer feedforward neural networks as the optimal predictor for impedance fingerprint recognition.

5.4.3 Combining 'Traditional' Tomography for a complete mixing analysis

The application of the computed tomography pixels can be extended to the visualisation of mixing phenomena and identification and prediction of process end points based upon temporal and spatial analyses of the cross-sectional impedance map (Simmons et al., 2009; Rodgers et al., 2009; Hosseini et al., 2010). These 'traditional' electrical tomography measurements may be coupled with the key quality attributes inferred by EIF to form a powerful characterisation tool. Within mixing applications, the rheological properties typically govern the mixing performance with SLES solutions varying from a Newtonian fluid with the viscosity of water to a soft solid at high concentrations (Rodgers et al., 2011). This microstructural change was also observed in the rheological data acquired for the SLES formulations used within this study. At low electrolyte concentrations, the formulations observe Newtonian behaviour with the viscosity in the orders of magnitude of 10^{-3}- 10^{-2} Pa s. This specific constitutive equation is appropriate until the electrolyte concentration is in excess of 6.0, 4.5, 3.0 and 1.5 wt% for 5, 10, 15 and 20 wt% surfactant solutions, respectively. This is reflective of an alteration in the interaction energies of the surfactant head groups, based upon electrolyte and surfactant concentration, to alter the geometric structures present and ultimately rheological properties. When exceeding these concentrations, shear thinning behaviour onsets with the rheological properties described by the power law constitutive equation, Eq. 5.11.

$$\tau = k\dot{\gamma}^n \tag{5.11}$$

where τ is shear stress, in Pa and $\dot{\gamma}$ is shear rate, in s^{-1}

With increasing sodium chloride content, the extent of shear thinning behaviour increases which is reflected by a large reduction in the power index, n, to as little as 0.10. The consistency index, k, is additionally seen to increase accordingly from as little as 4.64 x 10^{-3} to 72.1 Pa s^n. This change in rheological parameters is highlighted in the shear stress against shear rate curve for a number of 10 wt% SLES solutions, Figure 5.16a. The optimal

rheological model changes once again to a Carreau model for 15 wt% and 20 wt% SLES solution with an electrolyte concentration in excess of 5.25 wt%, indicating a further rearrangement of the micellar structure. Despite this, the power law model may still be applied with an average correlation coefficient of 0.96. The power law model has been selected as it has been extensively utilised when characterising SLES solutions (Rodgers et al., 2009) with all of the shear rheological parameters presented in Appendix A4.

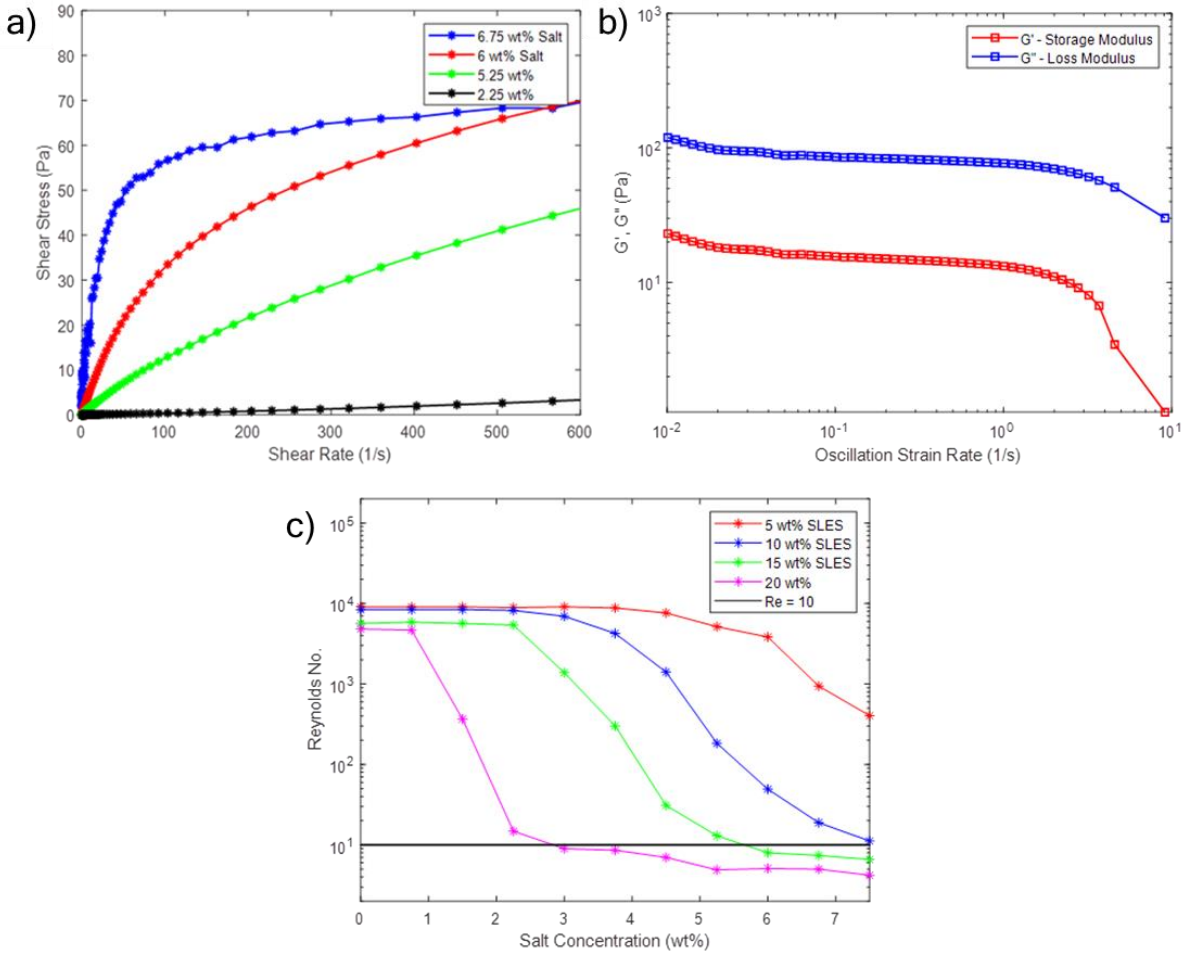

Figure 5.16 Rheological properties of experimental SLES formulations and resultant hydrodynamic conditions: a) shear rheology for 10 wt% SLES solution; b) oscillatory rheology - 10 wt% SLES, 7.5 wt% salt; c) Reynolds number within the stirred vessel

The viscoelastic properties of each fluid were also investigated using an amplitude sweep. For each material, the loss modulus, G'', was found to be greater throughout the entire range of oscillation frequencies indicating fluid-like behaviour in the linear viscoelastic region and a

very weak gel structure. This indicates that worm-like micelles were not formed during this study (Abdel-Rahim et al., 2014) with these viscoelastic properties presented in Figure 5.16b for a 20 wt% SLES solution with a 7.5 wt% electrolytic concentration.

Using this information, the generalised Reynolds number for a power law fluid in a stirred tank, Eq. 5.12 was calculated with the outputted values depicted in Figure 5.16c.

$$Re = \frac{\rho N^{2-n} D^2}{k} \tag{5.12}$$

where Re, is Reynolds number and N is impeller speed in s^{-1}

Aligned with drastic changes in rheological properties, the Reynolds number (Re) is seen to vary within the range of 4.24 – 9106. This represents differing flow regimes with laminar flow for Re < 10, fully turbulent for Re > 20,000 and transitional flow in-between (Paul et al., 2004). Mixing within the laminar and transitional regimes has a different fundamental behaviour and a knowledge of the real-time evolving rheology, provided by EIF, enables an unrivalled opportunity for understanding of both flow regime and scale-up. As a torque meter was not present in the experimental rig, the power number, Po, was estimated from a study conducted by McCabe et al (2001) based upon the calculated Reynolds numbers; this was obtained from a graph relating the power number to the Reynolds number. From this, the power consumption, P, was estimated via Eq. 5.13. Alongside the associated Reynolds numbers, the estimated power numbers are displayed in Appendix A4.

$$P = Po \cdot \rho N^3 D^5 \tag{5.13}$$

The calculated power consumption of the impeller, at a fixed impeller speed of 600 rpm, is seen to vary greatly depending upon the formulation present. When considering a 20 wt% SLES solution, the power consumption is increased by a factor of 12.2 when adjusting the addition of salt from 0.75 wt% to 7.5 wt%. Similarly, for a fixed salt concentration of 7.5 wt%, an increase in SLES concentration from 5 wt% to 20 wt% demonstrates a resultant increase in power consumption by a factor of 8.91. In this instance, a knowledge of the evolving

formulation, brought about by EIF, affords an opportunity to optimise the hydrodynamic conditions within the vessel, continuously optimise the aforementioned large power consumptions and ultimately reduce in-plant operating costs.

The spatial distribution of materials may be simultaneously visualised using computed conductivity pixels and coupled with the rheological parameters of the formulation present within the plane to provide a comprehensive mixing analysis. Example conductivity tomograms are depicted in Figures 5.17a to 5.17c. Prior to the addition of salt, $t < 0$ s, the surfactant-electrolyte solution tomograms are perceived to be well-mixed with low conductivity, indicated by the blue colour. Upon sodium chloride addition, an area of high conductivity is visible in the central, red, region of the lower plane vessel. This indicates poor mixedness with the salt-rich zone settling towards the bottom of this vessel. As a result of the dissolution and blending of this concentrated surfactant-electrolyte solution, the variance between the pixel values decreases until a homogeneous system is once again observed, Figure 5.17c.

The volume averaged conductivity of such tomograms have been extensively utilised to predict mixing times in stirred vessels (Simmons et al., 2009; Rodgers et al., 2011; Ein-Mozzafari, 2017). A coefficient of variance (COV) approach, Eq. 5.14, has been employed to predict mixing time using 12 pointwise measurements; the application of this approach to tomographic images reconstructed using the MSBP algorithm has been validated by Stephenson (2008). The pixels of each tomogram plane were segregated into 6 concentric zones, according to the zone scheme, Figure 5.17d, with the mean conductivity for each zone determined. This zone scheme was selected to determine if pseudo-caverns arise during mixing as a result of the highly shear-thinning nature of the test fluids and the flow regimes present within the vessel. The presence of pseudo-caverns is detrimental to mixing, heat and mass transfer operations with high power requirements for mixing in all regions of the vessel (Adams and Barigou, 2007).

$$COV = \frac{1}{n-1}\sum_{1}^{n}\sqrt{(C_i - C_\infty)^2} \tag{5.14}$$

The COV as a function of time are depicted in Figures 5.17e and 5.17f for the mixing of 5 wt% and 20 wt% SLES solutions, respectively. When interrogating the highest electrolyte concentration, the signal to noise ratio was ±2 % of the final conductivity with the 95 % mixing time, θ_{95}, selected accordingly. Moreover, θ_{95} has been extensively utilised in mixing studies to develop mixing time correlations with the vessel considered 95 % mixed if the logarithmic COV dropped below -2.60. Despite operating at a fixed impeller speed throughout, a general trend is observed with an increase in apparent viscosity of the fluid system gives rise to an increase in mixing time. This is expected due the transitional and laminar nature of the flows present within this study. Consequently, large variations in mixing times are observed, with the mixing time for step addition of 0.75 wt% salt seen to vary between 121.3 s and 1105 s, for a 20 wt% SLES solution. When coupled with the aforementioned power requirements, this represents an increase in dissipated energy of a factor of 74.6. Such increase energy consumption may be optimised based upon the selection of appropriate impeller conditions based upon a knowledge of the evolving structural parameters elucidated from EIF measurements. Furthermore, this 'traditional' EIT analysis can be exploited to identify process end points with EIF simultaneously utilised to characterise the finalised formulation to act as a quality, or feedforward process, control tool.

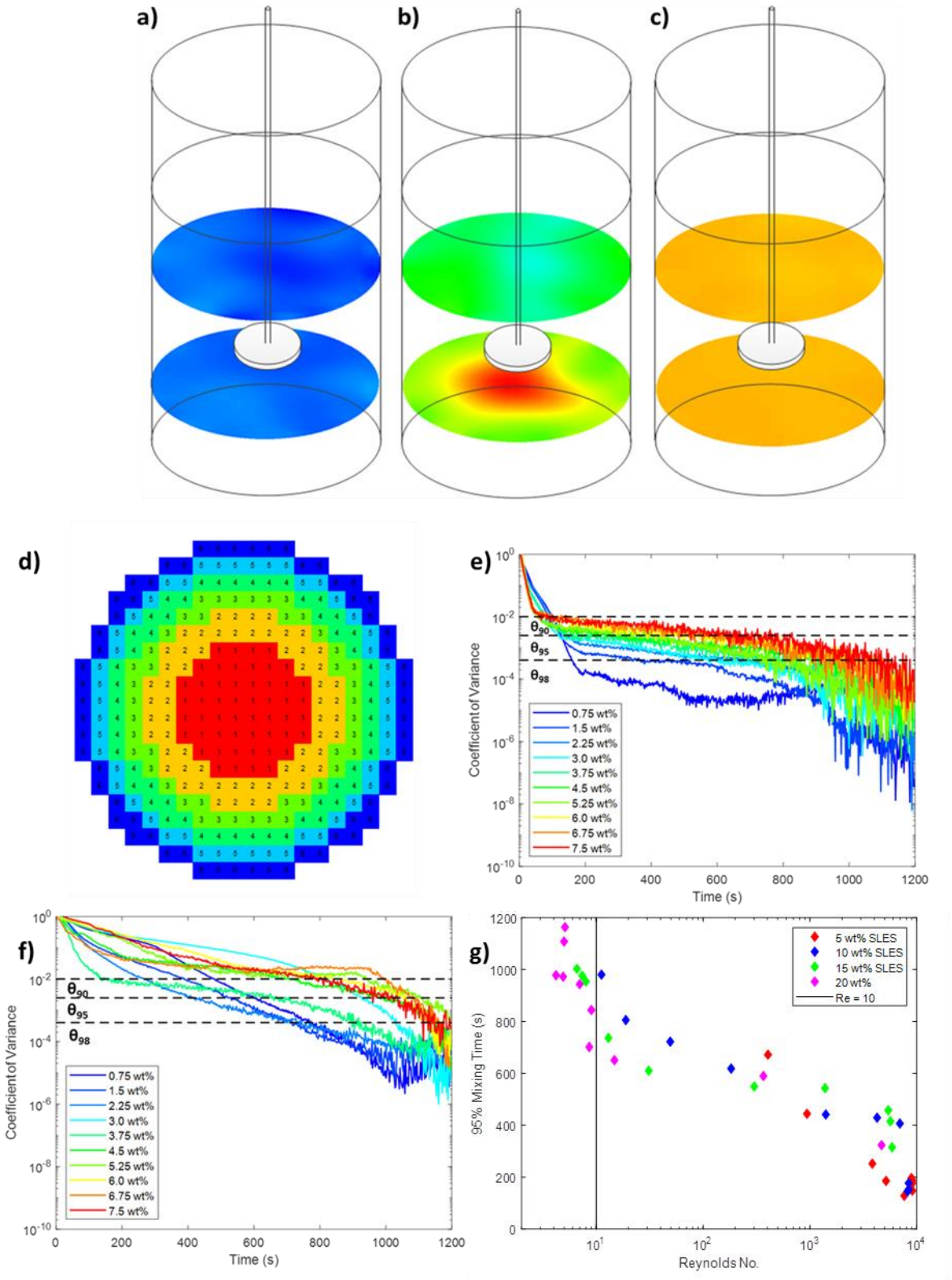

Figure 5.17 Mixing time analysis: a) t < 0 s; b) t = 100 s; c) t = 1200 s; d) 6-ring zone scheme; e) coefficient of variance – 5 wt% SLES with varying salt concentration; f) coefficient of variance with varying salt concentration – 20 wt% SLES; g) overall mixing times

In addition to extracting mixing time, the mixing phenomena may be visualised using the zoned averages. For each plane, the radial mixing behaviour was interrogated using the tomogram electrolyte concentration, Eq. 5.9, and resultant standard deviation of the measured zones. Within the transitional regime, Re > 10, good radial mixing was observed with the concentration within each zone being similar, Figure 5.18a. This is also reflected in the zoned standard deviation (ZSD) with a maximum deviation of 0.076 wt% ascertained during transitional flows. As the rheological properties are altered and the laminar flow regime dominates, the ZSD increases drastically to a maximum of 0.359 wt% indicating poor radial mixing within the laminar flow regime. Figure 5.18c, demonstrates this change in ZSD arises due to a high conductivity region around the impeller axis, indicating a concentrated region of micelles is present within zone 1. Such concentrated regions ensure that both blending and dissolution processes are required with mixing time of the latter not constant with agitation speed for dissolution (Rodgers et al., 2011).

Alongside inferring the likely micelle type within this region of enriched concentration, EIF is capable of determining the stirred tank flow regime to apply the appropriate governing equations to adaptively optimise the impeller conditions for this process and ultimately minimise energy usage. The potential formation of a pseudo-cavern was investigated; however, all averaged zoned conductivities converge ensuring that eventually the tank is radially mixed.

The entire 316 pixels of the tomogram are exploited to visualise the dissolution of the surfactant-rich zone, or agglomeration of surfactants. Pixels with relative conductivity in excess of 10% of the mean were attributed to the surfactant-rich region with its size subsequently determined in two dimensions. The thresholding of the tomogram gives rise to Figures 5.18d, with the yellow region indicating the presence of a micelle agglomerate. This technique is a similar approach adopted by Simmons et al. (2009) who utilised a linear ERT configuration to characterise cavern sizes in a Herschel-Bulkley fluid. Figure 5.18e,

demonstrates an apparent exponential decay in the concentrated micelle region with the dissolution time predicted via this approach.

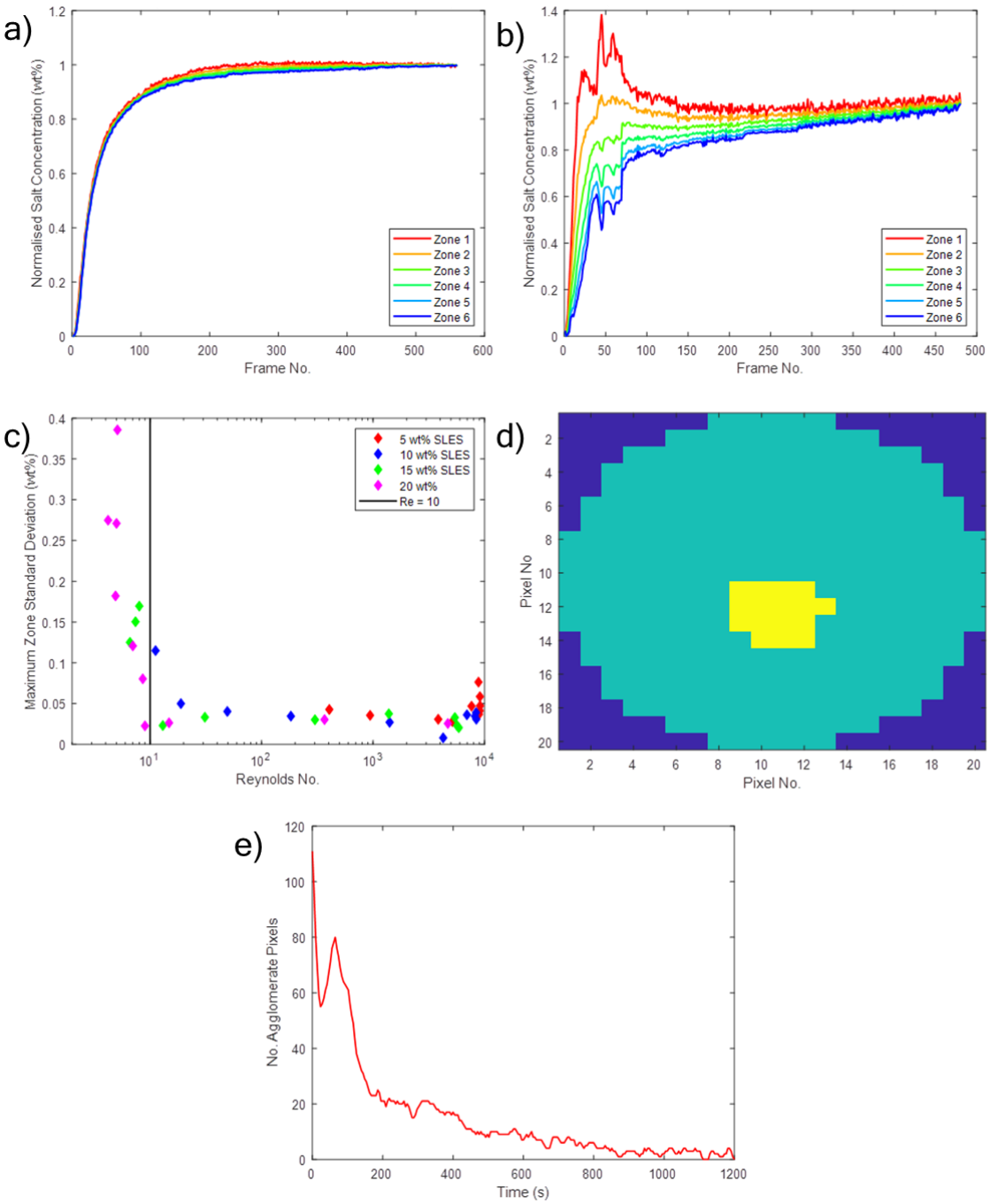

Figure 5.18 Radial mixing analysis: a) 20 wt% SLES, 2.25 wt% NaCl; b) 20 wt% SLES, 7.5 wt% NaCl; c) zoned standard deviation vs. Reynolds number; d) tomogram with threshold applied; e) decay of size of enriched zone

Rodgers et al. (2009) demonstrated that mixing small agglomerates increased the mixing time constant by an order of magnitude. The presence of enriched regions of surfactant mesophases ensure that the dominant mixing mechanism was dissolution with the capability to approximate the enriched region, or agglomerate, size with EIT coupled with knowledge of the formulation composition and structural properties able to provide by EIF to enhance understanding of the mixing processes. This exponential reduction in size with time further supports the high conductivity region arising from the presence of concentrated micelles and not from the presence of a pseudo-cavern.

A similar zoned analysis can be performed to determine the efficiency of axial mixing as the setup contained two interrogating planes located at different heights within the vessel. Employing the six cell ring zone scheme the mean computed conductivity pixels were once again averaged. These averages were compared across two-planes with the use of a parity plot with examples of 20 wt% SLES solutions with 0 wt% and 6.75 wt% salt depicted in Figures 5.19a and 5.19b, respectively. A linear regression to the identity line, $y = x$, was performed with the correlation coefficient utilised as an axial mixing performance indicator. A value of 1 represents good axial mixing with poor axial mixing represent by values closer to 0. The results of this study are depicted in Figure 5.19c, with a similar trend observed to radial mixing. When the mixing is within the laminar regime, poor axial mixing is achieved with EIF providing a capability to recognise this regime based upon evolving formulation properties with the agitation conditions optimised accordingly.

This section demonstrates that EIF can be enhanced further with the simultaneous visualisation of the spatial distribution of components to provide a comprehensive understanding of mixing behaviour within vessels. Consequently, the novel EIF/EIT technique affords new capabilities in the in-situ analysis and characterisation of fluids pertaining to formulated products to enhance process understanding and optimisation.

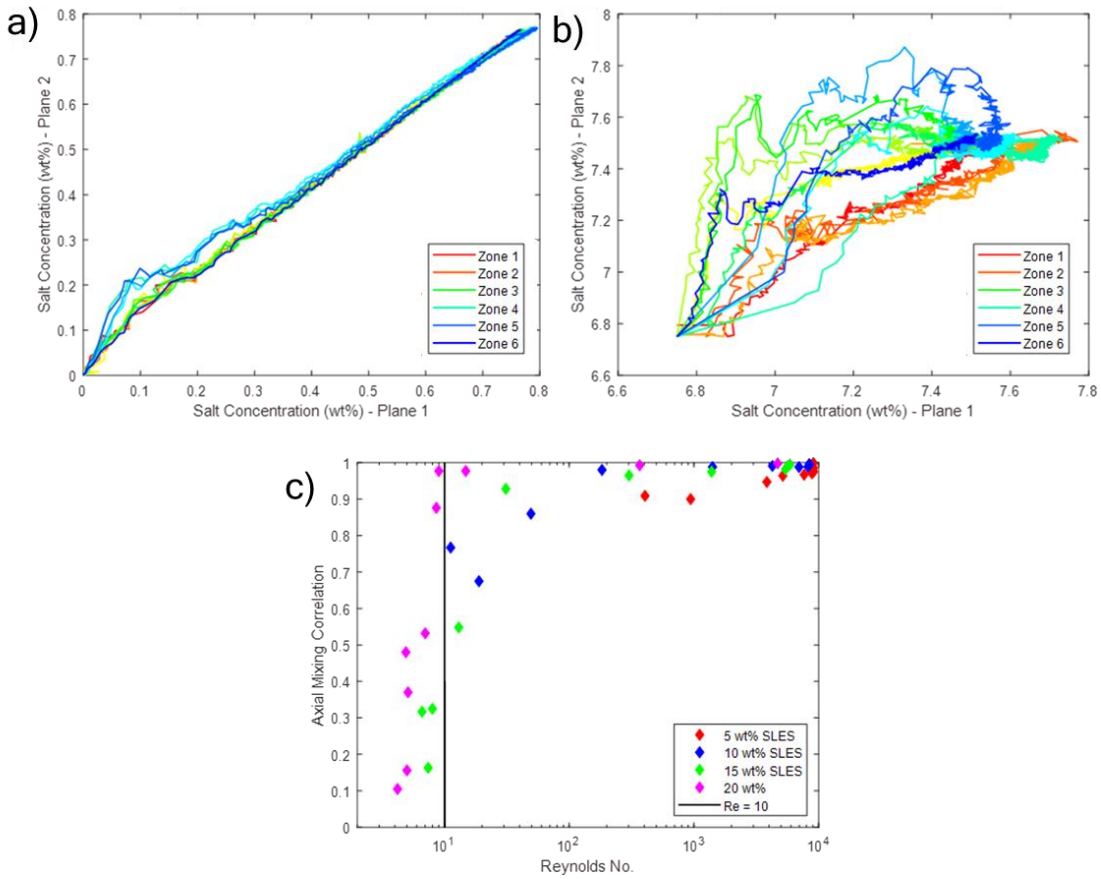

Figure 5.19 Axial Mixing: a) Correlation – 20 wt% SLES/ 0.75 wt% NaCl; b) Correlation – 20 wt% SLES/0.75 wt% NaCl; c) axial mixing correlation vs. Reynolds number

5.4.4 Application of EIF to Linear Measurement Protocol

The application of EIF to the linear measurement protocol has additionally been investigated. This configuration, described in Section 3, has been utilised extensively to study axial mixing behaviour of multi-phase fluids in stirred tanks (Forte et al., 2019; Simmons et al., 2009). An advantage of this setup is its ability to be retrofitted easily into stirred vessels reducing the capital costs and installation requirements for EIF.

5.4.4.1 The Linear Fingerprint

Unlike in circular arrays, low admittivity media does not give rise to a uniform parabolic fingerprint for each measurement cycle. Despite this, a repeatable saw-tooth pattern can be observed, Figure 5.20b, with exception of the first measurement cycle. According to the linear

adjacent measurement protocol, Figure 5.20a, the first current injection is performed across electrodes 1 and 16 with the differential voltage measured at the remaining adjacent pairs. The second cycle utilises electrodes 1 and 2 for the current injection with the outputted phase measurements representative of differential voltage measurements with increasing electrode number.

The repeatable saw-tooth pattern observed can be explained with use of the three-dimensional COMSOL model performed to analyse the in-pipe rheology sensor and the principal of tailored linear arrays, Chapter 3. This model represented an 8 electrode linear probe, situated within a pipe containing a low admittivity fluid, conductivity, 1 mS cm^{-1} and relative permittivity of 80. This sensor consists of an acrylic body with eight rectangular electrodes fabricated from copper; a further two ground electrodes of the same material are included. The excitation signal possessed an amplitude of 15 mA and frequency of 19.2 kHz. A single excitation cycle was performed with the second measurement cycle interrogated.

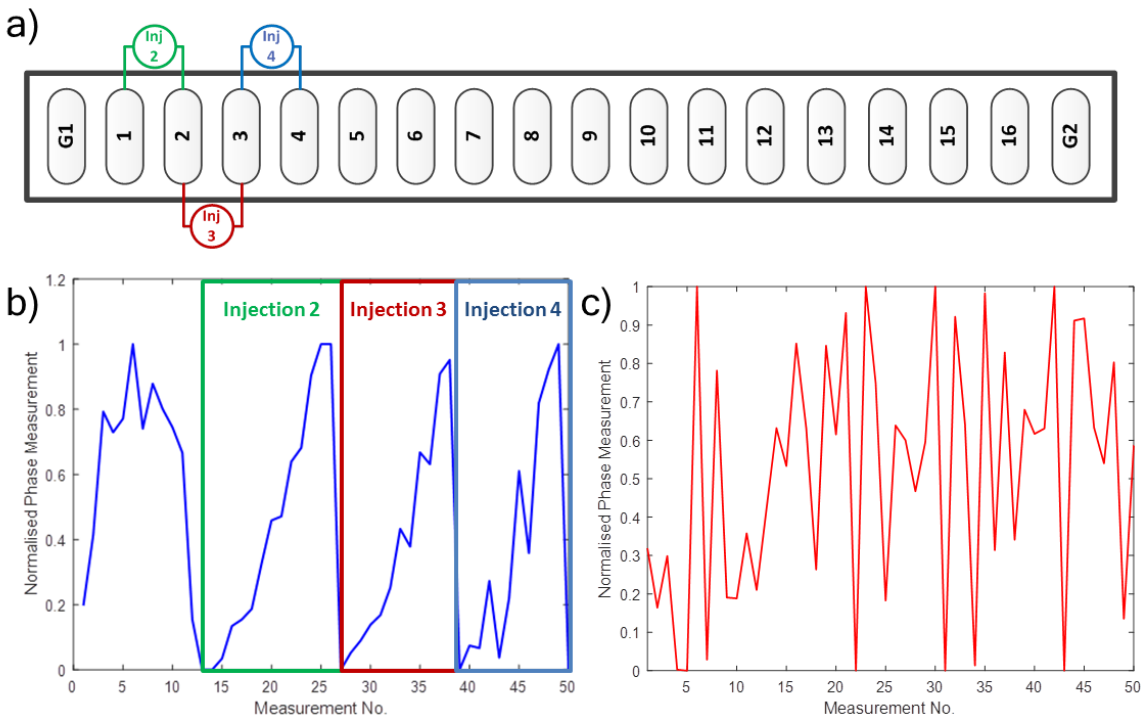

Figure 5.20 The linear Electrical Impedance Fingerprint: a) linear injection protocol; b) low admittivity media; c) high admittivity media

From Figures 3.2c to 3.2e, as the measurement electrodes become further away from the injection electrodes, an increase in the penetration of the electrical current into the fluid in all three dimensions is witnessed. Consequently, the path of the electrical field and hence material interaction is greater for electrodes located further away from the injection electrodes. As the phase is across adjacent pairs in EIF, the magnitude of the difference becomes larger giving rise to a saw-tooth shape for each measurement cycle. This behaviour supports the EIF phenomenon arising due to the confinement of the electric field and the uniform parabolic cycles observed in Figures 5.2 and 5.4.

When the admittivity of the fluid is changed, once again the EIF fingerprint begins to break down into a more disordered structure which has the capability to be identified and related to the key quality parameters of a formulation, Figure 5.20c.

5.4.4.2 Formulation Characterisation using a Linear Probe

To assess the capability of this protocol, a 16-electrode linear probe, with a sensing length of 10 cm, was placed within an unbaffled acrylic vessel to interrogate the working fluids. The setup was analogous to the aforementioned vessel, Section 5.3, with a 3-blade wide-blade hydrofoil utilised to agitate the fluids at a constant speed of 600 rpm. The linear complex protocol was selected alongside an alternating current injection of 30 mA at the optimised frequency of 19.2 kHz using the ITS p2+ system. The optimal neural network architectures for classification, Figure 5.6, and continuous analysis problems, Figure 5.7, were also employed for formulation recognition.

A classification approach was initially taken to quantify the electrolyte concentration within SLES solutions. Despite the variation in the fingerprint shape and protocol, 100 % accuracy was obtained with a minor average CEE of 3.31×10^{-7} across the entire dataset of 10,880 frames. This accuracy is highlighted in the confusion matrix, Figure 5.21a, and analogous to circular protocols which possessed a CEE of 2.93×10^{-7}.

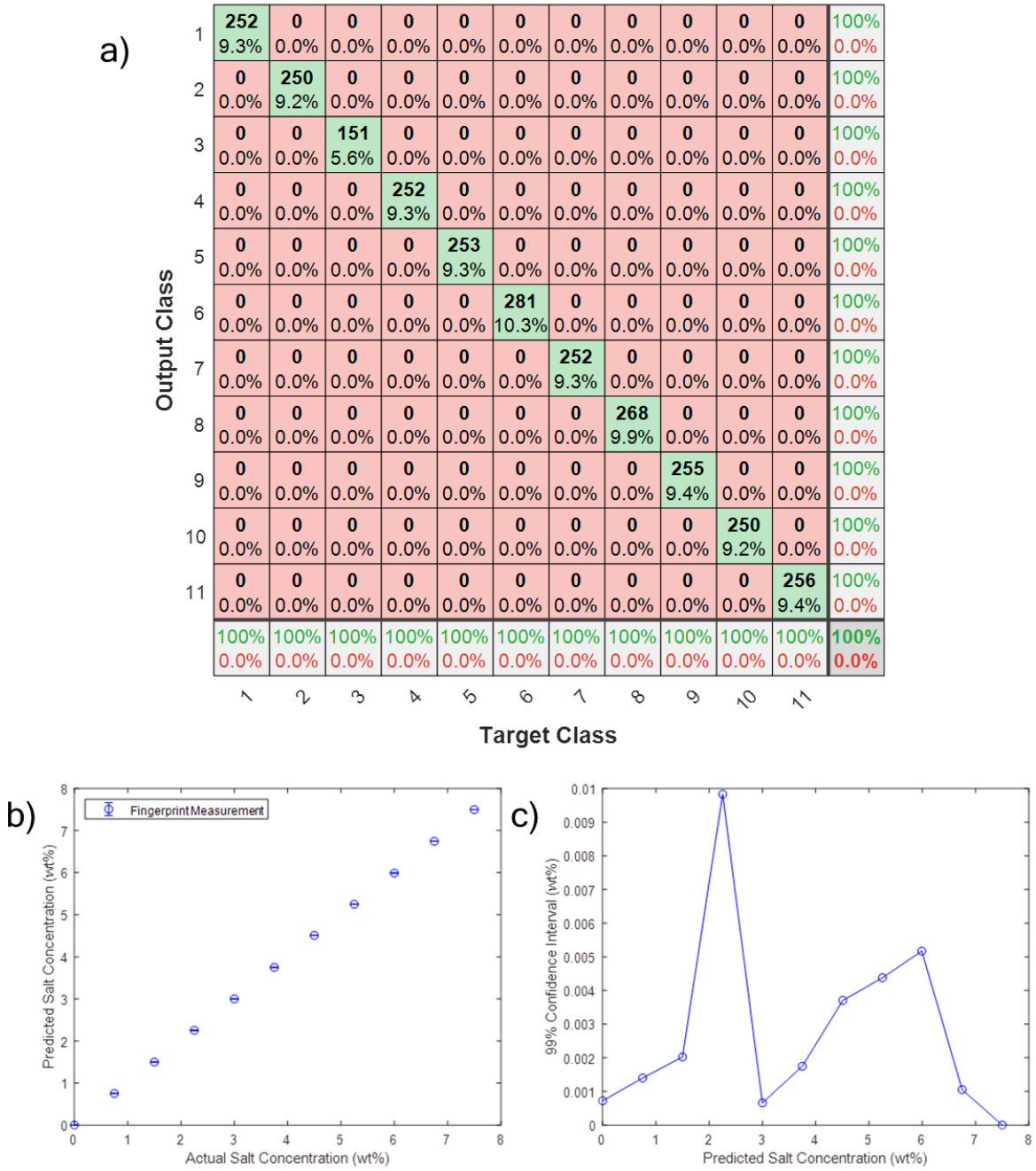

Figure 5.21 The characterisation of 10 wt% SLES formulations using the linear Electrical Impedance Fingerprint: a) salt concentration classification; b) parity plot; c) confidence intervals

The applicability of linear sensors to continuously identify formulations was additionally investigated. From this study, an average MSE of 0.018 wt% was obtained; this performance is improved when compared to the highly accurate circular arrays. The continuous model additionally demonstrated linearity with a linear regression to the measured sodium chloride

concentration yielding gradients of 1.00, 0.99, 1.00 and 1.00 for 5, 10, 15 and 20 wt% surfactant solutions, respectively. The overall parity plot and associated CI_{99} are depicted in Figures 5.21b and 5.22b, with a maximum confidence interval of 0.010 wt% observed. This performance demonstrates the capability of EIF to accurately predict the formulation, and hence key quality attributes of a system using linear EIT sensors. The applicability of EIF is additionally increased as a linear EIT configuration is able to be integrated directly into an existing vessel. Moreover, the axial mixing behaviour and process end point identification within the vessel may be studied simultaneously using the tomographic information, to provide novel in-situ analyses. The tailored linear arrays, exploited in in-pipe and in-vessel rheological measurements, can be additionally employed to target this information to process regions of interest i.e. the near wall region for clean-in-place applications.

5.5 Conclusions

A novel in-situ characterisation technique, Electrical Impedance Fingerprinting (EIF), has been developed which utilises phase information obtained from non-invasive microelectrical tomography sensors. It has been observed within the 104 phase measurements arising from the 16-electrode circular Electrical Impedance Tomography (EIT) protocol, low admittivity produces a uniform parabolic phase shape for each measurement cycle. As the admittivity of the media increases this pattern progressively begins to breakdown until the measurement cycles are no longer discernible. The origin of this phenomenon has been investigated with the changes in the Electrical Impedance Fingerprint arising due to the bulk fluid with the confinement of the electric field attributed to this. The Electrical Impedance Fingerprint behaviour was universal across two independent EIT systems which operate with different measurement protocols increasing the applicability of this technique.

Supervised machine learning techniques were then utilised to determine key quality parameters of formulated fluids based upon recognition of the Electrical Impedance

Fingerprint. 'Traditional' Machine Learning technique and artificial neural networks were explored with the optimal network architecture deemed to be two-layer feedforward neural networks with 40 neurons in the hidden layer. This hidden layer is applicable to both classification and continuous problems with the scaled conjugate gradients and Levenberg-Marquadt algorithms selected as the training algorithm for the respective aforementioned problem types.

This technique was utilised to identify the formulation of forty-four sodium lauryl ether sulphate (SLES) and electrolyte formulations. These were selected due to the relevance of SLES in personal care products, due to its detergency properties. The addition of sodium chloride alters the structural properties of the surfactant system to gives rise to large changes in physical attributes such as: rheological properties, surface tension and solubilisation. Initially, the applicability of EIF to pipe flow was investigated within a flow loop. When the SLES concentration is fixed, the electrolyte concentration was categorised without a single frame being mis-classified. The average cross-entropy error was 3.10×10^{-7} with no overfitting of the algorithm demonstrated. A continuous approach yielded a root-mean squared error (RMSE) of just 0.026 wt%, with linearity demonstrated throughout. This performance demonstrates the capability of EIF to accurately and repeatedly identify the formulation within a pipe for enhancement in quality or process control.

A similar analysis was performed on a 200 mm diameter vessel agitated by a 3-blade hydrofoil impeller, $D = 0.3\ T$, at a constant speed of 600 rpm. When categorising all formulations with a single neural network, an accuracy of 99.96 % was observed. The conductivities of the forty-four formulations were within the range of 11.3 – 43.9 mS cm^{-1} with a number of formulations possessing similar conductivity. The capability to distinguish between materials of similar conductivity with great accuracy highlights the impact of capacitive properties upon the phase measurement and increases the selectivity of the measurement. When adopting a continuous approach the salt concentration can be directly compared to values obtained from the associated conductivity tomogram using Maxwell's

effective media approximation. A linear regression of these two values yielded a correlation coefficient of 0.999, demonstrating the capability of the ANN models to predict non-trained formulations accurately.

The rheological properties of the formulations were additionally investigated using the power law model with the consistency and power indexes found to vary from 4.64 x 10^{-4} – 72.1 Pa s^n and 0.1 – 1, respectively. These evolving rheological properties can be determined from EIF with the resulting impact upon mixing behaviour simultaneously captured using the computed tomography pixels. From this study, blending and dissolution times were extracted alongside size of micelle enriched regions and axial and radial mixing performance as a function of hydrodynamic conditions. This demonstrated the capability of the EIT-EIF technique to offer extended insights into a number of unit operations relating to formulated products.

This technique was then extended to linear sensing configurations with a saw-tooth fingerprint observed for low admittivity media. Once again, the fingerprint was seen to progressively breakdown with an increase in admittivity. Similar performance was to a circular array was ascertained, with a CEE and RMSE of 3.305 x 10^{-7} and 0.018 wt% for categorical and continuous problems, respectively. This extends the in-plant applicability of this technique to a range of configurations with linear arrays able to be retrofitted into existing process equipment, reducing installation requirements and capital costs.

5.5.1 Future Work

Whilst EIF has been demonstrated to effectively recognise in-situ formulations with key quality and structure attributes then inferred, it may be extended to extract further key process information. Future work may be conducted to determine the extent of formulation and process characterisation information able to be provided by EIF during processing i.e. multi-phase flow regime and clean-in-place end points. This work has led to a successful international, Innovate UK, EUREKA grant application titled ‘Artificial Intelligence Tomography Systems’ (112422-650235) to develop EIF further.

5.6 References

Abdel-Rahem, R.A; Reger, M; Hloucha, M; Hoffman, H. (2014). Rheology of Aqueous Solutions Containing SLES, CAPB, and Microemulsion: Influence of Cosurfactant and Salt. *Journal of Dispersion Science and Technology: 3564-3575.*

Adams, L. W; Barigou, M. (2007). CFD analysis of caverns and pseudo-caverns developed during mixing of non-Newtonian fluids. *Chemical Engineering Research and Design: 85, 598 -604.*

Agarwal, C. C. (2018). *Neural Networks and Deep Learning: A Textbook.* Springer: New York.

Bernardes, R; Costelo-Branco, M. (2017). Optical coherence tomography – machine learning. *Acta Ophthalmologica.*

Birgin, E; Martinez, J. M. (2001). A spectral conjugate gradient for unconstrained optimization: *Applied Mathematics for Optimization: 43, 117-128.*

Breiman, L. (1994). *Bagging Predictors.* University of California: California.

Carletti, C; Bikic, S; Montante, G; Pagliante, A. (2018). Mass Transfer in Dilute Solid-Liquid Stirred Tanks. *Industrial and Engineering Chemistry Research.*

Cawley, G. C; Talbot, N. L. C. (2010). On overfitting in model selection and subsequent selection bias in performance evaluation. *Journal of Machine Learning Research: 2079-2107.*

Chawla, N.V; Lazarevic, A; O'Hall, L; Bowyer, K. (2003). SMOTEBoost: Improving prediction of the minority class in boosting. *Proc. Principles Knowledge and Discovery: Databases.*

Chitturi, V; Farrukh, N. (2017). Spatial Resolution in Electrical Impedance Tomography: A Topical Review. *Journal of Electrical Bioimpedance: 8(1), 66.*

Choy, T. C. (2016). *Effective Medium Theory: Principles and Applications: 2nd Ed.* Oxford Science Publications: Oxford.

Evans, D.F; Wennerström, H. (1999). *The Colloidal Domain – Where Physics, Chemistry, Biology and Technology meet.* Wiley-VCH: New York.

Forte, G; Alberini, F; Simmons, M. J. H; Stitt, E. H. (2019). Measuring gas hold-up in gas-liquid/gas-liquid-solid stirred tanks with and electrical resistance tomography linear probe. *American Institute of Chemical Engineering.*

Freund, Y; Schapire, R. (1996). Experiments with a new boosting algorithm. *Proceedings 13th International Conference of Machine Learning, 148-155.*

Goodfellow, I; Bengio, Y; Courville, A. (2016). *Deep Learning.*MIT Press, Massachusetts

Gurney, K. (1997). *An Introduction into Neural Networks.* UCL Press: London.

Hagan, M. T; Demuth, H. B; Beale, M. H; de Jesus, O. (1996). *Neural Network Design: 2nd Ed.*

Hastie, T; Tibshirani, R; Friedman, J. (2008). *Elements of Statistical Learning: Data Mining, Inference and Prediction.* Springer: New York

Hosseini, S; Patel, D; Ein-Mozaffari, F; Mehrvar, M. (2010). Study of Solid-Liquid Mixing in Agitated Tanks through Computational Fluid Dynamics Modeling. *Industry and Engineering Chemical Research: 49, 4426-4435.*

Johansen, R: Østby, T.G; Dupre A; Mylvaganam, S. (2018). Long Short-Term Memory Neural Networks for Flow Regime Identification using ECT. *WCIPT 9: Conf. Proceedings.*

Kazemzadeh, A; Ein-Mozaffari, F; Lohi, A; Pakzad, L. (2016). Effects of the Rheological Properties on the Mixing of Herschel-Bulkley Fluids with Coaxial Mixers: Applications of Tomography, CFD and Response Surface Methodology. *Canadian Journal of Chemical Engineering.*

Li, Y; Yang, W; Xie, C; Huang, S; Wu, Z; Tsamakis, D; Lenn, C. (2013). Gas/oil/water flow measurement by Electrical Capacitance Tomography. *Measurement Science and Technology: 24.*

Lindman, B; Wennerström, H. (1980). Amphiphile aggregation in aqueous solution. *Topics in current chemistry: 87(1), 1980.*

Machin, T.D; Wei, H; Greenwood, R.W; Simmons, M.J.H. (2018). In-pipe Rheology and Mixing Characterisation using Electrical Resistance Sensing. *Chemical Engineering Science: 187, 327-341.*

Marquadt, D. (1963). An algorithm for least squares estimation on non-linear parameters. *SIAM J App Maths*: 11, 431-444.

Mohammed-Saleh, J; Hoyle, B.S. (2002). Determination of multi-component flow process parameters based on electrical capacitance tomography data using artificial neural networks. *Measurement Science and Technology: 13, 1-7.*

Na, W; Jia, J; Yu, X; Faraj, Y; Wang, Q; Meng, Y; Wang, M; Sun, W. (2015). Imaging of gas-liquid annular flows for underbalanced drilling using electrical resistance tomography. *Flow Measurement and Instrumentation: 46B, 319-326.*

Nahvi, M; Holyle, B.S. (2008a). Electrical Impedance Spectroscopy Sensing for Industrial Processes. *Sensors.*

Nahvi, M; Hoyle, B.S; (2008b). Wideband Electrical Impedance Spectroscopy. *Measurement Science and Technology: 19(9).*

Neal, R. (1996). *Bayesian Learning for Neural Networks.* Springer: New York.

O'Brien, R.W. (1986). The high-frequency dielectric dispersion of a colloid. *Journal of Colloid and Interface Science:113(1): 81-93.*

Pagliante, A; Montante, G. (2018). Liquid Mixing Time and Solids Dissolution in Slurry Stirred Tanks. *9th WCIPT: Conf Proceedings.*

Paul, E. L; Atiemo-Obeng, V. A; Kresta, S. M. (2004). *Handbook of Industrial Mixing: Science and Practice*. John Wiley and Sons: New York.

Rashid, T. (2016). *Make your own neural network.* Elsevier: Amsterdam.

Rides, M; Jezek, J; Derham, B; Moore, J; Cerasloi, E; Simler, R; Perez-Ramirez. (2011). Viscosity of concentrated therapeutic protein compositions. *Advanced Drug Delivery Reviews:* 63(13), 1107-1117

Rodgers, T. L. (2009). Mixing and Dissolution Times for a Cowles Disk Agitator in Large-Scale Emulsion Preparation. *Industrial Engineering and Chemistry Research: 48, 6859 - 6868.*

Rosell, J; Riu, P. (1992). Common-mode feedback in electrical impedance tomography. *Clinical Physics and Physiological Measurements: 13(1).*

Ru, Y; Pradeep, C; Mylvaganam, S. (2011). Neural Networks in electrical capacitance tomography (ECT) - based detection. *Measurement Science and Technology: 22(10).*

Seiffert, C; Khoshggoftaar, T.M. (2010). RUSBoost: A Hybrid Approach to Alleviating Class Imbalance. *IEEE Transactions on Systems, Man and Cybernetics:* 40 (1), 185 – 196.

Stephenson, D. R. (2008). *Choices and Implications in Three-Dimensional Electrical Impedance Tomography.* EngD Thesis, University of Manchester.

Voggt, K; Jiang, H; Beaucage, G; Weaver, M. (2017). Free Energy of Scission for Sodium Laureth-1-Sulfate Wormlike Micelles.

Wang, A; Marashdeh, Q; Motil, B; Fan, L. (2014). Electrical Capacitance Volume Tomography for imaging of pulsating flows in trickle beds. *Chemical Engineering Science: 119, 77-87.*

Wang, M. (2004). *EIT Data Processing System and Method.* Patent No: WO2005022138A1

Wang, M. (2015). Industrial Tomography: Elsevier Science, Amsterdam.

Wang, M; Yin, W. (2001). *Electrical Impedance Tomography.* Patent No: US20040130338A1

Yildiz, O. C; Irsoy, O; Alpaydin, E. (2016). *Machine Learning for Health Informatics: Bagging Soft Decision Trees.* Springer: New York.

Chapter 6

The Characterisation of Kaolin/Sand Slurries for the optimisation of a non-nuclear density measurement

6.1 Introduction

In the previous chapter, formulations of colloidal, surfactant solutions of sodium lauryl ether sulphate (SLES) were extensively characterised based upon their electrical properties. This chapter extends the characterisation of fluid systems, using Electrical Impedance Tomography, to multi-phase, solid-liquid systems with a particular focus upon composition identification and ultimately slurry density.

Hydraulic conveying systems often rely upon the knowledge of density and flow parameters for the optimisation of their performance. These parameters ensure that sufficient mobile solids are being conveyed, pipeline blockage has not occurred and production targets are being achieved. Such continuous slurry density measurements typically exploit the attenuation of gamma ray photons; however, the use of nuclear sources poses complex safety, operational and economic concerns (Batey, 2012). These arise throughout the entire instrument lifetime from initial transport to disposal of the radioactive waste with significant costs incurred. Thus, there is a commercial demand to develop a non-nuclear alternative to the density measurement with numerous studies employing various sensing media,

including: ultrasound, microwave and Coriolis meters (Wei et al., 2016). Despite such attempts, these techniques were found to be unsuitable for applications in industrial pipelines due to material abrasiveness, process requirements and pipe diameter restrictions (Batey, 2012).

Electrical Resistance Tomography (ERT) provides an in-line, non-nuclear alternative to the density measurement via the extraction of computed conductivity pixels and subsequent application of effective media approximations, including the Maxwell-Garnett and Bruggeman equations (Wei et al., 2016). These effective media approximations, highlighted in Eq. 6.1 and Eq. 6.2, respectively, convert the conductivity distribution of macroscopically inhomogeneous media into the volume fraction of the dispersed phase (Markel, 2016). The Maxwell-Garnett equation was also utilised in Chapter 5 to extract the salt concentration within SLES formulations.

$$\alpha = \frac{2\sigma_c + \sigma_d - 2\sigma_m - \left(\frac{\sigma_m \sigma_d}{\sigma_c}\right)}{\sigma_m - \left(\frac{\sigma_d \sigma_m}{\sigma_c}\right) + 2(\sigma_c - \sigma_d)} \tag{6.1}$$

where α is the dispersed phase volume fraction, and σ_c, σ_d and σ_m are the continuous phase, dispersed phase and slurry conductivities, respectively.

$$\alpha = 1 - \left(\frac{\sigma_m - \sigma_d}{\sigma_c - \sigma_d}\right) \sqrt[3]{\frac{\sigma_c}{\sigma_m}} \tag{6.2}$$

ERT has been exploited extensively to monitor slurry flows within process equipment reinforcing the applicability of this technique to slurry systems (Faraj and Wang, 2012; Xu et al., 2009; Kotze et al., 2019). These studies described the visualisation of the distribution of solids within process equipment which can also be exploited within hydraulic conveying to identify the flow regime present. This additional information can help to inform process decisions and provide enhancements in pumping efficiency (Wei et al., 2018).

Despite ERT densitometers being employed successfully in marine installations across the world (Wei et al., 2018), there is still a requirement for a fundamental understanding of electrical interactions between dredged solids and ERT for slurries conveyed with a continuous phase of relatively low conductivity (< 20 mS cm^{-1}). These interactions are most prevalent in the transport of clays and clay mixtures due to their complex surface properties (Barany et al., 2015).

Clays are a broad class of aluminosilicates which contain various proportions of tetrahedral and octahedral layer structures held together by hydrogen bonding (Ndlovu et al., 2014). The physio-chemical properties of clays vary greatly enabling segregation into four major classifications: kaolinites, smectites, illites and vermiculites (Barany et al., 2015). Near the clay-water interface, excess countercharge ions accumulate to ensure electrical neutrality via ionisation, isomorphic substitution and ionic dissolution (Bergaya and Lagaly, 2013). Such charges often occur at the basal surfaces or near edges to give rise to non-uniform ionic conduction through a formed electrical double layer; this behaviour is known as surface conduction (Schoonheydt and Johnson, 2013). As clays form the basis of most marine soils, an understanding of the impact of surface conduction upon both ERT and Electrical Impedance Tomography (EIT) densitometry is vital for the optimisation of hydraulic transport solutions. The theory of surface conduction within the double layer was initially derived by Bikermann (1933) who described the behaviour of ions at an interface, Eq. 6.3; this behaviour may also be quantified by the Dukhin number (Lyklema, 1998).

$$K^{\sigma} = \frac{4F^2Cz^2D\left(1+\frac{3m}{z^2}\right)}{RT\kappa}\left(\cosh\left(\frac{zF\zeta}{2RT}\right)-1\right) \tag{6.3}$$

where K^{σ} is surface conduction; F is the Faraday constant, C mol^{-1}; T is absolute temperature, in K; R is the universal gas constant, in J mol^{-1} K^{-1}; C is the ionic concentration in the bulk fluid, in M; z is the ion valency; D is the diffusion coefficient, in m^2 s^{-1}, ζ is the electrokinetic potential, in V, and m is a parameter which characterises the contribution of electro-osmosis to the motion of ions within the double layer, as described in Eq. 6.4.

$$m = \frac{2\varepsilon_0 \epsilon_m R^2 T^2}{3\mu_c F^2 D} \tag{6.4}$$

where ε_0 and ε_m are the dielectric permittivity of free space and the continuous phase, respectively, in F m^{-1}, μ_c is the aqueous phase viscosity, in Pa s.

As can be seen from Eq. 6.3, surface conduction is a complex phenomenon which cannot be characterised by a single measurement and dependent upon both continuous and dispersed phase properties. The contribution of surface conduction is predominantly dictated by the ionic behaviour of the continuous phase and the slurry zeta potential. Yukselen and Kaya (2003) demonstrated that the zeta potential of aqueous kaolin slurries becomes increasingly negative with decreasing pH of the continuous phase. It is therefore important to study the impact of both pH and ionic concentration of the continuous phase upon this non-nuclear density measurement. The magnitude of surface conductivity can be simplified to a dependence upon the surface conduction and specific surface area of a mineral aligned with the electrical field. Consequently, the fine-grained nature of clays further heightens the impact of this phenomenon (Au and Leong, 2016).

Kaolins form some of the most common clays within the earth's crust and are commercially important commodities. Accordingly, kaolins have been studied extensively within literature (Mitchell and Soga, 2005) with a number of studies performed to quantify their electrical behaviour (Choo and Burns, 2014; Leroy and Revil, 2004; Oh et al., 2014; Cruz et al., 2005). Choo et al. (2016) investigated the effect of pore water conductivity and volume fraction of kaolinite consolidates and slurries upon surface conductance using a single-frequency four electrode cell. This study developed a semi-empirical relationship between conductivity at 10 kHz, similar to Archie's equation, which is unsuitable for use within densitometry (Cardoso and Diaz, 2017). However, from this a generalised relationship between the surface conductivity, continuous phase conductivity, σ_c and solids mass fraction, X, was able to be derived, Eq. 6.5.

$$\frac{K^{\sigma}}{K_c} \alpha \frac{1-X}{X} \cdot \frac{1}{\sigma_c} \tag{6.5}$$

where K_c is continuous phase conduction

Whilst this equation is simplified greatly, this highlights that the contribution of surface conductivity is increased with solids fraction and is inversely proportional to continuous phase conductivity. This reinforces the prior success of ERT densitometry in high conductivity continuous phase applications such as marine dredging due to the negligible impact provided by surface properties. However, a greater understanding of surface phenomena is required to ensure ERT densitometry is applicable to low conductivity continuous phases.

Blewett et al. (2003) stipulated that any non-magnetic material may be specified by the frequency-dependent parameters of dielectric constant and conductivity with the admittivity, or complex conductivity, able to be related to surface conductivity. Consequently, the electrical properties of kaolins were investigated using Electrical Impedance Spectroscopy (EIS) to gain an understanding of surface behaviour within the low frequency regime, 20 Hz – 2 MHz (Zhao et al., 2012; Zhao et al., 2011; Arroyo et al., 2000). These frequencies were selected, as typical EIT interrogating currents lay within this frequency range. When the interrogation frequencies are in excess of 10 kHz, the bulk of the solids are probed with an alternating current able to provide insight into particle mechanistic effects. In clay-water systems, the particle and counter-ions move in opposing directions to the propagating electrical field giving rise to a fluctuation in electrical current which acts as an alternating dipole (O'Brien, 1986). At such frequencies a phase lag exists between the particle and ionic layer movement (O'Konski, 1960). This frequency-dependent response may be captured using EIS to characterise the surface behaviour of clay systems.

In this study, the complex electrical properties, both capacitive and resistive, of kaolin slurries will be investigated using EIS. The knowledge obtained is then applied to experimental EIT data with the focus of optimising the non-nuclear density measurement in complex fluids. This study is repeated for multi-component kaolin/sand slurries as the conveyed material is

typically unknown. As the electrical properties of such slurries are known to be dependent upon both continuous and dispersed phase properties, the following in-line measurement challenges are addressed: impact of surface phenomena upon electrical properties; suitability of conventional effective media approximations to extract volumetric concentration; characterisation of the continuous phase properties and identification of the dispersed phase.

6.2 Methodology

6.2.1 Materials

Within aqueous-based hydraulic transport applications, the continuous phase properties are known to vary both in conductivity and pH within the ranges of 0.1 - 70 mS cm^{-1} and 5.5 – 8.5, respectively (Wright and Colling, 1995). As can be seen from Eq. 6.5, the surface phenomena are inversely proportional to the conductivity of the continuous phase, hence to maximise surface contributions the aqueous conductivity was reduced to 0.1 – 10 mS cm^{-1}. To create such continuous phases, ammonium acetate, supplied by Sigma-Aldrich, UK, was utilised to adjust the conductivity of de-ionised water, supplied by Hexal Chemicals Ltd, UK. Ammonium acetate was selected as it alters the ionic concentration without changing the pH and the acetate co-ions at the particle-particle interface prevent competition between negatively charged ions. Moreover, the ion valency, of one, is identical to sodium chloride, the most common electrolyte found in hydraulic transport applications (Wright and Colling, 1995). The pH was adjusted via the addition of either sodium hydroxide or glacial acetic acid, both supplied by Sigma-Aldrich, UK, to reduce and increase the pH, respectively. To ensure that the finalised conductivity and pH were as desired handheld HANNA conductivity and pH probes were utilised.

Varying concentrations of Kaolin SUPREME^{TM}, supplied by Imerys UK, were added to these aqueous solutions to formulate the experimental clay slurries. This kaolin was selected due to its especially platy nature (Imerys, 2018), resulting in a high surface area and ultimately

maximising the contribution of surface phenomena. Sand was soaked in de-ionised water for 24 hours to remove precipitated electrolytes and subsequently added to the aqueous solutions to form either sand or multi-component slurries. The Taguchi design of experiments technique was employed to orthogonally alias the impacting factors with the finalised design parameters displayed in Table 6.1 (Jones and Goos, 2011).

Table 6.1 Experimental Parameters

Slurry Parameter	Experimental Values
Aqueous Conductivity (mS cm^{-1})	0.15, 0.5, 1, 2, 5, 10
Dispersed Phase Concentration (wt%)	0, 5, 10, 20, 25, 30
Dispersed Phase Composition (wt%)	0, 20, 25, 33, 50, 100 (both kaolin and sand)
pH	5.5, 7, 8.5

6.2.2 Hardware Setup

To assess the complex electrical properties of such slurries, both EIT and EIS measurements were arranged in series within a 25.4 mm pipeline setup, Figure 6.1. The bespoke EIS arrangement consisted of two annular, stainless steel electrodes which were employed for signal injection and measurement; a square common ground electrode was also located adjacent to the annular electrodes. This electrode array was connected to a Keysight E4980A precision digital LCR meter with a resistor and capacitor in parallel equivalent circuit selected. The impedance of this equivalent circuit can be represented by Eq. 6.6, which is separated into its real and imaginary components to represents resistance and reactance, respectively.

$$Z = \frac{R}{1 + \omega^2 R^2 C^2} + \left(j \cdot \frac{\omega C R^2}{1 + \omega^2 R^2 C^2} \right) \tag{6.6}$$

where Z is impedance, in Ohms, R is resistance, in Ohms, ω is angular frequency in Hz, C is capacitance, in F, and j is the imaginary unit.

To capture frequency dependent behaviour, a logarithmic frequency ramp was applied across the range of 20 Hz – 2 MHz with 40 points per decade. A 1 V potential was also applied in an attempt to minimise electrolysing and polarising effects.

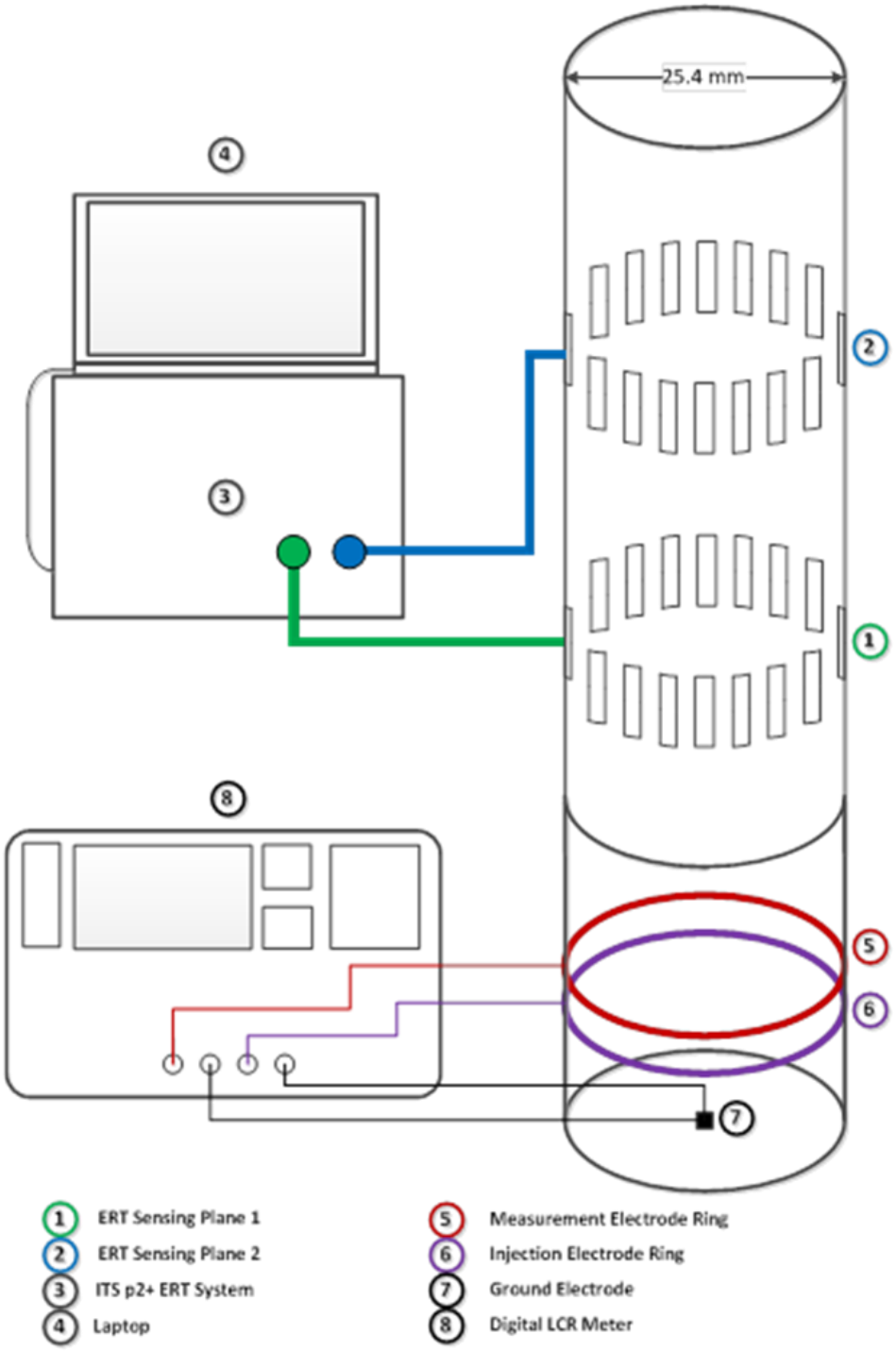

Figure 6.1 Electrical Impedance Tomography and Electrical Impedance Spectroscopy sensing setup

In series, a dual-plane, 16-electrode EIT sensor was connected to perform the densitometry analysis using the adjacent EIT measurement protocol described in Chapter 2. These arrays were connected to the ITS p2+ instrument with the setup identical to that described in the previous chapter, with the exception of a 15 mA current injection and associated current source setting. The current source, 1.5 – 15 mA, was selected to act as a compromise between the current source purity and to maximise the magnitude of outputted voltages based upon knowledge of the continuous phase ionic concentration. The capture of appropriate response voltages ensure that the integrity of the reconstructed tomographic data is preserved. A frequency optimisation step was additionally performed prior to testing with the optimal operating current injection frequency selected upon the criteria of temporal and spatial resolution and measurement stability. From this study, the optimised interrogation frequency range was observed to lie between 2.4 and 19.2 kHz for the ITS p2+ instrument. The latter frequency was selected for all EIT experiments due to its increased stability to complex measurements.

For each experimental condition described in Table 6.1, 250 frames of EIT data were captured to ensure repeatability of the real and imaginary voltage measurements. These voltage measurements were exported to MATLAB where the modified sensitivity back projection (MSBP) reconstruction algorithm was employed to reconstruct the absolute real and imaginary voltage measurements individually. The absolute values of the raw imaginary tomogram voltages were selected as the measured phase, and accordingly imaginary voltages, are typically negative and thus are not amenable to the robust MSBP reconstruction algorithm. A novel phase tomogram was additionally developed by the pixel-wise division of the imaginary and real tomograms, to gain an insight into the complex electrical behaviour. Including the modulus tomogram, extensive analyses of data obtained from both EIS and EIT were performed in MATLAB and JMP software, developed by SAS Institute.

6.2.3 Experimental Conditions

Measurements were performed under both agitated and pipe flow scenarios. In the former, end caps were attached to the flanges at one end with the test materials added; this consisted of 70 mL aliquots of the continuous phase solutions and solids in their specified concentrations. This sensor was aligned vertically with the solids suspended using a magnetic stirrer at a fixed rotational speed. Due to the small particle size, kaolin was easily suspended; however, to ensure the effective suspension of sand and sand-kaolin mixtures the just suspended criterion was observed (Zweitering, 1958). The EIS and EIT interrogation zones were equidistant from each end cap with the sensor configuration inverted to ensure the solids are measured at the same cloud height.

Pipeline experiments were additionally performed within a simple recirculating flow loop, in which a 7.5 L acrylic vessel, *T = 21 cm*, a peristaltic pump, supplied by Watson-Marlow, UK, and the aforementioned sensing setup were connected in series. Upon loading into the vessel, a four-blade down-pumping pitched blade turbine, *D = 0.3T,* was utilised to disperse the solids within the vessel. The clearance of this impeller from the bottom of the vessel, C, was additionally *C = 0.3T*. The Zwietering just suspended impeller speed, N_{js}, (Zwietering, 1958) was calculated for this setup, using Eq. 6.6, and implemented with the criterion visualised to validate this (Ayranci and Kresta, 2014).

$$N_{js} = S\left(\frac{g(\rho_d - \rho_c)}{\rho_c}\right)^{0.45} {d_p}^{0.2} X^{0.13} \left(\frac{\rho_d}{\mu_c}\right)^{0.1} D^{-0.85} \tag{6.6}$$

where S is a shape factor, X, g is the acceleration due to gravity, 9.81 m s^{-2}, ρ_c and ρ_d are the continuous phase and particle densities, in kg m^{-3}, respectively, d_p is mean particle size diameter, in m and μ_c is the continuous phase viscosity, in Pa s.

The suspended slurries are then circulated with the EIS-EIT sensor oriented vertically to minimise the number of flow regimes present, increase dispersion and reflect the operating conditions in which traditional nuclear density meters are installed (Golgoun et al., 2016).

Once steady state had been reached, the aforementioned EIS and EIT measurements were performed for each experimental condition.

6.3 Electrical Impedance Spectroscopy – Electrical Properties of Kaolin Slurries

6.3.1 Electrical Impedance Tomography Frequency Range: 2.4 kHz – 20 kHz

Electrical Impedance Spectroscopy measurements were performed to characterise the electrical behaviour of kaolin slurries within the typical EIT frequency range, 2.4 - 20 kHz. This information can then be directly related to EIT and utilised to optimise non-nuclear densitometry. Due to the complex nature of surface phenomena, kaolin slurries are initially investigated alone.

6.3.1.1 Conductance

The reciprocal of the resistive component of impedance is known as conductance; this is proportional to conductivity for a fixed electrode setup. As ERT monitors changes in relative conductivity, the relative changes in the EIS measurement are explored within this section. For all of the experimental kaolin formulations, the changes in slurry conductivity relative to the continuous phase are captured within Figure 6.2; this is inclusive of variations in pH and selected injection frequencies of 4.74 kHz, 9.46 kHz and 18.8 kHz, to mirror those exploited within ERT measurements. At such frequencies, only minor variations in the resistive properties are observed with a direct comparison demonstrating an average root mean squared error (RMSE) of 0.0098 and the mean relative changes equating to 1.011. The frequency independence of resistive properties across the optimised interrogation range ensures that the application of multi-frequency ERT measurements will yield little further information.

Whilst it appears that the resistive properties are independent of frequency, such properties vary greatly with the ionic concentration of the continuous phase with the kaolin slurries able to be segregated into three regimes:

- Conductive kaolin (σ_c < 0.5 mS cm^{-1})
- Ambivalent Region (0.5 ≤ σ_c <1 mS cm^{-1})
- Low conductivity kaolin (σ_c > 1 mS cm^{-1})

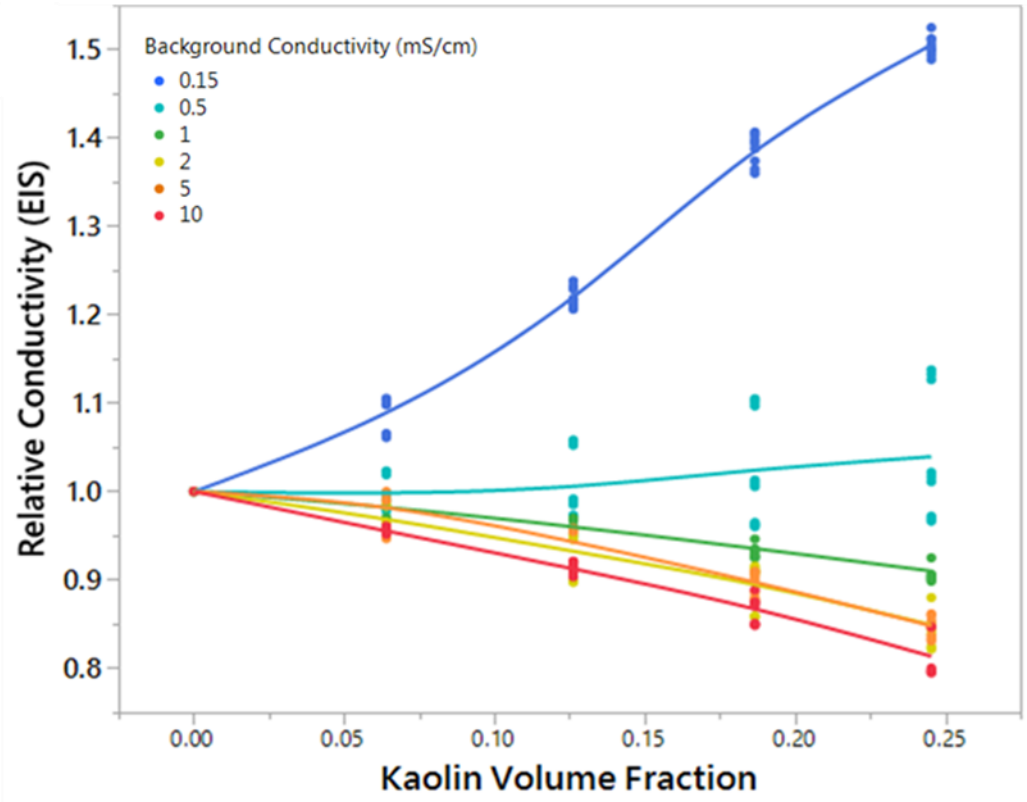

Figure 6.2 Relative changes in conductivity with kaolin volume fraction within the ERT frequency range

When the continuous phase conductivity is below 0.5 mS cm^{-1}, kaolin acts as a conductive solid which possesses a large contribution of surface conductivity; this is reflective of the literature and highlighted within Eq. 6.5. Employing the Akaike Information Criterion (AIC), the change in conductive properties with volume fraction of solids can be best described using an

exponential fitting with an exponent, P, of 1.73; this fitting yields a correlation coefficient of 0.991. Under the null-hypothesis, the p-value associated with a two-tailed test was less than 0.001 for the exponent, P, indicating that volume fraction of kaolin has a high statistical significance upon the resistive properties. This exponential relationship mirrors work conducted by Choo et al. (2016a) who utilised a semi-empirical modified, Archie's equation, to describe the change in conductivity with kaolin concentration, providing initial validity to the performed experiments. Archie's equation is a two parameter exponential function which relates conductivity to porosity for use within kaolin consolidates. This has been modified for use in densitometry with volumetric concentration employed to simplify the equation to one able to be described by a single parameter, Eq. 6.7. This exponential relationship is depicted in Figure 6.3a for a continuous phase with a pH of 7.

$$\frac{\sigma_m}{\sigma_c} = e^{\alpha P} \tag{6.7}$$

This relationship can be utilised to assess the impact that the associated increase in surface contributions, with increased kaolin concentration, have upon the density measurement. The Maxwell-Garnett and Bruggeman effective media approximations, see Eqs. 6.1 and 6.2, apply a single value to describe the resistive behaviour of the discrete phase. To assess the suitability of these approximations to evaluate the solids volume fraction when surface contributions are prevalent, an analysis was performed to optimise the relative discrete phase conductivity, σ_d. The Maxwell-Garnett equation may be re-arranged to make σ_d the subject of the equation, Eq. 6.8, with the known inputs then able to evaluate this equation. In each case the continuous phase conductivity was fixed to one to extract a relative discrete phase conductivity.

$$\sigma_d = \frac{\alpha\sigma_m + 2\sigma_c(\alpha - 1) + 2\sigma_m}{1 + \frac{\sigma_m}{\sigma_c}(\alpha - 1) + 2\alpha} \tag{6.8}$$

Utilising the exponential relationship, the optimal dispersed phase conductivity was calculated up to 35 vol%, the limiting solids concentration at which the Maxwell-Garnett

equation is applicable to EIT systems (Markel, 2016). It must be acknowledged, that this analysis was repeated for the Bruggeman approximation; however, this is not presented here as negligible differences were observed between the two models. This is expected, as the output of both these selected effective media approximations were similar when the volumetric solids concentration is below 35 vol% (Giordano, 2002).

From this analysis, at low kaolin content, 0.5 wt%, a relative discrete phase conductivity (σ_d) was found to be 5.101; however, an increase in kaolin concentration to 35 wt% sees the optimal σ_d increase to 5.904. This yields a 15.75 % increase in kaolin conductivity which is attributed to the surface phenomena of clay structures. Such changes are depicted in Figure 6.3b with the outcomes also supported in a study by Klein and Santamarina (2013) who demonstrated an increase in surface conductivity with the addition of kaolin as a result of a large increase in the total surface area.

As mentioned previously, only a single value of the σ_d is required as an input for the ERT density measurement to ensure that unique volumetric concentrations are achieved. From the previous study, the optimised σ_d values can be inputted back into the original Maxwell-Garnett equation, Eq. 6.1, across the entire solids loading to assess the associated error in outputted density. Derived from a mass balance, the slurry density was then calculated with the density of kaolin selected as 2,650 kg m^{-3} (Imerys, 2017). To perform this analysis, the minimum, maximum and optimised values of σ_d were interrogated with the associated errors depicted in Figures 6.3c and 6.3d. When selecting the minimum value of σ_d, which neglects the increase in surface conductivity with kaolin concentration, a root mean squared error (RMSE) of 16 kg m^{-3} was observed across the entire solids loading range. The largest error exists at the highest solids content with an overestimation of 43 kg m^{-3}, equating to just 2.72 % of the actual density. Whilst this error is low, the high cost of dredging requires a density sensor to have high accuracy within ± 1 % across the entire measurement range (Batey, 2012); this ensures that neglecting surface conductivity results in a measurement with insufficient resolution.

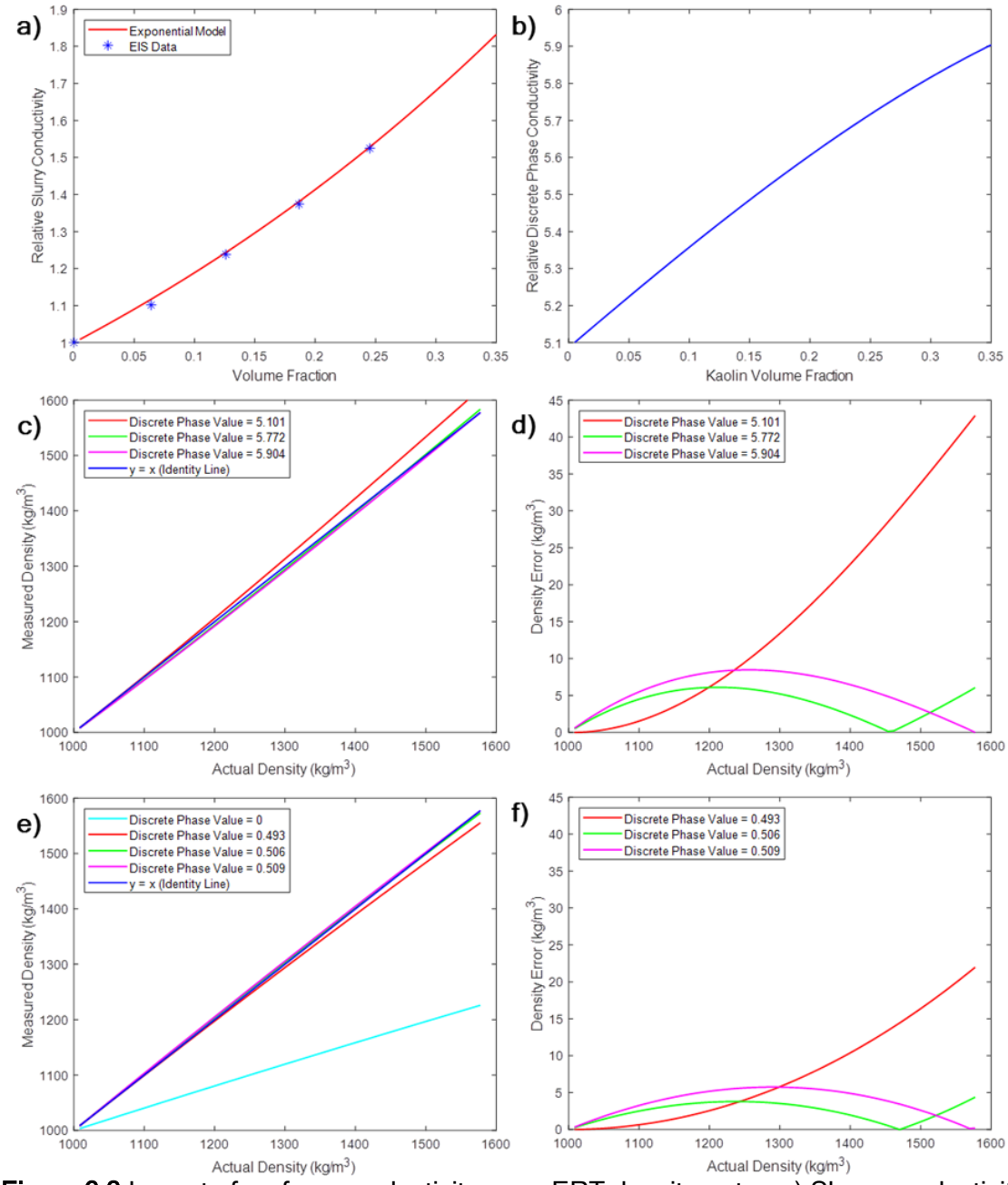

Figure 6.3 Impact of surface conductivity upon ERT densitometry: a) Slurry conductivity - 0.15 mS cm^{-1}, pH 7; b) Kaolin Conductivity - 0.15 mS cm^{-1}, pH 7; c) Density - 0.15 mS cm^{-1}, pH 7; d) Density error - 0.15 mS cm^{-1}, pH 7; e) Density - 2 mS cm^{-1}, pH 7; f) Density error - 2 mS cm^{-1}, pH 7

However, the RMSE can be reduced by a factor of three to 5.6 kg m^{-3} with the maximum error also greatly reduced to 8.5 kg m^{-3} when the maximum σ_d is selected and accordingly the maximum contribution of surface phenomena is considered. Whilst, this gives rise to an underestimation of 0.57 kg m^{-3} at low kaolin contents which equates 7.14 % of the

measurement, this is considered minimal as typical operation utilises the absolute error in the total slurry density. By employing a trial and error approach, the optimal σ_d was found to be 5.772 with the RMSE concurrently able to be minimised to just 3.8 kg m^{-3}; this is considered to be within the desired experimental error of in-line densitometry.

Despite the conductive kaolin regime observing the greatest contributions to surface conductivities, if careful consideration is taken by selecting an appropriate discrete phase input, the impact of the surface conductivities of clays can be practically negated with traditional analysis algorithms implemented. It must be acknowledged that these experiments are performed upon the clay and not the clay minerals which are typically present during hydraulic conveying. Clay minerals observe much reduced surface area and often contain parent rocks such as feldspars, micas and quartz which further diminish the impact of surface properties upon conductivity (Ramaswamy and Raghavan, 2011). Additional errors may arise during the tomographic reconstruction which impact upon the outputted cross-sectional conductivity and ultimately slurry density. Consequently, this removal of surface conductivity effects is required to be validated using tomography measurements; this analysis is performed later within this chapter.

A study was additionally performed to assess the impact upon changing pH with little variations observed. To assess the relationship between the pH, the AIC was determined with a linear fitting to the data within a continuous phase of pH 7 yielding negative values of -45.3 and -75.7 for aqueous suspensions of pH 5.5 and 8.5, respectively. Consequently, a linear regression was selected with a parity plot comparing the relative change in conductivity of a pH 7 continuous phase to pH 5.5 and 8.5 observing correlation coefficients of 0.991 and 0.990, respectively. To further demonstrate this linear behaviour the p-value obtained from a two-tailed test was found to be much less than 0.001 for both the intercept and gradient estimates demonstrating high statistical significance of the fitted parameters.

However, when the continuous phase conductivity is within the ambivalent region, 0.5 mS cm^{-1}, the zeta potential of the slurry is observed to impact greatly upon the resistive

properties. In this region, the ionic contribution of kaolin is similar to that of the continuous phase, with relative changes in conductivity likely attributed to surface phenomena. This results in the relative change in conductivity both increasing and decreasing depending upon the concentration of kaolin present. Yukselen and Kaya (2013) demonstrated an increase in the magnitude of the zeta potential with a reduction in pH of kaolin slurries. When this information is inputted into the Bikermann equation, Eq. 6.3, the surface conductivity increases with a reduction in pH with this phenomenon also reflected within this study. At pH 5.5, the relative change in conductivity is seen to increase throughout with an exponential relationship with kaolin content observed, owing to surface properties.

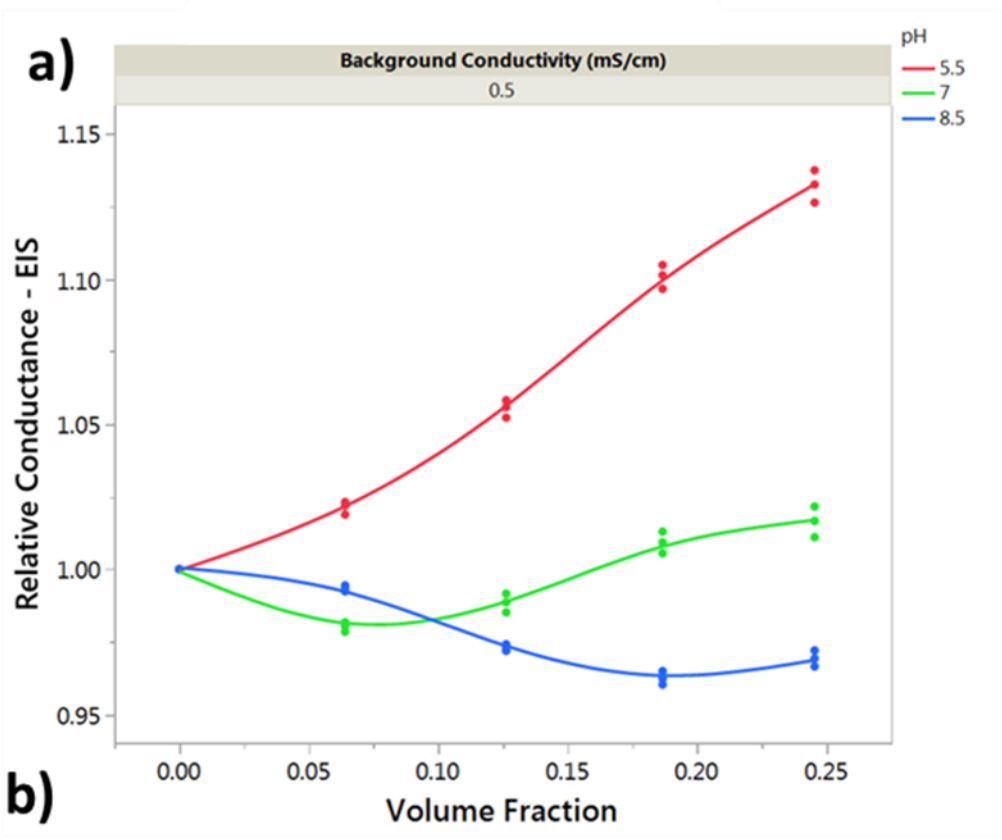

Source	LogWorth	PValue
pH	16.622	0.00000
Volume Fraction*pH	12.809	0.00000
Volume Fraction	6.969	0.00000
Frequency (Hz)	0.396	0.40136
Volume Fraction*Frequency (Hz)	0.233	0.58534
Frequency (Hz)*pH	0.080	0.83219
Volume Fraction*Frequency (Hz)*pH	0.046	0.89960

Figure 6.4 Ambivalent kaolin region; a) relative conductivity changes; b) variable analysis of a factorial model

As the pH is increased to 7, the relative change in conductance is reduced drastically, with an initial reduction in relative conductivity observed until approximately 5 vol% kaolin is added after which the conductivity begins to increase. Upon reaching approximately 16.3 vol% the conductivity is greater than the continuous phase with kaolin acting both more conductive and less conductive. This arises due to the previously demonstrated increase in surface conductivity with increases in kaolin content and is depicted in Figure 6.4a. Such behaviour is mirrored when the pH is increased to 8.5; however, this minimum exists at much greater solids content, at 19 vol %. With a unique solution unable to be obtained as a result of the presence of a minimum ensures that the real component of impedance is not applicable to monitor slurry density in low conductivity applications such as reservoir and river dredging.

In an attempt to derive a unique relationship between solids loading content and relative conductivity, eight, independent models were fitted with the highest correlation coefficients of 0.0996 and 0.0991 observed for linear and a two-parameter exponential fitting, respectively. When applying the former overall fitting to each individual pH, the RMSEs were found to be 0.094, 0.192, and 0.210, for suspensions of pH 5.5, 7 and 8.5, respectively. With no relationship between the parameters easily discernible, a full factorial model was developed with the independent variables of injection current frequency, pH and kaolin content. As expected, the pH is seen to have the greatest effect leverage with a minor probability value, p-value, less than 0.005, indicating statistical significance, and a total variable importance of 0.856; this is depicted in Figure 6.4b. Whilst displaying a similar p-value, the total variable importance of kaolin volume fraction is much reduced to 0.392. Such analysis highlights that the bulk solids content has little impact upon the real electrical properties within the ambivalent kaolin regime due to the balance of ionic and surface contributions. Consequently, such slurries are unsuitable for in-line ERT densitometry with a pH meter required, or an alternative solution developed. This model additionally demonstrated the lack of influence of injection current frequency in the existing ERT frequency range with the log worth 2.4 % of that of pH. Furthermore, the p-value was seen to be much greater with a value

of 0.4014, with only values below 0.05 indicating that a variable is of statistical significance to the fitting.

As the ionic concentration is increased and the continuous phase conductivity is in excess of 2 mS cm^{-1} the low conductivity kaolin regime is reached when kaolin becomes less conductive when compared to the background media and predictable resistive behaviour is observed. The surface conductivity analysis performed using the Maxwell-Garnett equation was repeated. For a 2 mS cm^{-1} aqueous solution, the maximum contribution of surface conductivity was reduced drastically to 3.28 % at 35 vol% compared to the 15.75 % in the conductive kaolin regime. Such findings are supported by Choo and Burns (2014) who observed a reduction in surface conductivity of kaolins with an increase in continuous phase conductivity. As it has been demonstrated that surface conductivity can be negated in densitometry in low conductivity systems, the surface conductivity can also be negated within the low conductivity kaolin regime. When considering the minimum and maximum σ_d, the range was reduced to just 0.0158 across the solids content range from 0.5 to 35 vol%. This range further reduces with an increase in continuous phase conductivity, as expected. In addition, the magnitude of the σ_d decreases in a similar manner and ultimately tends towards zero. Hence, to optimise ERT densitometry under these conditions there is a requirement to measure the real-time, in-line conductivity of the continuous phase. From such an understanding, appropriate analysis algorithms and reference selection may be implemented to enhance the integrity of the tomographic data.

In addition to the continuous phase properties, the discrete phase properties are additionally required to be known. Sand is known to be non-conductive and hence will have a σ_d of zero; however, it is likely that the exact solids being dredged are not entirely known. The impact of this has once again been assessed based on the associated error in measured density. For a 2 mS cm^{-1} aqueous phase, the error associated with surface conductivity, 3.9 kg m^{-3}, is dwarfed by the incorrect assumption the solid dredged is non-conductive. Such an assumption results in an increase in RMSE to 176 kg m^{-3} with a maximum error of 352 kg m^{-3}.

The maximum error accounts for 22.0 % of the measurement, which is vastly in excess of the desired ± 1% of the density and is reflected in Figures 6.3e and 6.3f. Despite a reduction in the σ_d from 0.509, when the continuous phase conductivity is 1 mS cm^{-1}, to 0.356 at 10 mS cm^{-1}, a resultant RMSE of 128 kg m^{-3} was observed which is additionally unsuitable. Using extrapolation, the assumption that kaolin may be assumed as non-conductive is valid when the continuous phase is in excess of 16.3 mS cm^{-1}. This finding aligns with the successful application of ERT densitometry in marine dredging as described by Wei et al. (2016) when the continuous phase conductivity is typically in excess of 30 mS cm^{-1} (Wright and Colling, 1995).

Nonetheless, to extend ET densitometry to river and reservoir dredging applications, the solids are required to be identified alongside the continuous phase for optimised operation. A secondary technique or development, is additionally required to be employed when interrogating materials within the ambivalent region with no discernible relationship between the kaolin content and bulk resistive properties. However, it has been determined that the Maxwell-Garnett and Bruggeman effective media approximations may be employed effectively when monitoring slurries with large surface contributions, if careful consideration of the dispersed phase conductivity input is performed.

6.3.1.2 Susceptance

Relative changes in the imaginary component of impedance, reactance, were simultaneously monitored with this component described by the imaginary part in Eq. 6.5. The reciprocal of reactance is known as susceptance and is analogous to conductance, with the fixed electrode setup able to distinguish relative changes in susceptibility. In low conductivity media, it has been observed the electrical properties are dominated by capacitive changes. Hence, large relative changes in the imaginary component are observed when compared to the real component, conductance. At the maximum solids loading, 35 vol%, the relative change in conductivity was found to be 1.9 and is appropriate for use in effective media approximations. However, this value is increased by a factor of 2.76 when considering the

susceptibility alone as depicted in Figure 6.5a. Such an increase is therefore able to enhance the sensitivity of the electrical densitometer measurement with EIT capable of offering new capabilities in densitometry. The optimal relationship between bulk susceptibility and kaolin content was once again found to be exponential based upon the Akaike Information Criterion. Similarly, the contributions of surface phenomena can be minimised by the appropriate selection of the dispersed phase susceptibility input. It has also been witnessed that the susceptibility has a greater dependency upon the frequency. This is reflected in Figure 6.5b with the largest relative changes in complex electrical properties observed at 9.6 kHz, for a continuous phase conductivity of 0.15 mS cm^{-1}.

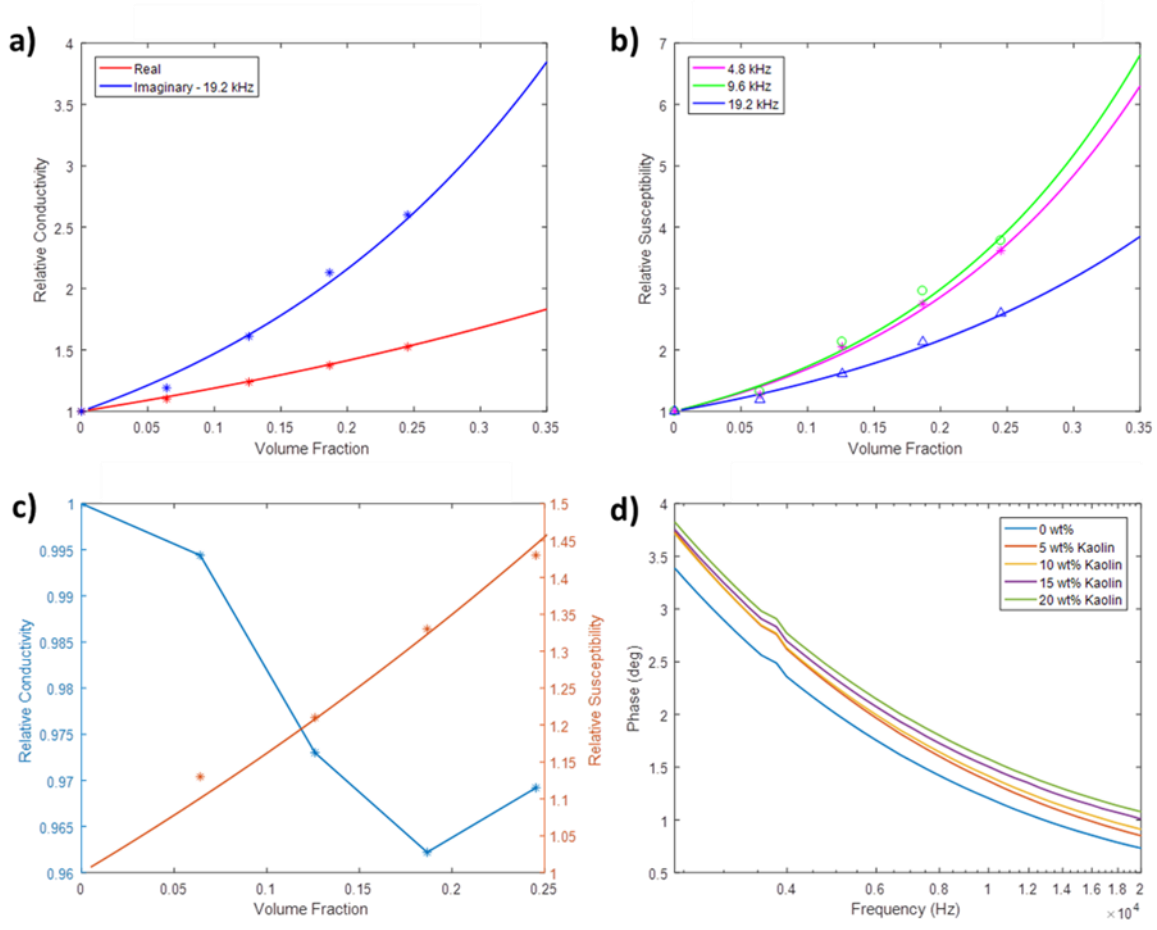

Figure 6.5 Relative changes in susceptibility: a) comparison to resistive properties - 0.15 mS cm^{-1}, pH 7; b) effect of frequency - 0.15 mS cm^{-1}, pH 7; c) comparison to resistive properties - 0.5 mS cm^{-1}, pH 8.5; d) phase measurement - 0.15 mS cm^{-1}, pH 7

As the continuous phase conductivity exceeds 0.15 mS cm^{-1}, the optimised interrogating frequency is increased to 19.2 kHz; this frequency is accordingly recommended to be employed for all EIT densitometry measurements. These conditions can be utilised to monitor the ambivalent region, 0.5 mS cm^{-1}. Whereas the real component of impedance demonstrated no discernible relationship with kaolin content, an almost linear relationship may be observed with susceptibility, as depicted in Figure 6.5c for a suspension at pH 8.5. This removes the problematic minima which arise from surface phenomena ensuring that a unique solution is able to be obtained.

Within existing EIT installations, both the real and imaginary components of impedance are captured to account for both capacitive and resistive changes with the modulus calculated. As the phase measurement is a maximum of 4° within the optimised ERT frequency range, this results in relative small contribution of susceptibility to impedance. From raw impedance spectroscopy measurements, it has been determined that the imaginary component contributes just 0.5 % to the impedance measurement to ensure that even when the modulus, or admittivity, is measured the capacitive behaviour is practically ignored. To highlight this, a linear regression was performed comparing relative changes in conductance and admittance with extremely high correlation coefficients of 0.9903, 0.9963 and 0.9987 observed at interrogating frequencies of 4.8 kHz, 9.6 kHz and 19.2 kHz, respectively. A similar regression was performed between relative changes in phase and susceptibility in which the phase measurement mirrors the susceptibility. This indicates that phase changes are dominated by the reactance within the conductive and ambivalent kaolin regimes. Accordingly, to optimise performance in such regimes, it is evident that a tomographic approach to the susceptibility alone is recommended to extend the applicability of the non-nuclear alternative to density measurement in low conductive continuous phases. This phase behaviour is depicted in Figure 6.5d demonstrating a positive change in the phase measurement with kaolin addition.

As the ionic concentration is increased, the alterations in resistive properties begin to dominate the phase measurement, with excellent agreement between these factors, offering little advantage over resistive behaviour alone. However, it also observed that the magnitude of the phase angle is increased from 1.3°, σ_c = 0.5 mS cm^{-1}, to 15.1° when the continuous phase is increased to 10 mS cm^{-1} at a frequency of 9.6 kHz. To reduce this contribution, as the kaolin content can be most effectively captured by the resistive properties alone the frequency is reduced to 19.2 kHz. This contribution of phase is reduced to 9.7° which enhances the influence of the resistive component upon the calculated modulus. From this, it is recommended that for aqueous conductivities within the range of 0.15 – 1 mS cm^{-1} the susceptibility is considered alone for densitometry measurements. However, when this range is exceeded the resistive component is monitored at a frequency of 19.2 kHz. Once again, this reinforces the importance in understanding the real-time continuous phase conductivity to select the appropriate algorithms for analysis.

6.3.2 Low Frequency Spectrum: 20 Hz – 2 MHz

Blewett et al. (2003) described that any non-magnetic material may be described by the frequency dependent parameters of dielectric constant and conductivity, which are also able to be related to surface parameters. Multi-frequency EIT techniques operate over an expanded range of interrogation frequencies and as a result the entire low frequency spectrum has been examined to determine its applicability to densitometry. Nahvi and Hoyle (2008) developed a wideband EIT technique using a single channel chirp excitation signal to extract tomographic information of foodstuffs with the frequency swept between 10 kHz to 510 kHz. From EIS data in low ionic concentration media, there appears to be little frequency-dependence in resistive properties, below 350 kHz with a uniform reduction in resistance for each kaolin addition. Within this range, ERT densitometry may be employed effectively with the most substantial relative changes occurring between 10^4 – 10^5 Hz. Above 350 kHz, the resistance of the slurries tend towards that of the aqueous phase until 1.41 MHz where the addition of kaolin gives rise to an increase in resistance and ultimately a reduction

in conductivity. This unique frequency dependence is depicted in Figure 6.6a and has the ability to act as a fingerprint to characterise the discrete phase material.

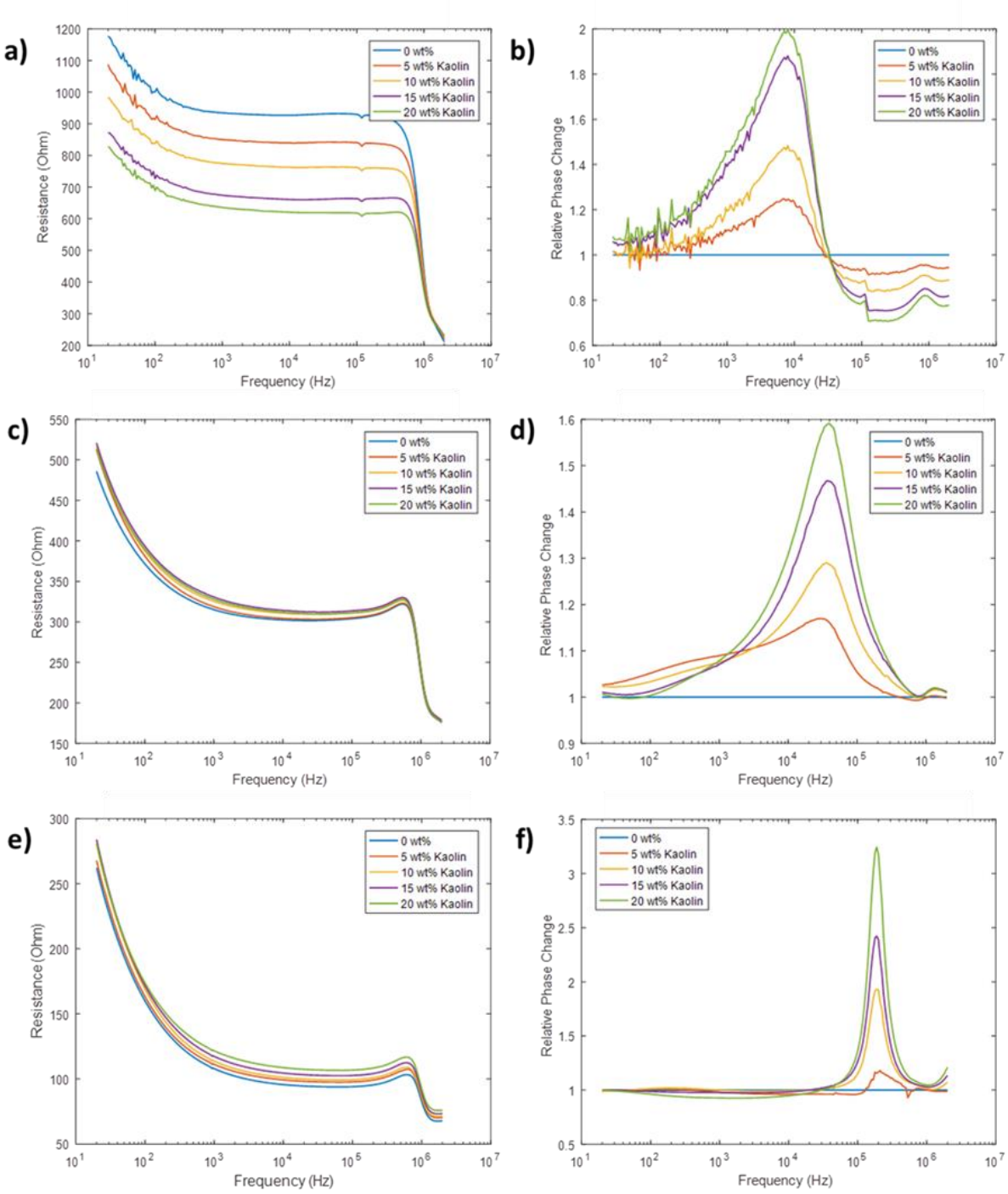

Figure 6.6 Kaolin properties – low frequency sweep: a) resistance – 0.15 mS cm^{-1}, pH 7; b) relative phase – 0.15 mS cm^{-1}, pH 7; c) resistance – 0.5 mS cm^{-1}, pH 7; d) relative phase – 0.5 mS cm^{-1}, pH 7; e) resistance – 2 mS cm^{-1}, pH 7; f) relative phase – 2 mS cm^{-1}, pH 7

The relative changes in phase behaviour additionally demonstrate the potential to perform this task, with these changes depicted in Figures 6.6b and 6.7b for kaolin and sand, respectively. Whilst the magnitude of phase in the EIT operating frequency region is seen to be small and lack contribution to the impedance properties, the relative changes are greatest within this range. This supports the use of a tomographic approach to phase information with a peak frequency in relative phase changes occurring at 7.51 kHz. An increase in the ionic concentration, to form continuous phases of conductivity 0.5, 1 and 2 mS cm^{-1}, results in the peak shifting towards higher frequencies due to the relaxation properties of the kaolin slurries. At such conductivities, a peak exists at 33.8, 106 and 224 kHz, respectively. As depicted in Figures 6.6d and 6.6f, these peaks are approximately normalised distributions and accordingly the highest relative changes in phase is found at the highest operable ERT frequency of 19.2 kHz. The use of the phase measurement is vital in the ambivalent regime, as across the entire frequency range the resistive properties are unable to resolve a unique relationship with kaolin content for each continuous phases with differing pH.

As expected, once the low conductive kaolin regime was entered, 2 – 10 mS cm^{-1}, the addition of kaolin brings about an increase in resistance across the entire frequency range, without inversion occurring at higher frequencies. For a 2 mS cm^{-1} aqueous suspension, the electrical properties are depicted in Figure 6.6e and 6.6f. From this, it can be reaffirmed that the resistive properties alone can be exploited in the densitometry measurement with the largest changes in such properties occurring within the ERT frequency regime of the ITS p2+ instrument. It must be acknowledged, that for continuous phases of 5 and 10 mS cm^{-1} above 1.3 MHz a negative capacitance was observed. This indicates the selected equivalent circuit model of a resistor and capacitor in parallel is no longer applicable due to the negligible effect of capacitive properties. Consequently, the susceptibility behaviour is unlikely to reflect upon the capacitive properties of kaolin.

6.4 Electrical Impedance Spectroscopy – Electrical Properties of Sand Slurries

In hydraulic transport systems, typically a range of solids are transported, with sand an extremely common discrete phase. Whilst it is well-established that sand is non-conductive, the entire frequency bounds of the digital LCR meter were interrogated with a particular focus upon phase. For this study, the working fluid range conductivity was extended to 0.1 – 10 mS cm^{-1}, with the former selected as it is the lower limiting conductivity of the ITS p2+ instrument.

As expected, across all of the interrogated slurries, sand was seen to be less conductive than the continuous phase to immediately demonstrate vast differences in electrical behaviour compared to kaolin. The analysis to determine the optimal σ_d was once again performed to ensure the non-conductive assumption is valid for use in densitometry. When the continuous phase conductivity is below 1 mS cm^{-1}, the average optimal σ_d was found to be 0.03, if the continuous phase is designated a value of one. This validates the non-conductive assumption with 0 selected resulting in a maximum sand content error of 0.9 vol%. Furthermore, as anticipated suspensions of sand do not observe changes in conductivity with solids content due to the lack of surface properties; this is depicted in Figure 6.7a.

When the continuous phase conductivity is increased further the optimal σ_d for sand becomes zero. This ensures significant variances in electrical behaviour are observed when compared to colloidal clay dispersion resulting in the requirement for different measurement inputs and analysis protocols for EIT densitometry depending upon the material being conveyed. Accordingly, it is imperative to characterise the solids within the slurry to effectively capture the volumetric concentration of the discrete phase.

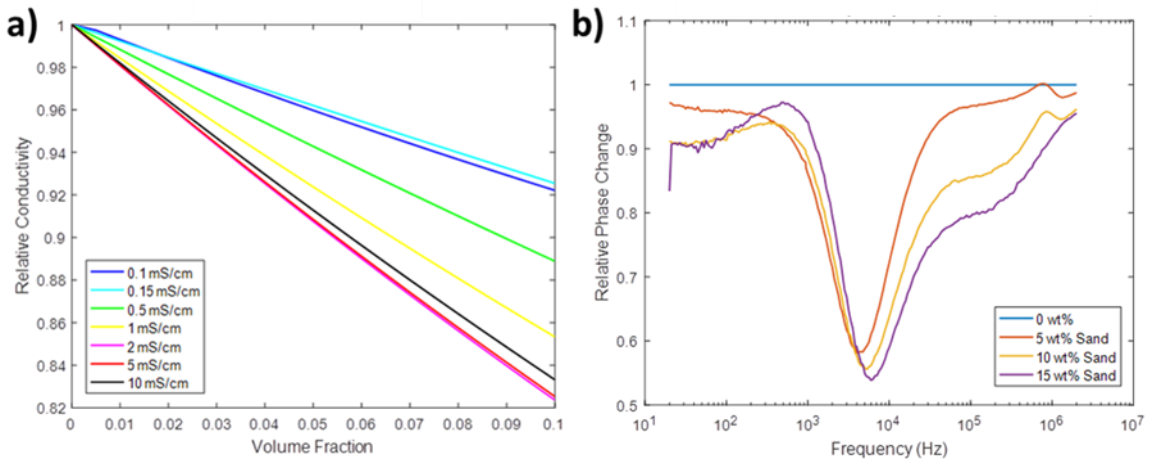

Figure 6.7 Sand properties – low frequency sweep: a) relative conductivity – 0.1 – 10 mS cm^{-1}; b) relative phase – 0.15 mS cm^{-1}, pH 7

Initial promise can be observed when interrogating the relative changes of the phase measurements. As depicted in Figure 6.7b, whilst a similar normalised distribution peak is observed, the relative change is reduced when sand is added. This highlights the capability of the direction of the phase measurement to distinguish between the two material types.

Despite altering the discrete phase to sand, the optimal operating frequency of the complex measurement remains the analogous to kaolin slurries. The greatest relative change can be found in the region of 5.32 – 7.61 kHz for a 0.15 mS cm^{-1} ensuring that a 9.6 kHz interrogating EIT frequency is optimal. Not only does this peak frequency increase with continuous phase conductivity, but also is seen to increase with the addition of sand with this behaviour investigated later within this chapter to be exploited in the determination of dispersed phase composition.

6.5 Electrical Impedance Tomography

The understanding obtained from EIS data may then be directly exploited to optimise the performance of EIT densitometry when monitoring kaolin and sand slurries. To ensure that EIS data is compatible with EIT, experimentation on all slurries was performed with a linear

regression utilised for direct comparison of relative changes in electrical conductivity, Figure 6.8.

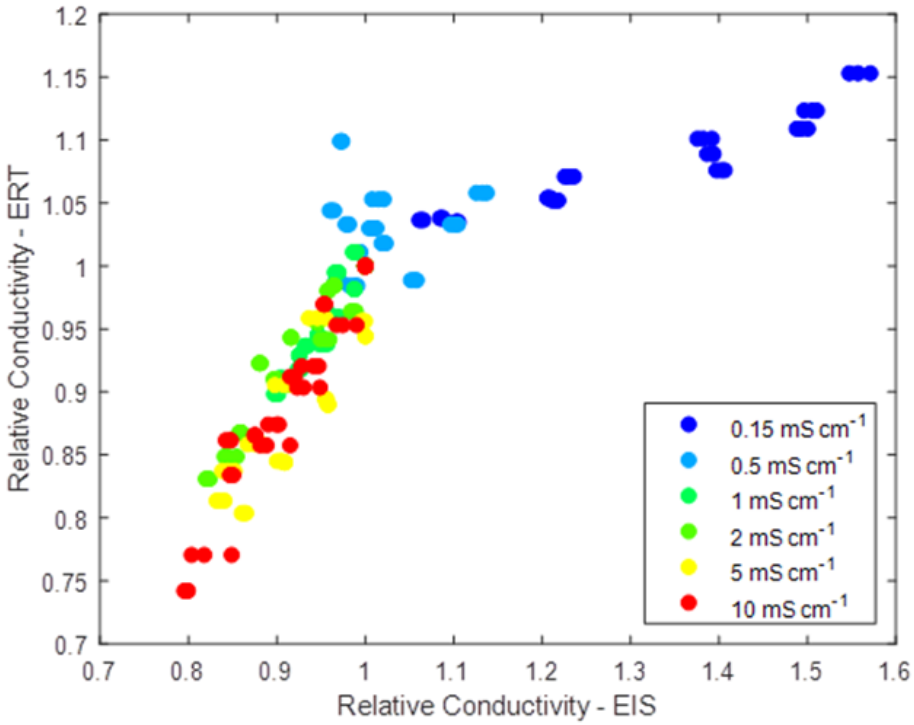

Figure 6.8 Parity plot – comparison of relative conductivity from EIS data to ERT measurements

In this regression, the y-axis considers the relative changes in the average of reconstructed conductivity pixels from EIT across 250 data frames and the x-axis the relative changes in EIS; this study considered all of the continuous phases, including those with variations in pH. Within the conductive kaolin regime, a strong agreement is observed with a correlation coefficient of 0.979 and a minor RMSE of 0.007. Despite observing a similar trend in resistive properties, this trend does not replicate the identity line, with an averaged gradient of 0.27 and y-intercept of 0.725. With a gradient below one, this represents an underestimation in the EIT measurement compared to EIS. This underestimation sees a resultant decrease in the optimised σ_d from 5.77 to 1.73. From the EIS data it has already been suggested that the sensitivity of densitometry in low conductivity continuous phases can be enhanced using the imaginary component of impedance with this reinforced by a further reduction in resistive changes when kaolin additions are monitored using EIT.

It was found that a similar regression approach can be utilised within the ambivalent region, in which surface conduction ensured that a unique relationship between resistive properties and kaolin content was able to be determined. A similar phenomenon is observed when monitoring these slurries using a conductivity tomogram reconstructed from EIT measurements with a unique solution unable to be obtained as a result of the presence of multiple minima. The linear correlation coefficient within this region is significantly decreased to 0.312, indicating almost no relationship between information obtained from EIT and EIS. However, this lack of correlation arises due to the small changes in resistive properties with additions of kaolin and a minor RMSE of 0.019 observed; this information is captured in Table 6.2. Such tomographic studies further highlight the lack of suitability of the real component of impedance to monitor kaolin behaviour due to the significant contribution of surface properties under such conditions.

Table 6.2 Linear regression of EIT and EIS measurements

Continuous Phase Conductivity/ mS cm^{-1}	Gradient	y-intercept	Correlation Coefficient	RMSE
0.15	0.27	0.725	0.979	0.007
0.5	0.26	0.749	0.312	0.019
1	1.02	-0.016	0.974	0.006
2	1.03	-0.032	0.979	0.008
5	1.06	-0.086	0.968	0.021
10	1.04	-0.047	0.973	0.013

As anticipated, when the continuous phase is in excess of 1 mS cm^{-1}, EIT begins to mirror the resistive behaviour of EIS with both a high correlation coefficient, on average 0.974, and gradients similar to one ascertained. Whilst EIT is known to interrogate the entire cross-sectional area of the pipe, due to the electrode arrangement EIS is only able to monitor the near-wall region. The penetration of the EIS electrical field has been found to be approximately 2 mm based upon a model derived in COMSOL which exploits Maxwell's

equations in matter, see Chapter 2. Despite this, the linear regression yields high correlation coefficients to fittings which are close to the identity line, y = x, to validate the well-dispersed assumption. Not only does this act to validate EIT, but also provides credibility to the experimental methodology as throughout this study it has been assumed that the discrete phases have been well-dispersed due to the selected vertical installation of the sensing arrangement. Consequently, it can be confirmed that the understanding gained from EIS can be directly applied to conductivity tomograms, obtained from EIT measurements, to accurately determine slurry density measurements with the lowest operable continuous phase conductivity 1 mS cm^{-1}. It must be acknowledged that this would require complex implementation with the identification of the continuous phase conductivity and discrete phase material required before these techniques may be implemented.

To achieve this, the complex EIT measurements are interrogated by exploiting the phase information obtained from phase sensitive demodulation, see Chapter 2. Combining phase information with real voltages is then utilised to extract imaginary voltages using trigonometry. Initially, eight different fit types, ranging in complexity from linear to Cauchy distribution models, were performed to determine whether a relationship exists between the phase information obtained from EIT and EIS measurements. However, based upon the Akaike Information Criterion, no discernible trends were discovered. To demonstrate this, a simple linear regression analysis may be performed using the measured EIS and EIT phase measurements, with the associated parity plot depicted in Figure 6.9. From such a plot, it is immediately evident that little similarity exists between these variables with a minimum RMSE of 11.4° authenticating this. These non-correlated measurements ensure that the absolute phase measurements obtained from EIT cannot be utilised effectively, with a tomographic approach recommended. This is likely due to the calibration protocol of the EIT phase measurement, described in Chapter 2.

The 104 EIT phase measurements are found to be positive at low conductivity values, 0.15 mS cm^{-1}; however, in excess of this the phase measurements become negative. As the

modified sensitivity back projection reconstruction (MSBP) algorithm is not amenable to negative voltages this may not be employed directly. Whilst other algorithms may be selected, the MSBP algorithm is considered the most robust in industrial applications (Wang, 2015); the MSBP algorithm is described in Chapter 2. The absolute value of the EIT phase measurement is then employed to ensure that novel susceptibility tomograms are able to be effectively reconstructed. A pixel-wise division of the susceptibility tomogram by the conductivity tomogram can then be utilised to develop a relative phase tomogram. Whilst the phase magnitude is conventionally represented as an angle, the relative change in phase is monitored in this second novel tomogram.

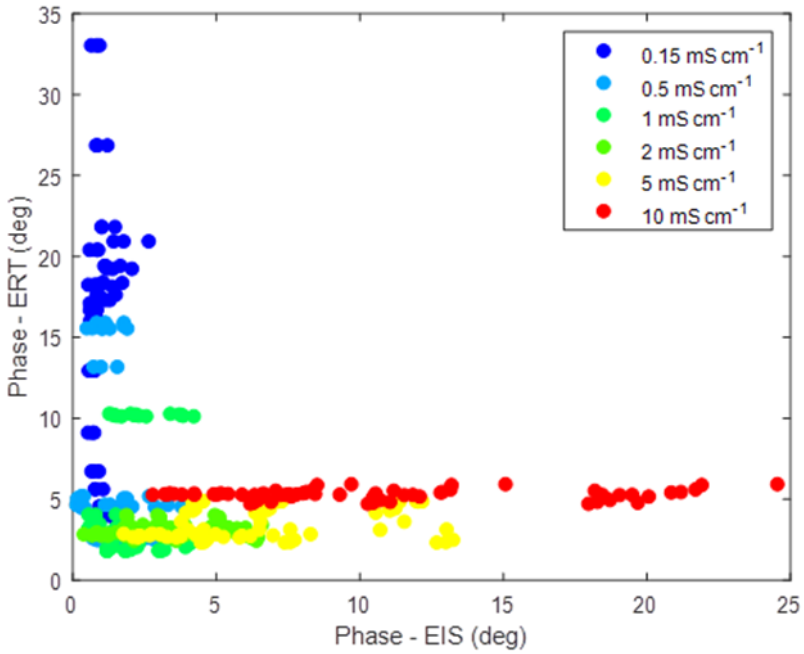

Figure 6.9 Parity plot containing the phase measurement from EIS and EIT

The application of these tomograms is demonstrated in continuous phases with low conductivity, < 1 mS cm^{-1}. In the hydraulic transport of sand, if sufficient electrolytes are not present within the carrier fluid, the contrast between the slurry conductivity and continuous phase conductivities is minimal ensuring poor sensitivity of non-nuclear densitometry. To mimic this scenario, a small amount of ammonium acetate was added to de-ionised water to give rise to a 103 µS cm^{-1} continuous phase. This was selected as it is the lowest recommended continuous phase conductivity able to be monitored with the ITS p2+

instrument. Averaging the 316 computed conductivity pixels of the tomogram yielded a relative change of just 0.65 % for the addition of 20 wt% sand; however, when the computed susceptibility pixels are averaged this relative change is increased by an order of magnitude to 6.31 % for the same addition. Accordingly, the sensitivity of EIT densitometry is increased by a factor of ten, greatly increasing the applicability of this technique to low conductivity applications such as reservoir dredging. A similar effect can be observed when considering a multi-component slurry within the aforementioned continuous phase; this system consisted of the 5 wt% sand with 5 wt% step additions of kaolin until 20 wt% was reached. As depicted in Figures 6.10a and 6.10b, at the highest kaolin content the relative conductivity changes were found to be 4.8 %. Despite this being sufficient, the performance of densitometry can once again be enhanced greatly with the relative change in susceptibility found to increase by a factor of 128 %.

Based upon Eq. 6.7, the imaginary component is seen to be a function of the square of the resistance, leading to a contribution to the change in susceptibility of 8.2 %. The remainder of this variance arises from the dominant contribution of the capacitive behaviour. This is further reflected in parity plots, Figures 6.10c and Figure 6.10d, which directly compare the computed pixel values obtained in the phase tomogram to those of the in the susceptibility and conductivity tomograms, respectively. From these linear fittings, the correlation coefficient with the susceptibility tomogram was found to be 0.999 and associated RMSE of 0.0043. When considering the resistive component alone, the coefficient is found to be significantly reduced to 0.611.

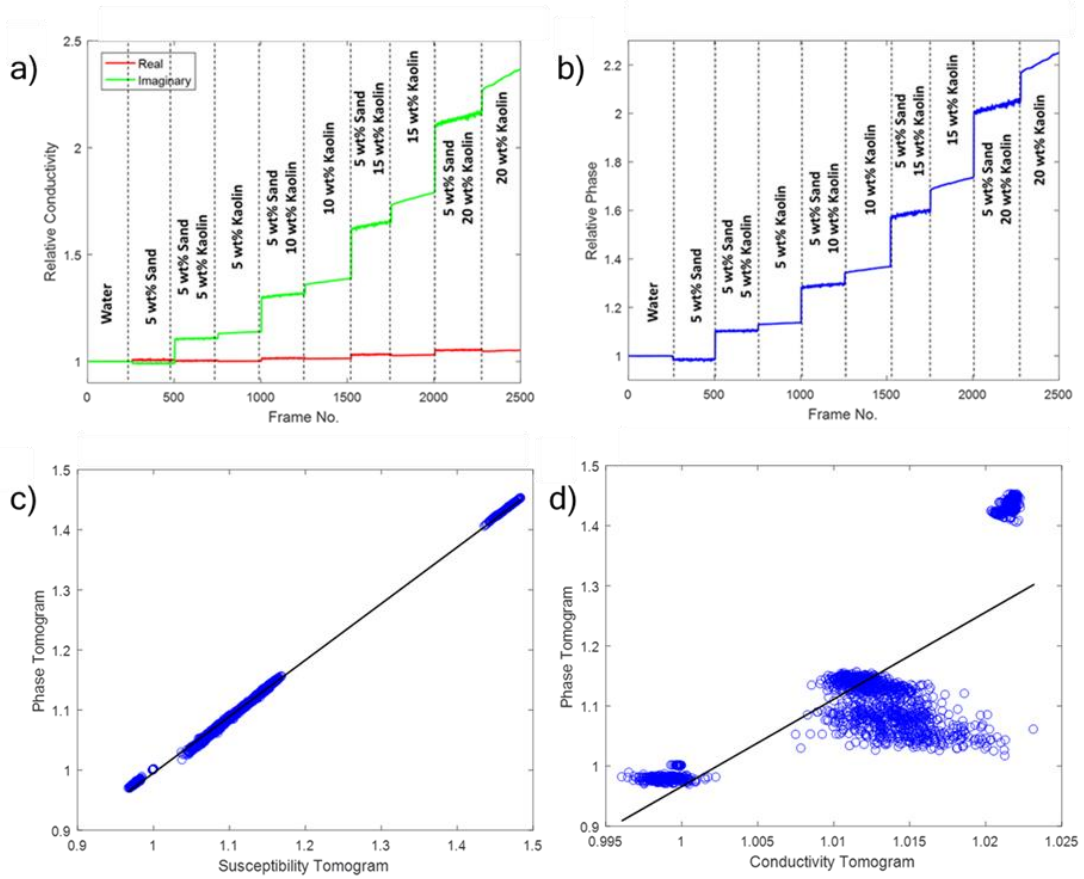

Figure 6.10 Imaginary Tomographic Component - 0.15 mS, pH 7 : a) comparison of relative change of conductivity and susceptibility pixels; b) relative changes in phase tomogram; c) parity plot comparing phase to susceptibility tomogram; d) parity plot comparing phase to conductivity tomogram

Similar behaviour is observed in the ambivalent region with relative changes in the conductivity and phase information obtained from tomographic data deemed to be non-linear with a correlation of 0.02315. As demonstrated using EIS, see Section 6.3, unlike resistive properties susceptibility is capable of providing a definitive relationship between kaolin concentration and relative changes in electrical properties. This has additionally been observed when employing the tomographic approach with relative changes in pixel-averaged conductivity and susceptibility of kaolin suspended in a continuous phase of 0.5 mS cm^{-1} and pH 8.5 displayed in Figure 6.11a. When considering an ERT approach, a minimum, or maximum, is once again observed; however, this is removed to an approximately linear

relationship when considering susceptibility. Consequently, the novel susceptibility tomogram is able to expand the operational conductivity range of the non-nuclear density measurement to continuous phases whose conductivity is in excess of 0.1 mS cm^{-1} i.e. river dredging.

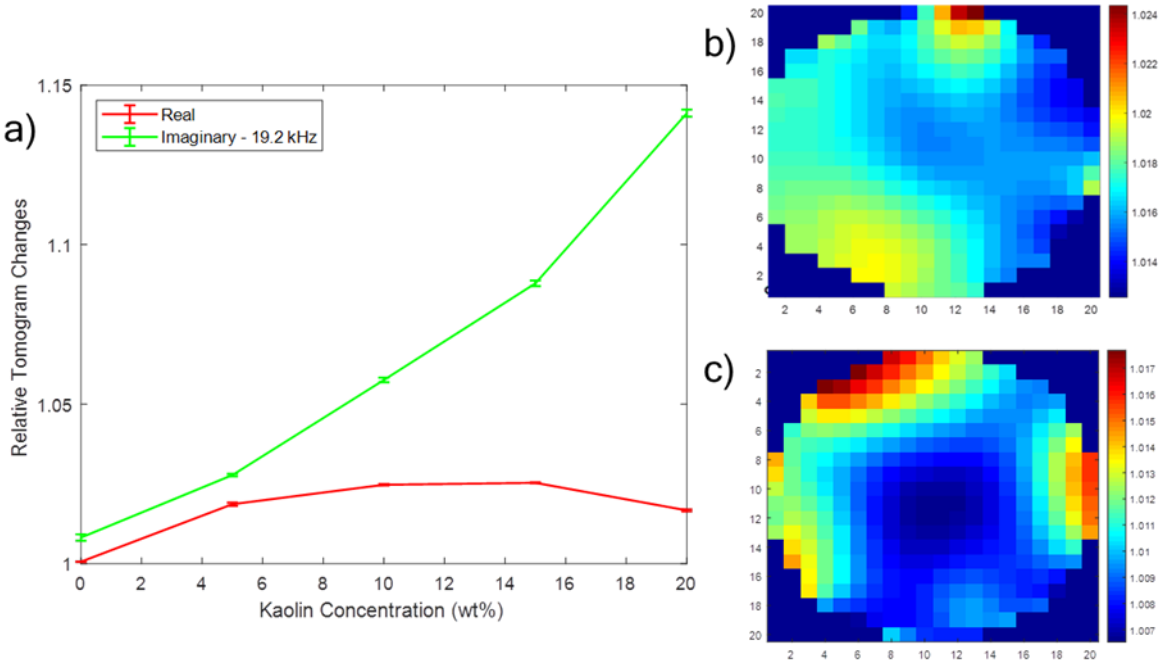

Figure 6.11 Imaginary component in the ambivalent region: a) comparison of relative changes in conductivity and susceptibility tomograms; b) conductivity tomogram; c) phase tomogram

The application of this tomogram can be extended to developing the aforementioned phase tomograms which can offer new insights into the analysis of multiphase systems. When the continuous phase conductivity is less than 1 mS cm^{-1}, kaolin observes an increase in the relative phase, whilst sand demonstrates a reduction in this measurement. This can be employed in a tomographic approach to identify kaolin and sand-rich regions with tomograms depicted in Figures 6.11b and 6.11c, for a 0.5 mS cm^{-1} solution with inclusions of 6.8 vol% of kaolin and 1.9 vol% of sand. Little change is observed in the conductivity tomogram; however, distinct regions are present within the phase tomogram. As the relative phase measurement is greater than one, it can be inferred that kaolin is dominant throughout the entire cross section. Despite kaolin being present throughout, the blue region of the tomogram located within the centre of the pipe, indicates a slight increase in sand

concentration. This variation within the phase tomogram is likely caused to be by the shear induced phase migration of the larger sand particles towards the centre of the pipe. It must be acknowledged that the range of relative phase change is extremely small throughout the entire cross-section, highlighting the aforementioned assumption of well-dispersed solids. Whilst such visualisation may be employed to enhance a wide range of processing applications with greater information able to be extracted from EIT measurements, it also presents an opportunity to identify which discrete phase is most prevalent, based upon real-time tomographic data alone.

6.6 Discrete Phase Identification

Within dredging and mining applications, the exact identity and composition of the conveyed solids is often unknown. In the former, the most common of which are clays, sands and silts, which have been demonstrated to have greatly differing electrical behaviour in previous sections. Accordingly, to employ the appropriate measurement protocol, the discrete phase is required to be identified. Similarly to the EIS studies, the relative change in the tomographic phase information is found to be increased when kaolin is added and decreased with the addition of sand. When detecting pure materials, this can provide an accurate basis to distinguish between differing discrete phases with relevant information i.e. discrete phase conductivity, which can be subsequently implemented to optimise the density measurement. However, in practice these materials exist in the form of multi-component slurry mixtures. As the discrete phase volume fraction is also unknown, too many degrees of freedom exist to effectively characterise the discrete phase using a single EIT measurement frequency. For a binary kaolin-sand slurry mixture within a continuous phase of conductivity 0.15 mS cm^{-1}, the phase change is found to be zero for a discrete phase composition of 70 – 72 vol% sand. As the direction is only able to be monitored, it is then unknown if solids are being conveyed based on phase measurements alone. Moreover, in EIT this information is lost when the

continuous phase is in excess of 1 mS cm^{-1}, as the phase measurement is dominated by the conductivity with little capacitive contribution. In this scenario, with both solids being less conductive than the continuous phase, single frequency tomographic measurements are unable to distinguish between these materials.

Hence, it is evident that multiple frequencies are required to distinguish between the materials. A number of multi-frequency tomography approaches exist with the most common a single-channel chirp excitation and pseudo-random binary signals (Amrani et al., 1998). Wideband EIT was developed using the former by Nahvi and Hoyle (2008) to image a range of vegetable foodstuffs. Despite this, chirp signals are prone to noise and are consequently difficult to implement. These noise sources are able to be removed with the use of a pseudo-random binary signal which generates a cyclical frequency sweep by utilising linear shift feedback register (Amrani et al., 1998). However, this technique is unable to target specific frequencies with the post-processing of data likely more complex. To mimic such techniques, the relative changes in the phase measurement from EIS were exploited. This information was extracted using a logarithmic frequency ramp with two points per decade selected to generate eleven individual phase measurements across the frequency range of 20 Hz – 2 MHz.

These were then coupled with the continuous phase conductivity, monitored using the handheld conductivity probe, to act as inputs to a two-layer feedforward neural network. The network architecture, optimised for SLES formulation recognition in the previous chapter, Figure 5.6 was selected to categorise the continuous phase into three classifications: sand (1), kaolin (2), multi-component mixture (3). Accordingly, three neurons were employed in the output layer alongside the softmax function, outlined in Chapter 5, alongside forty neurons selected for the hidden layer. Using supervised machine learning, the data was segregated into 70 % training, 15 % validation and 15 % test data to develop a predictive network. From this predictive network, the solids classification was predicted with an accuracy of 97.3 %.

This is reflected in Figure 6.12 which depicts the associated confusion matrix with the false negative rate.

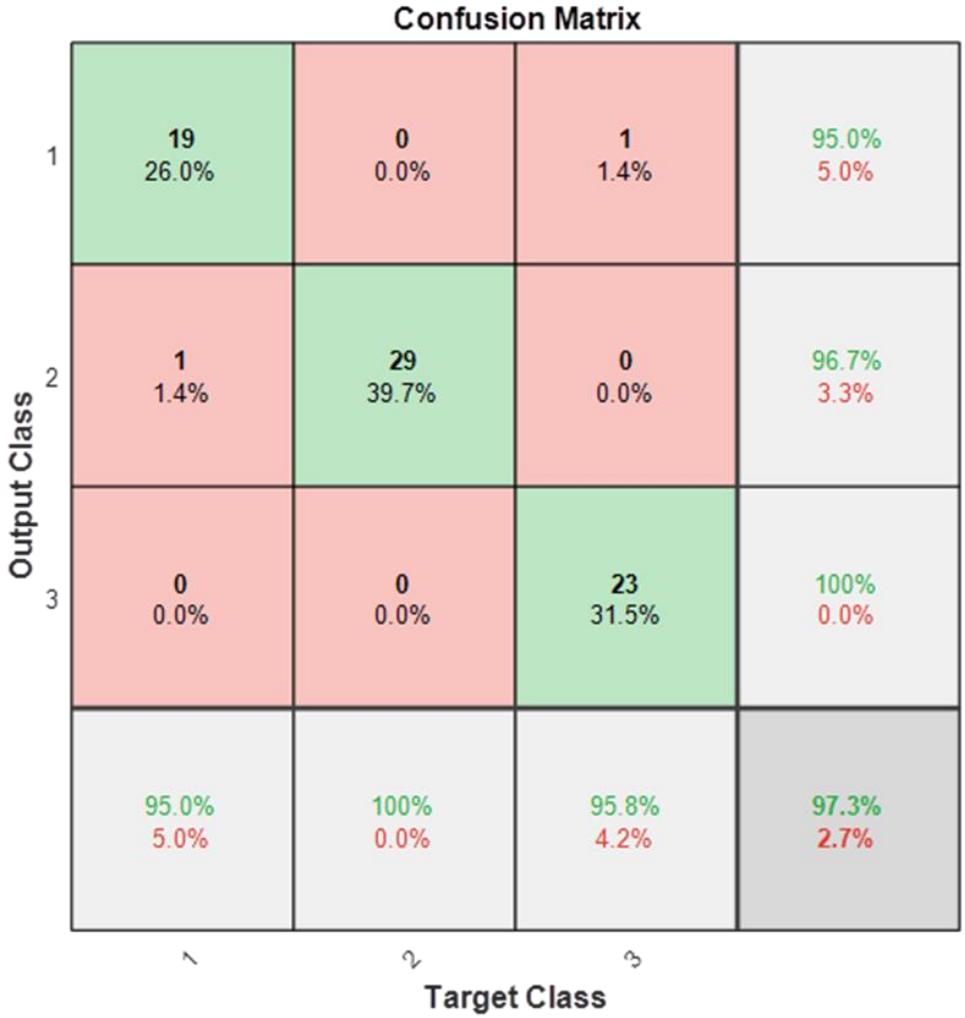

Figure 6.12 Confusion matrix of the neural network to predict solids classification

With the ability to accurately predict if kaolin, sand, or multi-component slurries are being transported across the conductivity range of 0.1 – 10 mS cm^{-1}, enables the assumption of non-conductive solids to be removed. When considering kaolin, this reduces the associated error greatly from 176 kg m^{-3} to 3.8 kg m^{-3}, as described in Section 6.3, to ensure that the accuracy required for high cost dredging applications is met (Batey, 2012). Moreover, this can be utilised to determine when a multi-component slurry is present within the sensor with further appropriate inputs selected. Whilst this technique is currently incapable of offering insights into the composition of the discrete phase; this predictor enhances the existing

capability of EIT densitometry. For this technique to function optimally there is a requirement for a robust in-line continuous phase conductivity measurement to act as an input for the discrete phase recognition algorithms.

To effectively characterise the composition of the solids, an increased number of frequencies is required. This can be achieved with the incorporation of a secondary technique into the system, with EIS preferred. The interrogation of the entire spectrum will possess an individual signature for each of the systems and hence the composition may be characterised. An example signature is highlighted as a Cole-Cole plot in Figure 6.13a. The measurement performed within this study has a temporal resolution of 0.025 Hz, twenty times smaller than that of EIT. This temporal resolution is impractical to achieve an effective, dynamic measurement with the requirement to remove a number of frequencies. At low frequencies, the ionic behaviour of the slurry is interrogated, whereas when the frequency is increased, relaxations of the double layer and polarisation processes begin to have an impact upon the electrical properties.

In this study, the reactance was selected as it encompasses both real and imaginary components and consequently aligns with a study by Blewett et al. (2003) who highlighted that these measurements are able to effectively characterise clay-water formulations. This is reflected in Figure 6.13b, which depicts the reactance as a function of frequency for both kaolin and sand dispersed within a 0.15 mS cm^{-1} continuous phase. Alongside the difference in relative changes, the relaxation frequency is seen to change depending upon the addition of solids with the addition of kaolin giving rise to an increase in the relaxation frequency due to the presence of surface properties. The peak of the continuous phase is observed at 632.5 kHz, whilst the addition of kaolin sees this increase to 893.4 kHz. This frequency shift is not observed during the addition of sand and hence may act as a distinguishing feature. The relative change in magnitude of the reactance is greater for an addition of kaolin compared to the same addition of sand as captured when interrogating the ionic region.

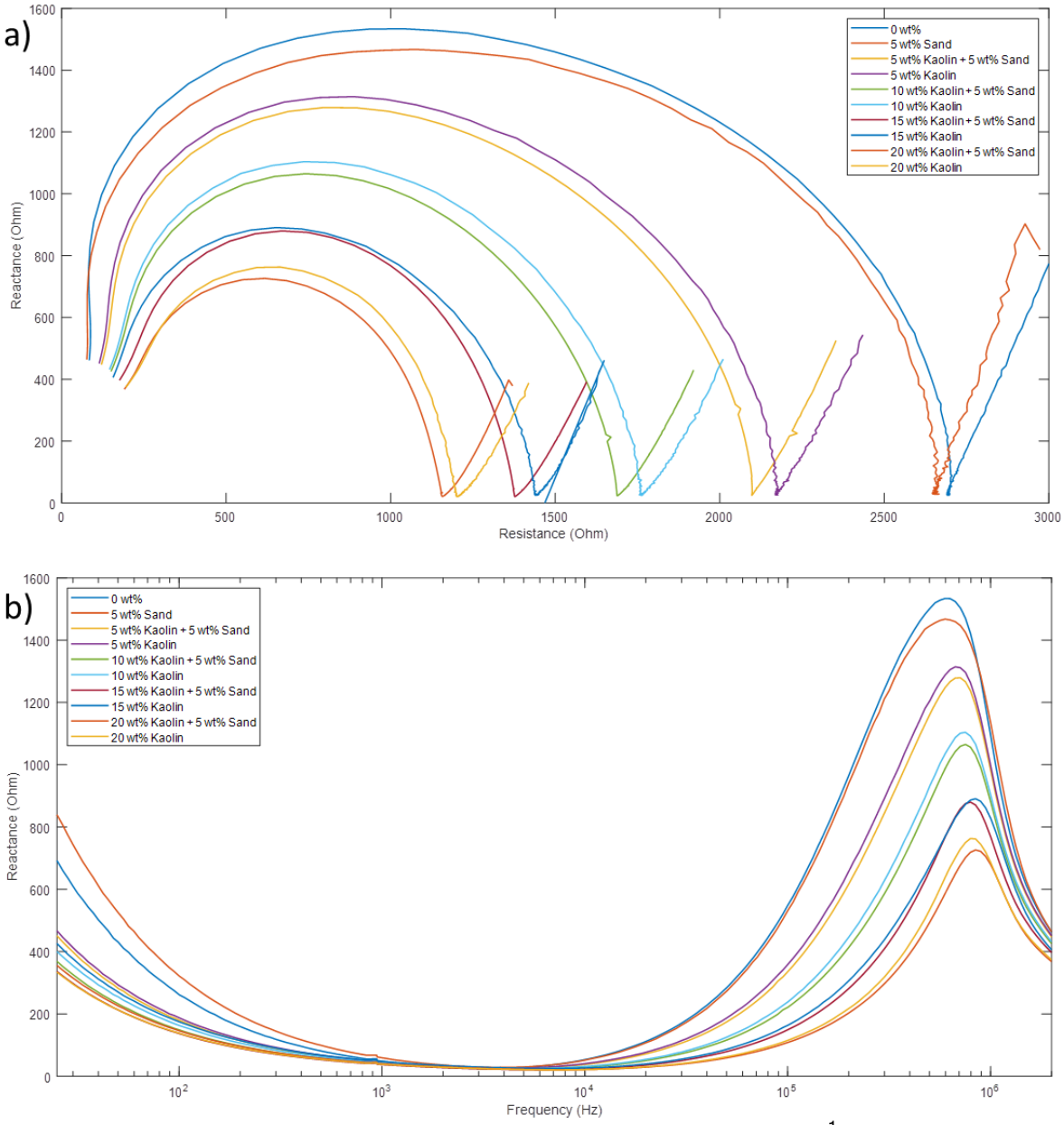

Figure 6.13 Reactance of a multi-component kaolin slurry – 0.15 mS cm^{-1}, pH 7: a) Cole-Cole plot; b) reactance as a function of frequency

Subsequently, to effectively capture the changes in ionic behaviour, the relative changes in reactance are extracted within the frequency range of 20 – 200 Hz, with forty points per decade selected. The polarisation and surface behaviour are then interrogated within the relative high frequency region, 200 kHz – 2 MHz, with the susceptibility normalised across this region using a similar logarithmic sweep. This gives rise to a similar signal to that depicted in Figure 6.14a, for a multi-component kaolin-sand slurry in a 0.15 mS cm^{-1} aqueous phase. The removal of 120 frequency measurements greatly increases the temporal resolution of

this technique and enables focusing upon spectral areas of interest. Furthermore, the frequencies which are no longer interrogated lie within the order of 10^2 – 10^5 Hz with information within the centre of this frequency range able to be captured by EIT measurements, if required.

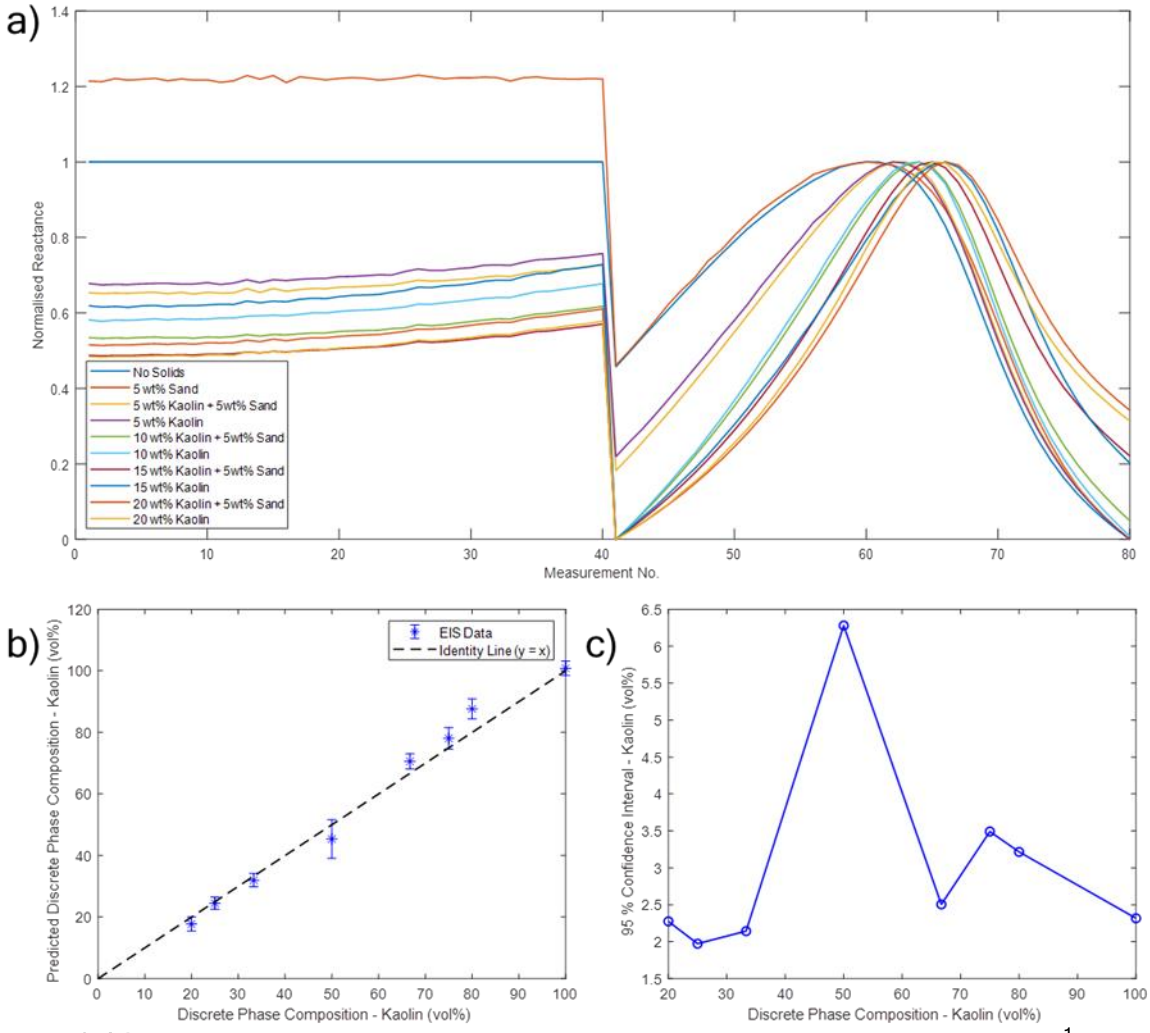

Figure 6.14 Prediction of the composition of a binary kaolin-sand – 0.15 – 10 mS cm^{-1}, pH 5.5 – 8.5: a) reactance signal; b) parity plot comparing the predicted with measured slurry composition; c) 95 % confidence interval of predicted slurry composition

After employing the initial neural network which is capable of accurately characterising whether kaolin, sand or multi-component slurry is present, these eighty relative reactances were utilised alongside the continuous phase conductivity as inputs to a second continuous neural network model. This network was identical to the optimised continuous neural network

described in Section 5.2, with forty neurons exploited alongside a sigmoidal transfer function within the hidden layer and a single output neuron accompanied by a linear transfer function. From this supervised training machine learning technique, the composition was able to be characterised with a RMSE of 6.43 wt% for a binary kaolin-sand mixture. When performing a linear regression of the measured composition compared to the predicted composition, the gradient was found to be 0.98, demonstrating linearity, with the R^2 of 0.9833. This is depicted within the parity plot in Figure 6.14b. Whilst this technique is highly promising and would enable the optimisation of the non-nuclear alternative to the density measurement, it is acknowledged that implementation into industrial processes may prove to be difficult, due to the inclusion of a secondary measurement technique.

6.7 Continuous Phase Identification

As stated throughout this chapter, an understanding of the in-line continuous phase conductivity is also vital in the optimisation of the EIT density measurement for appropriate algorithm and reference selection and voltage compensation. Whilst a conductivity probe is sufficient and are typically fitted into a number of installations, there are a number of drawbacks. To function appropriately, the conductivity probe is required to be submersed in the continuous phase without the presence of solids with access to this often unavailable in-line at the EIT sensing location. It is highly unlikely that the continuous phase stored elsewhere during processing is reflective of that flowing through the EIT sensor with an integrated approach highly desirable within dredging applications.

The novel Electrical Impedance Fingerprint technique, described in Chapter 5, can be adopted to identify the continuous phase conductivity and employed simultaneously with EIT densitometry. The 104 phase measurements initially appear independent of solids addition in dispersed phase flows; this is demonstrated in the parity plot, Figure 6.15, for a continuous phase of 0.15 mS cm^{-1}. Based upon an average AIC of -465.6, a linear relationship exists

between the phase measurements when both solids are present and not present. A linear regression of the phase measurements with and without solids, yielded correlation coefficients of 0.9982, 0.9975, 0.9970 and 0.9973 for 5, 10, 15 and 20 wt% kaolin additions, respectively. In each instance the p-values for the fitting were seen to be less than 0.001, demonstrating that the variables observed a high level of statistically significance. Alongside such linearity, the gradient of the aforementioned fittings were on average 1.000 indicating the magnitude of the phase fingerprint is identical.

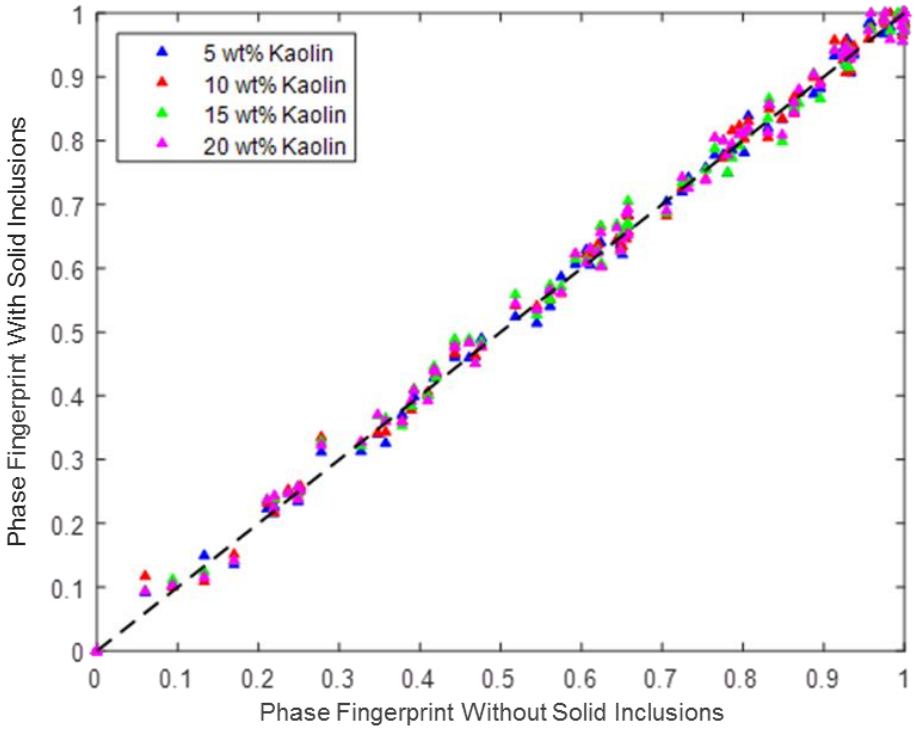

Figure 6.15 A parity plot demonstrating the impact of kaolin addition upon the Electrical Impedance Fingerprint

A two-layer feedforward neural network with a hidden layer consisting of forty neurons and a sigmoidal transfer function was again selected. A single neuron was selected as the output layer with a linear transfer function to provide a continuous conductivity. This network architecture was exploited alongside supervised machine learning techniques to form a predicting tool to extract the continuous phase conductivity which was measured using a HANNA conductivity probe. This network architecture is depicted in the previous chapter, Figure 5.7. A comparison was additionally made to traditional machine learning algorithms

using the bootstrap aggregated trees algorithm with thirty decision trees selected to ensure that artificial neural networks are the optimal predicting tool within this study. This was initially utilised to monitor the conductivity of continuous phase with and without the inclusion of solids for the conductivity range, 0.15 – 30 mS cm^{-1}.

The dataset was segregated into according to the newly developed EIF protocol, as described in Chapter 5, with 70 % selected as the training dataset. This training dataset consists of 34,300 electrical impedance fingerprint measurements which encompass 90 slurry compositions whose discrete phases consist of kaolin, sand, or both. Of these systems, the largest inclusion of solids equated to 28 vol% which encompasses the majority of the operational range of EIT densitometry, 0.5 - 35 vol%, and consequently provides a comprehensive analysis of any developed algorithms. Across the entire dataset, the RMSE error was found to be 0.055 mS cm^{-1} demonstrating a highly accurate prediction. This represents an improved performance over traditional machine learning techniques with a bagged decision tree algorithm possessing a RMSE of 0.094 mS cm^{-1}. The selection of multi-layer feedforward neural networks for use within all EIF applications irrespective of the interrogated media is reinforced.

As highlighted within a parity plot, Figure 6.16a, this derived artificial neural network exhibits linearity with the gradient found to be 1.001 with a y-intercept of 3.2 x 10^{-5} mS cm^{-1}. Moreover, the associated correlation coefficient of this linear regression has been found to be 0.9996. In addition to this, the 99% confidence interval, CI_{99}, has additionally been monitored with the calculated based upon a normal distribution, as in Eq. 5.8, with these values depicted in Figure 6.16b. From this figure, it has been demonstrated that the maximum CI_{99} was 0.127 mS cm^{-1} which represents just 0.44 % of the measured conductivity, to demonstrate the lack of uncertainty in the measurement. This linear comparison approach is justified due to an extremely negative AIC of -41198 with the repeatability of this technique demonstrated by 0.049 % of the entire dataset classified as outliers. Upon completing training, this model is capable of accurately making predictions of continuous phase

conductivity at a temporal resolution of 28,000 Hz. With this system parameter for EIT densitometry 0.5 Hz, when the standard baudrate of 9.6 kHz is selected, EIF can truly be considered as a real-time, in-situ, continuous phase conductivity measurement for use in optimising the non-nuclear measurement of density. Despite already high performance, it must be acknowledged that the performance of the system can be increased further when the conductivity range is segregated into two different predictive models, $0.15 < \sigma_c < 10$ mS cm^{-1} and σ_c in excess of 10 mS cm^{-1}. This can be segregated based upon the desired operational range of the process with the former extracting capable of continuous phase conductivity with a RMSE of 0.024 mS cm^{-1}.

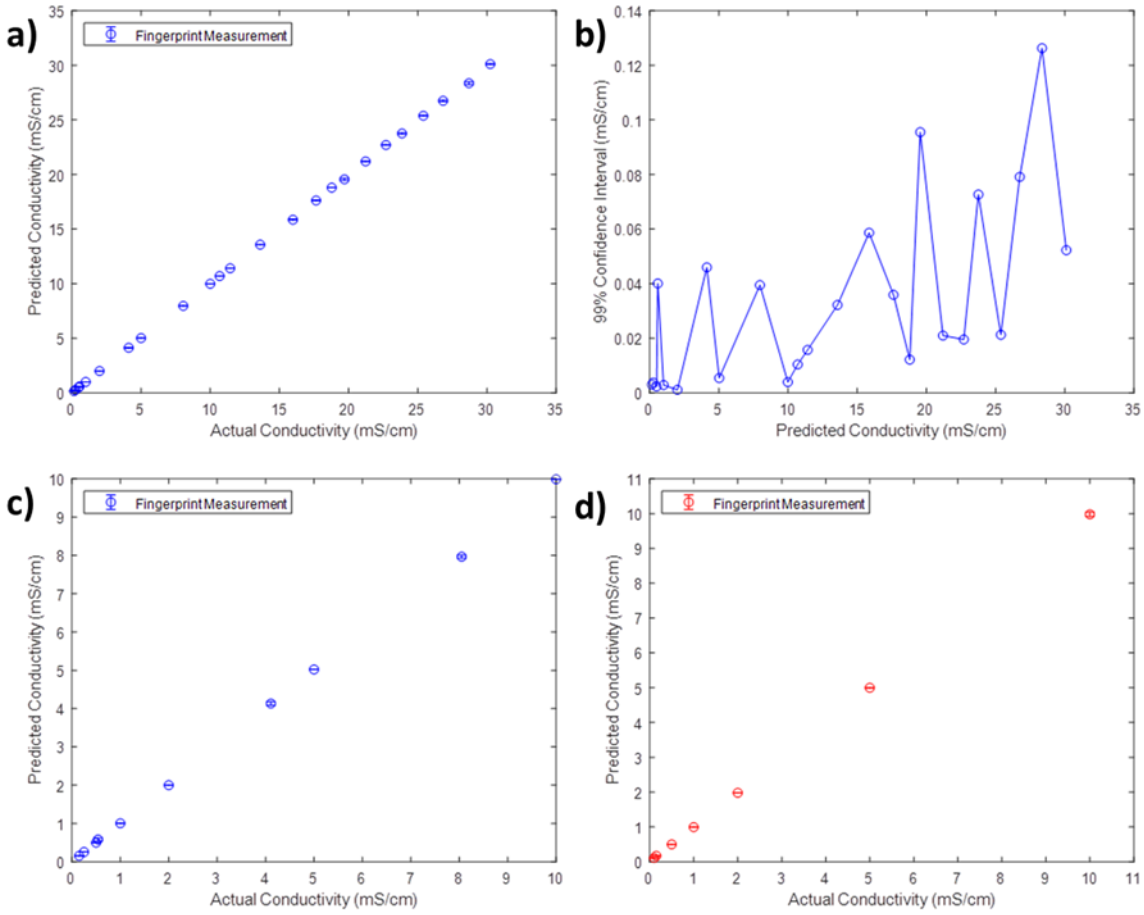

Figure 6.16 Continuous phase conductivity model: a) parity plot; b) 99 % confidence intervals; c) parity plot when no solids are added; d) parity plot when solids are added

To demonstrate the independence of EIF to material inclusions within dispersed flows for the measurement continuous phase conductivity, the datasets were segregated into those containing solids and those which did not. The previously derived neural network for the range of 0.15 – 10 mS cm^{-1}, was first applied to aqueous solutions where no solids were present with an associated RMSE of 0.026 mS cm^{-1} determined. Whilst this error is greater than the original model it represents an increase in error of 0.002 mS cm^{-1} ensuring it is able to provide a significant enhancement in the accuracy of EIT densitometry. Such a minor reduction in performance highlights the suitability of the algorithm to extract continuous phase conductivity irrespective of whether solids are present or not. This is reflected in the linearity of the parity plots presented in Figures 6.16c and 6.16d which represent the predicted continuous phase with and without solid inclusions, respectively, when the same algorithm is employed.

A limiting factor of other technologies which are applied to non-nuclear density measurement is a lack of robustness to the harsh environment which they are exposed to; this is especially prevalent in dredging operations (Batey, 2012). In some circumstances, electrodes may become inactive and no longer provide phase information. To mimic this, the phase information associated with the failure of both a single electrode and two adjacent electrodes opposite to the current source injection was removed. These scenarios are represented in Figures 6.17a and 6.17b, respectively, and reduce the number of independent phase measurements to 66 for the scenario of two adjacent electrodes failing.

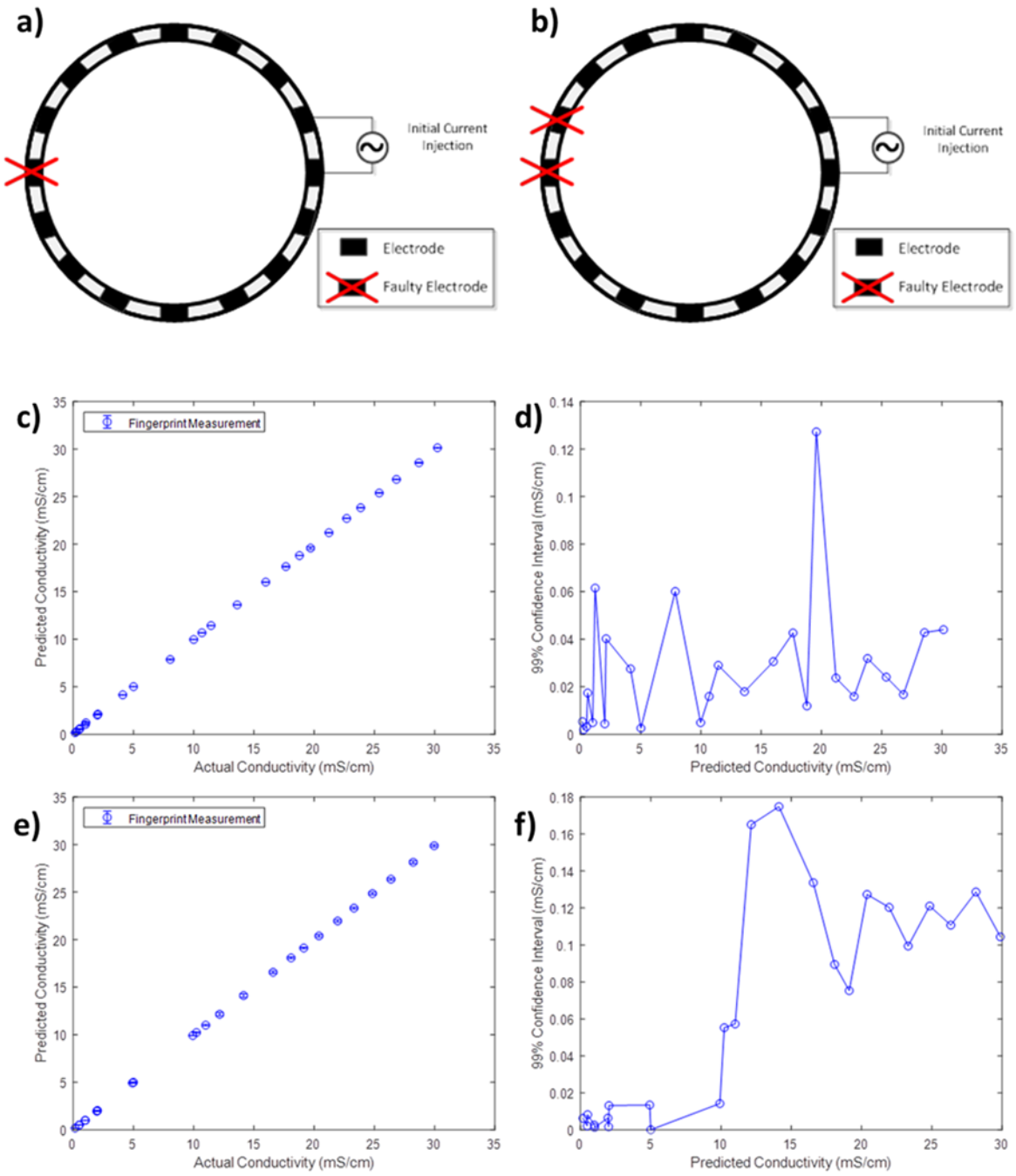

Figure 6.17 Assessment of EIF during electrode failure: a) single electrode failure (SEF); b) two-adjacent electrode failure (AEF); c) SEF parity plot; d) SEF 99% confidence intervals; e) SEF parity plot; f) SEF 99% confidence intervals

Initially, it was attempted to fit the previously developed model to the new fingerprint, with the inactive measurements fixed to 0. As anticipated, this yielded a much reduced correlation coefficient of 0.39 when the predicted conductivity is compared to the measured conductivity

with no predicted value in excess of 22 mS cm^{-1}. Thus, in both instances new networks were trained to generate significant improvements in the predictive behaviour. In the case of a single electrode failure (SEF), performance was analogous to that without electrode failure with a slightly improved RMSE of 0.049 mS cm^{-1} observed. A minor increase in the maximum CI_{99} was witnessed which was found to increase to 0.134 mS cm^{-1}, 0.46 % of the measured value, to demonstrate low uncertainty within the measurement. The negligible reduction in accuracy with the removal of inputs to the neural network presents an opportunity to further optimise EIF with respect to temporal resolution and computational efficiency. However, it is recommended that all 104 measurements are utilised in the majority of cases as the model is most robust and already considered adaptive.

A similar analysis can be repeated when two adjacent electrodes are inactive (AEF) with an increase in RMSE observed to 0.078 mS cm^{-1} and maximum CI_{99} of 0.178 mS cm^{-1}. Despite this increase this algorithm is still capable of accurately and repeatedly capturing the in-line continuous phase conductivity despite the removal of 37 % of the inputted phase information. This behaviour is captured in Figures 6.17c to 6.17d and Figures 6.17e to 6.17f for a SEF and AEF, respectively. It must additionally be noted in the latter scenario, if the inactive electrodes are no longer adjacent the number of measurements will alter ensuring the novel networks are unable to be applied; however, this would also be problematic for the primary EIT applications. This confirms that the EIF technique is not only promising, but also extremely robust to the harsh conditions exhibited during some hydraulic conveying systems, enhancing the applicability of EIF. It must be acknowledged that this setup would require an electrode self-check system to be implemented to appropriately select the secondary predictive neural networks.

Whilst nuclear density meters are often oriented vertically, it is acknowledged that the density measurement may be performed horizontally. In such transport setups an increase in the number of flow regimes occurs with bed flows likely. The presence of a large bed impacts upon the electrical impedance fingerprint with the uniform parabolic phase measurements

disturbed; the phase information for dispersed and a sliding beds flows are depicted in Figures 6.18a and 6.18b, respectively.

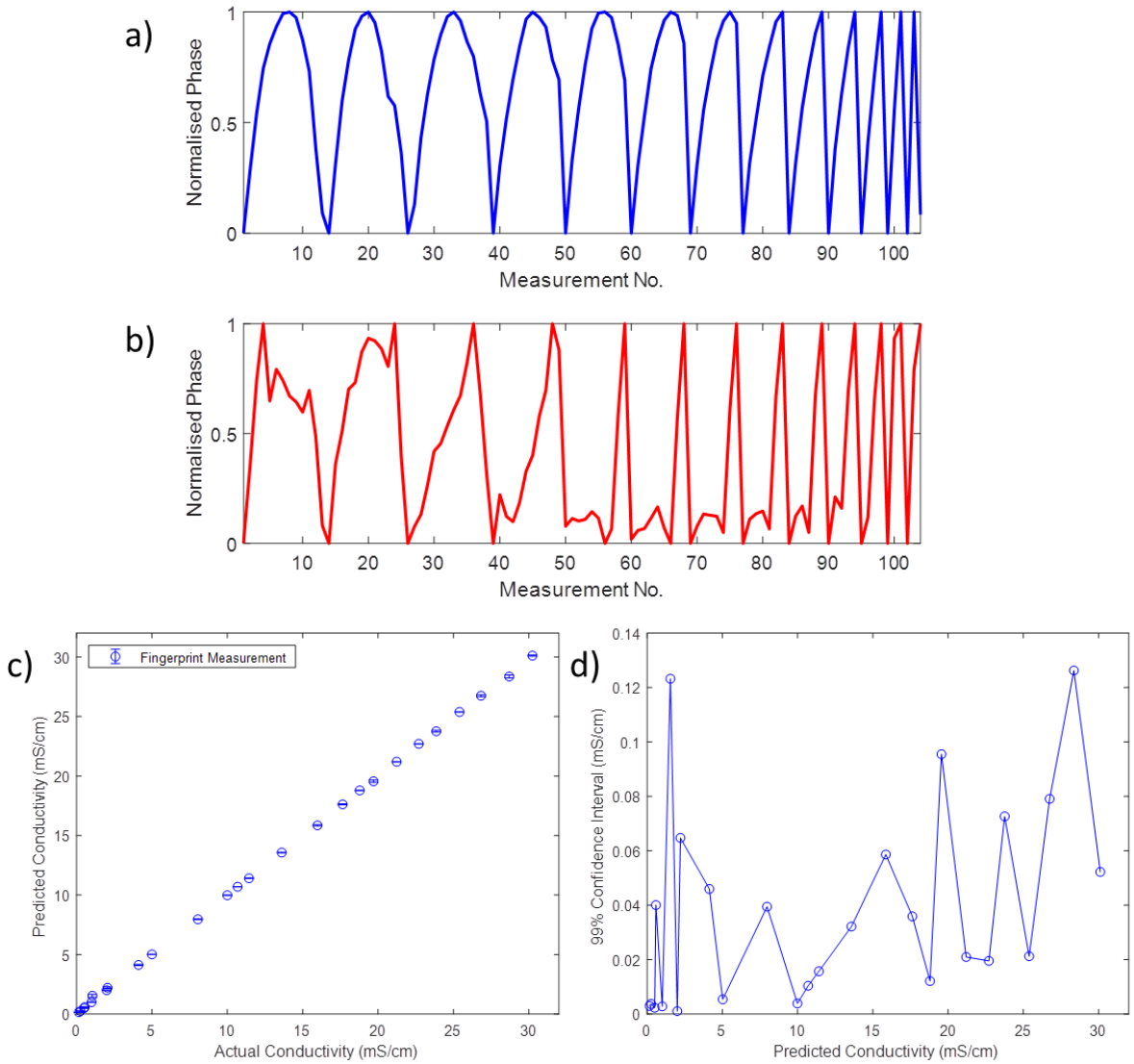

Figure 6.18 Electrical Impedance Fingerprint in different flow regimes: a) dispersed flow fingerprint – 0.5 mS cm^{-1}; b) horizontal bed flow fingerprint – 0.5 mS cm^{-1}; c) prediction of continuous phase conductivity in bed flow; d) confidence intervals in bed flows

As anticipated previously, this presents an opportunity of EIF to extract critical process information such as the flow regimes present multiphase systems across a wide range of unit operations i.e. solid-liquid mixing in stirred vessels. In the case of hydraulic transport, the flow regime is able to help inform process decisions with the pump efficiency able to be maximised. With the maximum measurable solids content 35 vol%, the maximum bed height

can be considered as 43.2 % of the diameter and hence the measurements from the top electrodes alone may be interrogated as they are present within a relatively dispersed phase. Using a similar approach the lower half measurements may be removed with only 8 – 13 and 89 – 104 points interrogated. Using this relatively small amount of phase information, a correlation coefficient of 0.998 is still obtained with a RMSE of 0.158 mS cm^{-1} to demonstrate the applicability of this technique to horizontal bed flows; this behaviour is depicted in Figure 6.18c. Utilising the null hypothesis, the p-values obtained from both parameter estimate, effect testing and variance analysis are below 0.001 indicating a high statistical significance between the predicted and monitored conductivity variables.

The capability of this technique can be adapted to select only the lower measurement electrode to initially identify when a partially filled pipe is present during hydraulic transport. Subsequently appropriately measurement protocols may be selected to enhance the integrity of the data and resultant outputs; this is a common state during dredging operations (Miedema, 2015). Upon selecting this protocol, the continuous phase within a partial pipe can be detected to further enhance the capability of EIT operating within hydraulic transport applications.

In typical hydraulic transport applications, the pipes can be up to a metre in diameter and hence an understanding impact which scaling up has upon the in-line continuous phase conductivity measurement is vital. To do so, a number of additional measurements were performed upon 16 electrode circular arrays with the following pipeline diameters: 0.102 m, 0.152 m, 0.203 m and 0.305 m. Across these sensor geometries, the conventional electrical impedance fingerprint is observed with a uniform parabolic shapes observed in low admittivity media. This is reflected in Figure 6.19a which depicts the impedance fingerprint for a 0.15 mS cm^{-1} aqueous solution in sensors of diameter 0.0254 m and 0.305 m. This similarity demonstrates the applicability of EIF to industrial pipeline setups. However, when performing a linear regression to compare individual measurements points between two sensing geometries the correlation coefficient was found to be 0.9062. Whilst similar, this ensures a

model developed upon a 0.0254 m sensor is unable to be directly applied to one with a diameter which is twelve times greater; in this scenario, the resultant RMSE would be 0.98 mS cm^{-1}, which is of insufficient accuracy. Accordingly, separate models were trained that observed RMSEs of 0.066 mS cm^{-1}, 0.055 mS cm^{-1}, 0.014 mS cm^{-1} and 0.047 mS cm^{-1} for sensors of diameter 0.102 m, 0.152 m, 0.203 and 0.305 m, respectively. In addition, the minimum correlation coefficient of 0.9995 demonstrates behaviour analogous to the previously tested sensor and hence scalability of EIF across a range of sensors.

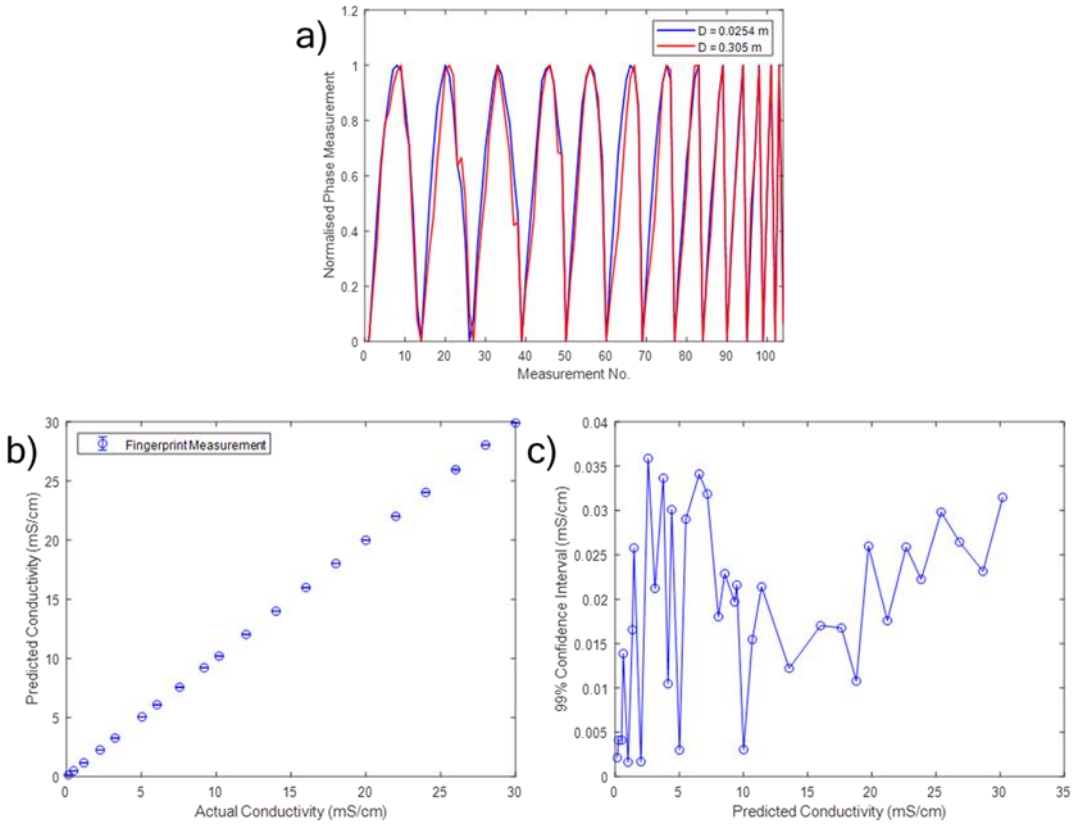

Figure 6.19 Scalability of EIF: a) comparison of electrical impedance fingerprint for sensor diameters – 0.0254 m and 0.305 m; b) parity plot of a single model across all sensor diameters; c) 99% confidence interval for the single model

Whilst data obtained from a single sensor geometry is unable to be directly applied to a sensor of a different diameter, data may be collected from all sensor diameters and included into the training data to develop a single model for all sensor geometries. This improves the simplicity of the technique with a single model able to be applied prior to the installation of the

sensor. Once derived, the RMSE was 0.070 mS cm^{-1} with a correlation coefficient of 0.9995, when fitted to the identity line across the aqueous phase conductivity range of 0.125 – 30 mS cm^{-1}, as demonstrated in Figure 6.19b. Despite a minor reduction in accuracy, exploiting a single model across the sensing range is advantageous, improves computational requirements and drastically reduces the requirements of training. The uncertainty in the measurement was additionally monitored with the CI_{99} depicted in Figure 6.19c. From this study, the greatest CI_{99} was found to be 0.0358 mS cm^{-1} to demonstrate low uncertainty in the measurement. This highlights the applicability of EIF to monitor continuous phase conductivity, robustly and accurately across a wide range of sensor geometries. As the continuous phase conductivity is required in the identification of the discrete phase, this ensures that both measurements are able to be performed in-line greatly enhancing their capabilities.

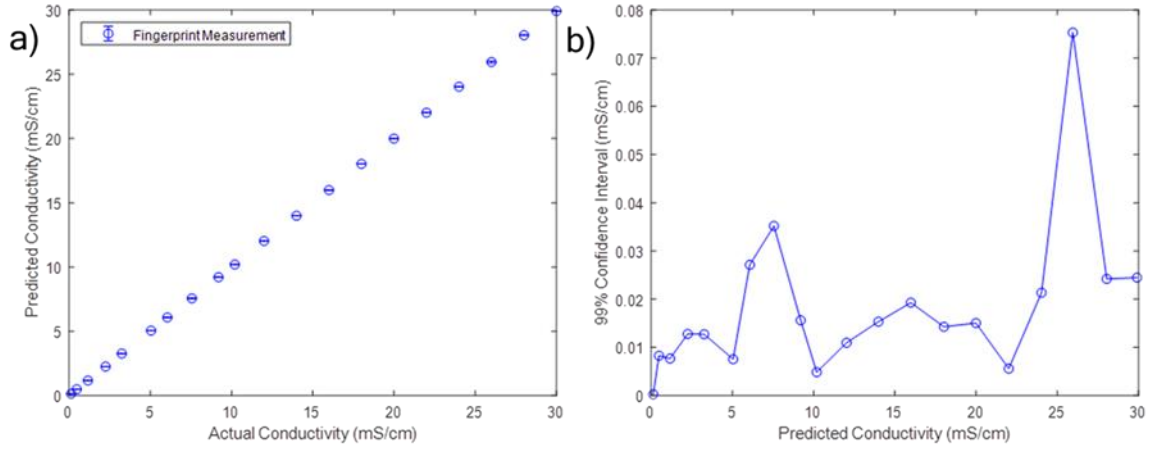

Figure 6.20 Linear in-line continuous phase conductivity prediction: a) parity plot; b) 99 % confidence interval

Typical setups within hydraulic conveying systems employ a circular arrangement; however, the ability to monitor continuous phase conductivity using linear arrays has also been investigated. Despite the electrical impedance fingerprint being saw-tooth in nature, and not uniformly parabolic, the linear array was able to capture the continuous phase conductivity effectively. This yielded a RMSE of 0.017 mS cm^{-1} which represents a minor improvement to

that obtained from the circular array. An improvement is also observed in the maximum confidence interval of 0.072 mS cm^{-1}; this is reflected in the parity plots depicted in Figure 6.20a and 6.20b. Linearity was additionally observed within this model, with a linear regression with a gradient of 1.002 and y-intercept of -0.0039 yielding a correlation coefficient of 0.9999. This highlights the flexibility of this in-line measurement technique to monitor continuous phase conductivity with such arrays able to be retrofitted into existing installations for additional applications of this technique i.e. monitoring the dissolution of solids in stirred tanks. The concept of tailored linear arrays, explored in Chapter 3, may also be employed with this information able to be targeted to regions of interest. In horizontal bed flows, such arrays may be utilised to target phase information to the upper pipe region, with the appropriate selection of array size. The upper pipe region is typically sparse in solids with the phase information then be employed more effectively to monitor continuous phase conductivity.

6.8 Conclusions

In hydraulic transport operations, the knowledge of density and flow parameters is vital for the optimisation of their performance. Typically, densitometry exploits the attenuation of nuclear sources to extract the discrete phase volume and ultimately slurry density. Due to the radioactive nature of these techniques there are often both safety and economic concerns associated. Electrical Resistance Tomography (ERT) has been established as a robust, non-nuclear density measurement within marine dredging applications. However, when conveying colloidal clay dispersions in continuous phases of lower conductivity, the complex surface phenomena of clays results in large inaccuracies in the measurement.

Accordingly, the electrical properties of kaolin and sand slurries were monitored using Electrical Impedance Spectroscopy (EIS) to gain an initial understanding of their behaviour. To capture typical operating conditions, the conductivity and pH of the continuous phases

were varied within the region of 0.15 – 10 mS cm^{-1} and 5.5 – 8.5, respectively. When the continuous phase conductivity is low, 0.15 mS cm^{-1}, an exponential relationship was observed between the kaolin volume fraction and relative change in conductivity. Via manipulation of the Maxwell-Garnett equation, the contribution of surface conductivity was found to be 15.75 % when 35 vol% of kaolin is added. Whilst this is large, upon careful optimisation of the discrete phase input, the root mean squared error in the density measurement was reduced to just 3.8 kg m^{-3}. As this represents 0.174 % of the measurement, this lies within the desired accuracy of ± 1 % for high value dredging applications. The reduction of this error demonstrates that the Maxwell-Garnett and Bruggeman effective media approximations are still able to be utilised in EIT densitometry when surface properties of the discrete phase are prevalent. A similar relationship was observed in the imaginary component of impedance; however, the relative change in susceptibility for an identical kaolin addition was increased by a factor of 2.76. Under these conditions, if the relative susceptibility was interrogated alone, the sensitivity of Electrical Impedance Tomography (EIT) densitometry could be enhanced accordingly.

The susceptibility was additionally found to be vital when an increase in ionic concentration yielded a continuous phase conductivity of 0.5 mS cm^{-1}. Due to contributions in the surface conductivity, no discernible relationship was observed between conductivity and kaolin addition with multiple minima observed to ensure that unique solutions are unable to be obtained. However, when exploiting relative changes in susceptibility an approximately linear relationship is witnessed, ensuring that densitometry is able to be performed within this region enabling the river and reservoir markets to be accessed by the sponsoring company.

As the conductivity of the aqueous phase increases, the contribution of surface conductivity diminished with conventional ERT measurements able to be performed. In such measurements, it is often assumed that the solids are non-conductive. Whilst this assumption has been validated when conveying sand, when it is applied to kaolin slurries the error in density can be as great as 352 kg m^{-3}. Thus, there is a requirement to identify the in-line

solids which are being conveyed during hydraulic transport. The non-conductive assumption provides an appropriate error in both kaolin and sand conveying once the continuous phase conductivity is in excess of 16.3 mS cm^{-1}; this validates the positive performance witnessed in existing marine dredging installations in which the continuous phase conductivity is often in excess of 30 mS cm^{-1}. Despite this, there is also a requirement to determine the in-line continuous phase conductivity without the inclusion of solids to ensure the appropriate analysis protocol can be employed.

The obtained EIS data was then compared to Electrical Impedance Tomography (EIT) measurements. With the exception of continuous phases of 0.5 mS cm^{-1}, a linear regression between relative changes in EIS and EIT measurements observes an average correlation coefficient of 0.974. This ensures that the information obtained from EIS can be directly employed to EIT measurements. Whilst the magnitude of phases obtained from EIS and EIT differ greatly, as demonstrated previously, a tomographic approach to phase measurements was found to yield vital information. To effectively interrogate the low conductivity media novel phase and susceptibility tomograms have been developed with the latter able to improve the sensitivity of EIT densitometry by a factor of ten. Moreover, this tomogram is capable of deriving a relationship between the average of computed susceptibility pixels and kaolin content, when the continuous phase conductivity is 0.5 mS cm^{-1}. This enables the operational range of this non-nuclear densitometry technique to be increased with the minimum operable aqueous conductivity of EIT densitometry lowered to 0.15 mS cm^{-1} for both sand and kaolin slurries.

Derived from a pixel-wise division of the susceptibility tomogram by the conductivity tomogram, the phase tomogram also affords new capabilities in discrete phase identification and the dispersion of solids in multi-component slurry systems. However, this technique is limited to characterise whether kaolin or sand is the most prevalent within the discrete phase, with appropriate algorithms able to be selected from this to optimise the density measurement. Phase information obtained from EIS measurements was then utilised to

demonstrate the capability of multi-frequency EIT (mfEIT) techniques to characterise the materials present within the discrete phase. In this instance, logarithmic phase information, captured at two points per decade was utilised as inputs to a two-layer feedforward neural network (TLFFNN); the continuous phase conductivity was additionally utilised as an input. The network architecture consisted of a hidden layer of forty neurons and a sigmoidal transfer function with the hidden layer containing three neurons to classify if the solids present are sand, kaolin or multi-component slurries. From this supervised learning technique, these categories were able to be classified with 97.3 % accuracy across the continuous conductivity range of 0.1 – 10 mS cm^{-1}. This accurate classification removes the assumption of non-conductive solids being present when a conductive material is being transported. Accordingly, the associated error in the density measurement of 352 kg m^{-3} is removed with the greatest error attributed to surface conductivity which can be minimised to 3.8 kg m^{-3} vastly increasing the performance of EIT densitometry.

From such mfEIT measurements, there was insufficient information to effectively extract the composition of multi-component slurries. To do so, a targeted approach to EIS was employed; this requires a secondary measurement of EIS to be performed simultaneously with EIT. At relatively low frequencies, the relative change in electrical properties is capable of capturing the ionic behaviour, whilst higher frequencies can be attributed to polarisation processes which are more prominent in kaolin. Accordingly, the relative change in susceptibility was monitored between the frequency range of 20 – 200 Hz, at forty points per decade. A similar logarithmic sweep of the susceptibility was monitored between 200 kHz and 2 MHz with the reactance normalised across this frequency range. Alongside these eighty spectral measurements, the continuous phase conductivity was inputted to a TLFFNN, once again. The hidden layer network architecture was identical to the discrete phase classification; however a single output neuron was selected for a continuous output. This once again yielded a highly accurate measurement technique with a RMSE of 6.4 wt%. When performing a linear regression of the measured and predicted variables, the optimal fitting was found to be linear, based upon the Akaike Information Criterion.

The most critical measurement in the optimisation of EIT densitometry, as highlighted throughout this Chapter, is a robust, in-line continuous phase measurement. The Electrical Impedance Fingerprint, described in detail in Chapter 5, was seen to be independent of solids addition in dispersed flows. This is reflected by correlation coefficients of 0.9982, 0.9975, 0.9970 and 0.9973 between the 104 phase measurements without the inclusion of solids and the addition of 5, 10, 15 and 20 vol% kaolin, respectively. Within the range of 0.1 – 30 mS cm^{-1}, the continuous phase conductivity was able to be predicted with a RMSE of 0.055 mS cm^{-1} across approximately 50,000 data frames which included a number of frames where solids were present. This technique is additionally applicable to linear arrays which demonstrate minor improvements to circular arrays with the RMSE of 0.017 mS cm^{-1} and the maximum 99 % confidence interval reduced from 0.127 mS cm^{-1} to 0.072 mS cm^{-1}. Within some installations, such as agitated vessels, the linear protocol is preferred as it is able to be retrofitted into existing equipment. This technique has also been demonstrated to be scalable across the sensor diameter range of 0.0254 – 0.305 m and robust with a minor reduction in performance when two electrodes become inactive. It must be acknowledged, that during bed flow, the addition of solids gives rise to alterations in the Electrical Impedance Fingerprint with a fixed continuous phase conductivity. However, with manipulation of the measurements the continuous phase conductivity is still able to be accurately predicted with a RMSE of 0.31 mS cm^{-1}. This affords an opportunity for Electrical Impedance Fingerprinting (EIF) to be able to characterise flow regimes within both pipelines and stirred vessels which can be utilised to optimise pumping and stirrer efficiency.

6.8.1 Future Work

With respect to the application of dredging, there has been vast enhancement in the understanding and development of EIT when dredging multiphase systems. However, there is a requirement to transition this information to industrial scale measurements, with the developed algorithms validated, off-line, upon data acquired from functioning EIT installations in operation. At present, the industrial EIT platform used in such measurements is only able

to record the modulus of the real and imaginary components, not the individual components. To extract such components, there is a requirement for the sponsoring company to develop of the industrial protocol which is able to obtain the raw voltage measurements for both the real and imaginary components.

Despite the novel phase tomogram providing some discriminating power, it has been found that there is a requirement to develop a multi-frequency EIT system if the composition of the discrete phase is to be wholly characterised. This complete characterisation would ensure that the errors in the density measurement which arise are entirely minimised. Such a development would require extensive development of both hardware and software to be undertaken. Nahvi and Hoyle (2008) demonstrated a successful feasibility study of a multi-frequency EIT system based upon a chirp signal. This would also provide an enhancement to existing EIT applications with the ability to characterise multi-component slurry systems with greater spatial resolution.

The neural networks characterisation techniques described within this chapter are to be extended further within the context of hydraulic conveying. This is likely to form a minor part of the Innovate UK grant, described in Chapter 5, with Section 6.6 providing initial confidence in the ability to detect the flow regime in hydraulic transport systems. Such setups also afford an opportunity to characterise the flow regime within multiphase systems in both pipelines and stirred vessels, which can provide vital information to inform process decisions and ultimately enhance pumping and stirrer efficiency.

6.9 References

Amrani, M.E.H; Dowdeswell, R.M; Payne, P.A; Persaud, K.C. (1998). Pseudo-random binary sequence interrogation technique for gas sensors. *Sensors and Actuators B: Chemical:* 47(1), 118-124.

Arroyo, F.J; Carrique, F; Jimenez-Olivares, M.L. (2000). Rheological and Electrokinetic Properties of Sodium Montmorillonite Suspensions II: Low-Frequency Dielectric Dispersion. *Journal of Colloid and Interface Science*: 229 (1), 118-122.

Ayranci, I; Kresta, S. M. (2014). Critical analysis of Zweitering correlation for solids suspension. *Chemical Engineering Research and Design:* 92 (3), 413-422.

Au, P; Leong, Y. (2016). Surface Chemistry and Rheology of Slurries of Kaolinite and Montmorillonite from different sources. *Kona Powder and Particle Journal*: 33, 17-32.

Barany, S: Meszaros, R; Taubaeva, R; Musabekov, K. (2015). Electrosurface properties of kaolin and bentonite particles in solutions of electrolytes and surfactants. *Colloid Journal:* 77 (6), 692-697.

Batey, R.H. (2012) A non-nuclear density meter and mass flow system for dredging slurries. *WEDA XXXII Technical Conference – Conference Proceedings: San Antonio, Texas.*

Bergaya, F; Lagaly, G. (2013). Introduction to Clay Science: Techniques and Applications. *Handbook in Clay and Science Characterisation*.

Bikerman, J.J. (1933). Surface Conduction. *Physik Chem*: 378.

Blewett, J; McCarter, W.J; Chrisp, T.M; Starrs, G. (2003). An experimental study on ionic migration through saturated kaolin. *Engineering Geology:* 70 (3), 281-291.

Cardoso, R; Dias, A. S. (2017). Study of electrical resistivity of compacted kaolin based on water potential. *Engineering Geology:* 226, 1 – 11.

Choo, H; Burns, S. (2014). Review of Archie's equation through theoretical derivation and experimental study on uncoated and hematite coated soils. *Journal of Applied Geophysics*: 105, 225 – 234.

Choo, H; Song, J; Lee, W; Lee, C. (2016a). Impact of pore water conductivity and porosity on the electrical conductivity of kaolinite. *Acta Geotechnica*: 11, 735-745.

Choo, H; Song, J; Lee, W; Lee, C. (2016b). Effects of clay fraction and pore water conductivity on electrical conductivity of sand-kaolinite mixed soils. *Journal of Petroleum Science and Engineering:* 147, 735-745.

Cruz, R.C.D; Reinshagen, J; Oberacker, R; Segadaes, A.M; Hoffman, M.J. (2005). Electrical conductivity and stability of concentrated aqueous alumina suspensions. *Journal of Colloid and Interface Science*, 579-588.

Faraj, Y; Wang, M. (2012). ERT investigation on horizontal and vertical counter-gravity slurry flow in pipelines. *Procedia Engineering:* 42, 588-606.

Golgoun, S.M; Sardari, D; Sadeghi, M; Mofrad, F.B. (2016) A novel method of combined detector model for gamma-ray densitometer: Theoretical calculation and MCNP4C simulation. *Applied Radiation and Isotopes:* 118, 246-250.

Jones, B; Goos, P. (2011). *Optimal Design of Experiments: A Case Study Approach.* John Wiley and Sons: New York.

Klein, K; Santamarina, J.C. (2003). Electrical Conductivity in Soils: Underlying Phenomena. *Journal of Environmental and Engineering Geophysics*: 8 (4), 1:11.

Kotze, R; Adler, A; Sutherland, A; Deba, C. N. (2019) Evaluation of Electrical Resistance Tomography imaging algorithms to monitor settling slurry pipe flow. *Flow Measurement and Instrumentation:* 68.

Leroy, P; Revil, A. (2004). A triple-layer model of the surface electrochemical properties of clay minerals. *Journal of Colloid and Interface Science*: 270, 371-380.

Lyklema, J; Minor, M. (1998). On surface conduction and its role in electrokinetics. *Colloids and Surfaces A*: 140, 33-41.

Markel, V. (2016). Introduction to the Maxwell-Garnett Approximation. *Journal of Optical Society of America A:* 1, 1-12.

Miedema, S. A. (2015). *The Delft Sand, Clay and Rock Cutting Model.* IOS Press BV: Amsterdam.

Mitchell, J; Soga, K. (2005). *Fundamentals of Soil Behaviour*. John Wiley and Sons Inc: New Jersey.

Nahvi, M; Hoyle, B.S. (2008). Wideband Electrical Impedance Tomography. *Measurement Science and Technology*: 19 (9), 9 - 11.

Ndlovu, B; Forbes, E; Farrokhpay, S; Becker, M; Bradshaw, D; Deglon, D. (2014). A preliminary rheological characterisation of phyllosilicate group minerals. *Minerals Engineering*: 55, 190-200.

O'Brien, R.W. (1986). The high-frequency dielectric dispersion of a colloid. *Journal of Colloid and Interface Science*: 113 (1), 81-93.

Oh, T; Cho, G; Lee, C. (2014). Effect of Soil Mineralogy and Pore-Water Chemistry on the Electrical Resistivity of Saturated Soils. *Journal of Geotechnology and Geoenvironmental Engineering*: 140 (11).

O'Konski, C.T. (1960) Electric Properties of Macromolecules: V - Theory of Ionic Polarization of Polyelectrolytes. *The Journal of Physical Chemistry*: 64 (5), 605-619

Ramaswamy, S; Raghavan, P. (2011). Significance of Impurity Mineral Identification in the value addition of Kaolin - A case study with reference to Acidic Kaolin. *Journal of Minerals and Minerals Characterization*: 10 (11), 1007 - 1025.

Schoonheydt, R.A; Johnston, C.T. (2013). Surface and Interface Chemistry of Clay Minerals. *Handbook in Clay Science and Characterisation*.

Wei, K; Qiu, C; McCormack, D; Primrose, K. (2016). ITS Dens-Itometer: An Electrical Resistance Tomography Based Densitometer. *WCIPT 8: Conference Proceedings, Brazil.*

Wei, K; Qiu, C; Primrose, K; Hazineh, W. (2018). Real time production efficiency based on measurement of flow velocity and flow profile. *Dredging Summit and Expo: Conference Proceedings.*

Wright, J; Colling, A. (1995). *Seawater: Its Composition, Properties and Behaviour.* Elsevier Science: Burlington.

Xu, J; Wu, Y; Zheng, Z; Wang, M; Munir, B; Oluwadarey, H; Schlaberg, H; Williams, R. (2009). Measurement of solid slurry flow via correlation of electromagnetic flow meter, electrical resistance tomography and mechanistic modelling. *Journal of Hyrodynamics: 21(4), 557-563*

Yukselen, Y; Kaya, A. (2003). Zeta potential of kaolinite in the presence of alkali, alkaline earth and hydrolysable metal ions. *Water, Air, and Soil Pollution:* 145(1), 155-158.

Zhao, Y; Wang, M; Hammond, R.B. (2011). Characterization of crystallisation processes with electrical impedance spectroscopy. *Nuclear Engineering and Design:* 241 (6), 1938 – 1944.

Zhao, Y; Wang, M; Hammond, R.B. (2012). Characterisation of nano-particles in colloids: Relationship between particle size and electrical impedance spectra. *Journal of Nanoscience and Nanotechnology*: 12, 1-5.

Chapter 7

Case Study: The Application of Electrical Resistance Rheometry to Personal Care and Laundry Products

Due to the successful development of Electrical Resistance Rheometry (ERR), described in Chapter 3, industrial pilot scale studies have been undertaken at a global manufacturer of home and personal care products. This case study focussed upon the characterisation of shampoos and fabric washes. The objective of this study was to directly compare rheological parameters obtained from ERR to off-line rotational rheometry and accordingly determine its suitability to operate as an in-line quality control technique for industrial fluids.

7.1 Methods

7.1.1 Materials

A wide range of personal and homecare products were selected for the industrial trial at the pilot scale, with shampoos and fabric wash the materials which are the focus of this chapter.

To analyse the rheological properties of these industrial fluids, a HAAKE Rheostress 1 rotational rheometer was employed (Thermo Fischer Scientific, USA) equipped with a smooth-walled, 1° stainless steel cone and plate geometry. Due to the thermosensitive

nature of some of the aforementioned products, a Peltier plate was utilised to hold each sample at 25 ± 0.1 °C, 30 ± 0.1 °C and 35 ± 0.1 °C. To assess the impact which the time-shear history received during processing had upon the structure, samples were collected and off-line measurements performed at each experimental flow rate. A new sample was loaded onto the rheometer for each experimental condition to minimise such effects further. Upon loading, a logarithmic shear rate ramp was applied across the shear rate range of 0.1 - 1000 s^{-1}, with 5 points per decade across 5 minutes. The obtained data was analysed using a non-linear least squares regression in the HAAKE Rheowin software, developed by Thermo Fischer Scientific, to extract the rheological parameters. This analysis was performed across the shear rate range of 0.1 - 100 s^{-1} which is reflective of the subsequent flow experiments.

7.1.2 Experimental Setup

The commercialised sensor, depicted in Figure 3.13, was installed within a recirculation loop, of pipe diameter 0.0254 m. This loop contained a 200 L jacketed vessel, agitated by an anchor impeller, the ERR setup, an electromagnetic flow meter and two digital pressure gauges (Hunang Yanheng Instrument Company, China) located 1 m apart. The jacket of the vessel was utilised to elevate the fluid temperature to 25 °C, monitored by a temperature probe at the vessel outlet, before the fluid was circulated at selected flow rates of 500 kg hr^{-1}, 750 kg hr^{-1} and 1000 kg hr^{-1}. At each of these flow rates, three ERR measurements were performed with the differential pressure measurement collected visually from each pressure gauge and then subtracted. It must be acknowledged that these pressure measurements were extremely unreliable with the fluctuations of a single pressure gauge up to 90 % of the overall differential pressure measurement. As a result, rheological parameters were unable to be computed, with the velocity profile the focus of this study. Upon completion, the fluid temperature was increased to 30 °C with the experimental protocol repeated; this was once again repeated at 35 °C.

To operate the industrial ERR measurement, the developed industrial software, described in Chapter 3, was employed with 10,000 data frames selected. Upon capturing the data in the ITS Electrical Resistance Rheometry software, the raw voltage data was exported to MATLAB to analyse numerous measurements simultaneously. Due to the importance of the differential pressure measurement, as described in Section 3.2, and the large variance in the digital pressure gauge measurements, this analysis has focussed upon a comparison of the outputted and theoretical velocity profiles.

7.2 Results

7.2.1 Fabric Wash

Under all of the process conditions, the fabric wash observed a large Newtonian plateau at low shear rates after which the structure begins to break down, > 100 s^{-1}; the data obtained from the rheometer is depicted in Figure 7.1. As this shear rate is similar to those observed in the pipe flow experiments, < 86.7 s^{-1}, the Newtonian model was selected for analysis with a parabolic profile therefore expected.

This Newtonian behaviour is observed within the velocity profile captured by ERR measurements with the correlation coefficient of the measured and theoretical velocity profile found to be 0.994, 0.992 and 0.990, for 25 °C, 30 °C and 35 °C fabric wash solutions, respectively. This is presented in Figure 7.2, which depicts the velocity profile obtained at each experimental condition. Not only does this provide initial validity to the measurement but also ensures that the experimental setup is appropriate. This ensures that the flow is irrotational with the removal of hydrodynamic entrance effects. Within this regime, the hydrodynamic boundary layer encompasses the entire pipe diameter and prevents flattening of the velocity profile; this ensures that laminar flow theory is able to be applied. The Reynolds numbers for the subsequent flow measurements were in the range of 3.58 - 23.1 with laminar flow regime observed at Re < 2,000 (Paul et al, 2004).

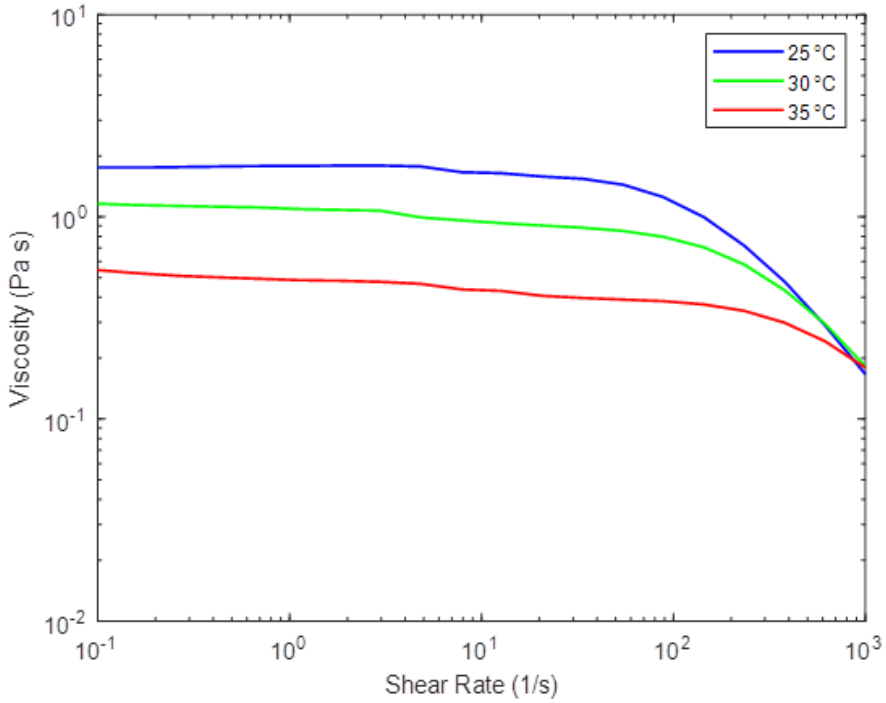

Figure 7.1 Rheological properties of fabric wash at experimental temperatures

When considering a 25 °C fabric wash solution, the velocity measurements were seen to be extremely repeatable across all of the measured flow rates. The average 99 % confidence interval across the entire velocity profile was found to be 0.0034 m s^{-1}, 0.0030 m s^{-1} and 0.051 m s^{-1}, for solutions flowing at 500 kg hr^{-1}, 750 kg hr^{-1} and 1000 kg hr^{-1}, respectively. In addition to this repeatability, the expected trend in the increase in magnitude of the measured velocity profile with an increase in the flow rate is additionally mirrored. This is demonstrated in Figures 7.2 with similar uncertainty in the measurements is observed throughout the entire temperature range which has been experimented upon.

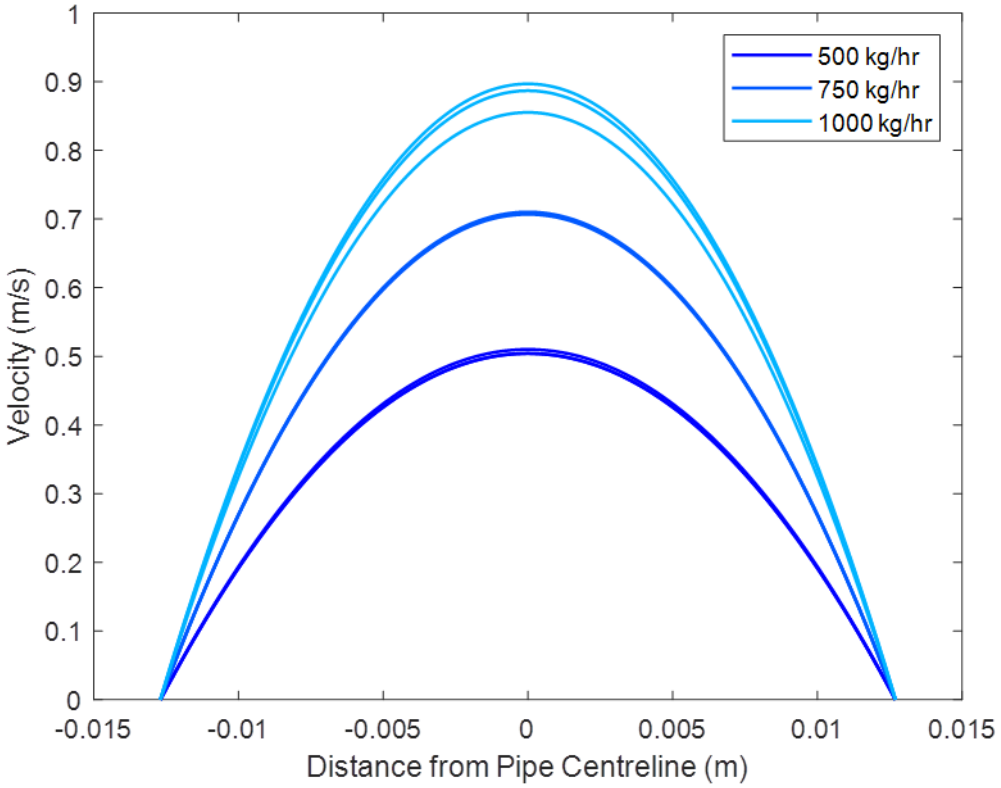

Figure 7.2 Fabric wash velocity profiles at 25 °C

Alongside demonstrating good repeatability, the fastest velocity captured within this experiment was 0.89 m s^{-1}. This is vastly in excess of the measured velocity profiles presented within Chapter 3, with a maximum velocity of approximately 0.28 ms^{-1}. The difference in captured velocity, represents an increase by a factor of 3.2, with the flow rate operational range of ERR increased proportionally for a Newtonian fluids. The flow rate may be increased further for a highly viscous shear thinning fluids. It must be acknowledged, that in order to apply appropriate rheological parameter extraction, the flow regime within the pipe must remain laminar. Nonetheless, this ensures that the operational flow rate range of the setup is increased and accordingly improves the in-plant applicability of ERR.

7.2.2 Shampoo

From off-line rotational rheometry, shampoo is seen to observe a Newtonian plateau followed by a region of shear thinning and may be described by the Carreau specific constitutive equation. When compared to fabric wash, Figure 7.3b, this region onsets at much lower shear rates, at approximately 2 s^{-1}. As the subsequent flow experiments are capable of capturing rheometric data up to shear rates in the order of 10^2 s^{-1}, the shear thinning nature will be reflected in the measured velocity profile. As demonstrated within Chapter 3, this shear thinning behaviour gives rise to a blunting of the velocity profile. This has been captured in the measured velocity profiles obtained from the ERR measurements, Figure 7.4, demonstrating the capability of ERR to distinguish between rheological properties based upon the velocity profile alone.

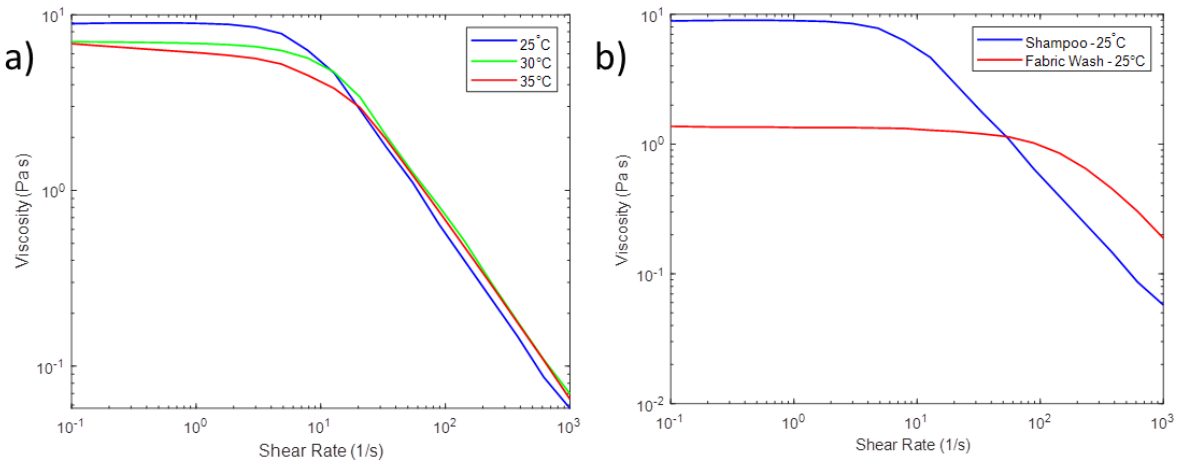

Figure 7.3 Rotational rheometry data for shampoo and fabric wash a) the dependence of shampoo rheology upon temperature; b) comparison of shampoo and fabric wash

This anticipated change in the velocity profile as a response to the rheological properties of the velocity profile is observed, demonstrating the capability of ERR to capture such rheological properties. The acquired ERR data is once again found to be extremely repeatable with a 99 % confidence interval in the velocity profile found to be 0.0032 m s^{-1},

0.0064 m s^{-1} and 0.062 m s^{-1}, for experimental flow rates of 500 kg hr^{-1}, 750 kg hr^{-1} and 1000 kg hr^{-1}, respectively. Such little uncertainty in the measurement across all experimental flow rates demonstrates that despite the increase in complexity of the monitored fluid, the confidence within the ERR velocity profile remains similar. These uncertainties additionally lie within the fluctuation range of the flow rate, based upon flow meter readings.

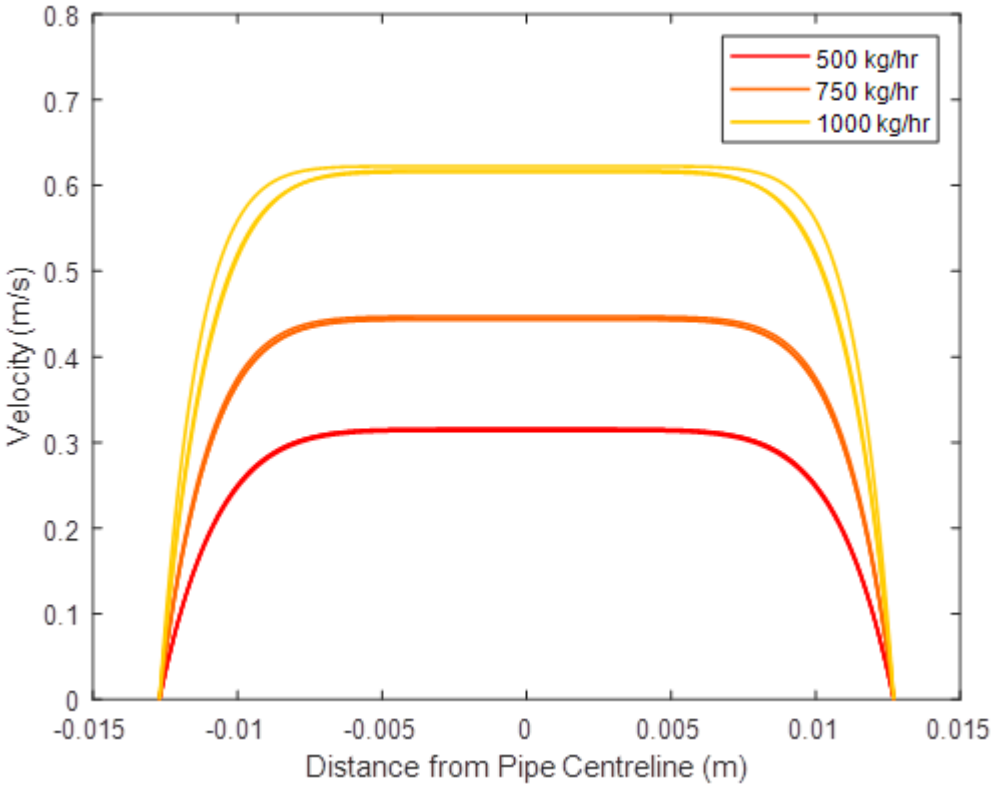

Figure 7.4 Shampoo velocity profiles

Whilst a quantitative analysis was unable to be performed due to the unsuitable differential pressure measurement, this study demonstrated that ERR is capable of distinguishing between industrial fluids of differing rheological properties. Not only are the velocity profiles in agreement with the off-line rheological data, but also are seen to be extremely repeatable throughout. This highlights the suitability of ERR for the in-situ characterisation of rheology for industrial fluids within pipes.

7.3 Conclusions

Electrical Resistance Rheometry (ERR) has been interrogated within an industrial pilot plant at a multinational manufacturer. This industrial case study focussed upon the characterisation of personal and homecare products with shampoos and fabric washes presented here. This study was performed within a recirculating flow loop with the commercial ERR sensor installed. In addition, the developed ITS ERR software was also employed to execute the measurement and analysis protocol described in Chapter 3. Due to limitations of the experimental setup, the differential pressure measurement was unable to be captured effectively and hence only an analysis of the ERR velocity profiles was performed.

Based upon off-line rotational rheometry, fabric wash was seen to observe Newtonian properties in the shear rate range of the flow experiments, with a parabolic flow profile subsequently expected. This was observed in the ERR profile across all of the experimental conditions, with the parabolic nature ensuring that hydrodynamic entrance effects were not present. Not only were the expected profiles observed, but also low uncertainty was found in the measurement with a 99 % confidence interval of 0.003 m s^{-1} obtained across the entire velocity profile. During this experiment, the maximum velocity captured was greatly increased compared to those presented in Chapter 3; this enhances the in-plant applicability of this technique.

When shampoo was interrogated, the expected blunting of the velocity profile was observed and hence in agreement with the rotational rheometer. Such findings enable the rheological properties of the two experimental fluids to be distinguished by the velocity profile alone. Once again, the ERR velocity profiles remained repeatable with the uncertainty in the profile akin to that found in fabric wash. This demonstrates that despite the increase in complexity of the measured rheological properties, the velocity profile was still capable of performing accurately. It can therefore be stipulated that the industrial ERR sensor and analysis protocol is suitable and applicable for use in industrial fluids and setups.

Chapter 8

Overall Conclusions and Future Work

Aligned with the critical process sectors of the sponsoring company, this thesis focusses upon the in-situ characterisation of product microstructures, surfactant-electrolyte systems and non-Newtonian solid/liquid mixtures using Electrical Tomography. To achieve this aim, there is a requirement to develop novel data interpretation methods and sensing techniques for each formulated product area.

8.1 Characterisation of Product Microstructures

To characterise the product microstructure, two novel techniques have been developed which extract in-situ rheological properties, within both pipes and vessels.

8.1.1 In-pipe Rheometry

The product microstructure and rheological properties of a fluid system govern both in-process efficiency and final product quality and thus are critical in chemical and physical processing. Electrical Resistance Rheometry (ERR) has been developed to characterise in-line rheological properties within pipes by cross-correlating functions of computed conductivity pixels obtained from microelectrical tomography sensors to capture the velocity profile. The acquired laminar flow velocity profiles were then validated using Particle Image Velocimetry, with the independent velocimetry techniques in excellent agreement; these measurements also acts to validate the assumptions made in the rheological extraction.

Once coupled with the measurement of differential pressure, the rheological properties were elucidated. The rheological parameters were compared to off-line rotational rheometry, with ERR possessing an accuracy of 98 % for both Newtonian and non-Newtonian fluids. Thus, it has been demonstrated that ERR offers new capabilities of true in-situ analysis of fluids relevant to formulated products with ERR capable of elevating rheometry from a quality control tool to one which is capable of optimising and controlling processes. In-pipe, spatial and temporal analyses of the pipe cross-section afford the simultaneous capture of localised and global mixing behaviour to combine two significant engineering concepts of rheology and mixing.

Due to the success of this development, ERR has been developed further with industrial sensors and software developed with a view to its commercialisation by the sponsoring company. Such industrial developments have been utilised in a pilot scale case study performed at a global manufacturer of personal and homecare products. The velocity profiles and rheological properties of shampoo and fabric wash were examined to demonstrate that ERR is amenable to industrial fluids and processes.

8.1.2 In-vessel Viscometry

ERR is the first technique to successfully demonstrate the application of tailored linear arrays to target tomographic information to process regions of interest, by simply manipulating their geometry. These principles were expanded to monitor the near-wall velocity profile within stirred vessels for the development of an inferential viscosity measurement in stirred tanks. Tailored linear arrays were utilised to resolve the axial and tangential velocity components in this region and ultimately the shear rate at the wall.

Aqueous solutions of glycerol were interrogated within a vessel agitated by an up-pumping pitched blade turbine (PBT-u). In addition to observing the expected trends in velocity with increases observed when increasing impeller speed and reducing viscosity; the typical flow fields for a PBT-u were observed with the secondary counter rotating loop of a PBT-u

captured. These anticipated flow fields were also present within Particle Image Velocimetry measurements, with PIV able to validate the velocity profiles obtained from the microelectrical tomography sensors.

The averaged shear rate at the wall was computed and coupled with the measurement of torque to act as an inferential measurement of in-vessel viscosity. Combining these two measurement techniques presented vastly improved selectivity to fluid viscosity compared to the application of a torque meter alone. The obtained results mimic the trend observed by off-line rotational rheometry; however due to underlying assumptions made within the analysis, this technique does not provide a general solution which is applicable across all geometries and impeller types. Despite this, for any fixed configuration electrical resistance sensing is capable of acting as an inferential viscosity measurement and helps afford new insights into in-vessel characterisation during mixing.

8.2 Characterisation of Surfactant-electrolyte Formulations using Electrical Impedance Sensing

A novel in-situ characterisation technique has been developed, Electrical Impedance Fingerprinting (EIF), which is capable of identifying formulations with key quality parameters then able to be subsequently elucidated. Within the 104 phase measurements attained from a 16-electrode circular Electrical Impedance Tomography (EIT) sensor, low admittivity media produce a uniform parabolic phase shape for each measurement cycle. As the admittivity of the media is increased, this progressively begins to break down until the measurement cycles are no longer discernible. Such changes have been validated using two independent EIT systems which operate with different measurement protocol ensuring that it is widely applicable.

Supervised machine learning techniques were then utilised to determine key quality parameters based upon the recognition of the Electrical Impedance Fingerprint. From a trial and error approach, artificial neural networks were selected as the training algorithms based upon the criteria of accuracy, adaptability, computational requirements and interpretability. Due to the visible variations of the fingerprint with differing formulations, deep learning techniques were not required with the optimal network architecture deemed to be a two-layer feedforward neural network.

This technique was utilised to identify forty-four sodium lauryl ether sulphate (SLES) and electrolyte formulations, due their relevance in personal care products. Within both pipe flow and vessels, EIF was seen to be highly accurate with a mis-classification rate of 0.31 % when interrogating all of the fluids. This accuracy was observed during a continuous analysis with root-mean squared errors (RMSE) in sodium chloride content of 0.022 wt% observed. Within the vessel, the mixing process was continually monitored with the sodium chloride content determined via the Maxwell effective media approximations. A linear regression of these techniques yields a correlation coefficient of 0.999, demonstrating linearity of the model and the capability of the neural networks to predict non-trained parameters.

Information obtained from EIF was combined with 'traditional' EIT to simultaneously capture mixing behaviour, such as mixing and dissolution times and visualisation of mixing phenomena, which can then be related to key structural attributes of each formulation. The application of the EIF-EIT technique was extended to the linear sensing configuration with a saw-tooth fingerprint observed for low admittivity media with high performance once again observed with respect to formulation characterisation.

The development of EIF ensures that the aim to effectively characterise surfactant-electrolyte systems has been attained. This novel data interpretation methodology enables the in-situ analysis of such systems, with the formulation able to be continuously identified. The real-time identification of the formulation may be then related to evolving key structural parameters, i.e. heat transfer coefficient and rheology, for use in process optimisation.

8.3 Characterisation of the Composition and Density of Non-Newtonian Solid/liquid Mixtures

Electrical Resistance Tomography (ERT) has been established as a robust, non-nucleonic alternative to the measurement of density in marine dredging applications. However, when conveying clay dispersions in continuous phases of lower conductivity, the complex surface phenomena of clays results in large inaccuracies in the measurement. Accordingly, the electrical properties of kaolin and sand slurries were monitored using Electrical Impedance Spectroscopy (EIS) to understand of their electrical behaviour. Large kaolin surface contributions were observed in continuous phases with low conductivity. However, via optimisation of the Maxwell-Garnett effective media approximation inputs, the RMSE in the density output was able to be reduced within the desired accuracy of ± 1 % required for high value dredging applications.

In such applications, if the imaginary component of impedance is considered alone, the sensitivity of this measurement was able to be enhanced greatly. This component, or susceptibility, was found to be vital when dispersed within a continuous phase conductivity of 0.5 mS cm^{-1}. Due to contributions in the surface conductivity, no discernible relationship was observed between conductivity and kaolin addition with density unable to be resolved. When exploiting relative changes in susceptibility a linear relationship is developed, ensuring that densitometry is able to be performed within this region.

As continuous phase conductivity increases, the contribution of surface conductivity diminished with conventional ERT measurements able to be performed. In these measurements, it is often assumed that the solids are non-conductive. Whilst valid when conveying sand, when applied to kaolin slurries the error in density was found to be large. Thus, there is a requirement to identify the in-line solids which are being conveyed during hydraulic transport.

The obtained EIS data was then compared to Electrical Impedance Tomography (EIT) measurements, with good agreement observed. A tomographic approach to phase measurements was found to be effective in interrogating low conductivity media with novel susceptibility tomograms developed to improve the sensitivity of EIT densitometry by a factor of ten. Moreover, this tomogram is capable of deriving a relationship between the average of computed susceptibility pixels and kaolin content, when the continuous phase conductivity is 0.5 mS cm^{-1}. This enables the operational range of this non-nuclear densitometry technique to both reservoir and river dredging applications and increase the market share of the sponsoring company.

Phase information obtained from EIS measurements was then utilised to demonstrate the capability of multi-frequency EIT (mfEIT) to characterise the discrete phase. In this instance, phase information was utilised as inputs to a two-layer feedforward neural network (TLFFNN); the continuous phase conductivity was additionally utilised as an input. From this supervised learning technique, these categories were able to be classified with 97.3 % accuracy across a range of continuous phase conductivities. To extract the composition of the multi-component slurries, a targeted approach to EIS was employed. Alongside spectral EIS measurements, the continuous phase conductivity was inputted to a TLFFNN to yield a highly accurate composition prediction technique.

The Electrical Impedance Fingerprint was seen to be independent of solids addition in dispersed flows. Within the range of 0.1 – 30 mS cm^{-1}, the continuous phase conductivity was able to be predicted with a RMSE of 0.055 mS cm^{-1}. This technique has also been demonstrated to be scalable across the sensor diameter range of 0.0254 – 0.305 m and robust with a minor reduction in performance when two electrodes become inactive. It must be acknowledged, that during bed flow, the addition of solids alters the Electrical Impedance Fingerprint at a fixed continuous phase conductivity. However, with manipulation of the measurements the continuous phase conductivity is still able to be predicted with an appropriate accuracy.

The in-situ characterisation of continuous phase conductivity and slurry composition may be employed to select the appropriate measurement and analysis protocols for the density measurement. This optimisation enables the market of this non-nuclear densitometry technique to be expanded to reservoir and river dredging applications and the multi-component slurry characterisation objective to be achieved.

8.4 Future Work

Whilst Electrical Resistance Rheometer (ERR) is currently being developed with a view to commercialisation by the sponsoring company, the techniques and algorithms may be utilised further. The polymer and petrochemical industries account for 62.02 % of the total rheometer market, by value, with Electrical Capacitance Tomography (ECT) capable of monitoring the in-line rheological properties of dielectric materials. The adaptation of ERR to ECT would facilitate access of this market to the sponsoring company. A potential application for the development of Electrical Capacitance Rheometry is to extract the rheological properties of drilling muds, which are utilised within the petrochemical industry to lubricate cutting tools.

The development of the ERR sensor also demonstrates the first successful application of tailored linear arrays. These sensors may be adapted to a wide range of processing applications to target tomographic information to specific process regions of interest. For example, this information may be targeted to the near-wall region of the pipe in clean-in-place (CIP) applications to determine its cleanliness. Such behaviour may be exploited in further process characterisation applications across a wide range of unit operations.

The potential industrial applications of EIF are also vast, with a wide range of process information able to be captured. This work has led to a successful, international EUREKA grant application, titled ‘Artificial Intelligence Tomography Systems’ (112422-650235). This funding will be utilised to establish and enhance the EIF technique further with a number of

target processes: formulation characterisation, multiphase flow monitoring, in pipes and vessels, and clean-in-place applications. From these studies, the aim is to gain an understanding of the extent of the information able to be captured from EIF measurements, relative to formulation and process characterisation; determine applicability to industrial processing; investigate scaling up and optimise artificial intelligence algorithms.

There is also a requirement to extend the knowledge gained from EIS and EIT measurements, regarding multi-component slurries, to real process data. Whilst a number of useful data interpretation methodologies have been developed, their application to multi-component slurries in industrial process conditions must be also interrogated.

Appendix A1

Tailored Linear Arrays – Electrical Field Penetration Depth

Preliminary experiments were performed to validate the radial positioning for each of the tailored linear array tomogram zones; this information is taken from Machin et al. (2018b). The conductivity of an aqueous glycerol solution, 75 wt%, was varied between 0.025 and 10 mS cm^{-1}, with the acquired velocity profile measured using the tailored linear arrays. These experiments were performed within the flow loop setup described in Chapter 3; the electrical resistance sensing setup and analysis outlined in Chapter 3 was also employed. As glycerol is known to exhibit Newtonian properties and observe a parabolic velocity profile, the measured velocity points were fitted to the theoretical velocity profile to determine the optimal electrical field penetration; the results displayed in Figure A1.1. A penetration factor may then be derived, Eq. A1, using the optimised radial position of each measurements and the tailored array length. Once obtained, this electrical field penetration depth is kept constant throughout all experiments conducted in Chapter 3.

$$Pentration\ Factor = \frac{Optimised\ Radius}{Sensor\ Length} \qquad (A1)$$

The ITS v5r ERT instrument is a voltage driven measurement, with the amplitude of the applied current precisely controlled based upon the fluid conductivity. Therefore, the penetration factor should remain constant irrespective of fluid conductivity; this behaviour is depicted in Figure A1.1b.

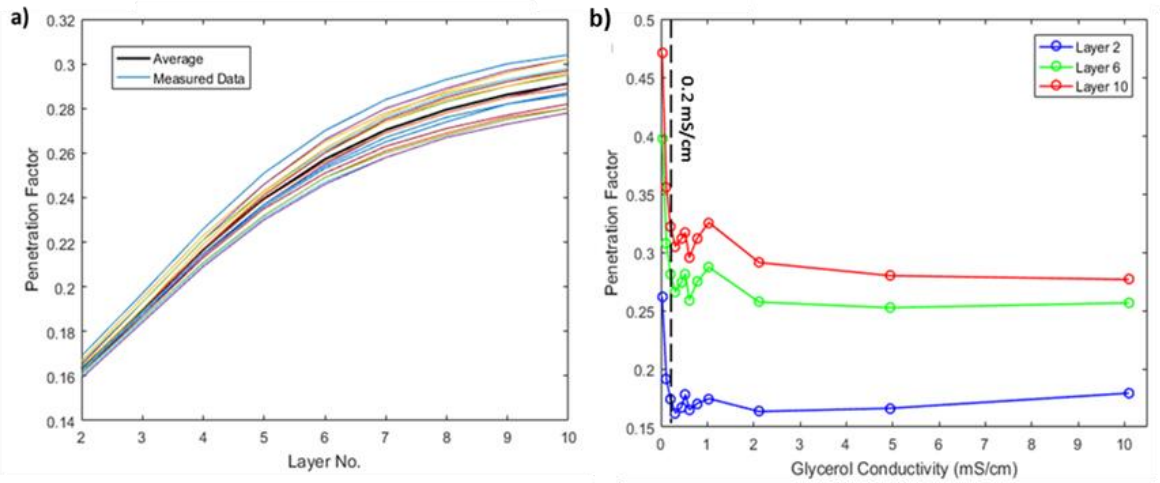

Figure A1.1 Penetration Factor a) Penetration factor for a 75 wt% glycerol solution of conductivity 2 mS cm^{-1}, b) variation in penetration factor with conductivity

For all glycerol solution conductivities, the electrical field penetration was seen to repeatedly be parabolic in nature, with the largest variations observed at the largest radial distance away from the pipe wall. At this position, for a tailored array length of 12 mm this equates to a positional variation of the electrical field of just 0.5 mm. When altering the conductivity, below 0.2 mS cm^{-1} an increase in the penetration factor is observed; however, above this point it plateaus to a constant value of 0.3 for the layer furthest away from the wall. These findings are in agreement with studies performed by Bolton et al. (2004) who utilised Maxwell 3D software to simulate the electrical fields of a linear configuration. It can therefore be said that tailored linear arrays when analysed by the ITS v5r instrument are able to operate at constant penetration depth for the conductivity of 0.2 – 10 mS cm^{-1}. This repeatable phenomena is expected to also occur at much higher conductivities as the ITS v5r instrument is amenable to higher conductivities up to 200 mS cm^{-1}.

Appendix A2

Computational Simulation of the Electrical Impedance Fingerprint

To validate the electrical impedance fingerprinting behaviour further, a 3D EIT sensor has been modelled in COMSOL Multiphysics. This model aims to capture the distribution of electrical current density and averaged potentials of the electrode surfaces when interrogating a range of fluids with varying electrical properties. The modelled sensor, Figure A2.1a, consists of a hollow acrylic cylinder, with inner and outer diameters of 25.4 mm and 30 mm, respectively. A single plane of 16 rectangular electrodes arranged is around the periphery in a circular arrangement. These electrodes were fabricated from copper with the same material utilised for a square ground electrode located 32 mm from the sensing plane.

As in the ITS p2+ instrument, an alternating electrical current excitation signal was applied across two measurement electrodes employing the adjacent measurement protocol; the excitation signal possessed an amplitude of 15 mA and frequency of 19.2 kHz. A single stimulation cycle was monitored with electrode 1 and electrode 16 selected as terminal and ground electrodes, respectively. The obtained voltage potential and electrical field lines that were generated from the model are depicted in Figure A2.1.

The developed model neglects induction, assumes that the electrical field is curl free and is derived from Maxwell's equations in matter, see Chapter 2. These equations additionally govern the mathematical formulation of all electrical tomography modalities and hence considered appropriate to model an EIT sensor (Wang, 2015).

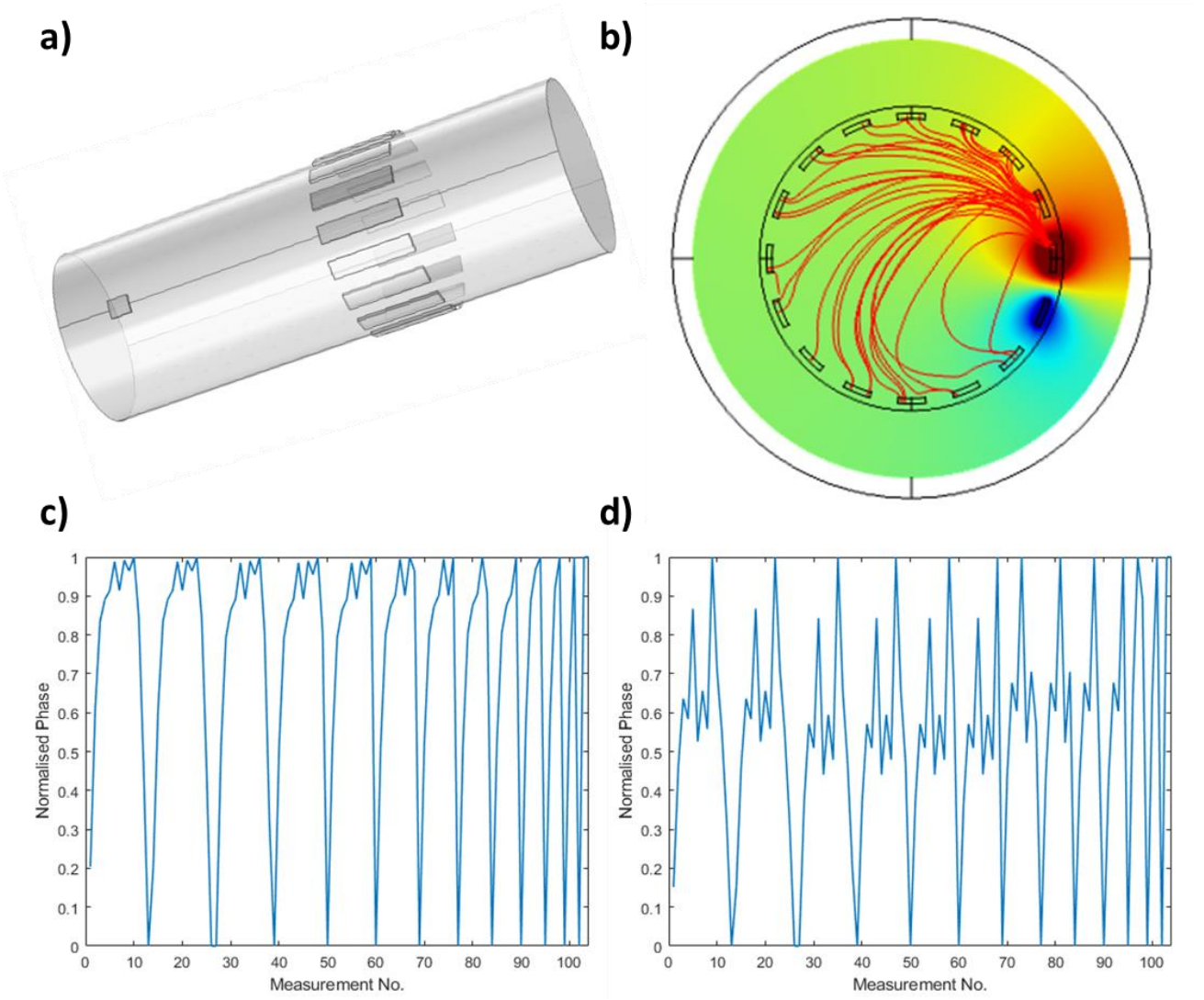

Figure A2.1 Electrical Impedance Fingerprint COMSOL Model: a) sensing geometry; b) voltage distribution and electrical field lines when a interrogating a fluid of 0.1 mS cm^{-1} conductivity and relative permittivity of 80; c) EIF for a 0.1 mS cm^{-1} fluid; d) EIF for a 5 mS cm^{-1} fluid

The measurement electrodes were selected as floating potentials with the surface averaged potential obtained for each electrode. The electrode surface potentials were converted to phase using the inverse tangent of the ratio of the imaginary and real components. Once obtained from the model, the phase measurements were inputted into MATLAB to generate the phase fingerprint across multiple cycles.

The modelled phase fingerprints for fluids of conductivity 0.1 mS cm^{-1} and 5 mS cm^{-1} are depicted for Figures A2.1c and A2.1d, respectively. The phase fingerprint phenomenon once again appears to mirror that described in Chapter 5 with uniform parabolic measurement cycles observed in low admittivity media. This simulated phase fingerprint is seen to be increasingly disordered when interrogating fluids of higher admittivity. As this model is not connected to an EIT electronics system these findings indicate that the EIF phenomenon does not arise as a result of the chosen EIT system electronics and EIF is interrogating the electrical properties of the media within the fluid.

Appendix A3

Characterisation of aqueous model fluids using Electrical Impedance Fingerprinting

In addition to characterising the formulations of surfactant-electrolyte solutions in Chapter 5, Electrical Impedance Fingerprinting (EIF) has been utilised to characterise in-line properties of model fluids, namely aqueous solutions of xanthan gum, *from Xanthomonas Campestris,* and Carbopol 940. These experiments were performed to determine the applicability of EIF to extract differing vital quality parameters across a range of fluids.

A3.1 Methodology

Two model aqueous-based fluids were selected which exhibit behaviour of two common rheological constitutive models, namely solutions of xanthan gum, *from Xanthomonas Campestris* (Sigma-Aldrich, UK) and Carbopol 940 (Lubrizol, UK).

The formulated test fluids consisted of 0.1 wt%, 0.5 wt% and 1.0 wt% xanthan gum powder dissolved in water to form 15 L of aqueous solutions which exhibit shear thinning power law behaviour. A single Carbopol concentration was selected for this study, 0.1 wt% Carbopol, which is known to act as a rheological mimetic for an industrial fluid (Simmons et al., 2009). The pH of the aqueous Carbopol solutions was adjusted within a flow loop by the

incorporation of 0.1 M sodium hydroxide, supplied by Sigma-Aldrich, to induce a gel matrix whose evolving rheological behaviour may be described using the Herschel-Bulkley constitutive law (Alberini et al., 2014). The pH was continuously monitored within the loop by a handheld pH probe supplied by HANNA instruments.

The rheological properties of all of the fluids were analysed using a Discovery HR-1 rotational rheometer (TA Instruments) equipped with a smooth-walled, 4.006° stainless steel cone and plate geometry, of diameter 40 mm. The sample was held at 23 ± 0.1°C using an Peltier plate, before a logarithmic shear rate ramp was applied across the shear rate range of 0.01 - 1500 s^{-1}, over a duration of 600 seconds with 20 points per decade. The selected temperature was chosen as it is reflective of the temperature of the fluid in the subsequent flow experiments. To analyse the obtained data, a non-linear least squares regression was applied in the TRIOS software, developed by TA instruments, to extract fitted rheological parameters. The obtained rheological properties of the fluid are presented within Table A3.1.

A simple recirculating pipeline, similar to that in Chapter 5, was setup which consisted of a flexible impeller pump (Liverani Pumps, UK) and an electromagnetic flow meter (Endress and Hauser, UK) to ensure a fixed flowrate of 300 L hr^{-1}. A 16 electrode, circular microelectrical tomography sensor, of diameter 25.4 mm, was placed within this loop. This sensor was connected to a p2+ EIT instrument (Industrial Tomography Systems Ltd. (ITS), UK) with the circular complex, adjacent measurement protocol selected. The excitation signal in each case was fixed to 30 mA and frequency of 19.2 kHz in each case with 20 delay cycles using the ITS p2+ software. The network architectures and training algorithms optimised in Chapter 5 were utilised for this study and performed within MATLAB. The desired characterisation outputs included xanthan gum concentration and in the case of Carbopol 940, the evolution of pH.

A3.2 Results and Discussion

The use of the phase fingerprint in pipes enables the formulation to be identified from which process decisions may be informed. Initially, three concentrations of xanthan gum were examined upon a categorical basis to determine whether EIF could distinguish between differing formulations. For this, a classification approach was taken; this is analogous to a scenario to determine whether a fluid is on- or off- specification. This simple problem yields a classification accuracy of 99.9 % with just 3 frames misclassified from a dataset of 2,516. This accuracy is reflected in the confusion matrix displayed in Figure A3.1a, with the fall-out rate of less than 1 % also demonstrated. The optimal predictor utilised 10 decision trees with a training time of just 1.68 s enabling adaptive models to be rapidly classified based upon new data; however, it is acknowledged that this initial investigation is a simple problem. This rapid nature is inherent of the bagged decision tree predictor as the trees do not required to be reconstructed but simply refined when new data is provided.

The concentration of xanthan gum can be associated with a number of physical properties including thermal conductivity and rheology with an increase in the concentration yielding an increase in the shear thinning behaviour. The knowledge of such properties may be utilised to optimise a number of upstream or downstream, chemical and physical processes with the shear rheology displayed in Table A3.1 for both xanthan gum and 0.1 wt% Carbopol 940 at differing pH.

Similarly, the rheology of Carbopol 940 evolves with the adjustment of pH; this may also be inferred using EIF. Whilst being recirculated within the pipeline setup the pH of Carbopol 940 was gradually increased from 3.6 to 7.0. This was achieved using 12 aliquots of Sodium Hydroxide with the data analysed using a regression learner to assess the applicability of EIF to continuous pipe processes. This regression is depicted and analysed using a parity plot, Figure A3.1b, which compares the measured pH to the predicted pH. The error bars associated with this figure represent the 99 % confidence intervals (CI_{99}) of the measurement

with the value of the CI_{99} calculated and depicted in Figure A3.1. From this figure it can be seen that maximum 99 % confidence interval is 0.016.

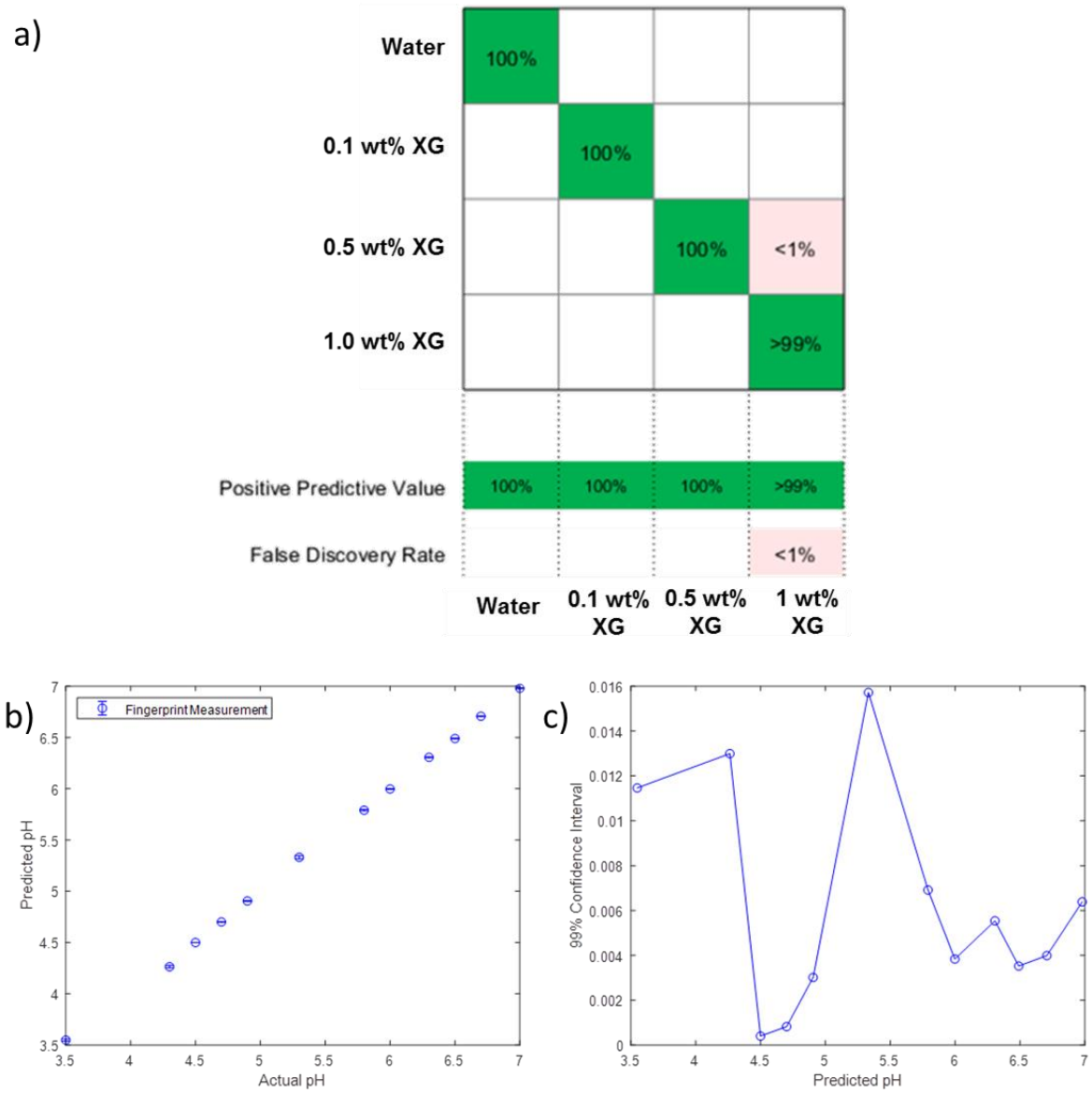

Figure A3.1 EIF Formulation Recognition in pipes: a) categorical identification of xanthan gum; b) continuous recognition of Carbopol pH; c) 99% confidence intervals of Carbopol pH recognition.

The developed model also possessed a root mean squared error (RMSE) of 0.082, mean absolute error (MAE) of 0.032 and excellent agreement with a correlation coefficient, R^2, of 0.99. Such a correlation was observed, despite only a small change observed in the real component of impedance, with a variation in conductivity from 117 - 438 μS cm^{-1}. In this instance, the changes in phase fingerprint are most likely attributed to the imaginary

component. The developed model additionally has the capability to make 21,000 predictions per second; this far exceeds the temporal resolution of the performed EIT measurements which was approximately 1 Hz to ensure the algorithm is adaptive.

Table A3.1 Rheological properties of xanthan gum and Carbopol 940 solutions

Fluid	Yield Stress (Pa)	Consistency Index (Pa s^n)	Power Index
0.1 wt% Xanthan Gum		0.0712	0.723
0.5 wt% Xanthan Gum		1.27	0.350
1.0 wt% Xanthan Gum		6.13	0.195
0.1 wt% Carbopol 940, pH 5	7.44	6.32	0.36
0.1 wt% Carbopol 940, pH 7	1.42	14.6	0.30

The use of xanthan gum and Carbopol 940 has demonstrated that model fluids may be identified, both categorically and continuously, using EIF. From this the evolving, quality properties may be captured, in-situ, for use in process optimisation.

Appendix A4

Hydrodynamic and Rheological Parameters of Sodium Lauryl Ether Sulphate Solutions

This appendix contains supporting information for the characterisation of sodium lauryl ether sulphate and electrolyte systems in Chapter 5. This presents the obtained rheological parameters and resultant hydrodynamic properties within the agitated vessels for 5 wt%, 10 wt%, 15 wt% and 20 wt% aqueous solutions in Tables A4.1 to A4.4, respectively.

Table A4.1 Rheological parameters and hydrodynamic conditions for 5 wt% SLES formulations

5 wt % SLES				
Electrolyte Content (wt%)	Consistency Index (Pa s^n)	Power Index	Reynolds Number	Power Number
0	4.64×10^{-3}	1	9106	0.30
0.75	4.66×10^{-3}	1	9066	0.30
1.50	4.65×10^{-3}	1	9086	0.30
2.25	4.74×10^{-3}	1	8913	0.30
3.00	4.64×10^{-3}	1	9106	0.30
3.75	4.79×10^{-3}	1	8820	0.30
4.50	5.53×10^{-3}	1	7640	0.30
5.25	8.19×10^{-3}	1	5159	0.30
6.00	0.011	1	3841	0.30
6.75	0.062	0.86	940	0.34
7.50	0.199	0.72	405	0.42

Table A4.2 Rheological parameters and hydrodynamic conditions for 10 wt% SLES formulations

10 wt % SLES				
Electrolyte Content (wt%)	Consistency Index (Pa s^n)	Power Index	Reynolds Number	Power Number
0	5.02×10^{-3}	1	8416	0.30
0.75	5.03×10^{-3}	1	8397	0.30
1.50	5.01×10^{-3}	1	8433	0.30
2.25	5.15×10^{-3}	1	8203	0.30
3.00	6.08×10^{-3}	1	6949	0.30
3.75	9.93×10^{-3}	1	4255	0.30
4.50	0.03	1	1408	0.32
5.25	0.43	0.73	183	0.58
6.00	2.59	0.52	49.3	1.01
6.75	12.2	0.26	18.9	1.83
7.50	22.2	0.21	11.2	2.12

Table A4.3 Rheological parameters and hydrodynamic conditions for 15 wt% SLES formulations

15 wt % SLES				
Electrolyte Content (wt%)	Consistency Index (Pa s^n)	Power Index	Reynolds Number	Power Number
0	7.45×10^{-3}	1	5671	0.30
0.75	7.44×10^{-3}	1	5876	0.30
1.50	7.45×10^{-3}	1	5671	0.30
2.25	7.80×10^{-3}	1	5416	0.30
3.00	0.031	1	1385	0.32
3.75	0.198	0.85	301	0.49
4.50	3.88	0.54	31	1.31
5.25	14.5	0.35	13	2.05
6.00	31.1	0.23	8.0	2.54
6.75	37.5	0.18	7.4	2.64
7.50	44.2	0.16	6.6	2.78

Table A4.4 Rheological parameters and hydrodynamic conditions for 20 wt% SLES formulations

20 wt % SLES				
Electrolyte Content (wt%)	Consistency Index (Pa s^n)	Power Index	Reynolds Number	Power Number
0	8.74×10^{-3}	1	4834	0.30
0.75	9.02×10^{-3}	1	4684	0.30
1.50	0.115	1	367	0.46
2.25	11.1	0.41	14.8	2.02
3.00	26.9	0.24	9.0	2.41
3.75	33.3	0.17	8.6	2.46
4.50	44.9	0.13	7.0	2.70
5.25	63.5	0.13	4.9	3.18
6.00	60.1	0.14	5.1	3.13
6.75	67.1	0.10	5.0	3.16
7.50	72.1	0.14	4.2	3.42